frontiers | Research Topics

Global developments towards continuous-wave free-electron lasers

Edited by
Ye Chen, Winni Decking, Yuantao Ding, Julien Branlard,
Ji Qiang, Nicholas Walker, Bo Liu and Tor Raubenheimer

Published in
Frontiers in Physics

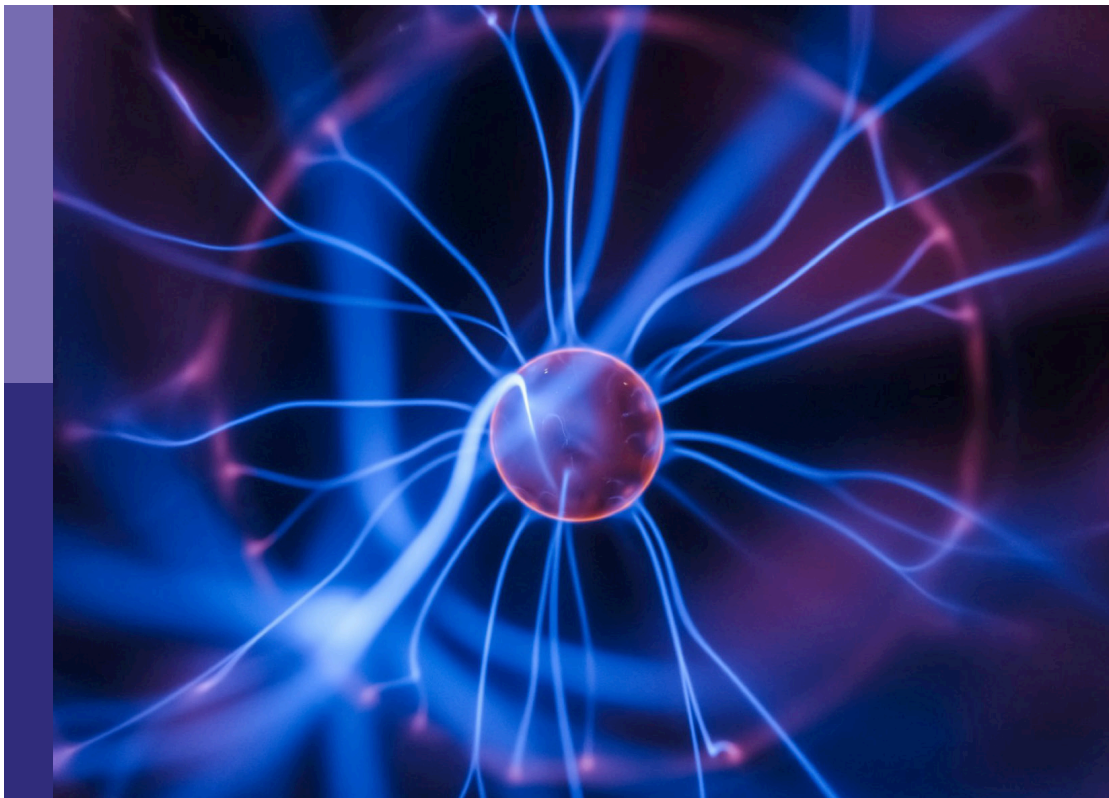

ISSN 1664-8714
ISBN 978-2-8325-3865-4
DOI 10.3389/978-2-8325-3865-4

About Frontiers

Frontiers is more than just an open access publisher of scholarly articles: it is a pioneering approach to the world of academia, radically improving the way scholarly research is managed. The grand vision of Frontiers is a world where all people have an equal opportunity to seek, share and generate knowledge. Frontiers provides immediate and permanent online open access to all its publications, but this alone is not enough to realize our grand goals.

Frontiers journal series

The Frontiers journal series is a multi-tier and interdisciplinary set of open-access, online journals, promising a paradigm shift from the current review, selection and dissemination processes in academic publishing. All Frontiers journals are driven by researchers for researchers; therefore, they constitute a service to the scholarly community. At the same time, the *Frontiers journal series* operates on a revolutionary invention, the tiered publishing system, initially addressing specific communities of scholars, and gradually climbing up to broader public understanding, thus serving the interests of the lay society, too.

Dedication to quality

Each Frontiers article is a landmark of the highest quality, thanks to genuinely collaborative interactions between authors and review editors, who include some of the world's best academicians. Research must be certified by peers before entering a stream of knowledge that may eventually reach the public - and shape society; therefore, Frontiers only applies the most rigorous and unbiased reviews. Frontiers revolutionizes research publishing by freely delivering the most outstanding research, evaluated with no bias from both the academic and social point of view. By applying the most advanced information technologies, Frontiers is catapulting scholarly publishing into a new generation.

What are Frontiers Research Topics?

Frontiers Research Topics are very popular trademarks of the *Frontiers journals series*: they are collections of at least ten articles, all centered on a particular subject. With their unique mix of varied contributions from Original Research to Review Articles, Frontiers Research Topics unify the most influential researchers, the latest key findings and historical advances in a hot research area.

Find out more on how to host your own Frontiers Research Topic or contribute to one as an author by contacting the Frontiers editorial office: frontiersin.org/about/contact

Global developments towards continuous-wave free-electron lasers

Topic editors

Ye Chen — German Electron Synchrotron, Helmholtz Association of German Research Centres (HZ), Germany

Winni Decking — German Electron Synchrotron, Helmholtz Association of German Research Centres (HZ), Germany

Yuantao Ding — Stanford University, United States

Julien Branlard — German Electron Synchrotron, Helmholtz Association of German Research Centres (HZ), Germany

Ji Qiang — Berkeley Lab (DOE), United States

Nicholas Walker — German Electron Synchrotron, Helmholtz Association of German Research Centres (HZ), Germany

Bo Liu — Shanghai Advanced Research Institute, Chinese Academy of Sciences (CAS), China

Tor Raubenheimer — Stanford University, United States

Citation

Chen, Y., Decking, W., Ding, Y., Branlard, J., Qiang, J., Walker, N., Liu, B., Raubenheimer, T., eds. (2023). *Global developments towards continuous-wave free-electron lasers*. Lausanne: Frontiers Media SA.

doi: 10.3389/978-2-8325-3865-4

Table of contents

frontiers | Frontiers in Physics

TYPE Editorial
PUBLISHED 20 October 2023
DOI 10.3389/fphy.2023.1319861

OPEN ACCESS

EDITED AND REVIEWED BY
Alex Hansen,
Norwegian University of Science and Technology, Norway

*CORRESPONDENCE
Ye Chen,
ye.lining.chen@desy.de

RECEIVED 11 October 2023
ACCEPTED 13 October 2023
PUBLISHED 20 October 2023

CITATION
Chen Y, Branlard J, Decking W, Ding Y, Liu B, Qiang J, Raubenheimer T and Walker N (2023), Editorial: Global developments towards continuous-wave free-electron lasers.
Front. Phys. 11:1319861.
doi: 10.3389/fphy.2023.1319861

Editorial: Global developments towards continuous-wave free-electron lasers

Ye Chen[1]*, Julien Branlard[1], Winfried Decking[1], Yuantao Ding[2], Bo Liu[3], Ji Qiang[4], Tor Raubenheimer[2] and Nicholas Walker[1]

[1]Deutsches Elektronen-Synchrotron DESY, Hamburg, Germany, [2]SLAC National Accelerator Laboratory, Menlo Park, CA, United States, [3]Shanghai Advanced Research Institute, Chinese Academy of Sciences, Pudong, Shanghai, China, [4]Lawrence Berkeley National Laboratory, Berkeley, CA, United States

KEYWORDS

linear accelerator, free-electron lasers, continuous-wave, MHz repetition rate, photoinjector, beam dynamics, low-level RF, undulator

Editorial on the Research Topic
Global developments towards continuous-wave free-electron lasers

Linear accelerator-based free-electron lasers (FELs) provide fully coherent X-rays with ultra-high peak powers and femtosecond-duration pulse lengths. The X-ray peak brightness is approximately one billion times greater than that available at synchrotron radiation facilities. This enables high-resolution analysis of the atomic structure of crystalline matter, opening up new frontiers across many fields of science and motivating a vast amount of interdisciplinary applications.

Self-amplified spontaneous emission (SASE) is the most common operational mechanism for FELs. While proving excellent performance, the SASE FEL is rapidly approaching towards its next-generation for delivering intense SASE radiation at a MHz-level repetition-rate in a continuous-wave (CW) mode. The MHz-level CW FEL can significantly extend the capability of existing FELs by allowing for more flexibility in the photon beam time patterns and an increased average brightness.

The pulse repetition rate is determined by the acceleration technology, and it is much higher in superconducting facilities. Confronting challenges in developing MHz-level CW X-ray FELs, several world-class FEL machines are put into practice, the Linac Coherent Light Source II in the USA [1], [2], the Shanghai high repetition rate XFEL and extreme light facility in China [3], and the European X-ray Free-Electron Laser in Germany [4]. Tremendous efforts are being made worldwide, not only by the afore-stated pioneering facilities, but also almost every facility in the FEL community contributing to individual technical aspects of this global development.

Realization of MHz-level CW X-ray FELs calls for dedicated research and development (R&D) programs in physical design and technical development. This includes necessary modifications of relevant sub-systems in an existing FEL facility, and also start-to-end beam physics simulation of the developed accelerator and photon beam lines. Specific R&D programs are demanded in many aspects including but not being limited to CW electron sources, superconducting radio-frequency (SRF) accelerator cryomodules, cryogenics, cavities, RF power sources, Low-Level RF (LLRF), controls and undulators. The goal of this Research Topic is to summarize the obtained achievements and report on the

development status of MHz-level CW X-ray FELs covering a selection of the aforementioned aspects. A state-of-the-art summary of the Research Topic is thus given.

A suitable electron source should demonstrate stable performance at a MHz-level repetition rate and deliver high-quality beams. Stringent requirements are thus posed on the choice of photocathode and its drive laser system, CW electron gun and the associated photoinjector configuration. As included in this Research Topic, Zhang et al. report a high repetition-rate photoinjector laser system, capable of generating 257.5 nm ultraviolet (UV) laser of more than 2 W average power with both spatial and temporal shaping functionalities. This has been tested for long-term stability showing good operating performance for a planned CW FEL facility located in Shenzhen, China. Zhao et al. address an important aspect in photocathode research by theoretically evaluating the quantum efficiency (QE) of semiconductor cathodes at cryogenic temperature. This is exemplarily demonstrated for the K-Cs-Sb photocathode used in a DC-SRF photoinjector at Peking University in China. A comprehensive summary of the requirements for an electron injector to operate in a high-duty-cycle (HDC) X-ray FEL is given by Sannibale, with a focus placed on the technological choices that the high duty cycle imposes, and on the beam dynamics implications that such choices cause. It is generally well known, that the most critical component in a photoinjector is the electron gun. As for this aspect, Zhou et al. provide a detailed overview of CW electron guns, including diverse types of DC, SRF, hybrid DC-SRF and normal-conducting RF. In particular, the gun performance, evaluated from the very recent commissioning for the LCLS-II injector, is demonstrated. A 0.5-μm emittance for 50 pC bunches with the desired bunch length has been obtained. It is also worth summarizing, for the past two decades, the highly valuable results obtained in the R&D of the SRF technology based photoinjectors, as the SRF guns have great potential to provide the high-brightness, high-current beams as required for the CW X-ray FELs. From this perspective, Xiang et al. have provided a detailed summary of the SRF photoinjectors worldwide.

A crucial role still plays by the electron-beam-physics based design and optimization of the key accelerator components and the whole transfer line from the electron source to the entrance of the undulators. Here two Research Topics are selected. Zhang et al. propose a so-called multiplexed configuration for the beam dynamics optimization of the LCLS-II photoinjector, aiming to enhance the flexibility of beam manipulation for the improvement of multiplexing capabilities of the FEL facility. Downstream the photoinjector, it is of significant importance to preserve the quality of the optimized electron beam as traveling through the whole beam transfer line. Effects that may lead to the dilution of the transverse bunch emittance and the longitudinal bunch length must be eliminated to a large extent. Zhang and Jiao re-address noteworthy issues with the emission of coherent synchrotron radiation (CSR) and the longitudinal dispersion causing degradation of the bunch quality. An advanced design and optimization are further proposed for a compact 180 deg transport arc, comprised of muti-triple-bend achromat (TBA) cells, for efficiently suppressing the undesirable effects mentioned above and thus maintaining the achieved bunch quality from the injector.

Another key aspect of an HDC upgrade (e.g., an improvement in the present machine duty factor from about 1% at the European XFEL to more than 5% and up to CW) of existing FELs lies in the production of required SRF cavities with high Q values and high gradients. This has motivated extensive studies of cavity production via nitrogen doping and infusion; Interrelated R&D topics, as a request of operating SRF modules in the CW mode, are under investigation aiming to bring the cryogenic load and the capacity of the cryogenics systems in line with each other; Attention has also been drawn to the development of CW RF power sources and couplers. Of equal importance is the development of the precision low-level RF (LLRF) controls which are mandatory for stabilizing the very narrow bandwidth associated with CW-operated SRF cavities. Specifically, in this Research Topic, development of a feedforward resonance control scheme is proposed by Bellandi et al. for the HDC upgrade of the European XFEL. This allows the LLRF system to accurately track and control the cavity resonance frequency for acheiving the desired accelerating gradient.

Superconducting undulators (SCUs), capable of reaching higher peak field on axis with respect to all other available technologies, covering a larger photon energy tunable range and showing stronger radiation hardness with respect to permanent magnet undulators, have drawn great attention in the community for potential applications in the high repetition rate FELs. Here we collect two articles on the R&D of SCUs. Wei et al. explicitly present the development of NbTi planar SCUs at the institute of high energy physics (IHEP) in China. Casalbuoni et al. introduce SCU activities at the European XFEL describing the general potential of SCUs for X-ray FELs and corresponding R&D efforts. In additional consideration of generating variable polarization, a Research Topic by Yu et al. is included for developing an APPLE III undulator prototype for SHINE, where it is planned to install several elliptically polarizing undulators (EPUs) as afterburners behind the planar undulator section to obtain nearly-saturated circularly polarized FEL radiation.

Closely following the development status of CW FELs worldwide, the editorial team notes that, first lasing results have been obtained at the LCLS-II, successfully demonstrating soft X-ray lasing from 250 eV to 1000 eV and hard X-ray lasing up to 3.8 keV [5]. In the meantime, commissioning of the soft X-ray FEL line of SHINE is expected in 2025 as explicitly introduced by Liu et al. The working principle of few-femtosecond X-ray pulse generation and pulse duration control is demonstrated by Fan et al. using the Shanghai Soft X-ray Free Electron Laser Test Facility (SXFEL-TF) [6], [7]. At the European XFEL, extensive R&D studies have been carried out [8–10]. Detailed technical developments of relevant subsystems for an HDC upgrade of the facility are on the way.

This editorial is devoted to briefly present the overall scope of the Research Topic and the included papers regarding selected aspects towards the development of CW FELs. The editorial team takes the opportunity to thank all authors of the articles published on this Research Topic for their valuable contributions and the Frontiers in Physics team for the technical assistance with publishing.

Author contributions

YC: Investigation, Project administration, Validation, Writing–original draft, Writing–review and editing. JB: Investigation, Project administration, Validation, Writing–review and editing. WD: Investigation, Project administration, Validation, Writing–review and editing. YD: Investigation, Project administration, Validation, Writing–review and editing. BL: Investigation, Project administration, Validation, Writing–review and editing. JQ: Investigation, Project administration, Validation, Writing–review and editing. TR: Investigation, Project administration, Validation, Writing–review and editing. NW: Investigation, Project administration, Validation, Writing–review and editing.

Conflict of interest

The authors declare that the research was conducted in the absence of any commercial or financial relationships that could be construed as a potential conflict of interest.

Publisher's note

References

1. Emma P, Akre R, Arthur J, Bionta R, Bostedt C, Bozek J, et al. First lasing and operation of an ångström-wavelength free-electron laser. *Nat Photon* (2010) 4:641–7. doi:10.1038/nphoton.2010.176

2. Stohr J. *Linac coherent light source II (LCLS-II) conceptual design report*. TRN: US1200028. Menlo Park, CA, United States: SLAC National Accelerator Lab (2011). doi:10.2172/1029479

3. Zhu ZY, Zhao ZT, Wang D, Liu Z, Li RX, Yin LX, et al. SCLF: an 8-GEV CW SCRF linac-based x-ray FEL facility in Shanghai. In: Proceedings of the 38th International Free-Electron Laser Conference; August 2017; Santa Fe, NM, United States (2017). p. 182–4. doi:10.18429/JACoW-FEL2017-MOP055

4. Decking W, Abeghyan S, Abramian P, Abramsky A, Aguirre A, Albrecht C, et al. A MHz-repetition-rate hard X-ray free-electron laser driven by a superconducting linear accelerator. *Nat Photon* (2020) 14:391–7. doi:10.1038/s41566-020-0607-z

5. SLAC . SLAC fires up the world's most powerful X-ray laser: LCLS-II ushers in a new era of science (2023). https://www6.slac.stanford.edu/news/2023-09-18-slac-fires-worlds-most-powerful-x-ray-laser-lcls-ii-ushers-new-era-science (Accessed October 6, 2023).

6. Zhao Z, Wang D, Gu Q, Yin L, Gu M, Leng Y, et al. Status of the SXFEL facility. *Appl Sci* (2017) 7:607. doi:10.3390/app7060607

7. Liu B, Zhang W, Fang W, Wang Z, Zhou Q, Leng Y, et al. The SXFEL upgrade: from test facility to user facility. *Appl Sci* (2021) 12:176. doi:10.3390/app12010176

8. Brinkmann R, Schneidmiller EA, Sekutowicz J, Yurkov MV. Prospects for CW and LP operation of the European XFEL in hard x-ray regime. *Nucl Instr Methods Phys Res Section A: Acc Spectrometers, Detectors Associated Equipment* (2014) 768:20–5. doi:10.1016/j.nima.2014.09.039

9. Sekutowicz J, Ayvazyan V, Barlak M, Branlard J, Cichalewski W, Grabowski W, et al. Research and development towards duty factor upgrade of the European X-Ray Free Electron Laser linac. *Phys Rev ST Accel Beams* (2015) 18:050701. doi:10.1103/PhysRevSTAB.18.050701

10. Bazyl D, Chen Y, Dohlus M, Limberg T. CW operation of the European XFEL: SC-gun injector optimization, S2E calculations and SASE performance (2021) https://arxiv.org/abs/2111.01756 (Accessed November 2, 2021).

frontiers | Frontiers in Physics

TYPE Original Research
PUBLISHED 13 March 2023
DOI 10.3389/fphy.2023.1122608

OPEN ACCESS

EDITED BY
Yuantao Ding,
Stanford University, United States

REVIEWED BY
Zhen Zhang,
Stanford University, United States
Enrico Allaria,
Elettra Sincrotrone Trieste, Italy

*CORRESPONDENCE
Chao Feng,
fengchao@zjlab.org.cn
Zheng Qi,
qizheng@zjlab.org.cn

SPECIALTY SECTION
This article was submitted to Interdisciplinary Physics, a section of the journal Frontiers in Physics

RECEIVED 13 December 2022
ACCEPTED 22 February 2023
PUBLISHED 13 March 2023

CITATION
Fan W, Qi Z, Feng C and Zhao M (2023), Few-femtosecond X-ray pulse generation and pulse duration control in a seeded free-electron laser.
Front. Phys. 11:1122608.
doi: 10.3389/fphy.2023.1122608

Few-femtosecond X-ray pulse generation and pulse duration control in a seeded free-electron laser

Weijie Fan[1,2], Zheng Qi[3]*, Chao Feng[3]* and Minghua Zhao[1,2]

[1]Shanghai Institute of Applied Physics, Chinese Academy of Sciences, Shanghai, China, [2]University of Chinese Academy of Sciences, Beijing, China, [3]Shanghai Advanced Research Institute, Chinese Academy of Sciences, Shanghai, China

With the development of ultrafast science, free-electron lasers (FELs) with ultrashort pulses have become a state-of-the-art tool in ultrafast phenomena studies. In an externally seeded FEL, the output pulse duration is usually determined both by the seed laser pulse duration and FEL amplification process, which can hardly reach the timescale of a few femtoseconds. In this study, through a simple method of changing the relative time delay and correspondingly the pulse energy of the two seed lasers employed in a seeded FEL, we demonstrated the possibility of generating few-femtosecond soft X-ray pulses and controlling the final FEL pulse durations. Based on theoretical calculations and practical experiments, we conducted a detailed study on the capabilities and limitations to this method with the parameters of the Shanghai Soft X-ray FEL Facility. Start-to-end simulations indicate that we can achieve ultrashort soft X-ray FEL pulses with the pulse duration down to 5.2 fs, and the final pulse durations can also be controlled in terms of relative time delays.

KEYWORDS

free-electron laser, ultrashort pulse, pulse duration, cascaded EEHG–HGHG, energy modulation, slippage effect

1 Introduction

The X-ray free-electron laser (XFEL) with high brightness, short pulse durations, superior coherence, and wide tuning ranges has become a powerful tool in numerous scientific research areas, such as molecular, atomic, and electronic motions. Comparing with synchrotron radiation, the XFEL has extraordinary advantages of high resolution in both temporal and spatial dimensions. Today, with the realization of a high-gain free-electron laser, several large-scale FEL facilities around the world have been built up to provide XFEL pulses [1–6]. XFELs usually have a pulse duration of tens to hundreds of femtoseconds. To shorten the pulse length down to a few femtoseconds or even sub-femtosecond timescale, several approaches have been proposed [7–13]. Ultrashort X-ray pulses having a few to tens of femtoseconds can image the dynamics of individual nanostructures and protein nanocrystals, which will promote a promising development in the fields of structural biology, medicine dynamics, and neuroscience [14–21].

The basic working scheme of XFELs is self-amplified spontaneous emission (SASE) [22–24], which has a relatively low temporal coherence and high pulse-energy fluctuations since the initial signal is derived from a shot noise of the electron beam. Throughout the last decade, the self-seeding method [25–29] has been proven highly effective to significantly

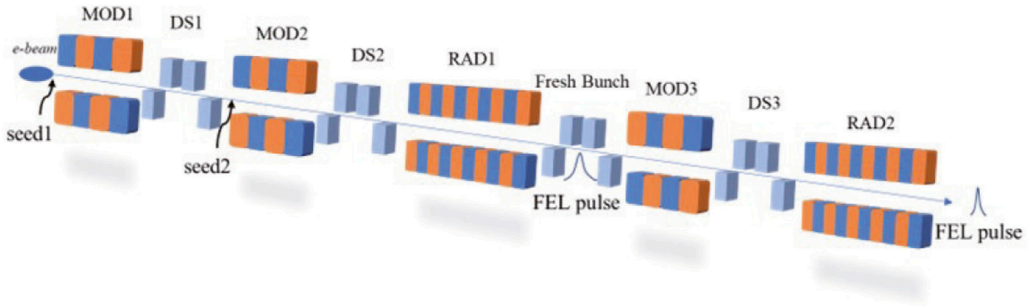

FIGURE 1
Schematic layout of the SXFEL-UF.

increase the temporal coherence of the SASE XFEL pulses. Using a monochromator and a bypass chicane implemented between two undulator sections, the self-seeding method can obtain monochromatic light from the SASE FEL pulse developed in the up-front undulator section and amplify it to saturation in the subsequent undulator section. However, there are still noticeable shot-to-shot fluctuations in the output pulse energy. Another effective way to improve the temporal coherence and stability of high-gain FELs is through the external seeding strategy, which includes the high-gain harmonic generation (HGHG) [30–34] and the echo-enabled harmonic generation (EEHG) [35–41]. EEHG is also one of the most promising configurations for generating a fully coherent FEL radiation at the Shanghai High-Repetition-Rate XFEL and Extreme Light Facility (SHINE) [42]. Although they can hardly reach tender X-ray and hard X-ray regimes, the externally seeded FELs can produce fully coherent soft X-ray radiation pulses. The pulse duration in a seeded soft X-ray FEL is usually determined both by the seed laser pulse duration and FEL amplification process, which can hardly reach the timescale of a few femtoseconds [43–46]. The latest study has found that externally seeded FELs can generate few-femtosecond extreme-ultraviolet FEL pulses with the superradiant cascade technique, but the duration of these pulses cannot be flexibly controlled [47].

In this paper, a simple method has been studied for generating few-femtosecond soft X-ray pulses and controlling the final FEL pulse durations in an externally seeded FEL. The method is mainly based on the EEHG scheme. By changing the relative time delay of the two seed lasers employed in EEHG, there will appear a finite bunched part in the electron beam, which can radiate ultrashort soft X-ray FEL pulses, and the pulse durations can be varied in terms of different relative time delays. Through theoretical calculations and practical experiments, we conduct a detailed study on the performance of the method in both the single-stage EEHG and the cascaded EEHG–HGHG scheme based on the Shanghai Soft X-ray FEL Facility (SXFEL).

2 Theoretical analysis and optimization

The principles of EEHG have been promoted for a decade, which primarily focuses in producing fully coherent soft X-ray FEL pulses. The cascaded EEHG–HGHG scheme was proposed then to further extend the photon energy coverage and obtain a narrower spectrum. SXFEL can work both on the SASE and external seeding modes, in which the single-stage EEHG scheme and cascaded EEHG–HGHG scheme are all applicable. The schematic layout of the cascaded EEHG–HGHG in SXFEL is shown in Figure 1. The whole beamline comprised an EEHG as the first stage and an HGHG as the second stage, with a fresh-bunch chicane located in between. The first-stage EEHG setup consists of two modulation sections (MOD1 and MOD2), two dispersion sections (DS1 and DS2), and an FEL radiator (RAD1). The second-stage HGHG setup consists of a modulator (MOD3), a dispersion section (DS3), and a final FEL radiator (RAD2). The electron beam from the upstream LINAC will first go through the EEHG-FEL setup to generate an initial radiation pulse in RAD1. With appropriate delays of the electron beam in the fresh-bunch chicane, the first-stage EEHG-FEL radiation pulse will slip ahead into the head of the electron beam and work as a seed laser in the following HGHG-FEL setup.

In a typical EEHG scheme, assuming a seed laser with a Gaussian power profile of an rms width σ_s and central wavelength λ_s, the electric field distribution along the electron beam can be characterized as

$$E(s) = E_0 e^{-s^2/4\sigma_s^2} e^{i(k_s s+\phi_0)}, \tag{1}$$

where s is the longitudinal coordinate along the electron bunch, E_0 is the peak electric field intensity, $k_s = 2\pi/\lambda_s$ is the wavenumber of the seed laser, and ϕ_0 is the initial carrier-envelope phase of the laser. As to the energy exchange in the modulator, the energy modulation $\Delta\gamma$ for an electron beam with central kinetic energy γ can be given as

$$\Delta\gamma(s) = \int_0^z \frac{eK[JJ]}{2\gamma mc^2} E(s)dz, \tag{2}$$

where K is the unitless undulator parameter ($K = 0.934B\lambda_u$ with B in Tesla and λ_u in centimeter), and $[JJ]$ and z characterize the modified Bessel factor $[JJ] = J_0[K^2/(4+2K^2)] - J_1[K^2/(4+2K^2)]$ and the length of the modulator, respectively. Normally, the two seed lasers employed in the two modulators in EEHG should be synchronized, interacting in the same position within the electron bunch, so that the EEHG effect can be fulfilled at the most. However, in the proposed method, to generate ultrashort EEHG FEL pulses, two seed lasers are designed to have a relative time delay of δs, and in the overlapped area, the laser intensities are

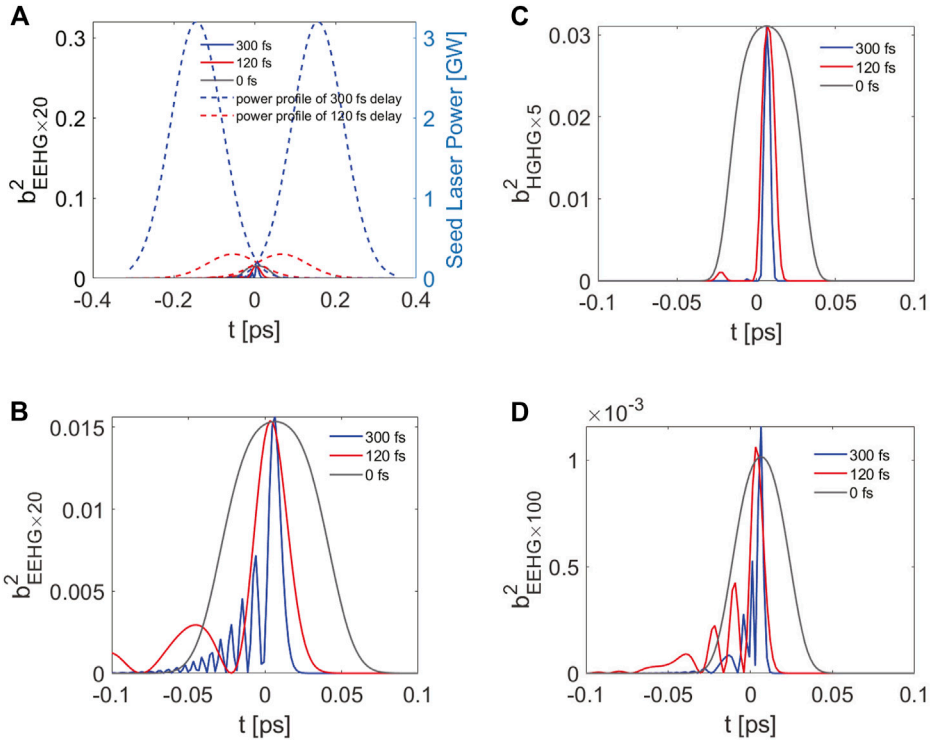

FIGURE 2
(A) Squared bunching factors of the cascaded scheme at the entrance of RAD1 with different time delays and the corresponding power profiles of the seed lasers. **(B)** Zoomed bunching factors of Figure 2A. **(C)** Squared bunching factors of the cascade scheme at the entrance of RAD2 with different relative time delays of the two seed lasers. **(D)** Squared bunching factors of the single-stage EEHG scheme at the entrance of the radiator with different relative time delays of the two seed lasers.

set to optimized values for given dispersive strengths of chicanes. Under this condition, the maximum bunching factor will appear in the intermediate position $s + \delta s/2$. Considering the situation here, the energy modulation in the first modulator (MOD1) can be written as$\Delta\gamma_1 = \frac{eK[JJ]}{2\gamma mc^2} E(s)z$, while in the second modulator (MOD2), $\Delta\gamma_2 = \frac{eK[JJ]}{2\gamma mc^2} E(s+\delta s)z$. The maximum bunching factor is optimized at the new modulation position $s + \delta s/2$. To satisfy the modulation strength requirements at this position, the pulse energy of the seed lasers should change simultaneously, according to the relative time delay of the two seed lasers. At the exit of the second dispersion section (DS2), the bunching factor of the hth harmonic number at the selected modulation position can be similarly written as

$$b_h(s) = \left|\exp^{-[-B_1+(m-1)B_2]^2/2} J_m[-(m-1)A_2(s+\delta s)B_2] \times J_{-1}\{-A_1(s)[-B_1+(m-1)B_2]\}\right|, \quad (3)$$

where $h = m - 1$ with an integer m. $A = \Delta\gamma/\sigma_\gamma$ denotes the modulation amplitude in the modulators, and $B = R_{56}k_s\delta_\gamma/\gamma$, where R_{56} represents the dispersive strength of the chicanes. $\Delta\gamma$ is the modulation depth. δ_γ is the slice energy spread. After the fresh-bunch chicane, the first-stage EEHG-FEL radiation will interact with a fresh part of the electron beam in MOD3 in the second-stage HGHG with an amplitude of $\Delta\gamma = \frac{eK[JJ]}{2\gamma mc^2} E(s')z$ at the new position s'. After DS3, the bunching factor can be described as

$$b(s') = \left|\exp^{-B_3^2/2} J_n(nA(s')B_3)\right|. \quad (4)$$

Here, we adopt the configurations of the SXFEL-UF to conduct the calculations of our proposed method. The calculations are performed based on the cascaded EEHG-HGHG scheme with relative time delays of 0, 120, and 300 fs. For the 120-fs case, the maximum energy modulation amplitudes A_1 and A_2 of the two seed lasers are both 4.8. For the 300-fs case, the maximum energy modulation amplitudes A_1 and A_2 are both 15.7. At the local manipulation position, the energy modulation amplitudes are all optimized to be 4. The energy modulation amplitude in MOD3 is about 5. The strength of DS1 is about 5.38. The harmonic number of the first stage EEHG is 20 and that of the second stage HGHG is 5. Hence, the total frequency up-conversion number is 100. Using the aforementioned theory, the squared bunching factors at the entrance of RAD1 and RAD2 with different time delays are shown in Figures 2A,C. The peak power of the seed lasers is also shown in Figure 2A. We can see that the smaller the relative time delay, the lower the peak power. In addition, we can obtain a qualitative analysis of the pulse durations based on the bunching factor distributions. Figure 2B shows a local enlarged image of Figure 2A that shows the bunching factor distributions in the overlapped region. One can find out that with the increase of the relative time delay, the pulse durations of the first-stage EEHG and the second-stage HGHG will both be shortened. We can also see that the first-stage EEHG has

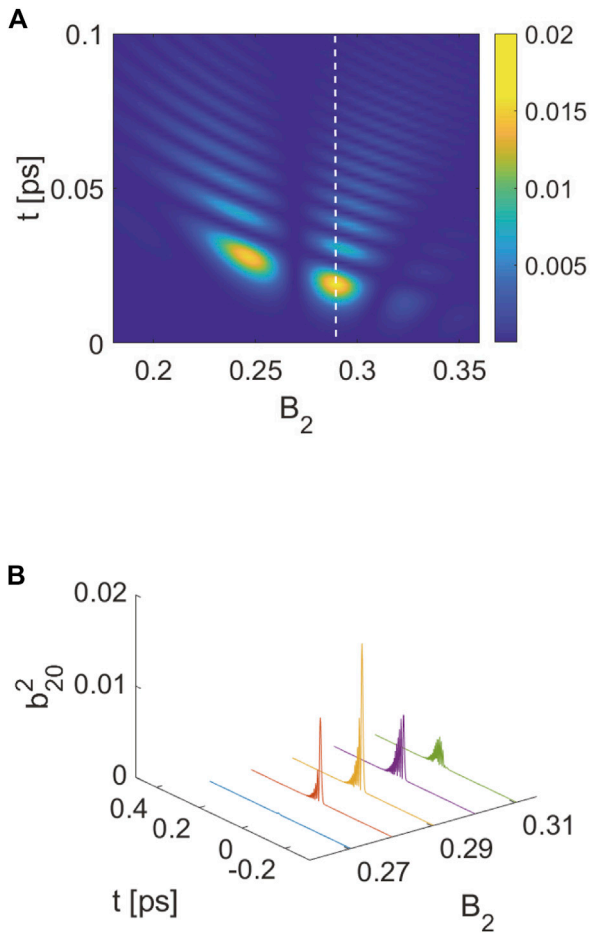

FIGURE 3
Optimization of B_2 of EEHG. **(A)** Squared bunching factor distributions with respect to different dispersion strengths B_2. The white dashed line is the optimized strength of DS2. **(B)** Projection around the white dashed line.

several side peaks, while the second-stage HGHG does not. To make comparisons, the squared bunching factors of the single-stage EEHG with the parameters optimized for the harmonic number of 100 are shown in Figure 2D, where one can also find that the bunching factor distributions under longer time delays will have narrower pulse durations. Also, the final pulse duration is comparable to that in the cascaded EEHG-HGHG scheme. However, considerable side peaks appeared in the single-stage EEHG scheme will result in similar longitudinal profiles of the FEL output, while in the cascaded EEHG-HGHG scheme, an isolated pulse can be generated.

Generally, the dispersion strength B_2 of DS2 in the first-stage EEHG setup is critical to bunching properties. We demonstrate the optimization results of the bunching factor distributions with respect to different B_2 values, as shown in Figure 3. Figure 3A shows a large-scale three-dimensional scanning map. In addition, we select the right hot spot to be the optimized value of B_2 for a higher bunching factor and narrower width, which is 0.29 in dimensionless. Figure 3B shows the projection around the white dashed line. We can clearly see that there are many satellite side peaks along the bunching factor distributions. In addition, the satellite side peaks arising here can barely be eliminated. The reason is that, in the EEHG mechanism, the bunching properties are sensitive to the second modulation amplitude A_2, which is gradually changing with respect to their longitudinal positions due to the practical power profile of the overlapped seed laser part. Furthermore, the satellite peaks will appear when the changing amplitudes A_2 meet the local optimized conditions for a fixed given B_2 value. However, in the cascaded EEHG-HGHG scheme, even though the side peaks are nearly inevitable in the first-stage EEHG, by selecting an appropriate dispersion strength of DS3, they can be eliminated in the second-stage HGHG. In MOD3, the modulation amplitudes are relatively large at the main peak and relatively small at the side peaks. After DS3, with an R_{56} value optimized for the main peak, density modulation at the main peak will show a higher bunching factor than that at the side peaks. Hence, the main peak will generate ultrashort FEL pulses in RAD2 without side peaks. The strength of DS3 is set to be 0.24 to meet the optimized condition of the HGHG section and eliminate the side peaks from EEHG.

TABLE 1 Parameters for the SXFEL-TF experiments.[49].

Parameter	Value	Unit
Electron beam		
Energy	800	MeV
Peak current	400	A
Bunch length (FWHM)	1.3	ps
Normalized emittance	1.5	mm·mrad
Seed laser		
Wavelength	266	nm
Pulse energy (seed 1/seed 2)	10/30	μJ
Pulse duration (FWHM)	170	fs
Modulator (MOD1/MOD2/MOD3)		
Period length	0.08/0.08/0.055	m
Total length	1.44/1.44/1.65	m
Radiator (RAD1/RAD2)		
Period length	0.04/0.0235	m
Total length	3 × 4/3 × 6	m

3 Experiments at the soft X-ray free-electron laser test facility

With the aforementioned theoretical analysis, we have conducted calculations and experiments at the Shanghai Soft X-ray Free-Electron Laser Test Facility (SXFEL-TF) to demonstrate the performance of the method. The parameters of the SXFEL-TF are shown in Table 1. Cascaded EEHG–HGHG is the basic working scheme at the SXFEL-TF, in which the harmonic number of the first-stage EEHG is 6 and that of the second-stage HGHG is 5. We can eventually achieve 8.8-nm soft x-ray FEL

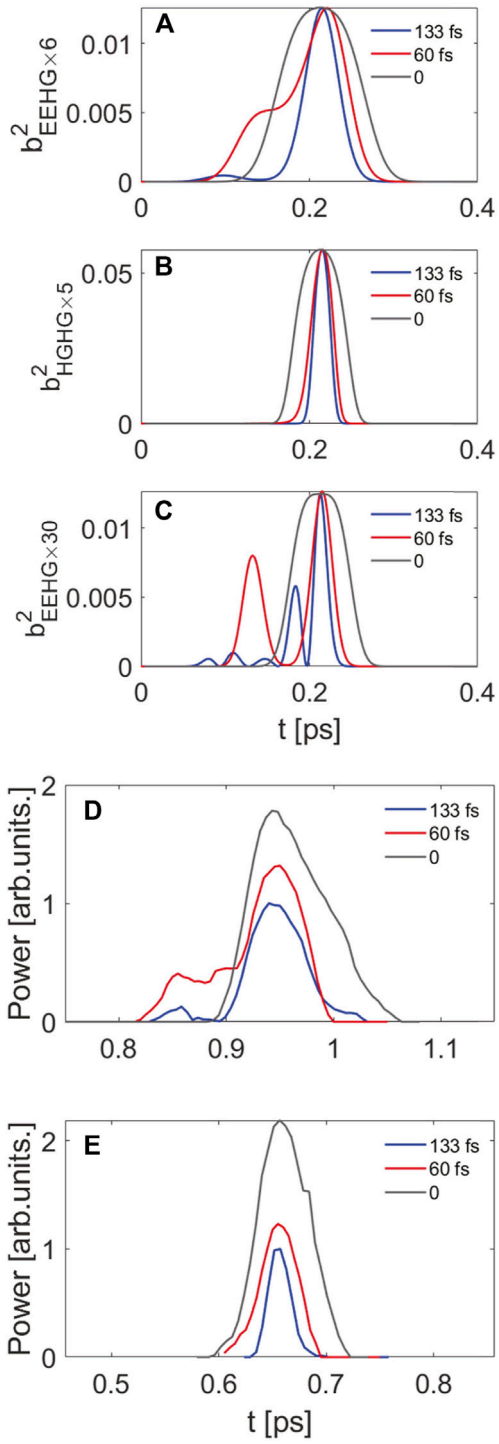

FIGURE 4
(A) Squared bunching factors of the first-stage EEHG with different time delays. **(B)** Squared bunching factors of the second-stage HGHG with different time delays. **(C)** Squared bunching factors of the single-stage EEHG with different time delays. Experimental results of the normalized reconstructed FEL power profiles for different time delays: **(D)** the first-stage EEHG-FEL pulses; **(E)** the second-stage HGHG-FEL pulses.

radiation from the 264-nm ultra-violet external seed laser. Based on the typical parameters and configurations of the SXFEL-TF, we conducted the numerical calculations and practical experiments for

TABLE 2 Parameters for the start-to-end simulations.

Parameter	Value	Unit
Electron beam		
Energy	1,563	MeV
Peak current	800	A
Sliced energy spread	0.013%	
Normalized emittance	1.5	mm·mrad
Seed laser		
Wavelength	266	nm
Pulse energy	480	μJ
Pulse duration (FWHM)	150	fs
Modulator (MOD1/MOD2/MOD3)		
Strength of DS1/DS2	1.7e3/93	μm
Period length	0.08/0.08/0.03	m
Total length	1.6/1.6/1.5	m
Radiator (RAD1/RAD2)		
Strength of DS3	6.9	μm
Period length	0.03/0.0235	m
Total length	3 × 4/3 × 4	m

our method with different relative time delays of the two seed lasers employed in the first-stage EEHG. The results are shown in Figure 4. In the calculations, the squared bunching factors after the first-stage sixth harmonic EEHG and after the second-stage fifth harmonic HGHG with respect to different time delays are shown in Figures 4A,B. We can see that although the maximum bunching factors are basically the same, the approximately equivalent pulse durations of the first-stage EEHG and the second-stage HGHG are both shorter for the relatively larger time delay of 133 fs. In comparison, the squared bunching factors of the single-stage 30th harmonic EEHG are shown in Figure 4C. We can clearly see that there exist side peaks beside the main bunching peak for the 133-fs time delay case, while for cascaded EEHG-HGHG, the final bunching factor distributions shown in Figure 4B are much cleaner.

In the experiments, with the increase of the relative time delay of the two seed lasers, the pulse energy was also increased. The pulse energy is 30 μJ for the relative time delay of 133 fs, while for the 60-fs case, it is 10 μJ. The results of the experiments are shown in Figures 4D,E. We have reconstructed the normalized FEL radiation profiles with the relative time delay 0 fs, 60 fs, and 133 fs [48,49]. The power profiles shown in Figure 4D correspond to the first-stage EEHG, while Figure 4E corresponds to the second-stage HGHG. Figure 4D shows that there exist small side peaks in the first-stage EEHG radiation with the time delay being 60 fs and 133 fs, while Figure 4E shows that the second-stage HGHG can deliver single spike pulses with narrower durations. The duration of the FEL pulse from the first stage is about 85 fs (FWHM) for the 0-fs time delay case, and around 58 fs (FWHM) for the 60-fs and 133-fs delay cases, as shown in Figure 4D. The FEL pulse durations from RAD2 will further be

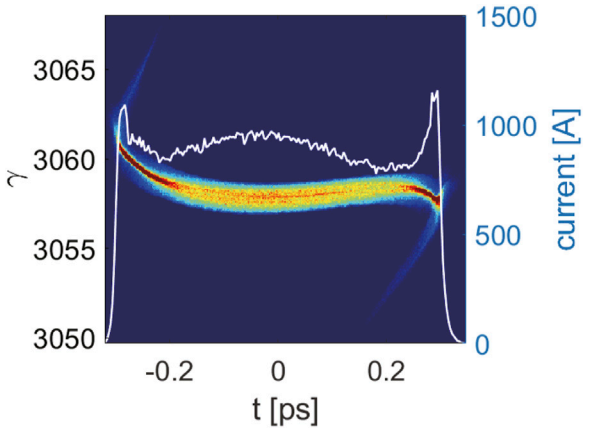

FIGURE 5
Longitudinal phase space and current distribution of the electron beam by the end of the LINAC of the SXFEL-UF.

shortened due to the pulse shortening effect [49–51]. The final pulse duration for the 0-fs time delay is about 57 fs (FWHM), for the 60-fs time delay is about 41 fs (FWHM), and for the 133-fs time delay is about 25 fs (FWHM), as shown in Figure 4E. These experimental results demonstrate that the proposed method can be used for pulse duration control in a seeded FEL by changing the relative time delay of the two seed lasers. However, the shortest pulse duration is limited to about 25 fs due to the slippage effect, which is about 18 fs in RAD2 in accordance with this experiment.

4 Three-dimensional simulations based on the soft X-ray free-electron laser user facility

With a shorter radiation wavelength, it is possible to further reduce the output pulse duration due to the shorter slippage length. Here, we adopt the main parameters of the SXFEL user facility (SXFEL-UF), as shown in Table. 2, to perform three-dimensional start-to-end simulations. The schematic layout of the SXFEL-UF is shown in Figure 1. The initial beam is generated by Astra [52], a program package imitating the beam dynamics from a photoinjector, taking into consideration the space charge effects. The acceleration process in the LINAC is conducted with the beam tracking code ELEGANT [53], considering the coherent synchrotron radiation (CSR) and incoherent synchrotron radiation (ISR) effects. The final FEL amplification process is simulated by the 3D time-dependent code GENESIS [54]. Figure 5 shows the longitudinal phase space and current distribution of the electron beam using the end of the LINAC. In our simulations when generating shorter FEL pulses, the relative time shift should increase. At the same time, to keep a relatively large bunching factor at the local overlapped area, the energy modulation amplitudes increase too, and the pulse energy of the seed lasers should increase correspondingly. To maintain reasonable seed laser pulse energy, the maximum relative time delay of the two seed lasers is set to be 300 fs. To satisfy the modulation strength requirements at this position, the pulse energy of the seed lasers should change simultaneously with the relative time delay of the seed lasers changing. Thus, the two seed lasers employed in the first-stage EEHG both have a pulse duration of 150 fs (FWHM) and a maximal pulse energy of 480 μJ.

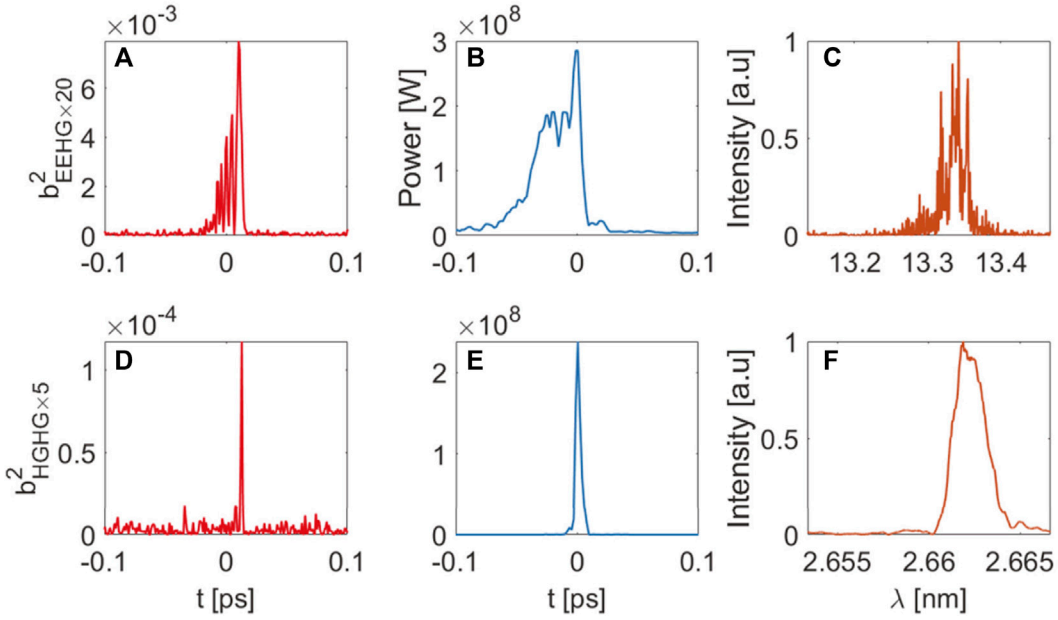

FIGURE 6
(A) Squared bunching factor of the simulation results at the entrance of RAD1 with a harmonic number of 20. **(B)** Power of the EEHG-FEL radiation. **(C)** Spectrum of the EEHG-FEL radiation. **(D)** Squared bunching factor of the simulation results at the entrance of RAD2 with a harmonic number of 5. **(E)** Power of the HGHG-FEL radiation. **(F)** Spectrum of the HGHG-FEL radiation.

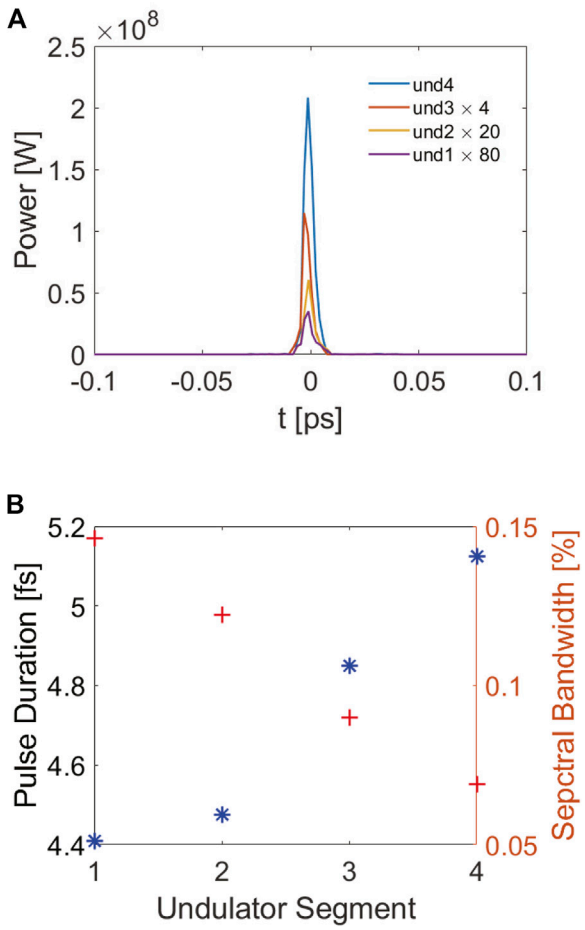

FIGURE 7
(A) Radiation power profiles at various undulator segments along RAD2. **(B)** FEL pulse duration and spectral bandwidth evolutions at various undulator segments along RAD2.

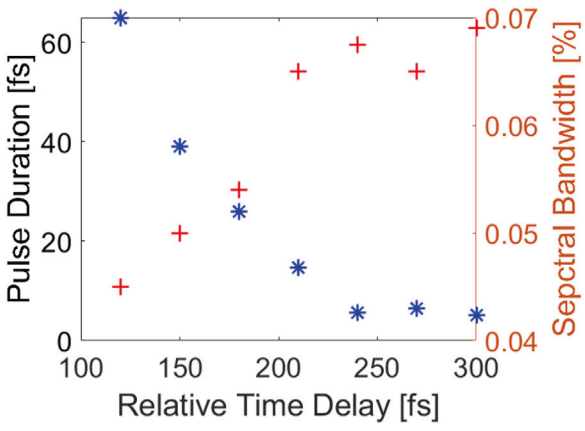

FIGURE 8
FEL pulse duration and spectral bandwidth with respect to different relative time delays between the two seed lasers.

Figure 6 shows the FEL performances in the first and second stages. At the entrance of RAD1, the maximum bunching factor is about 9%, as shown in Figure 6A. Figure 6B shows an ultrafast 13.3 nm radiation with a peak power of about 300 MW, and a pulse duration of about 36 fs (FWHM) is generated through RAD1. We can see that there exist satellite side peaks. The corresponding spectrum is shown in Figure 6C. After DS3, the maximum bunching factor at the entrance of RAD2 is about 1.2%, and a final FEL pulse at 2.66 nm is obtained over a 200-MW peak power through RAD2, as shown in Figures 6D,E. The final FEL pulse duration can also be efficiently shortened to about 5.2 fs. The corresponding spectrum is shown in Figure 6F. For seeded FELs, the dispersion strength has an important impact on the output pulse properties [45,46]. Thus, to obtain a shorter pulse duration, the R_{56} value of DS3 is chosen to be a little bit weaker than the calculated optimized value, and the bunching factor is also smaller than the calculation results. According to the equations in Section 2, this weaker R_{56} value will be of significant benefit to smearing out the density modulation of the side peaks, thus shortening the final FEL pulse duration in RAD2.

The evolution of the pulse duration and the corresponding spectrum along RAD2 has also been shown in Figure 7. The FEL radiation pulse has a pulse duration of about 4.41 fs at the exit of the first undulator segment. After that, the pulse duration is increased by approximately 1.12 fs per undulator segment and finally increases to about 5.2 fs after a total of four undulator segments, as shown in Figure 7B. Due to the slippage effects, the pulse duration of the final FEL at the exit of RAD2 will always be several times the slippage length, which will be a limitation to generate even shorter FEL radiation pulses.

We also provide the simulation results of controlling the final FEL pulse durations at a wavelength of 2.66 nm with different time delays from 120 fs to 300 fs. Figure 8 shows that for the relative time delay of 120-fs case, the final pulse duration from RAD2 is about 65 fs. Also, with the increase of the relative time delay, the pulse duration can gradually be decreased. For the 300-fs time delay, the final FEL pulse duration is only about 5.2 fs, as we have presented previously. Moreover, to maintain the optimized condition of the bunching factor, the pulse energy of the seed lasers should be increased accordingly. In our simulation, the seed laser pulse energy for 120-fs time delay is about 30 μ J, while for the 300-fs time delay, it is increased to more than 480 μ J. The required seed laser pulse energy grows rapidly with the increase of the relative time delay.

5 Conclusion

In this article, we have studied a simple method to generate few-femtosecond fully coherent ultrashort soft X-ray FEL pulses and control the final FEL pulse durations in a seeded FEL. This method also holds promising prospects for generating fully coherent ultrashort FEL radiation pulses in high-repetition-rate FEL facilities. By changing the relative time delay and correspondingly the pulse energy of the two seed lasers employed in EEHG, bunching properties of the electron beam

can be manipulated and ultrashort FEL pulses can be generated. Based on the SXFEL, we studied the performances of the method through theoretical analysis, numerical simulations, and practical experiments. The experimental results are consistent with the theories and simulations. The simulation results indicate that an isolated 5.2-fs FEL pulse at 2.66 nm can be obtained with a peak power of about 200 MW, and the pulse duration is controllable with respect to the relative time delay. The final output FEL radiation pulse duration is essentially limited by the slippage length in the radiator, indicating that even shorter pulses can be generated at higher harmonics.

Data availability statement

The raw data supporting the conclusion of this article will be made available by the authors, without undue reservation.

Author contributions

WF and CF contributed to the conception and design of the study. WF performed the statistical analysis. WF, CF, and ZQ wrote the first draft of the manuscript. CF and ZQ conducted the experiments. MZ and CF are the supervisors. All authors contributed to manuscript revision, reading, and approved the submitted version.

Funding

This work is supported by the National Natural Science Foundation of China (12122514 and 11975300) and the Shanghai Science and Technology Committee Rising-Star Program (20QA1410100).

Acknowledgments

The authors would like to thank the SXFEL group on the experiments.

Conflict of interest

The authors declare that the research was conducted in the absence of any commercial or financial relationships that could be construed as a potential conflict of interest.

Publisher's note

References

1. Emma P, Akre R, Arthur J, Bionta R, Bostedt C, Bozek J, et al. First lasing and operation of an ångstrom-wavelength free-electron laser. *Nat Photon* (2010) 4:641–7. doi:10.1038/nphoton.2010.176

2. Ishikawa T, Aoyagi H, Asaka T, Asano Y, Azumi N, Bizen T, et al. A compact X-ray free-electron laser emitting in the sub-ångström region. *Nat Photon* (2012) 6:540–4. doi:10.1038/nphoton.2012.141

3. Allaria E, Castronovo D, Cinquegrana P, Craievich P, Dal Forno M, Danailov MB, et al. Two-stage seeded soft-X-ray free-electron laser. *Nat Photon* (2013) 7:913–8. doi:10.1038/nphoton.2013.277

4. Kang HS, Min CK, Heo H, Kim C, Yang H, Kim G, et al. Hard X-ray free-electron laser with femtosecond-scale timing jitter. *Nat Photon* (2017) 11:708–13. doi:10.1038/s41566-017-0029-8

5. Milne CJ, Schietinger T, Aiba M, Alarcon A, Alex J, Anghel A, et al. SwissFEL: The Swiss X-ray free electron laser. *Appl Sci (Switzerland)* (2017) 7:720–57. doi:10.3390/app7070720

6. Decking W, Abeghyan S, Abramian P, Abramsky A, Aguirre A, Albrecht C, et al. A MHz-repetition-rate hard X-ray free-electron laser driven by a superconducting linear accelerator. *Nat Photon* (2020) 14:391–7. doi:10.1038/s41566-020-0607-z

7. Giannessi L, Musumeci P, Spampinati S. Nonlinear pulse evolution in seeded free-electron laser amplifiers and in free-electron laser cascades. *J Appl Phys* (2005) 98:043110. doi:10.1063/1.2010624

8. Yan J, Deng HX, Wang D, Dai ZM. EEHG-assisted FEL schemes for attosecond X-ray pulses generation. *Nucl Instr Methods Phys Res Section A: Acc Spectrometers, Detectors Associated Equipment* (2010) 621:97–104. doi:10.1016/j.nima.2010.06.099

9. Huang S, Ding Y, Huang Z, Marcus G. Generation of subterawatt-attosecond pulses in a soft x-ray free-electron laser. *Phys Rev Acc Beams* (2016) 19:080702. doi:10.1103/PhysRevAccelBeams.19.080702

10. Tanaka T, Rebernik Ribič P. Shortening the pulse duration in seeded free-electron lasers by chirped microbunching. *Opt Express* (2019) 27:30875. doi:10.1364/oe.27.030875

11. Duris J, Li S, Driver T, Champenois EG, MacArthur JP, Lutman AA, et al. Tunable isolated attosecond X-ray pulses with gigawatt peak power from a free-electron laser. *Nat Photon* (2020) 14:30–6. doi:10.1038/s41566-019-0549-5

12. Maroju PK, Grazioli C, Di Fraia M, Moioli M, Ertel D, Ahmadi H, et al. Attosecond pulse shaping using a seeded free-electron laser. *Nature* (2020) 578:386–91. doi:10.1038/s41586-020-2005-6

13. Xiao Y, Feng C, Liu B. Generating isolated attosecond x-ray pulses by wavefront control in a seeded free-electron laser. *Ultrafast Sci* (2022) 2022:9812478. doi:10.34133/2022/9812478

14. Clark JN, Beitra L, Xiong G, Higginbotham A, Fritz DM, Lemke HT, et al. Ultrafast three-dimensional imaging of lattice dynamics in individual gold nanocrystals. *Science* (2013) 341:56–9. doi:10.1126/science.1236034

15. Hantke MF, Hasse D, Maia FR, Ekeberg T, John K, Svenda M, et al. High-throughput imaging of heterogeneous cell organelles with an X-ray laser. *Nat Photon* (2014) 8:943–9. doi:10.1038/nphoton.2014.270

16. Kupitz C, Basu S, Grotjohann I, Fromme R, Zatsepin NA, Rendek KN, et al. Serial time-resolved crystallography of photosystem II using a femtosecond X-ray laser. *Nature* (2014) 513:261–5. doi:10.1038/nature13453

17. Clark JN, Beitra L, Xiong G, Fritz DM, Lemke HT, Zhu D, et al. Imaging transient melting of a nanocrystal using an X-ray laser. *Proc Natl Acad Sci United States America* (2015) 112:7444–8. doi:10.1073/pnas.1417678112

18. Van Der Schot G, Svenda M, Maia FR, Hantke M, Deponte DP, Seibert MM, et al. Imaging single cells in a beam of live cyanobacteria with an X-ray laser. *Nat Commun* (2015) 6:5704–9. doi:10.1038/ncomms6704

19. Gorman MG, Briggs R, McBride EE, Higginbotham A, Arnold B, Eggert JH, et al. Direct observation of melting in shock-compressed bismuth with femtosecond X-ray diffraction. *Phys Rev Lett* (2015) 115:095701. doi:10.1103/PhysRevLett.115.095701

20. Fletcher LB, Lee HJ, Döppner T, Galtier E, Nagler B, Heimann P, et al. Ultrabright X-ray laser scattering for dynamic warm dense matter physics. *Nat Photon* (2015) 9:274–9. doi:10.1038/nphoton.2015.41

21. Ekeberg T, Svenda M, Abergel C, Maia FR, Seltzer V, Claverie JM, et al. Three-dimensional reconstruction of the giant mimivirus particle with an X-ray free-electron laser. *Phys Rev Lett* (2015) 114:098102–6. doi:10.1103/PhysRevLett.114.098102

22. Kondratenko AM, Saldin EL. Generation of coherent radiation by a relativistic electron beam in an ondulator. *Part Acc Print* (1980) 10:207–216.

23. Bonifacio R, Pellegrini C, Narducci LM. Collective instabilities and high-gain regime in a free electron laser. *Opt Commun* (1984) 50:373–8. doi:10.1016/0030-4018(84)90105-6

24. Andruszkow J, Aune B, Ayvazyan V, Baboi N, Bakker R, Balakin V, et al. First observation of self-amplified spontaneous emission in a free-electron laser at 109 nm wavelength. *Phys Rev Lett* (2000) 85:3825–9. doi:10.1103/PhysRevLett.85.3825

25. Geloni G, Kocharyan V, Saldin E. A novel self-seeding scheme for hard X-ray FELs. *J Mod Opt* (2011) 58:1391–403. doi:10.1080/09500340.2011.586473

26. Amann J, Berg W, Blank V, Decker FJ, Ding Y, Emma P, et al. Demonstration of self-seeding in a hard-X-ray free-electron laser. *Nat Photon* (2012) 6:693–8. doi:10.1038/nphoton.2012.180

27. Stoupin S, Blank VD, Terentyev SA, Polyakov SN, Denisov VN, Kuznetsov MS, et al. Diamond crystal optics for self-seeding of hard X-rays in X-ray free-electron lasers. *Diamond Relat Mater* (2013) 33:1–4. doi:10.1016/j.diamond.2012.12.009

28. Zhang K, Qi Z, Feng C, Deng H, Wang D, Zhao Z. Extending the photon energy coverage of an x-ray self-seeding FEL via the reverse taper enhanced harmonic generation technique. *Nucl Instr Methods Phys Res Section A: Acc Spectrometers, Detectors Associated Equipment* (2017) 854:3–10. doi:10.1016/j.nima.2017.02.039

29. Inoue I, Osaka T, Hara T, Tanaka T, Inagaki T, Fukui T, et al. Generation of narrow-band X-ray free-electron laser via reflection self-seeding. *Nat Photon* (2019) 13:319–22. doi:10.1038/s41566-019-0365-y

30. Yu LH. Generation of intense uv radiation by subharmonically seeded single-pass free-electron lasers. *Phys Rev A* (1991) 44:5178–93. doi:10.1103/PhysRevA.44.5178

31. Yu LH, Ben-Zvi I. High-gain harmonic generation of soft X-rays with the "fresh bunch" technique. *Nucl Instr Methods Phys Res Section A: Acc Spectrometers, Detectors Associated Equipment* (1997) 393:96–9. doi:10.1016/S0168-9002(97)00435-X

32. Dattoli G, Ottaviani PL. Design considerations for x-ray free electron lasers. *J Appl Phys* (1999) 86:5331–6. doi:10.1063/1.371528

33. Liu B, Li WB, Chen JH, Chen ZH, Deng HX, Ding JG, et al. Demonstration of a widely-tunable and fully-coherent high-gain harmonic-generation free-electron laser. *Phys Rev Spec Top - Acc Beams* (2013) 16:020704. doi:10.1103/PhysRevSTAB.16.020704

34. Allaria E, Badano L, Bassanese S, Capotondi F, Castronovo D, Cinquegrana P, et al. The FERMI free-electron lasers. *J Synchrotron Radiat* (2015) 22:485–491. doi:10.1107/S1600577515005366

35. Xiang D, Stupakov G. Echo-enabled harmonic generation free electron laser. *Phys Rev Spec Top - Acc Beams* (2009) 12:030702. doi:10.1103/PhysRevSTAB.12.030702

36. Zhao ZT, Wang D, Chen JH, Chen ZH, Deng HX, Ding JG, et al. First lasing of an echo-enabled harmonic generation free-electron laser. *Nat Photon* (2012) 6:360–3. doi:10.1038/nphoton.2012.105

37. Xiang D, Colby E, Dunning M, Gilevich S, Hast C, Jobe K, et al. Evidence of high harmonics from echo-enabled harmonic generation for seeding X-Ray free electron lasers. *Phys Rev Lett* (2012) 108:024802. doi:10.1103/PhysRevLett.108.024802

38. Hemsing E, Dunning M, Hast C, Raubenheimer TO, Weathersby S, Xiang D. Highly coherent vacuum ultraviolet radiation at the 15th harmonic with echo-enabled harmonic generation technique. *Phys Rev Spec Top - Acc Beams* (2014) 17:070702. doi:10.1103/PhysRevSTAB.17.070702

39. Hemsing E, Dunning M, Garcia B, Hast C, Raubenheimer T, Stupakov G, et al. Echo-enabled harmonics up to the 75th order from precisely tailored electron beams. *Nat Photon* (2016) 10:512–5. doi:10.1038/nphoton.2016.101

40. Ribič PR, Roussel E, Penn G, De Ninno G, Giannessi L, Penco G, et al. Echo-enabled harmonic generation studies for the FERMI free-electron laser. *Photonics* (2017) 4:19. doi:10.3390/photonics4010019

41. Feng C, Deng H, Zhang M, Wang X, Chen S, Liu T, et al. Coherent extreme ultraviolet free-electron laser with echo-enabled harmonic generation. *Phys Rev Acc Beams* (2019) 22:050703. doi:10.1103/PhysRevAccelBeams.22.050703

42. Zhu ZY, Zhao ZT, Wang D, Liu Z, Li RX, Yin LX, et al. Sclf: An 8-GEV CW SCRF linac-based x-ray FEL facility in Shanghai. In: Proceedings of the 38th International Free-Electron Laser Conference, FEL 2017; 20-25 August 2017; Santa Fe, NM, United States (2017). p. 182–184. doi:10.18429/JACoW-FEL2017-MOP055

43. Haixiao D, Xingtao W, Zhimin D. Short-pulse length effects of the seed laser in high-gain harmonic generation free-electron laser. *Phys Rev Spec Top - Acc Beams* (2008) 11:040703. doi:10.1103/PhysRevSTAB.11.040703

44. Labat M, Joly N, Bielawski S, Szwaj C, Bruni C, Couprie ME. Pulse splitting in short wavelength seeded free electron lasers. *Phys Rev Lett* (2009) 103:264801. doi:10.1103/PhysRevLett.103.264801

45. Gauthier D, Ribič PR, De Ninno G, Allaria E, Cinquegrana P, Danailov MB, et al. Spectrotemporal shaping of seeded free-electron laser pulses. *Phys Rev Lett* (2015) 115:114801. doi:10.1103/PhysRevLett.115.114801

46. Finetti P, Höppner H, Allaria E, Callegari C, Capotondi F, Cinquegrana P, et al. Pulse duration of seeded free-electron lasers. *Phys Rev X* (2017) 7:021043. doi:10.1103/PhysRevX.7.021043

47. Mirian NS, Di Fraia M, Spampinati S, Sottocorona F, Allaria E, Badano L, et al. Generation and measurement of intense few-femtosecond superradiant extreme-ultraviolet free-electron laser pulses. *Nat Photon* (2021) 15:523–9. doi:10.1038/s41566-021-00815-w

48. Zeng L, Feng C, Gu D, Wang X, Zhang K, Liu B, et al. Online single-shot characterization of ultrafast pulses from high-gain free-electron lasers. *Fundam Res* (2022) 2:929–36. doi:10.1016/j.fmre.2022.01.027

49. Feng C, Liu T, Chen S, Zhou K, Zhang K, Qi Z, et al. Coherent and ultrashort soft x-ray pulses from echo-enabled harmonic cascade free-electron lasers. *Optica* (2022) 9:785. doi:10.1364/optica.466064

50. Ratner D, Fry A, Stupakov G, White W. Laser phase errors in seeded free electron lasers. *Phys Rev Spec Top - Acc Beams* (2012) 15:030702. doi:10.1103/PhysRevSTAB.15.030702

51. Wang G, Feng C, Zhang T, Wang D, Deng H. Study on the seed laser phase error multiplication in seeded free electron lasers. *Nucl Instr Methods Phys Res Section A: Acc Spectrometers, Detectors Associated Equipment* (2014) 737:237–41. doi:10.1016/j.nima.2013.11.020

52. Floettmann K. ASTRA users manual (1999). Available at: https://www.desy.de/~mpyflo/ (Accessed March, 2017).

53. Borland M. Elegant: A flexible SDDS-compliant code for accelerator simulation. In: Proceedings of 6th International Computational Accelerator Physics Conference; 11-14 September 2000; Darmstadt, Germany (2000). 1–11. doi:10.2172/761286

54. Reiche S. Genesis 1.3: A fully 3D time-dependent FEL simulation code. *Nucl Instr Methods Phys Res Section A: Acc Spectrometers, Detectors Associated Equipment* (1999) 429:243–8. doi:10.1016/S0168-9002(99)00114-X

frontiers | Frontiers in Physics

TYPE Original Research
PUBLISHED 27 March 2023
DOI 10.3389/fphy.2023.1166216

OPEN ACCESS

EDITED BY
Riccardo Meucci,
National Research Council (CNR), Italy

REVIEWED BY
Enrico Allaria,
Elettra Sincrotrone Trieste, Italy
Jiawei Yan,
European X-Ray Free Electron Laser, Germany

*CORRESPONDENCE
Zhen Zhang,
zzhang@slac.stanford.edu

SPECIALTY SECTION
This article was submitted to Interdisciplinary Physics, a section of the journal Frontiers in Physics

RECEIVED 14 February 2023
ACCEPTED 15 March 2023
PUBLISHED 27 March 2023

CITATION
Zhang Z, Ding Y, Huang Z and Zhou F (2023), Multiplexed photoinjector optimization for high-repetition-rate free-electron lasers.
Front. Phys. 11:1166216.
doi: 10.3389/fphy.2023.1166216

Multiplexed photoinjector optimization for high-repetition-rate free-electron lasers

Zhen Zhang*, Yuantao Ding, Zhirong Huang and Feng Zhou

SLAC National Accelerator Laboratory, Menlo Park, CA, United States

The multiplexing capabilities of superconducting X-ray free-electron lasers (FELs) have gained much attention in recent years. The demanding requirements for photon properties from multiple undulator lines necessitate more flexible beam manipulation techniques to achieve the goal of "beam on demand". In this paper, we investigate a multiplexed configuration for the photoinjector of high-repetition-rate FELs that aims to simultaneously provide low-emittance electron beams of different charges. A parallel, multi-objective genetic algorithm is implemented for the photoinjector parameter optimization. The proposed configuration could drastically enhance the flexibility of beam manipulation to improve multiplexing capabilities and realize the full potential of the facility.

KEYWORDS

free-electron laser, beam on demand, multiplexing capability, photoinjector, VHF gun, genetic algorithm

1 Introduction

Recently there is increasing interest in the multiplexing capabilities of high-repetition-rate X-ray free-electron lasers (FELs) across the community as the development of superconducting radio-frequency (SRF) linac based FEL facilities such as LCLS-II Raubenheimer et al. [1] and its high energy upgrade Raubenheimer et al. [2], SHINE Zhu et al. [3] and European XFEL Decking et al. [4]. The high-repetition rate of electron beams up to megahertz (MHz) in these facilities make it feasible to feed multiple undulator lines simultaneously, significantly increasing the user experiment time. The concept of generating bunches with different properties to drive more than one FELs in parallel has been already done both at superconducting FELs Faatz et al. [5]; Fröhlich et al. [6] and normal conducting FELs Paraliev et al. [7]. However, the wide range of photon property requirements from multiple undulator lines presents a major challenge for satisfying these requirements with a single photoinjector and SRF linac.

To achieve the full potential of high-repetition-rate FEL facilities such as LCLS-II, the concept of "beam on demand" has been proposed to provide tailored beam properties for each undulator line at the desired repetition rate Zhang et al. [8]. These properties include, but are not limited to, beam current, bunch length, beam charge, beam energy, and energy chirp. To achieve shot-by-shot control of bunch length and peak current, a continuous-wave (CW) normal conducting cavity, called a "chirper", which is located upstream of the first magnetic chicane, has been proposed and studied Nasr et al. [9]; Zhang et al. [10]. Different methods have been explored to produce the desired beam energy for each beamline from a

single SRF linac, such as using an achromatic and isochronous electron delay system and fast kickers Yan and Deng [11] or off-frequency detuning in SRF cavities Zhang et al. [12]. Laser heater shaping allows for customized shaping of the beam's slice energy spread, resulting in various beam current profiles for different applications Marinelli et al. [13]; Roussel et al. [14]; Cesar et al. [15]. It is worth noting that all these techniques are performed after the photoinjector and assume consistent beam properties at the photoinjector exit for all shots.

The photoinjector is the low energy (≲100 MeV) part of the accelerator, where space charge effects and non-relativistic kinematics play an critical and even dominant role. The photoinjector is usually optimized for a specific beam charge, but changing the beam charge requires re-optimization of the entire injector settings. To achieve the goal of "beam charge on demand", a multiplexed configuration for photoinjector is needed to preserve low emittance for different beam charges at the same time. Due to the intensity of space charge, most of the parameters in the photoinjector are non-linearly coupled. In this paper, a simulation code, ASTRA, which has been extensively tested against experiments and other codes Flottmann [16], is used to model the beam dynamics in the photoinjector. A multi-objective genetic optimizer based on the continuous non-dominated sorting genetic algorithm (NSGA-II) Deb et al. [17] is used for the parameter optimizations of photoinjector. NSGA-II is a popular evolutionary algorithm, that is, widely used in various fields, including engineering, finance, and computer science. NSGA-II can handle multiple objectives and constraints simultaneously, and can effectively generate a set of Pareto-optimal solutions, which are the optimal solutions that cannot be improved in one objective without worsening another objective. The choice of population size in NSGA-II algorithm depends on several factors, including the complexity of the problem, the number of objectives, and the available computational resources. A larger population size can lead to better diversity in the population, which can improve the convergence and quality of the optimization results. However, a larger population size also requires more computational resources and longer computation time. This method has been widely adopted in the field of accelerator during the last decades Bazarov and Sinclair [18]; Hajima and Nagai [19]; Hofler et al. [20]; Papadopoulos et al. [21]; Chen et al. [22]; Zhu et al. [23]; Neveu et al. [24]. In this study, the population size of each generation is set to be 128, taking into account the decision variables of photoinjector optimization and the available computational resources.

The paper is structured as follows: in Section 2, we will present the optimized results of the LCLS-II photoinjector for three typical beam charges as a baseline. The method to optimize multiplexed configurations is described in Section 3, including the optimal results of three multiplexed configurations with different customized knobs. Finally, in Section 4, we provide some discussion and concluding remarks.

2 Baseline of LCLS-II photoinjector

To illustrate the proposed multiplexed configuration for the photoinjector, we first show the optimization results for different beam charges individually optimized with the same input variables, serving as the facility's baseline. We use the photoinjector of LCLS-II as an example in the following simulations, which is depicted in Figure 1. The photoinjector consists primarily of a very-high-frequency (VHF) gun, two solenoids (labeled SOL1 and SOL2), a 2-cell normal conducting continuous-wave 1.3 GHz buncher cavity, and eight 9-cell 1.3 GHz cavities (labeled 1–8). The RF gun is a replica of the APEX Sannibale et al. [25] gun developed at Lawrence Berkeley National Laboratory, which allows LCLS-II to operate in continuous-wave mode with an electron beam repetition rate of 1 MHz. The drive laser used for generating electrons at the Cs_2Te cathode is an ultraviolet laser at 257.5 nm, a fourth harmonic from an infrared laser operating at 1,030 nm Gilevich et al. [26]. The longitudinal profile of the laser pulse can have either a Gaussian or uniform distribution. The implementation of the latter relies on successful laser pulse shaping to suppress any initial density modulation, as failure to do so may introduce a strong microbunching instability in the accelerator Huang et al. [27] In this study, we assume a uniform transverse and longitudinal laser density profile. The laser spot radius and pulse duration are also considered as optimization variables. The maximum gradient of the gun is fixed at 20 MV/m in the simulations, equivalent to a maximum beam energy of 750 keV. The gradient of the buncher cavity is also fixed to produce a maximum energy gain of 200 keV. Both the gun and buncher's relative acceleration phases are optimization variables. The two solenoids are utilized to control the beam size along the photoinjector and implement the emittance compensation technique Carlsten [28]; Serafini and Rosenzweig [29]. For the downstream cryomodule, the first three cavities are considered as optimization variables, while the others are set to be on-crest acceleration with a fixed gradient.

A high brightness electron beam at the exit of the photoinjector is a crucial requirement. This is typically measured by the transverse emittance and the bunch length, which have an inverse relationship. Minimizing both of these parameters in the optimization process typically results in a "Pareto front," which represents the minimum possible transverse emittance for a given bunch length. Aside from these two objectives, other constraints must also be considered to ensure that the results are feasible. These include the total beam energy and projected energy spread, which must be within acceptable limits for the downstream laser heater. For high-repetition rate FELs, it is also important to consider higher-order (>2) correlated energy spread, as it can lead to current horns after beam compression. In this study, we focus on optimizing the transverse emittance and bunch length as our two main objectives. We maintain cylindrical symmetry throughout the photoinjector, so only the horizontal emittance (ϵ_{nx}) was used as our metric for transverse emittance. Other constraints will be examined to ensure they fall within reasonable limits.

In our simulations, the mean transverse energy (MTE) of electrons at cathode emission is 330 meV, which corresponds to an initial intrinsic emittance of 0.8 mm-mrad/mm (also known as thermal emittance). This estimate of the intrinsic emittance is considered to be conservative and reasonable for Cs_2Te cathodes.

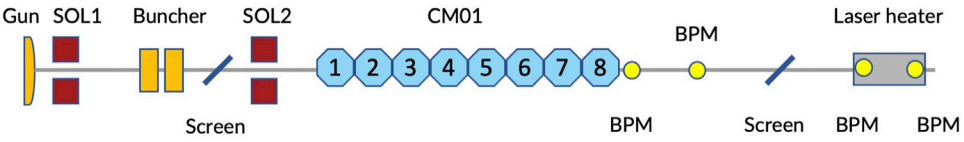

FIGURE 1
A schematic layout of the VHF gun photoinjector for LCLS-II.

TABLE 1 Optimization variables and constants in the LCLS-II photoinjector.

Variable/Constant	Value	Unit
Laser transverse distribution	radial uniform	—
Laser spot radius	0.1 ~ 1	mm
Laser longitudinal distribution	uniform	—
Laser pulse duration (rms[1])	5 ~ 24	ps
Beam charge	100/50/20	pC
VHF gun gradient	20	MV/m
VHF gun off-crest phase	-30 ~ 30	degree[2]
Buncher cavity gradient	1.8	MV/m
Buncher cavity off-crest phase	-120 ~ -40	degree
CAV-1 and CAV-3 peak gradient[3]	10 ~ 32 or turn off	MV/m
CAV-1 and CAV-3 off-crest phase	-60 ~ 40	degree
CAV-2	Turn off	—
CAV-4 to CAV-8 peak gradient	32	MV/m
CAV-4 to CAV-8 off-crest phase	0	degree
SOL1 B peak field	0.05 ~ 0.065	T
SOL2 B peak field	0.02 ~ 0.04	T

[1] RMS width equals full width divided by $\sqrt{12}$ in uniform distribution.
[2] All phases are based on the corresponding RF, wavelength.
[3] Average gradient of CM, cavity equals peak gradient divided by 1.93.

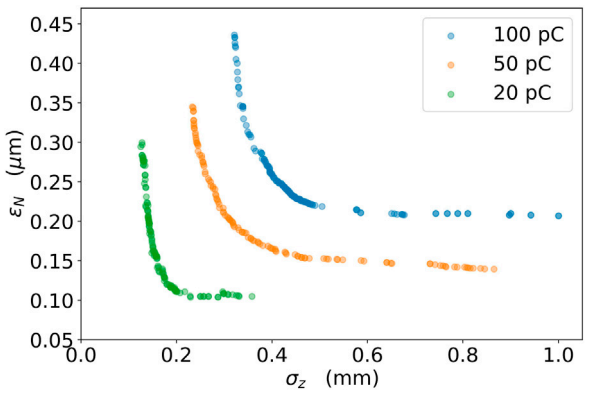

FIGURE 2
Pareto fronts of transverse emittance ϵ_{nx} and rms bunch length σ_z for individual configurations with different beam charges.

To balance the computational resources and accuracy, we use 10,000 macro particles in each simulation run with ASTRA, and a grid of 25 by 50 in the radial and longitudinal directions, respectively. Once the optimization has converged, we select one of the optimized solutions from the Pareto front and run it again with higher accuracy, using 200,000 particles and a grid of 75 by 125 to minimize numerical errors. Notably, we have observed good agreement between simulations with both low and high numbers of particles, with differences being negligible for our study.

The variables and constants used in the simulation of the LCLS-II photoinjector are listed in Table 1. The drive laser pulse is assumed to have a uniform radial shape and density profile in the transverse direction. Previous optimization work has shown that the gradient of the second cavity (CAV-2) in the cryomodule is very low (< 5 MV/m) for emittance compensation Mitchell et al. [30], Neveu and Ding [31], and is purposely turned off during LCLS-II commissioning. For simplicity, we also assume on-crest acceleration with fixed gradient from CAV-4 to CAV-8, as these cavities have little effect on the beam emittance and bunch length. During the machine operation, the phases and amplitudes of these cavities can be further adjusted to correct the beam energy and correlated energy spread based on the measurements.

In this study, we explore the performance of the LCLS-II photoinjector for three different beam charges: 100 pC, 50 pC, and 20 pC. To find the optimal combination of transverse emittance and bunch length, we conduct two-objective optimizations for each of these beam charges. The results are displayed in Figure 2, which shows the Pareto fronts of the two objectives for each beam charge. The Pareto fronts are obtained after 150 generations with 128 samples per generation. As a result of the optimizations, the following values of transverse emittance and bunch length are selected as baseline solutions: 0.22 μm at σ_z = 0.8 mm for 100 pC, 0.15 μm at σ_z = 0.5 mm for 50 pC, and 0.10 μm at σ_z = 0.3 mm for 20 pC. These solutions will be used as the reference points for following optimizations of the multiplexed configuration. We note that while the Pareto fronts in Figure 2 suggest that shorter bunch lengths can be achieved with a slight increase in emittance, shorter bunch lengths can also lead to stronger high-order energy chirp on the beam due to space charge force, which may ultimately degrade beam properties after downstream compression. As such, we prioritize selecting a reasonable range for the bunch length, rather than choosing the shortest possible value.

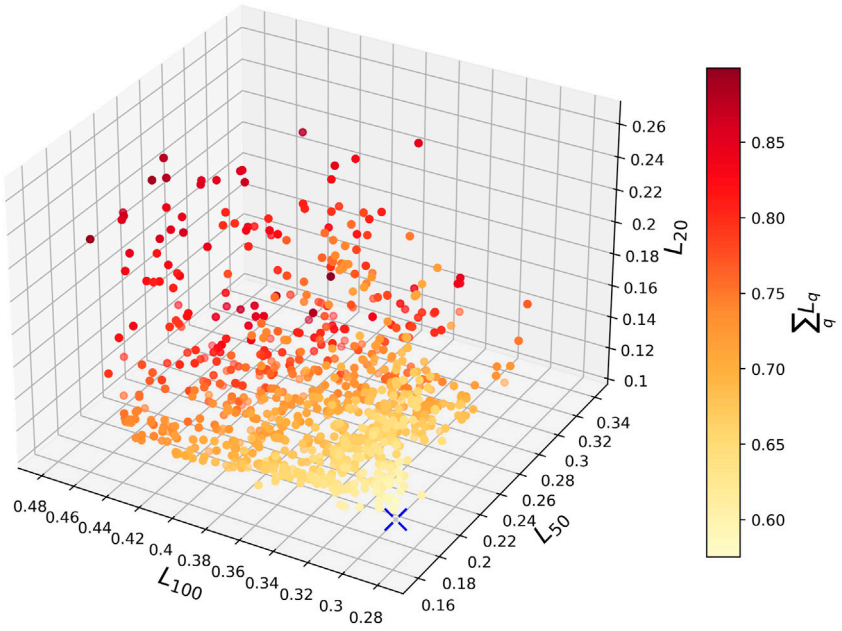

FIGURE 3
Loss function L_q distribution of three beam charges of the last 40 generations in the optimization of multiplexed configuration with customized laser spot size. The color map means the sum of three loss functions. The blue cross represents the optimal point with minimum sum of loss functions.

3 Multiplexed configuration for LCLS-II photoinjector

The objective of the multiplexed configuration for photoinjector is to produce high-brightness electron beams with different beam charges (100 pC, 50 pC, and 20 pC) alternatively at high repetition rate. To achieve this goal, certain settings in the photoinjector must remain constant for all beam charges, such as the field of the solenoid and the gradient of the RF cavities. The most challenging task in this work is to preserve low emittance for all charges with limited knobs. To simplify the optimization and reduce the number of objectives, the bunch lengths of different charges are specified at specific values and the emittance is minimized. A loss function L_q is defined for a given beam charge q as

$$L_q = \epsilon_{nx} + max\left(abs\left(\sigma_z - \sigma_z^{(q)}\right) - r_q, 0\right) \times \lambda, \quad (1)$$

where ϵ_{nx} is the value of emittance in unit of μm and σ_z is the rms bunch length in unit of mm. When the bunch length is within the range of $\sigma_z^{(q)} \pm r_q$, the loss function is exactly the value of emittance. λ is a regularization parameter to control the penalty when bunch length is out of the desired range. In our simulations, we choose $\lambda = 2$. These loss functions of different beam charges are used as objectives in optimizations. In this work, we consider two groups of target bunch lengths: (I) 1.0 ± 0.1 mm for 100 pC, 0.8 ± 0.1 mm for 50 pC, 0.6 ± 0.1 mm for 20 pC; (II) 0.8 ± 0.1 mm for 100 pC, 0.5 ± 0.075 mm for 50 pC, 0.3 ± 0.05 mm for 20 pC.

In the multiplexed configuration of the photoinjector, several parameters associated with magnetic and RF fields must remain constant for all beam charges. However, other parameters, primarily those related to the drive laser pulse, can be adjusted as needed for different charges. These adjustable parameters include the laser spot size at the cathode, laser pulse duration, and laser injection time. Our preliminary studies have shown that the laser injection time is not a significant knob in preserving the emittance. This can be attributed to the fact that the wavelength of the VHF gun is much longer than that of the downstream RF cavities and the laser pulse duration, and thus, adjusting the laser injection time within a reasonable range for the downstream RF cavities does not significantly affect the space charge effect in the low-energy electron beam, i.e., the emittance compensation process. In this work, we consider three cases (A) no customization of parameters, i.e., all variables in Table 1 are adjusted together and kept the same for the three bunch charges (B) customization of the laser spot size, allowing the laser spot size as a free variable for each charge while keeping all other variables the same for the three charges; and (C) customization of laser pulse duration, which is similar with (B) but allowing the laser pulse duration as a free variable for each charge. The optimal solutions will be compared with the results obtained in the previous section for individual configurations.

Figure 3 displays the distribution of the three loss functions during the optimization of the multiplexed configuration with a customized laser spot size. The color map represents the sum of the three loss functions. The optimization process converges after approximately 200 generations, and the optimal solution, with the minimum sum of the three loss functions, is indicated in the figure by a blue cross.

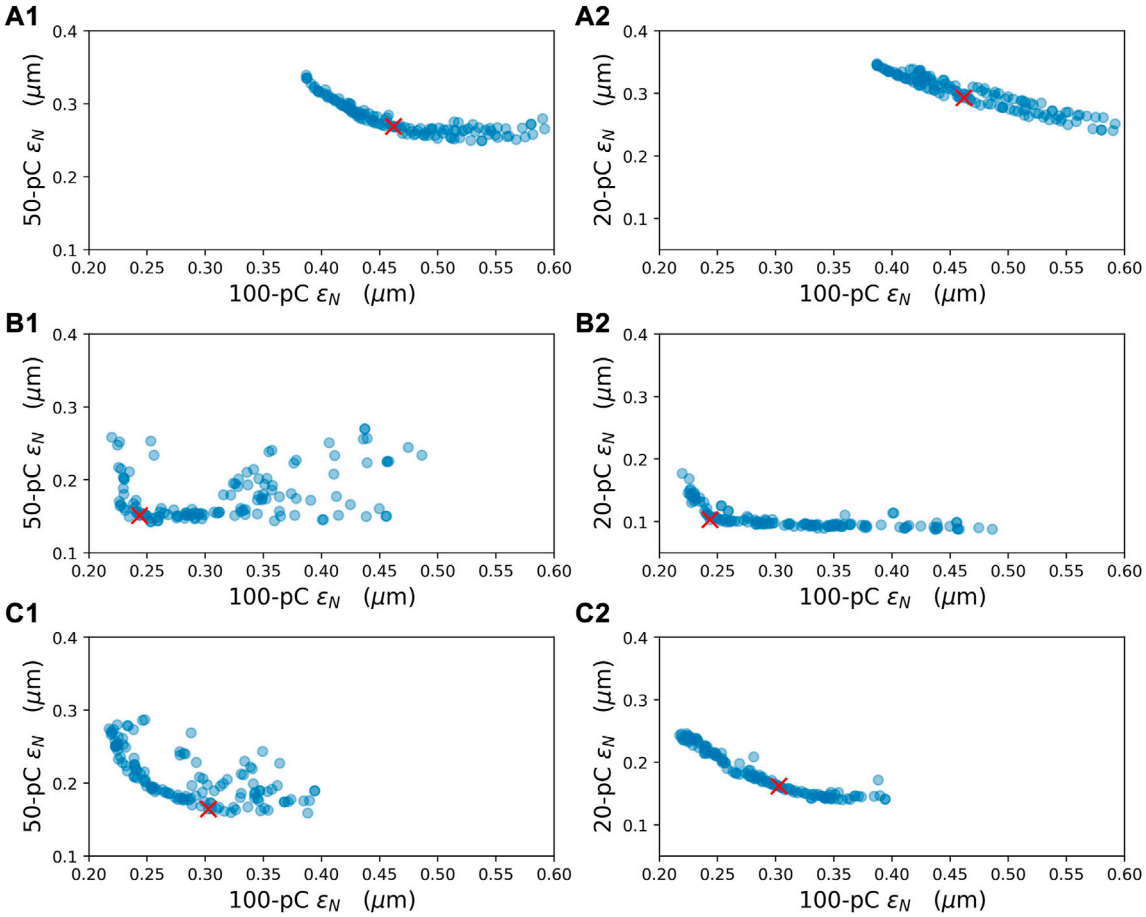

FIGURE 4
Distribution of beam emittance between 100 pC and 50 pC (left column), 100 pC and 20 pC (right column) in the multiplexed configuration. The desired rms bunch length is 1.0 $\pm$ 0.1 mm for 100 pC, 0.8 $\pm$ 0.1 mm for 50 pC and 0.6 $\pm$ 0.1 mm for 20 pC, respectively, in the loss functions. (Top) case **(A)** no customized knob. (Middle) case **(B)** customized laser spot size. (Bottom): case **(C)** customized laser pulse duration. The red cross represents the optimal point with minimum sum of the emittance of three beam charges in each configuration.

For a given desired bunch length range (e.g., group I), the emittance distribution for each of the two beam charges for the three cases is shown in Figure 4. A clear "Pareto front" between the emittances of each pair of beam charges can be observed. In each configuration, the optimal solution is chosen to minimize the sum of emittances, as indicated by a red cross in the figure. The detailed bunch lengths and emittances of these three configurations are listed in Table 2. Both configurations with a customized knob perform better than the one without any knobs. The multiplexed configuration with a customized laser spot size (case B) outperforms the other two configurations, with a total increase of around 9% in the sum of emittances, compared to the baseline individually optimized configurations for each beam charge. The emittances of the 50 pC and 20 pC beams remained almost the same as the baseline. The performance of the configuration with a customized laser pulse duration (Figure 4C) is not as good as that of case B, but it is still much better than the one without any customizations (Figure 4A). For different bunch length combinations, the total emittance increase of the multiplexed configuration may vary, but it is crucial that they remain within a reasonable range for facility operation.

From these three cases, we can see that a solution of a unified injector configuration working for all the three bunch charges can be found. If the laser parameters can be varied, the laser spot size is the most effective knob for optimizing the multiplexed configuration. Among the two desired bunch length ranges, the multiplexed configuration performs better for group I, which suggests that choosing an appropriate desired bunch length range can further reduce the increase in emittance in the multiplexed configuration.

In the multiplexed configuration with customized laser spot size (Figure 4B), the optimal laser spot radius for 100 pC, 50 pC, and 20 pC are found to be 0.29, 0.21, and 0.12 mm, respectively. The results show that the ratio of the square of the laser spot radius to the beam charge is nearly constant, meaning that the laser spot size is adjusted to keep the same charge density near the cathode emission, thus preserving emittance. This is a significant finding as it implies that the multiplexed configuration can be easily adapted to other beam charges beyond the three beam charges used in the optimization study.

TABLE 2 Electron bunch length and the corresponding optimal emittance of three beam charges in the baseline and three multiplexed configurations. Case (A) no customization of parameters for the three bunch charges; case (B) customization of the laser spot size for each charge; and case (C) customization of laser pulse duration for each charge. Details see the text.

Group no.	Parameter	Unit	Baseline	Case A	Case B	Case C
I	100-pC σ_z	mm	1.00	1.08	1.10	1.06
	50-pC σ_z	mm	0.80	0.87	0.80	0.83
	20-pC σ_z	mm	0.60	0.58	0.55	0.69
	100-pC ϵ_n	μm	0.20	0.46	0.24	0.30
	50-pC ϵ_n	μm	0.15	0.27	0.15	0.16
	20-pC ϵ_n	μm	0.10	0.29	0.10	0.16
	sum of ϵ_n	μm	0.45	1.02	0.49	0.62
II	100-pC σ_z	mm	0.80	0.83	0.86	0.72
	50-pC σ_z	mm	0.50	0.55	0.58	0.55
	20-pC σ_z	mm	0.30	0.29	0.33	0.35
	100-pC ϵ_n	μm	0.21	0.33	0.28	0.36
	50-pC ϵ_n	μm	0.15	0.38	0.17	0.20
	20-pC ϵ_n	μm	0.10	0.33	0.12	0.18
	sum of ϵ_n	μm	0.46	1.04	0.57	0.74

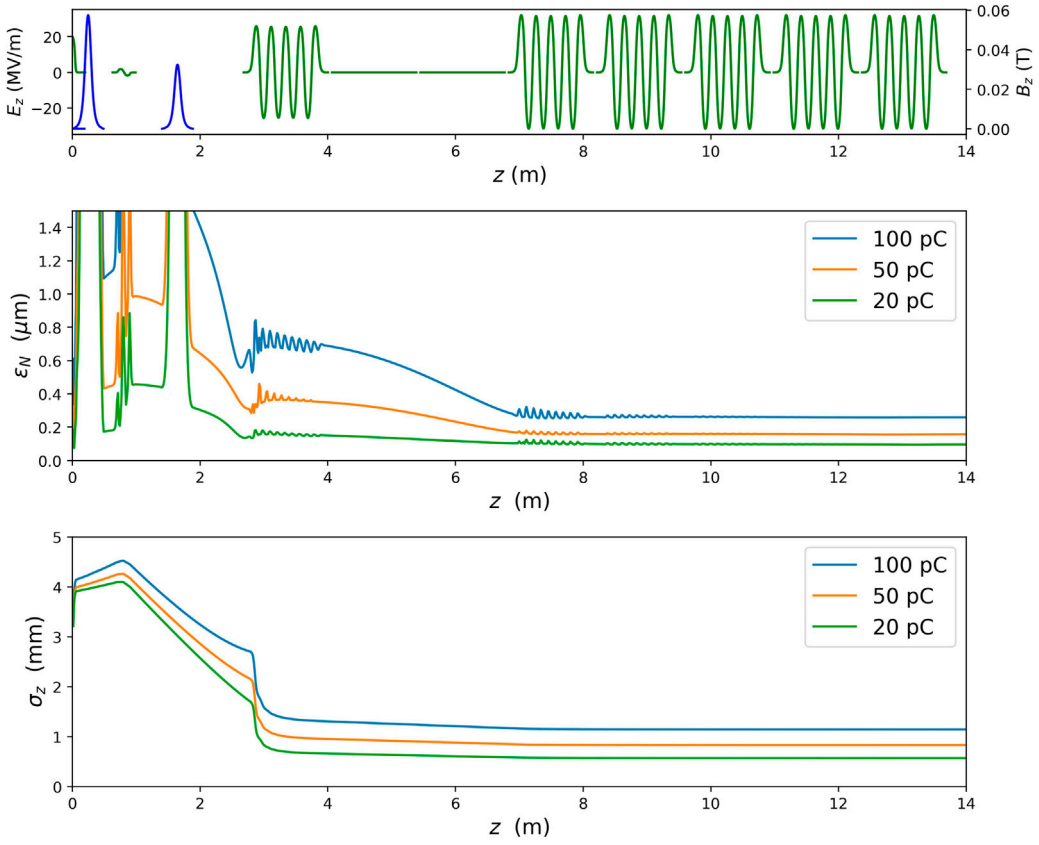

FIGURE 5
Electric and solenoid field (top), normalized emittance (middle) and rms bunch length (bottom) of three beam charges in the multiplexed configuration with customized laser spot size (case B in group I).

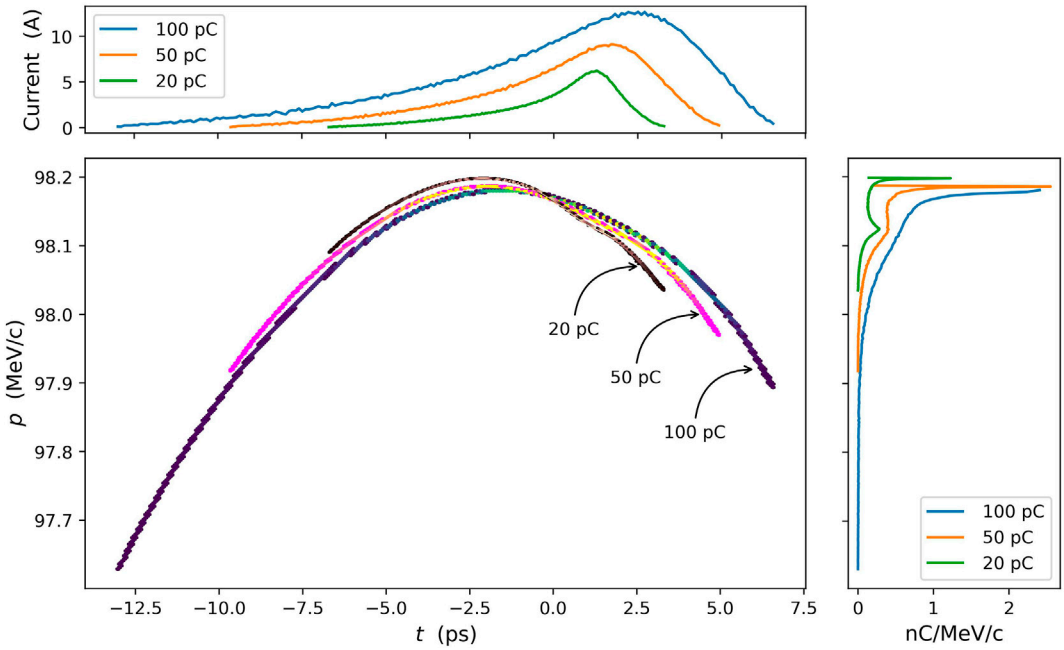

FIGURE 6
Longitudinal phase space of electron beams at the exit of photoinjector of three beam charges in the multiplexed configuration with customized laser spot size (case B in group I). To distinguish between each beam, we used a different color map for density representation, which is not shown in the figure.

For the optimal settings of case B in group I, the evolution of the emittance and the rms bunch length, as well as the electric and solenoid fields, are displayed in Figure 5. The emittance reaches its minimum value just before being frozen at high beam energy, and the rms bunch length stays constant after CAV-1. Although there is some correlated energy chirp on the beam at the end of the injector if all the last five cavities are set at on-crest acceleration, it can be removed by shifting their acceleration phase by approximately 6°. The longitudinal phase space of three beams and their current and energy profiles are shown in Figure 6. It can be observed that the average beam energy and arrival time of these three beams are very close, a result of the same acceleration phases of all RF cavities and the same laser pulse duration. Different beam charges may result in different wakefields along the SRF linac and therefore different beam compression in the downstream chicane compressors, but this can be adjusted shot-by-shot using the proposed chirper cavity for LCLS-II and its high energy upgrade Zhang et al. [10].

4 Discussions and conclusions

In this study, we investigated the possibility of multiplexed configurations for the photoinjector of SRF-based FELs to deliver low-emittance electron beams with different beam charges at high repetition rates. We evaluated three different configurations, two of them with a different customization of the drive laser system for different beam charges. Our results showed that the laser spot size, which can be technically customizable for each beam charge, was the most effective factor in preserving beam emittance. Additionally, we found that maintaining the same charge density on the cathode by adjusting the laser spot size made it possible to apply the optimized multiplexed configuration to other beam charges. The implementation of these multiplexed configurations in the photoinjector of SRF-based FELs will enable the delivery of beam charges on demand for each individual beamline, thus maximizing the multiplexing capabilities of the facilities.

Data availability statement

The original contributions presented in the study are included in the article/Supplementary Material, further inquiries can be directed to the corresponding author.

Author contributions

ZZ, YD, ZH, and FZ contributed to conception and design of the study. ZZ performed the simulations and the statistical analysis. ZZ and YD wrote the first draft of the manuscript. ZZ, YD, ZH, and FZ

contributed to the manuscript revision. All authors approved the publication of the content.

Funding

This work was supported by United States Department of Energy Contract No. DE-AC02-76SF00515.

Acknowledgments

The authors would like to thank Jingyi Tang and Christopher Mayes from SLAC for their valuable help and discussions on the optimizations of photoinjector with genetic algorithm.

Conflict of interest

The authors declare that the research was conducted in the absence of any commercial or financial relationships that could be construed as a potential conflict of interest.

Publisher's note

References

1. Raubenheimer T, et al. *Lcls-ii final design report. technical report*. SLAC Technical Report. SLAC National Acclerator Laboratory (2015). No. LCLSII- 1.1-DR-0251-R0.

2. Raubenheimer T, et al. The lcls-ii-he, a high energy upgrade of the lcls-ii. In: 60th ICFA Advanced Beam Dynamics Workshop on Future Light Sources (FLS'18); 5-9 March 2018; Shanghai, China. Geneva, Switzerland: JACOW Publishing (2018). p. 6–11.

3. Zhu Z, Zhao Z, Wang D, Liu Z, Li R, Yin L, et al. Sclf: An 8-gev cw scrf linac-based x-ray fel facility in shanghai. In: Proceedings of the FEL2017; Santa Fe, NM, USA (2017). p. 20–5.

4. Decking W, Abeghyan S, Abramian P, Abramsky A, Aguirre A, Albrecht C, et al. A mhz-repetition-rate hard x-ray free-electron laser driven by a superconducting linear accelerator. *Nat Photon* (2020) 14:391–7. doi:10.1038/s41566-020-0607-z

5. Faatz B, Plönjes E, Ackermann S, Agababyan A, Asgekar V, Ayvazyan V, et al. Simultaneous operation of two soft x-ray free-electron lasers driven by one linear accelerator. *New J Phys* (2016) 18:062002. doi:10.1088/1367-2630/18/6/062002

6. Fröhlich L, Aghababyan A, Balandin V, Beutner B, Brinker F, Decking W, et al. Multi-beamline operation at the European xfel. In: Proceedings of the International Free-Electron Laser Conference (FEL'19); Hamburg, Germany (2019). p. 26–30.

7. Paraliev M, Alarcon A, Arsov V, Bettoni S, Biffiger R, Boll M, et al. Swissfel double bunch operation. *Phys Rev Acc Beams* (2022) 25:120701. doi:10.1103/physrevaccelbeams.25.120701

8. Zhang Z, Ding Y, Huang Z Beam on demand for high-repetition-rate x-ray free-electron lasers. In: 12th International Particle Accelerator Conference (IPAC'21); 24-28 May 2021; Campinas, SP, Brazil. Geneva, Switzerland: JACOW Publishing (2021). p. 3995–8.

9. Nasr MH, Emma PJ, Tantawi S A cw normal conducting rf cavity for fast chirp control in the lcls-ii. In: 7th Int. Particle Accelerator Conf.(IPAC'16); May 8-13, 2016; Busan, Korea. Geneva, Switzerland: JACOW (2016). p. 1817–9.

10. Zhang Z, Snively E, Dolgashev V, Huang Z. *Fast and flexible control of beam longitudinal phase space for high-repetition-rate x-ray free-electron lasers* (2023). doi:10.1063/5.0135658

11. Yan J, Deng H. Multi-beam-energy operation for the continuous-wave x-ray free electron laser. *Phys Rev Acc Beams* (2019) 22:090701. doi:10.1103/physrevaccelbeams.22.090701

12. Zhang Z, Ding Y, Adolphsen C, Raubenheimer T. Multienergy operation analysis in a superconducting linac based on off-frequency detune method. *Phys Rev Acc Beams* (2019) 22:110702. doi:10.1103/physrevaccelbeams.22.110702

13. Marinelli A, Coffee R, Vetter S, Hering P, West G, Gilevich S, et al. Optical shaping of x-ray free-electron lasers. *Phys Rev Lett* (2016) 116:254801. doi:10.1103/physrevlett.116.254801

14. Roussel E, Ferrari E, Allaria E, Penco G, Di Mitri S, Veronese M, et al. Multicolor high-gain free-electron laser driven by seeded microbunching instability. *Phys Rev Lett* (2015) 115:214801. doi:10.1103/physrevlett.115.214801

15. Cesar D, Anakru A, Carbajo S, Duris J, Franz P, Li S, et al. Electron beam shaping via laser heater temporal shaping. *Phys Rev Acc Beams* (2021) 24:110703. doi:10.1103/physrevaccelbeams.24.110703

16. Flottmann K. *Astra: A space charge tracking algorithm* https://www.desy.de/~mpyflo/Astra_manual/Astra-Manual_V3.2.pdf. Tech. rep. (1997).

17. Deb K, Pratap A, Agarwal S, Meyarivan T. A fast and elitist multiobjective genetic algorithm: Nsga-ii. *IEEE Trans Evol Comput* (2002) 6:182–97. doi:10.1109/4235.996017

18. Bazarov IV, Sinclair CK. Multivariate optimization of a high brightness dc gun photoinjector. *Phys Rev Spec Topics-Accelerators Beams* (2005) 8:034202. doi:10.1103/physrevstab.8.034202

19. Hajima R, Nagai R. Multiparameter optimization of an erl injector. *Nucl Instr Methods Phys Res Section A: Acc Spectrometers, Detectors Associated Equipment* (2006) 557:103–5. doi:10.1016/j.nima.2005.10.060

20. Hofler A, Terzić B, Kramer M, Zvezdin A, Morozov V, Roblin Y, et al. Innovative applications of genetic algorithms to problems in accelerator physics. *Phys Rev Spec Topics-Accelerators Beams* (2013) 16:010101. doi:10.1103/physrevstab.16.010101

21. Papadopoulos C, Emma P, Filippetto D, Raubenheimer T, Sannibale F, Schmerge J, et al. *Rf injector beam dynamics optimization for lcls-ii* 2014 http://accelconf.web.cern.ch/FEL2014/papers/thp057.pdf. FEL2014, Basel, August.

22. Chen H, Zheng L-M, Gao B, Li Z-Z, Du Y-C, Li R-K, et al. Beam dynamics optimization of very-high-frequency gun photoinjector. *Nucl Sci Tech* (2022) 33:116. doi:10.1007/s41365-022-01105-y

23. Zhu Z, Gu D, Yan J, Wang Z, Yang H, Zhang M, et al. Inhibition of current-spike formation based on longitudinal phase space manipulation for high-repetition-rate x-ray fel. *Nucl Instr Methods Phys Res Section A: Acc Spectrometers, Detectors Associated Equipment* (2022) 1026:166172. doi:10.1016/j.nima.2021.166172

24. Neveu N, Chang TH, Franz P, Hudson S, Larson J. Comparison of multiobjective optimization methods for the lcls-ii photoinjector. *Comp Phys Commun* (2023) 283:108566. doi:10.1016/j.cpc.2022.108566

25. Sannibale F, Filippetto D, Papadopoulos C, Staples J, Wells R, Bailey B, et al. Advanced photoinjector experiment photogun commissioning results. *Phys Rev Spec Topics-Accelerators Beams* (2012) 15:103501. doi:10.1103/physrevstab.15.103501

26. Gilevich S, Alverson S, Carbajo S, Droste S, Edstrom S, Fry A, et al. The lcls-ii photo-injector drive laser system. In: 2020 Conference on Lasers and Electro-Optics (CLEO); 10-15 May 2020; San Jose, CA, USA. IEEE (2020). p. 1–2.

27. Huang Z, Borland M, Emma P, Wu J, Limborg C, Stupakov G, et al. Suppression of microbunching instability in the linac coherent light source. *Phys Rev Spec Topics-Accelerators Beams* (2004) 7:074401. doi:10.1103/physrevstab.7.074401

28. Carlsten BE. New photoelectric injector design for the los alamos national laboratory xuv fel accelerator. *Nucl Instr Methods Phys Res Section A: Acc Spectrometers, Detectors Associated Equipment* (1989) 285:313–9. doi:10.1016/0168-9002(89)90472-5

29. Serafini L, Rosenzweig JB. Envelope analysis of intense relativistic quasilaminar beams in rf photoinjectors: Ma theory of emittance compensation. *Phys Rev E* (1997) 55:7565–90. doi:10.1103/physreve.55.7565

30. Mitchell C, Emma P, Qian H, Qiang J, Raubenheimer T, Sannibale F, et al. Rf injector beam dynamics optimization and injected beam energy constraints for lcls-ii. In: Proc. 7th Int. Particle Accelerator Conf. (IPAC'16) (2016). p. 1699–702.

31. Neveu N, Ding Y. *LCLS-II standard configuration with a Gaussian-profile injector laser* https://www-lcls.slac.stanford.edu/web/technotes/LCLS-II-TN-20-03.pdf. Tech. rep., Technical Report LCLS-II-TN-20-03. SLAC National Accelerator Laboratory (2020).

frontiers | Frontiers in Physics

TYPE Original Research
PUBLISHED 28 March 2023
DOI 10.3389/fphy.2023.1157729

OPEN ACCESS

EDITED BY
Ji Qiang,
Berkeley Lab (DOE), United States

REVIEWED BY
Feng Zhou,
Stanford University, United States
Erdong Wang,
Brookhaven National Laboratory (DOE), United States

*CORRESPONDENCE
Huamu Xie,
hmxie@pku.edu.cn

SPECIALTY SECTION
This article was submitted to Interdisciplinary Physics, a section of the journal Frontiers in Physics

RECEIVED 03 February 2023
ACCEPTED 15 March 2023
PUBLISHED 28 March 2023

CITATION
Zhao Y, Ouyang D, Xie H, Liu K and Huang S (2023), QE evolution of bialkali photocathode at cryogenic temperature. *Front. Phys.* 11:1157729. doi: 10.3389/fphy.2023.1157729

QE evolution of bialkali photocathode at cryogenic temperature

Yonglong Zhao, Dongming Ouyang, Huamu Xie*, Kexin Liu and Senlin Huang

State Key Laboratory of Nuclear Physics and Technology, Peking University, Beijing, China

Photocathode plays an important role in generating high brightness and low emittance electron beam and K-Cs-Sb photocathode is preferred in SRF injectors for its high quantum efficiency, long lifetime, and low thermal emittance. To predict the QE change of K-Cs-Sb at cryogenic temperature more correctly, we have modified the QE formula of Spicer's photoemission model considering the temperature dependence of work function and mean free path of photocathode material, which is obtained by fitting experimental data. The calculated QE drop of about 90.1% at 36.4 K fits well with the measured QE change in DC-SRF photoinjector at Peking University. This improved formula could provide a method to evaluate the QE performance of semiconductor photocathodes at cryogenic temperature.

KEYWORDS

photocathode, SRF injector, quantum efficiency, cryogenic effect, macro-pulse operation

1 Introduction

Accelerator-based large scientific devices, such as X-ray free electron lasers (XFEL) [1, 2] and electron cooling [3], require electron beams with high brightness, low emittance, and high average current. While most electron injectors adopt photocathodes to generate high-quality beams, the beam emittance at the injector exit still needs to be improved for practical applications [4–7]. With the development of the high-gradient accelerating technique and the optimization of beam dynamics, the emittance growth caused by the RF field and space charge force would have a minor contribution to the final beam emittance. Hence the thermal emittance of the photocathode has become the main limiting factor of the final beam emittance [8].

Thermal emittance represents the ratio of the normalized emittance at the cathode surface to the RMS size of the driving laser, and it can be evaluated using the mean transverse energy (MTE) of emitted electrons. According to [9], the MTE can be roughly estimated as $E_{excess}/3$, where $E_{excess}=(\hbar\omega-\phi)$ is the excess energy defined as the difference between the photon energy, $\hbar\omega$, and the work function, ϕ, of the photocathode material. Therefore, any method that reduces the excess energy of photoelectrons would lead to a smaller thermal emittance of the photocathode. For decreasing thermal emittance, three methods are mainly used: near-threshold emission [10], back-illumination [11], and photocathode cooling [12, 13]. Among these methods, cooling the photocathode down to cryogenic temperature is more promising for superconducting radio frequency (SRF) injectors because it is compatible with the photoinjectors' operating environment. Thus, only minor changes in the structure of photoinjectors are needed. For semiconductor photocathodes with an

initial QE of ~ 10^{-2} [14, 15], electron beams with lower emittance and relatively high average current could be generated at cryogenic temperature. For example, a MTE of 22 meV was reported for the Cs_3Sb photocathode cooled down to 90 K with a QE larger than 7×10^{-5} [12].

Among semiconductor photocathodes, K-Cs-Sb is an ideal candidate for electron sources [7, 16, 17] to obtain low-emittance beams at cryogenic temperature due to its high QE, low thermal emittance, and months-long lifetime in SRF injectors [15]. However, it is necessary to investigate the performance of the K-Cs-Sb photocathode at cryogenic temperature to establish a proper theoretical model for predicting the temperature-dependent behavior of QE. It was reported that the K-Cs-Sb photocathode suffered from QE degradation when the temperature drops to cryogenic temperature [13, 18–20], and different models for the observed behaviors were proposed.

BNL first established a QE formula based on the Maxwell-Boltzmann energy distribution of conduction band electrons and concluded that the increase in work function was the main reason for the QE drop at low temperatures [13]. However, the linear fit overestimated the work function at cryogenic temperature [21], limiting the temperature range where this model can be used. A photoemission model based on the Fermi-Dirac distribution of electrons was developed by the University of Wisconsin [22], and it was used to fit the experimental spectral response data of K-Cs-Sb by JLab. The basic assumption of this model is that the work function is independent of temperature, which is unsuitable for the K-Cs-Sb semiconductor photocathode [20].

Thus, it is necessary to establish the correct work function to predict the QE change of K-Cs-Sb at cryogenic temperature more precisely. The temperature dependence of transport property should also be included [23]. Cornell laboratory considered the influence of temperature change on the scattering rate of phonons in their photoemission models of Cs_3Sb [24] and GaAs [25]. In the photoemission model of Cs_3Sb proposed by Tsinghua University, the contribution from the acceptor level was included. While the absence of photoelectrons from the acceptor level was considered to cause QE drop at cryogenic temperature [26], the application to K-Cs-Sb should be careful due to its weak doping property [27, 28].

Therefore, to obtain a more accurate photoemission model of K-Cs-Sb at cryogenic temperature, the temperature dependence of work function and electron transport property should be considered. In this paper, we tried to modify the QE formula of Spicer's three-step model for K-Cs-Sb, and compared the calculated results with experimental data of our DC-SRF photoinjector in which the temperature of the K-Cs-Sb photocathode is about 36.4 K.

2 Performance of a bialkali photocathode at cryogenic temperature

The performance of the K-Cs-Sb photocathode at cryogenic temperature was tested with the DC-SRF photoinjector proposed and developed at Peking University [29]. With the improvements in using K-Cs-Sb photocathode instead of Cs_2Te and drive laser of truncated Gaussian distribution in the transverse direction and a flat-topped distribution in the longitudinal direction, replacing the original 3.5-cell SRF cavity with a new 1.5-cell cavity, careful design of DC high voltage electrode structure and beam dynamics, the emittance of electron beams from DC-SRF photoinjector has been decreased obviously.

TABLE 1 Comparison of QE in the DC-SRF photoinjector and a suitcase for four K-Cs-Sb samples.

Sample index	QE in suitcase	QE in DC-SRF photoinjector
	[%]	[%]
#1	4.3	0.33
#2	3.0	0.31
#3	5.2	0.47
#4	4.5	0.44

To improve the performance of the K-Cs-Sb photocathode, we developed an improved sequential deposition procedure [17], where a faster Cs evaporation rate was adopted, and the cesiation process took less than 10 min. The K-Cs-Sb samples fabricated according to this recipe exhibited a typical QE of 5%–8%, and could be stored without deterioration for more than 2 weeks.

During the commissioning of the DC-SRF photoinjector, we observed a QE drop at the temperature of about 36.4 K. The temperature of the K-Cs-Sb photocathode was estimated using Comsol software [30] according to the heat distribution. The accuracy of temperature simulation has been verified by the measured values of upstream and downstream beam tubes using thermocouples, and the simulation results agreed well with the measured values. We compared different K-Cs-Sb samples, and the results are listed in Table 1. The typical QE drop is about 90%, and the QE could recover to its initial value when we transferred the K-Cs-Sb photocathodes to a room temperature environment after 2 weeks of operation [17].

3 Analytical QE formula

For describing the QE-related behavior of K-Cs-Sb photocathode at cryogenic temperature, we modified the QE formula as a function of temperature based on Spicer's three-step model, which is widely used to describe the photoemission process of semiconductors [31]. Band bending [32], initial photoelectrons generated from the doping energy level [26], and the built-in electric field [24] were discussed in the simulation process of GaAs and Cs_3Sb photocathodes. For K-Cs-Sb photocathode, less change was added, and the band gap was mostly focused on [13, 20]. This seems reasonable at room temperature because K-Cs-Sb is a weak p-type or even intrinsic semiconductor [27, 28], and suffers little influence from acceptor impurity. However, when we try to estimate the photoemission performance at cryogenic temperature, the changes of phonon scattering [23–25] and conductivity [33] should also be considered, because they affect the scattering rate [34], main scattering channel [35] and energy loss rate [36], changing the transport process compared to that at room temperature.

3.1 Basic QE formula

Generally, the initial electron energy distribution is related to the band gap, and the emission probability is influenced by the electron affinity [37]. For the convenience of analysis, we consider the contributions of band gap and electron affinity together as a threshold [38], and only photoelectrons with energy higher than work function could emit from the surface. Therefore the QE can be expressed as [38]:

$$\mathrm{QE}(\hbar\omega) = \int_0^D (1 - R(\hbar\omega))\alpha_p(\hbar\omega)G(z,\hbar\omega)e^{-\alpha_T(\hbar\omega)}dz, \quad (1)$$

where $R(\hbar\omega)$ and $\alpha_T(\hbar\omega)$ are the reflectivity and absorption coefficient of K-Cs-Sb at the photon energy of $\hbar\omega$, respectively, $\alpha_p(\hbar\omega)$ is the part that contributes to photoemission, and $G(z, \hbar\omega)$ is the probability of an electron excited at depth z by a photon of energy $\hbar\omega$ escaping from the material.

By applying relations $\alpha_p(\hbar\omega) = C(\hbar\omega - \phi)^{3/2}$ [38] and $G(z, \hbar\omega) = Ae^{P\hbar\omega}e^{-z/\lambda}$ [39], we obtain the final QE formula:

$$QE(\hbar\omega) = (1 - R(\hbar\omega))C\frac{(\hbar\omega - \phi)^{3/2}}{1/\lambda + \alpha_T(\hbar\omega)}e^{P\hbar\omega}\left[1 - e^{-(1/\lambda+\alpha_T(\hbar\omega))D}\right], \quad (2)$$

where C is a constant, λ is the mean free path of electrons, D is the thickness of the photocathode, and P is the photocathode parameter characterizing disorder degree and emission properties.

Eq. (2) represents the QE of the photocathode at a specific photon energy, with included photoemission parameters, like work function, mean free path and cathode's thickness, enabling the calculation of the spectral responses of different photocathode materials using related experimental data. By changing the structure parameter P and the work function value, it can also be used to fit the spectral responses of degraded photocathodes.

While the calculated spectral responses fit well with experimental results for many alkali photocathodes [38], Eq. (2) is only suitable at room temperature since some photoemission parameters are temperature-dependent. To evaluate the cryogenic performance of a photocathode more precisely, the work function and mean free path should be considered as a function of temperature.

3.2 Temperature dependence of work function

Typically, the work function of semiconductors consists of the band gap, electron affinity, bulk potential and surface potential [40], which have different temperature coefficients. As K-Cs-Sb is almost an intrinsic semiconductor where band bending at the surface can be omitted [28], and the electron affinity, which is related to the surface state, can be considered constant, we assume that the temperature dependence of the work function originates only from the band gap [41]. As shown in many experimental results, the band gap of semiconductors increases as the temperature decreases [21, 41, 42]. Here, we choose a simplified phonon dispersion model [43], which includes the influence of electron-phonon interaction and lattice thermal expansion and thus is almost suitable for all semiconductor materials [42], to explain the pinch effect in band gap. The band gap and work function with respect to temperature can be expressed as follows [43]:

$$E_g(T) = E_{gcn} - \Delta E_{ZP}\left(1 + \frac{2}{e^{\frac{\hbar\omega_{op}}{k_BT}} - 1}\right) \quad (3)$$

$$\phi(T) = \phi_{gcn} - \Delta E_{ZP}\left(1 + \frac{2}{e^{\frac{\hbar\omega_{op}}{k_BT}} - 1}\right), \quad (4)$$

where E_g and T are the band gap and temperature of the K-Cs-Sb photocathode, respectively, E_{gcn} and ϕ_{gcn} are constants, ΔE_{ZP} is the electron-phonon coupling strength parameter, $\hbar\omega_{op}$ is the energy of optical phonon, and k_B is the Boltzmann constant.

It is generally assumed that the K-Cs-Sb photocathode has a band gap of 1.2 eV and an electron affinity of 0.7 eV [33]. However, the work function values reported by different laboratories usually vary by about 0.1 eV around 1.9 eV [20, 44] due to different fabrication processes. Since the work function of the photocathode is a key parameter in the QE formula, it is necessary to use a suitable value to fit the QE behavior of the K-Cs-Sb photocathode fabricated using our fast-cesiation method [17].

Figure 1 shows the spectral response curves of the K-Cs-Sb photocathode measured using our cryogenic platform. The cathode was first slowly cooled down from 302 to 95.5 K, and then warmed up to 178 K and 302 K in turn using a pressured N_2 flow cooled by liquid nitrogen. The laser wavelength varied from 300 to 600 nm with a step of 20 nm. The measured QE at 520 nm decreased by more than 30% at the temperature of 95.5 K, but it gradually recovered during the cathode's warming up, giving almost the same spectral response as before the cooling-warming circle at room temperature.

Near the photoemission threshold, QE approximately satisfies the following relationship with photon energy [37]:

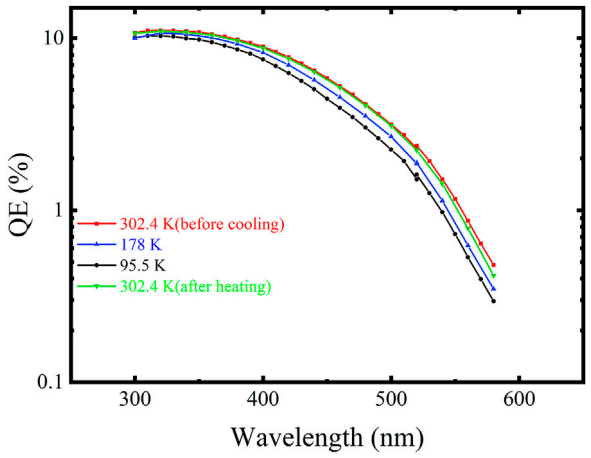

FIGURE 1
Spectral responses of the K-Cs-Sb photocathode at 302.4, 178, and 95.5 K during a cooling-warming cycle.

TABLE 2 The work function of the K-Cs-Sb photocathode at different temperatures.

Temperature [K]	Work function [eV]
302.4	1.838
178	1.901
95.5	1.922

$$\sqrt{QE} \propto (\hbar\omega - \phi). \tag{5}$$

Then the values of the work function at different temperatures are derived by linear fitting of the data in Figure 1, and the results are shown in Table 2. The average work function of K-Cs-Sb samples is 1.838 eV at room temperature, which is slightly lower than the value of 1.9 eV. This is probably caused by our fabrication procedure, where the fast cesiation process generates excess Cs on the photocathode surface and, thus, decreases electron affinity [45]. Besides, the work function increases by 0.084 eV when the cathode is cooled to 95.5 K, which is consistent with the BNL result [13]. Using the data in Table 2, the parameters in Eq. (4) are determined to be $\phi_{\mathrm{gcn}} = 2.015\ [eV]$ and $\Delta E_{ZP} = 0.084\ [eV]$.

3.3 Temperature dependence of mean free path

The change in electron transport property also needs to be considered when evaluating the QE of a photocathode at cryogenic temperature. Typically, the scattering rate and energy loss from lattice scattering decrease at low temperatures due to weakened lattice vibration [46]. Thus, the QE of alkali-antimonide photocathodes at high photon energies should increase as the temperature decreases [19]. However, the imperfection of the crystal structure and the micro-grained and porous nature of the photocathode [47] additionally complicate the situation, where the actual energy loss rate seems to be less temperature dependent [35], and the photoemission might be limited by the high resistivity of the photocathode [47]. As we focus more on the average scattering effect in the analytical model, this problem can be simplified by considering the temperature dependence of mean free path, which is proportional to free drift time. The movement of photoelectrons belongs to the transport process of non-equilibrium carriers, where the free drift time τ between two scattering events can be evaluated as follows [46]:

$$\tau = \frac{\sigma}{n_c e}, \tag{6}$$

where σ is the electric conductivity of the material, n_c is the density of carriers, and e is the electric charge.

For semiconductors, the electric conductivity decreases as the temperature decreases [33], indicating a shorter free drift time.

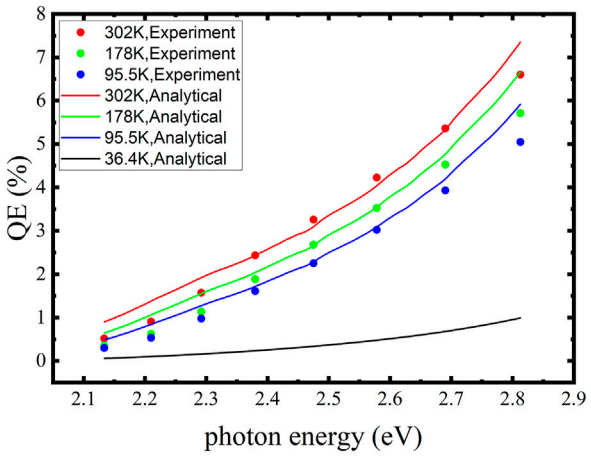

FIGURE 2
Comparison of the analytical and experimental results of spectral responses for the K-Cs-Sb photocathode at different temperatures. The black line represents the calculated spectral response at 36.4 K.

TABLE 3 Parameters used to calculate QE from Eq. 9.

Parameters	Value
Reflectivity, $R\ (\hbar\omega)$	Results from [48]
C	55.5
ϕ_{gcn}	2.015 eV
Coefficient of band gap contraction, ΔE_{ZP}	0.084 eV
λ_0	2.601×10^5 nm [31]
Characteristic temperature, T_0	4.2×10^6 K [47]
Absorption coefficient, $\alpha_T\ (\hbar\omega)$	Results from [49]
Photocathode parameter, P	0.89 [39]
Cathode's thickness, D	32 nm
Optical phonon energy, $\hbar\omega_{op}$	0.027 eV [13]
Photon energy, $\hbar\omega$	2.134–2.813 eV

Other researchers measured the temperature dependence of the conductivity of K-Cs-Sb and expressed it as follows [47]:

$$\sigma(T) = \sigma_0 e^{-\left(\frac{T_0}{T}\right)^{1/4}}, \tag{7}$$

where T_0 and σ_0 are calculated as 4.2×10^6 K and $7 \times 10^3\ (\Omega m)^{-1}$, respectively.

Therefore, the mean free path as a function of temperature can be evaluated as follows:

$$\lambda(T) = \lambda_0 e^{-\left(\frac{T_0}{T}\right)^{1/4}}, \tag{8}$$

where the constant λ_0 can be calculated as 2.601×10^5 nm when the mean free path of K-Cs-Sb at room temperature is estimated to be 5 nm [31].

Combining Eqs 2, 4, and 8, we obtained the general QE formula as follows:

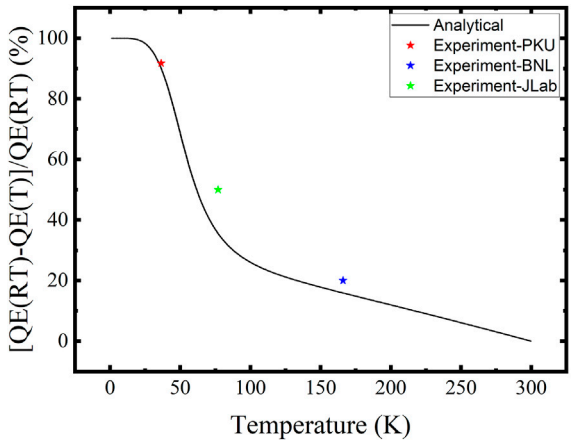

FIGURE 3
Calculated relative QE drop at 519 nm of K-Cs-Sb in DC-SRF photoinjector compared to room temperature; star dots represent the experimental results. The blue [13] and green [20] dots were reported by other laboratories with an extraction voltage of less than 300 V; therefore, the discrepancies might originate from the differences in work function and the lack of the Schottky effect.

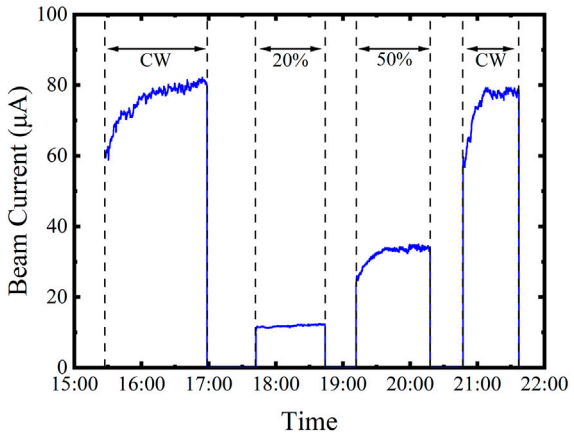

FIGURE 4
Macro-pulse operation results of a QE-degraded K-Cs-Sb sample with a fixed laser power during each operation. The applied laser power was 375 mW during the CW operation. For macro-pulse operation at the duty cycle of 20% and 50%, the laser power was 75 and 187.5 mW, respectively. The average beam current increased by more than 20 μA during the CW operation, but there was a minor increase at 20% duty cycle.

$$QE(\hbar\omega,T) = (1-R(\hbar\omega))C\frac{\left(\hbar\omega-\phi_{\mathrm{gcn}}+\mathrm{E}_{ZP}\left(1+\frac{2}{e^{\frac{\hbar\omega_{op}}{k_BT}}-1}\right)\right)^{3/2}}{e^{\left(\frac{T_0}{T}\right)^{1/4}}\Big/\lambda_0+\alpha_T(\hbar\omega)} \times e^{P\hbar\omega}\left[1-e^{-\left(e^{\left(\frac{T_0}{T}\right)^{1/4}}\Big/\lambda_0+\alpha_T(\hbar\omega)\right)D}\right]. \quad (9)$$

The temperature dependence of QE originates from the changes in work function and mean free path.

4 Discussion

To verify the validity of the obtained analytical formula, we compared the calculated spectral responses and relative QE drop of the K-Cs-Sb photocathode with experimental results.

4.1 Validation of the QE formula

Figure 2 shows the spectral responses of K-Cs-Sb at different temperatures calculated using the parameters in Table 3. The experimental and analytical results generally agree, but some discrepancies exist at longer and shorter wavelengths. This might be due to the neglect of electron-electron scattering and trajectory change after scattering.

When operating in SRF injectors, the Schottky effect of a strong surface field should also be considered to evaluate the QE of photocathodes, as the applied electric field would cause a decrease in electron affinity, which can be evaluated as follows [50]:

$$\Delta\phi = \sqrt{\frac{e}{4\pi\varepsilon_0}\frac{\varepsilon-\varepsilon_0}{\varepsilon+\varepsilon_0}E_{cat}}, \quad (10)$$

where ε_0 and ε are the permittivity of vacuum and photocathode, respectively, and E_{cat} is the applied electric field strength. For DC-SRF photoinjector, a drive laser of 519 nm and a cathode surface field strength of 3.1 MV/m are adopted, causing a decrease of 0.059 eV in work function, where the permittivity of K-Cs-Sb is estimated as $7.87\varepsilon_0$ [50]. Figure 3 shows the calculated relative QE drop compared to the value at room temperature with the photon energy of 2.38 eV. At a temperature higher than 100 K, the increase in work function is the main mechanism of the QE drop. The huge decrease in electric conductivity at lower temperatures, which causes a shorter mean free path, contributes to the rapid drop. The analytical curve predicts a QE drop of 90.1% at 36.4 K, which fits well with our experimental result of about 90% in DC-SRF photoinjector. The QE drops reported by other laboratories were also compared, showing some discrepancies that might originate from the differences in work function caused by fabrication procedures and the influence of the Schottky effect.

4.2 QE variation during macro-pulse operation at different duty cycles

In our model, we assign the QE drop at cryogenic temperature to the changes in work function and mean free path. However, gas trapping at the emission surface in the cryogenic temperature environment may also cause a QE decrease. To verify whether gas trapping is the main reason, we measured the average beam current during macro-pulse operation at different duty cycles with DC-SRF photoinjector, where the extraction electric field strength was 3.1 MV/m, and the laser spot size and FWHM pulse width were set to 5 mm and 24 ps, respectively.

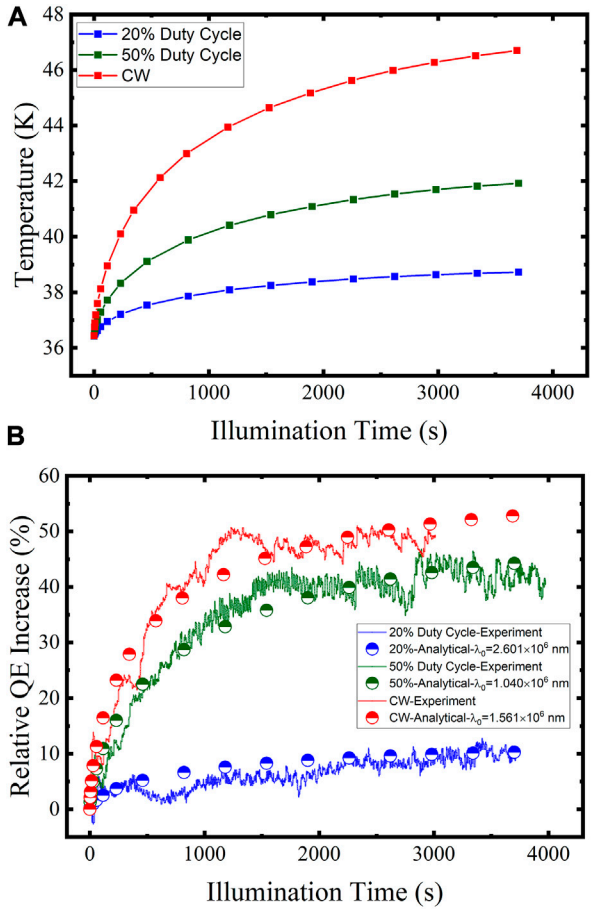

FIGURE 5
Simulation of QE changes in DC-SRF photoinjector during macro-pulse operation at different duty cycles. **(A)** Simulated temperature rise during laser illumination. **(B)** Comparison between the experimental data and the calculated relative QE increase using Eq. 9 with different λ_0 values.

Figure 4 shows the extracted beam current from a degraded K-Cs-Sb sample during macro-pulse operation at different laser duty cycles, where the laser power remains constant during each operation. During the first CW operation, the beam current increased from 60 to 81 μA with a fixed laser power of 375 mW. At a duty cycle of 20%, the beam current increased slightly from 11.5 to 12.2 μA with the laser power of 75 mW. When the duty cycle increased to 50%, the beam current increased faster and gradually stabilized at 34.3 μA. Finally, during the second CW operation, the beam current showed the same behavior as the first CW operation. The intervals between operations at different duty cycles were long enough to reach the thermal equilibrium of the photocathode.

In the UHV environment of injectors, the average time to form a single molecular layer was in the range of several seconds, much longer than the macro pulse duration [51]; therefore, the effective number of absorbed gas molecules decreased continuously during operation, which resulted in the QE recovery before stabilization. If the QE degradation is mainly caused by gas trapping, after enough time, the QE should be able to recover to the same value for low and high duty cycles, as the single laser pulse energy is the same at different duty cycles. From the experimental data, we found that the QE recovered to different values at low and high duty cycles. Thus, we can conclude that gas trapping is not the main reason for the QE drop at cryogenic temperature. The different duty cycles of the drive laser only changed the temperature of the cooled photocathode by thermal effect, which was the real reason for the QE increase during macro-pulse operation.

The heating effect of the drive laser arises from the relaxation of photoelectrons during transport and the non-radiative recombination of non-emitted electrons [52]. For simplification, we used a conversion coefficient $\eta_{thermal}$ to express the proportion of thermal energy in the absorbed laser energy, and the heat power can be expressed as follows:

$$P_{heat} = (1 - R(\hbar\omega))\eta_{thermal}P_{laser}, \tag{11}$$

where P_{laser} is the laser power at a specific duty cycle.

We used Comsol software to simulate the temperature rise of the photocathode in DC-SRF photoinjector when illuminated by a 5-mm-diameter laser spot of different powers. The conversion coefficient $\eta_{thermal}$ is fitted to 0.7, so the maximum heat power of 0.205 W was applied to the cathode surface during the CW operation. Figure 5A shows the simulation results of the temperature change during macro-pulse operation. Within 60 min, the photocathode temperature increased from 36.4 to 38.7 K at the duty cycle of 20%, while the increase during the CW operation was 10.3 K.

The calculated results of QE changes during macro-pulse operation are shown in Figure 5B, which agree well with the experimental results and show the same trend as the temperature rise in Figure 5A. Due to the low initial value and rapid change rate at cryogenic temperature, the QE increases by nearly 50% during the CW operation, but less than 10% at 20% duty cycle, and the difference is obviously caused by the slow temperature increase at a lower duty cycle. This confirms that the laser-induced temperature rise of the cold photocathode is the main reason for the QE increase during macro-pulse operation.

5 Summary

Based on Spicer's three-step model, we modified the analytical formula of QE for semiconductor photocathodes at cryogenic temperature. The temperature dependence of work function and mean free path of the photocathode material is included in the expression. The calculated QE drop of about 90.1% at 36.4 K fits well with the measured QE change in DC-SRF photoinjector at Peking University. This modified formula provides a method to evaluate the QE performance of semiconductor photocathodes at cryogenic temperature more precisely, and may help design photocathode SRF injectors to generate ultra-low emittance electron beams. The reliability of this analytical formula needs to be confirmed with more experimental results.

Data availability statement

The raw data supporting the conclusion of this article will be made available by the authors, without undue reservation.

Author contributions

YZ: Methodology, Software, Investigation, Data curation, Writing—original draft. DO: Investigation, Data curation. HX: Conceptualization, Validation, Methodology, Funding acquisition, Writing—review and editing. KL: Conceptualization, Supervision, Project administration, Funding acquisition, Writing—review. SH: Funding acquisition. All authors contributed to the article and approved the submitted version.

Funding

This work was supported by the National Key Research and Development Program of China under Grant No. 2017YFA0701001 and by the National Natural Science Foundation of China under Grant No. 12075012.

Conflict of interest

The authors declare that the research was conducted in the absence of any commercial or financial relationships that could be construed as a potential conflict of interest.

Publisher's note

References

1. Musumeci P, Navarro JG, Rosenzweig JB, Cultrera L, Bazarov I, Maxson J, et al. Advances in bright electron sources. *Nucl Instr Methods Phys Res* (2018) 907:209–20. doi:10.1016/j.nima.2018.03.019

2. Simone DM. On the importance of electron beam brightness in high gain free electron lasers. *Photonics* (2015) 2:317–41. doi:10.3390/photonics2020317

3. Willeke F, Beebe-Wang J. Electron ion collider conceptual design report 2021 Report No.BNL-221006-2021-FORE TRN: US2215154 (2021). doi:10.2172/1765663

4. Gulliford C, Bartnik A, Bazarov I, Cultrera L, Dobbins J, Dunham B, et al. Demonstration of low emittance in the cornell energy recovery linac injector prototype. *Phys Rev Spec Topics-Accelerators Beams* (2013) 16:073401. doi:10.1103/physrevstab.16.073401

5. Sannibale F, Filippetto D, Qian H, Mitchell C, Zhou F, Vecchione T, et al. High-brightness beam tests of the very high frequency gun at the advanced photo-injector experiment test facility at the lawrence berkeley national laboratory. *Rev Scientific Instr* (2019) 90:033304. doi:10.1063/1.5088521

6. Petrushina I, Litvinenko V, Jing Y, Ma J, Pinayev I, Shih K, et al. High-brightness continuous-wave electron beams from superconducting radio-frequency photoemission gun. *Phys Rev Lett* (2020) 124:244801. doi:10.1103/physrevlett.124.244801

7. Dunham B, Barley J, Bartnik A, Bazarov I, Cultrera L, Dobbins J, et al. Record high-average current from a high-brightness photoinjector. *Appl Phys Lett* (2013) 102:034105. doi:10.1063/1.4789395

8. Pierce CM, Andorf MB, Lu E, Gulliford C, Bazarov IV, Maxson JM, et al. Low intrinsic emittance in modern photoinjector brightness. *Phys Rev Acc Beams* (2020) 23:070101. doi:10.1103/physrevaccelbeams.23.070101

9. Bazarov I, Cultrera L, Bartnik A, Dunham B, Karkare S, Li Y, et al. Thermal emittance measurements of a cesium potassium antimonide photocathode. *Appl Phys Lett* (2011) 98:224101. doi:10.1063/1.3596450

10. Maxson J, Cultrera L, Gulliford C, Bazarov I. Measurement of the tradeoff between intrinsic emittance and quantum efficiency from a naksb photocathode near threshold. *Appl Phys Lett* (2015) 106:234102. doi:10.1063/1.4922146

11. Lee H, Cultrera L, Bazarov I. Intrinsic emittance reduction in transmission mode photocathodes. *Appl Phys Lett* (2016) 108:124105. doi:10.1063/1.4944790

12. Cultrera L, Karkare S, Lee H, Liu X, Bazarov I, Dunham B. Cold electron beams from cryocooled, alkali antimonide photocathodes. *Phys Rev Spec Topics-Accelerators Beams* (2015) 18:113401. doi:10.1103/physrevstab.18.113401

13. Xie H, Ben-Zvi I, Rao T, Xin T, Wang E. Experimental measurements and theoretical model of the cryogenic performance of bialkali photocathode and characterization with Monte Carlo simulation. *Phys Rev Acc Beams* (2016) 19:103401. doi:10.1103/physrevaccelbeams.19.103401

14. Xiang R, Teichert J. Photocathodes for high brightness photo injectors. *Phys Proced* (2015) 77:58–65. doi:10.1016/j.phpro.2015.11.010

15. Wang E, Litvinenko V, Pinayev I, Gaowei M, Skaritka J, Belomestnykh S, et al. Long lifetime of bialkali photocathodes operating in high gradient superconducting radio frequency gun. *Scientific Rep* (2021) 11:4477. doi:10.1038/s41598-021-83997-1

16. Pinayev I, Altinbas Z, Belomestnykh S, Ben-Zvi I, Brown K, Brutus JC, et al. *Record performance of srf gun with csk2sb photocathode*. Upton, NY (United States): Tech. rep., Brookhaven National Lab.BNL (2016).

17. Ouyang D, Zhao Y, Xie H, Zhang X, Zhao S, Feng L, et al. Performance of bialkali photocathode in dc-srf photoinjector. *Nucl Instr Methods Phys Res Section A: Acc Spectrometers, Detectors Associated Equipment* (2022) 1026:166204. doi:10.1016/j.nima.2021.166204

18. Konomi T, Honda Y, Kako E, Kobayashi Y, Michizono S, Miyajma T, et al. Development of srf gun applying new cathode idea using a transparent superconducting layer. In: Proceedings of the 59th ICFA Advanced Beam Dynamics Workshop on Energy Recovery Linacs; June 18-23, 2017; Geneva, Switzerland (2017). p. 18–23.

19. Nathan R, Mee C. Photoelectric and related properties of the potassium—Antimony—Caesium photocathode. *Int J Elect* (1967) 23:349–54. doi:10.1080/00207216708961542

20. Mamun M, Hernandez-Flores M, Morales E, Hernandez-Garcia C, Poelker M. Temperature dependence of alkali-antimonide photocathodes: Evaluation at cryogenic temperatures. *Phys Rev Acc Beams* (2017) 20:103403. doi:10.1103/physrevaccelbeams.20.103403

21. Panish M, Casey H, Jr. Temperature dependence of the energy gap in gaas and gap. *J Appl Phys* (1969) 40:163–7. doi:10.1063/1.1657024

22. Fowler RH. The analysis of photoelectric sensitivity curves for clean metals at various temperatures. *Phys Rev* (1931) 38:45–56. doi:10.1103/physrev.38.45

23. Ghorai A, Bhattacharya D. Effect of non-parabolic band on the scattering rates of free electrons in high purity semiconductors at low lattice temperatures. *physica status solidi (b)* (1991) 163:247–58. doi:10.1002/pssb.2221630125

24. Gupta P, Cultrera L, Bazarov I. Monte Carlo simulations of electron photoemission from cesium antimonide. *J Appl Phys* (2017) 121:215702. doi:10.1063/1.4984263

25. Karkare S, Bazarov I. Effect of nanoscale surface roughness on transverse energy spread from gaas photocathodes. *Appl Phys Lett* (2011) 98:094104. doi:10.1063/1.3559895

26. Huang PW, Qian H, Du Y, Huang W, Zhang Z, Tang C. Photoemission and degradation of semiconductor photocathode. *Phys Rev Acc Beams* (2019) 22:123403. doi:10.1103/physrevaccelbeams.22.123403

27. Ghosh C. Photoemissive materials. *Phys Thin Films* (1982) 12:53–166.

28. Fisher D, McDonie A, Sommer A. Band-bending effects in na2ksb and k2cssb photocathodes. *J Appl Phys* (1974) 45:487–8. doi:10.1063/1.1663009

29. Quan S, Hao J, Lin L, Zhu F, Wang F, Feng L, et al. Stable operation of the dc-srf photoinjector. *Nucl Instr Methods Phys Res Section A: Acc Spectrometers, Detectors Associated Equipment* (2015) 798:117–20. doi:10.1016/j.nima.2015.07.025

30. Multiphysics C. *Introduction to comsol multiphysics®*. Burlington, MA: COMSOL Multiphysics (1998).

31. Spicer WE, Herrera-Gomez A. Modern theory and applications of photocathodes. Photodetectors and Power Meters *(SPIE)* (1993) 2022:18–35.

32. Karkare S, Dimitrov D, Schaff W, Cultrera L, Bartnik A, Liu X, et al. Monte Carlo charge transport and photoemission from negative electron affinity gaas photocathodes. *J Appl Phys* (2013) 113:104904. doi:10.1063/1.4794822

33. Ghosh C, Varma B. Preparation and study of properties of a few alkali antimonide photocathodes. *J Appl Phys* (1978) 49:4549–53. doi:10.1063/1.325465

34. Ridley BK. *Quantum processes in semiconductors*. Oxford, United Kingdom: Oxford University Press (2013).

35. Sen R, Vast N, Sjakste J. Hot electron relaxation and energy loss rate in silicon: Temperature dependence and main scattering channels. *Appl Phys Lett* (2022) 120: 082101. doi:10.1063/5.0082727

36. Shah J, Pinczuk A, Gossard A, Wiegmann W. Energy-loss rates for hot electrons and holes in gaas quantum wells. *Phys Rev Lett* (1985) 54:2045–8. doi:10.1103/physrevlett.54.2045

37. Rao T, Dowell DH. *An engineering guide to photoinjectors*. arXiv preprint arXiv: 1403.7539 (2014).

38. Spicer WE. Photoemission and related properties of the alkali-antimonides. *J Appl Phys* (1960) 31:2077–84. doi:10.1063/1.1735505

39. Zhao M, Sun J, Qian Y, Si S, Jin M, Jian L, et al. Theoretical investigation of spectral response characteristics of k2sbcs photoelectric cathode. *Infrared Tech* (2018) 40: 289–93.

40. Mönch W, Koenders L. On the temperature coefficient of the ionization energy in iii-v compound semiconductors. In: Proceedings of the 17th International Conference on the Physics of Semiconductors; August 6–10, 1984; San Francisco, California, USA (1985). p. 85–8.

41. Chen B, Zhuang C, Wang X. Work function change of hydrogen chemisorped si(100) surface. *Chin J Semiconductors* (1983) 4:403.

42. Zhang A, Chen P, Zhou J, Li Y, Yang Y, Mao X, et al. Study on temperature dependence of semiconductor bandgap. *Optoelectronic Tech* (2019) 39:160.

43. Giustino F. Electron-phonon interactions from first principles. *Rev Mod Phys* (2017) 89:015003. doi:10.1103/RevModPhys.89.015003

44. Mohanty S, Rocco GG, Hillert W, Krasilnikov M, Michelato P, Monaco L, et al. Development of multialkaliantimonides photocathodesfor high brightness photoinjectors. In: Proc. IPAC'21; 24 - 28 May 2021; Geneva, Switzerland (2021). p. 1416–9.

45. Yang Z, Zou JJ, Niu J, Zhang YJ, Chang BK. Research on high temperature cs activated gaas photocathode. *Guang Pu Xue Yu Guang Pu Fen Xi* (2010) 30:2038.

46. Zohuri B. *Physics of cryogenics an ultralow temperature phenomenon*. Amsterdam, Netherlands: Elsevier (2013).

47. Hirohata T, Mizushima Y. Conductivity mechanism of cs-sb-type photoemissive cathode film. *Jpn J Appl Phys* (1990) 29:1795. doi:10.1143/JJAP.29.1795

48. JARVIS. Jvasp-22672 (2018). Available from: https://www.ctcms.nist.gov/~knc6/jsmol/JVASP-22672.html.

49. Kalarasse L, Bennecer B, Kalarasse F. Optical properties of the alkali antimonide semiconductors, and. *J Phys Chem Sol* (2010) 71:314–22. doi:10.1016/j.jpcs.2009.12.083

50. Xie HM, Wang ED, Liu KX. Analytical model and simulation of the Schottky effect on a cryo-cooled bialkali photocathode. *Nucl Sci Tech* (2018) 29:71. doi:10.1007/s41365-018-0400-6

51. Gao B, Cui S. *Vacuum Physics*. Beijing, China: Science Press (1983).

52. Meyer JR, Bartoli FJ, Kruer MR. Optical heating in semiconductors. *Phys Rev B* (1980) 21:1559–68. doi:10.1103/PhysRevB.21.1559

frontiers | Frontiers in Physics

TYPE Original Research
PUBLISHED 05 April 2023
DOI 10.3389/fphy.2023.1153005

OPEN ACCESS

EDITED BY
Nicholas Walker,
Helmholtz Association of German Research Centres (HZ), Germany

REVIEWED BY
Gianluca Ghigo,
Polytechnic University of Turin, Italy
Winni Decking,
Helmholtz Association of German Research Centres (HZ), Germany

*CORRESPONDENCE
Yuhui Li,
liyuhui@ihep.ac.cn

SPECIALTY SECTION
This article was submitted to Interdisciplinary Physics, a section of the journal Frontiers in Physics

RECEIVED 28 January 2023
ACCEPTED 23 March 2023
PUBLISHED 05 April 2023

CITATION
Wei J, Yang X, Chen Z, Zhang X, Bian X and Li Y (2023), Development of NbTi planar superconducting undulators at the IHEP.
Front. Phys. 11:1153005.
doi: 10.3389/fphy.2023.1153005

Development of NbTi planar superconducting undulators at the IHEP

Junhao Wei[1], Xiangchen Yang[2], Zilin Chen[2,3], Xiangzhen Zhang[2,3], Xiaojuan Bian[2] and Yuhui Li[2]*

[1]China Spallation Neutron Source, Institute of High Energy Physics, Chinese Academy of Sciences, Dongguan, Guangdong, China, [2]Institute of High Energy Physics, Chinese Academy of Sciences, Beijing, China, [3]School of Nuclear Science and Technology, University of Chinese Academy of Sciences, Beijing, China

Superconducting undulators (SCUs) have the advantages of generating stronger magnetic field and the radiation hardness compared to permanent magnet undulators. Therefore, SCUs are valuable to be applied in the free-electron lasers (FELs) driven by high-repetition-rate linear accelerators. The Insertion Device Group at the Institute of High Energy Physics (IHEP) in China started an R&D project to produce NbTi planar SCU prototypes with 15 mm period length. Several SCU prototypes, including short mock-ups, a 0.5-m-long SCU, and a 1.5-m-long SCU, have been successfully produced and cryogenic tested. The short mock-up coils were cooled by a liquid helium free cryostat to be quench trained at 4 K. The maximum current in the coils reached 500 A and the magnetic peak field exceed 1 T with 7 mm gap. The 0.5-m-long SCU was tested by using a vertical test system. The correction coils were confirmed with the ability in both correcting the magnetic field integrals and the phase error. The 1.5-m-long SCU was not only vertically tested, but also installed in a cryostat to be operated with high current over a long time. We applied the gap adjustment method to reduce the phase error within 9 degrees. The development of SCUs at the IHEP is introduced in this paper in detail.

KEYWORDS

superconducting undulator, NbTi, free-electron laser, vertical test, phase error

1 Introduction

The next-generation self-amplified spontaneous emission (SASE) free-electron lasers (FELs) operating in the continuous-wave (CW) mode with a MHz-level repetition rate have become a focus of research. Such FEL facilities will increase the average brightness and offer more flexible time patterns of the beam. Undulators are key devices in accelerator-based FELs that can provide several orders of magnitude higher flux rates than bending magnets. Undulators consist of periodic arrays of permanent magnets or superconducting coils. Electrons are forced to undergo oscillations when traveling through the periodic magnet structure and thus to radiate photon beams concentrated in narrow energy bands. The quality of the radiation directly depends on the performance of the undulator.

Currently, permanent magnet undulators (PMUs) are mainly used in accelerators. In order to increase the magnetic field strength of PMUs at a short period length, researchers developed the in-vacuum undulator (IVU) by installing the permanent magnet arrays and supporting structure in a large vacuum chamber. In this case, the vacuum chamber in the undulator gap is removed and the gap distance can be compressed down to about 5 mm.

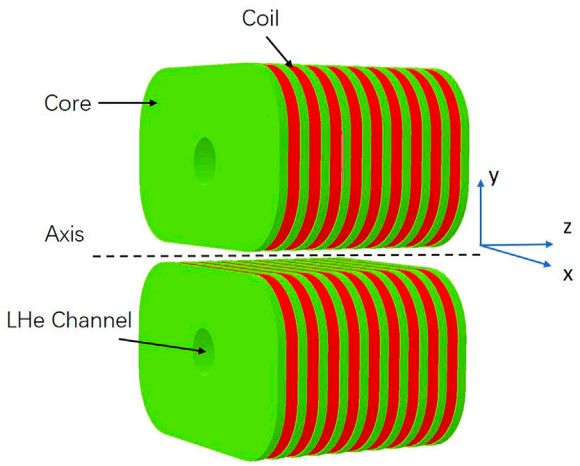

FIGURE 1
Simulation model of the short SCU in the OPERA-3D program.

Based on IVUs, the cryogenic permanent magnet undulator (CPMU) has been developed by cooling the permanent magnet with liquid nitrogen to increase the remanence of the magnetic material. However, the permanent magnet could be demagnetized by the radiation when the beam loss happens at the undulator section during the accelerator operation. For IVUs and CPMUs, the damage could be more serious because there is no vacuum chamber in the gap. Although CPMUs use the magnetic materials with large coercive force at low temperature to reduce the demagnetization effect, the radiation damage risk cannot be ignored. Radiation damage may be even worse for the CW-FEL facilities due to the high beam current. In addition, the magnetic field strength of PMUs reaches an upper limit due to limitations in the available magnetic materials. Superconducting undulators have better radiation hardness with no risk of material remanence and can provide stronger magnetic fields than PMUs [1–4]. In this case, it is important to develop SCUs for valuable applications in CW-FELs.

SCUs have been developed in many institutes worldwide and are successfully operated at two light sources: the KIT synchrotron and APS [5–8]. The Institute of High Energy Physics (IHEP) in China started an R&D project to develop NbTi planar undulators in 2020. In this paper, we introduced the progress of the NbTi SCU project at the IHEP, including the development of three different SCU prototypes. The SCU structure was determined using the simulation program OPERA-3D [9]. The effect of the correction coil on the magnetic field and the field deviation caused by the pole and coil errors were also analyzed. Several short mock-up coils with 4.5 periods were produced at the beginning of the project to test the manufacturing techniques and to obtain quench training experience. A liquid helium-free cryostat was specially designed to test the short SCU prototype under 4.2 K [10]. The load current in the mock-up coils successfully reached up to 500 A, and the corresponding magnetic peak field exceeded 1 T. Then, a 0.5-m-long SCU prototype was manufactured and fabricated. A vertical test system was set up to test the SCU prototypes in a Dewar submerged in liquid helium [11]. The vertical test system contained magnetic field measurement equipment to obtain the field distribution of the SCU on the axis. During the test, the current in the main coils of the SCU reached 480 A, giving a corresponding magnetic field of over 1 T after several quenches. The ability of the correction coils to optimize the first and second field integrals was also verified. In addition, the phase error of the magnetic field can be also corrected with a suitable correction current. The final target of our R&D project was to develop a 1.5-m-long SCU. Recently, the 1.5-m-long SCU prototype was produced and tested vertically in a Dewar. After the vertical test, the cryogenic test was conducted by installing this 1.5-m-long SCU in a large cryostat horizontally, and thus 1.5-m-long SCU was proved to be successful under low temperatures.

TABLE 1 Parameters of the short SCU simulation model.

Parameter	Value
Period length	15 mm
Pole length	3 mm
Groove region	4.5 × 6.5 mm^2
Core width	90 mm
Core height	47 mm
Gap	7 mm
Peak field	≥1 T

2 SCU simulation

The SCU model is simulated using the OPERA-3D program. The magnet core is of a vertical racetrack type that enables a continuous coil winding scheme with a single strand. The size of the coil pack is designed to reach the target peak field on the axis, while the magnetic field in the conductors should be relatively small to allow a large load current. Figure 1 shows the 3D simulation model for the short SCU prototype and the coordinate axes defined for the model. The cores and poles are made of pure electric iron DT4, and each core consists of 4.5 periods with a period length of 15 mm. The coils are wound with round NbTi/Cu strands with 0.6 mm diameter. Each coil contains 72 turns of NbTi wires within 11 layers. The odd layers have seven turns of conductors, and the even layers have six turns of conductors. There is a cylindrical channel through the iron core which contains liquid helium for cooling the magnet in the cryostat. Table 1 lists the main parameters of the SCU.

The coil groove is 4.5 mm width in the z-direction and 6.5 mm deep in the y-direction. The adjacent grooves are separated by the pole with 3 mm width. The limit of the load current in the NbTi wire depends on the maximum magnetic fields and the temperature on the coils [12,13]. The simulation results show that the maximum current that can be applied to the coils is 629 A, with a corresponding peak field of 1.27 T, and the operation current is about 438 A to reach a 1 T peak field.

In the first two grooves at each end of the iron core, correction coils are wound in order to correct the first and second integrals of

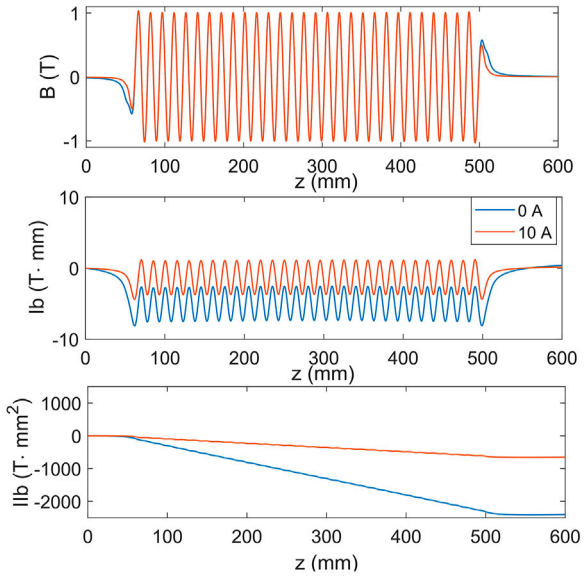

FIGURE 2
Magnetic field on the axis (top) and the corresponding first integral curves (middle) and second integral curves (bottom) with 0 A and 10 A correction currents, respectively, for a 0.5-m-long SCU model.

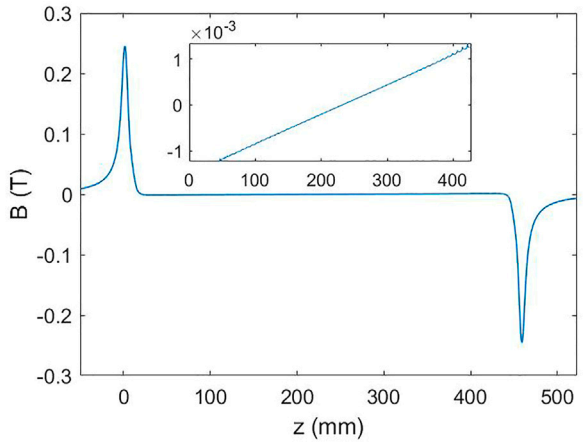

FIGURE 3
Magnetic field difference caused by 10 A correction currents.

the magnetic field. The first and second magnetic field integrals are related to the beam trajectory angle and transverse position, respectively, as given in the following equations:

$$x'(z) = -\frac{e}{\gamma m_0 v_z}\int_0^z B_y(z_1)dz_1 = -\frac{e}{\gamma m_0 v_z} I_1(z), \quad (1)$$

$$x(z) = -\frac{e}{\gamma m_0 v_z}\int_0^z I_1(z_2)dz_2 = -\frac{e}{\gamma m_0 v_z} I_2(z), \quad (2)$$

where e is the beam charge, γ is the relativistic factor, m_0 is the electron rest mass, $I_1(z)$ is defined as the first integral of the magnetic field, and $I_2(z)$ is the second integral of the magnetic field. The main

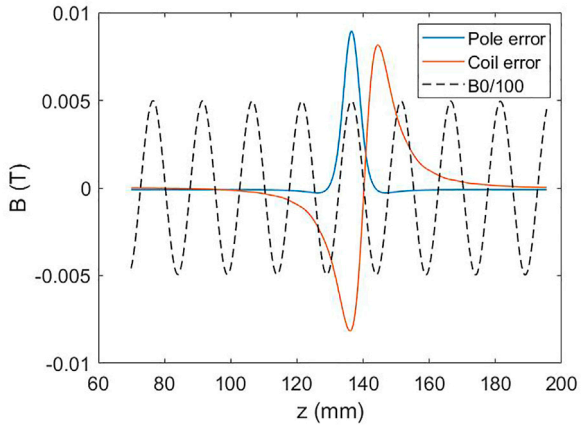

FIGURE 4
Field deviation caused by 0.2 mm displacement of a single pole and a single coil bundle. The black dashed curve indicates the ideal field whose amplitude was reduced to 1/100.

function of the correction coils is to optimize the field integrals with a suitable current. Figure 2 gives the magnetic field distribution and the corresponding field integral curves for a 0.5-m-long SCU simulation model with 0 A and 10 A correction currents, respectively. The figure shows that the first and second magnetic field integrals are optimized significantly.

The difference curve between the magnetic fields with and without the correction current is plotted in Figure 3. The field caused by the correction coils mainly focuses on the two ends of the SCU, which can kick the beam and thus change the beam trajectory. The center field is approximate to a line through the undulator center, which can affect the field integral slightly and increase the magnetic field phase error.

We want to modify the local field of the 1.5-m-long SCU by adjusting the local magnetic gaps. In this case, the field deviation caused by the position errors of the poles and coils in the y-direction needs to be evaluated. Figure 4 shows the field error caused by a single pole or a single coil bundle with 0.2 mm displacement close to the beam axis. The black dashed curve indicates the reduced magnetic field on the axis with 341 A main current. The pole displacement induces a field error in the pole location, while the coil bundle displacement causes an antisymmetric disturbance of the magnetic field that mainly affects the two adjacent peaks. The amplitude of the field deviation is linearly dependent on the position error of the pole and coil bundle. Therefore, the gap adjustment of the SCU can be determined according to the difference in the peak fields.

3 Short mock-up coils

Several short mock-up coils were manufactured to study the processing technologies. The magnet mainly consisted of an iron core, poles, and side plates, as shown in Figure 5. The core made of DT4 was machined precisely as a whole component. Poles and side plates were processed independently and then inserted into

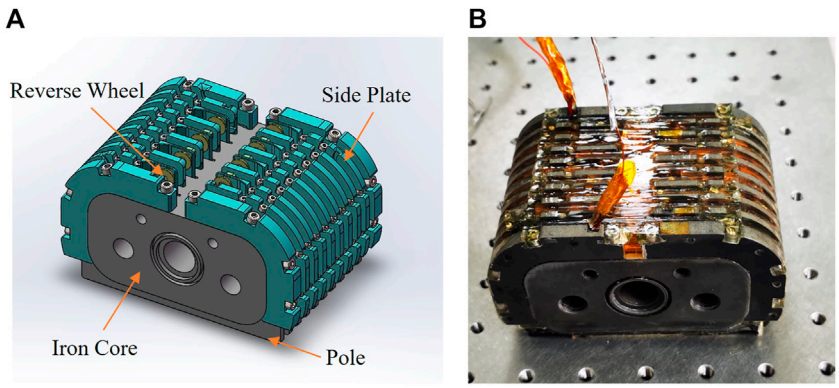

FIGURE 5
The structure model **(A)** and the photo **(B)** of the SCU short mock-up.

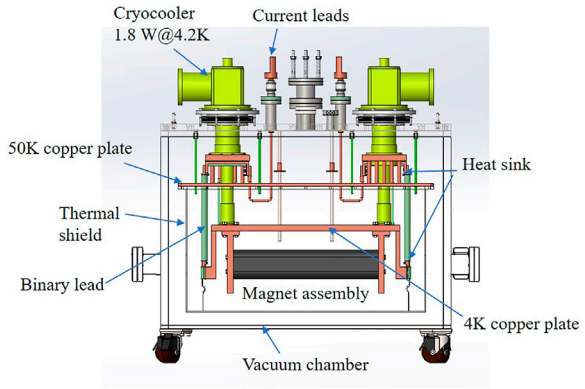

FIGURE 6
Schematic drawing of the LHe-free cryostat.

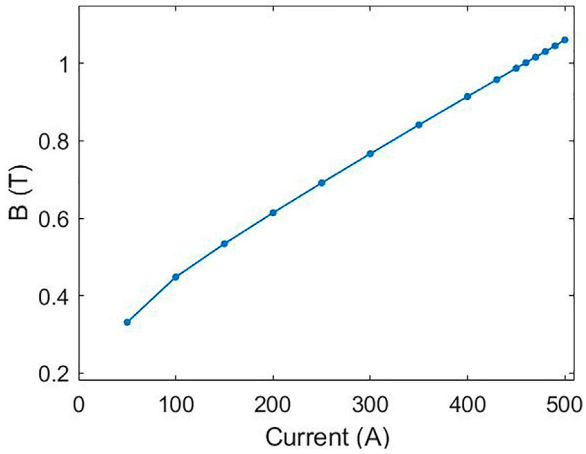

FIGURE 7
Relation curve between the peak magnetic field and the load current for short mock-up coils.

the core. We tried two different materials to prepare the side plates: Al and G10. The Al side plates can enhance the capacity of heat transmission, while the G10 plates have better insulation performance. Reverse wheels were installed on the side plates to change the winding direction of the NbTi strand from one groove to the next. A continuous scheme with a single strand was achieved with the help of the reverse wheels. The coils were wound by Kapton to enhance the insulation behavior of the iron core. The coils-to-ground insulation can tolerate a voltage more than 2000 V. After coil winding, the short mock-up was epoxy-impregnated to fix the coil position during quench training. The short SCU structure and a mock-up after impregnation are shown in Figure 5.

In order to reduce the high cost of the cryogenic test using liquid helium (LHe), a LHe-free cryostat was specially designed and fabricated. A structure diagram of the cryostat is presented in Figure 6. The cryostat was cooled by two G-M-type two-stage cryocoolers, which provided a cooling capacity of 3.6 W at 4.2 K. The heat declined, and magnet assembly in the cryostat can reach the target temperature through conduction cooling. The thermal shield was installed under the 50 K plate, which was connected to the first stage cryocoolers by copper strips. The second-stage coolers were connected to the 4 K plate, where the magnet was mounted. A pair of binary leads consisting of copper rods and high temperature superconductors (HTSs) was used to connect SCU coils and the power supply for loading the current. The HTS was installed between the 50 K and 4 K cold mass. The cold structure was surrounded by the vacuum box to reach the vacuum environment with the order of 10^{-5} Pa. The total heat load of the cryostat was about 0.34 W, which can be covered by cryocoolers [10]. Temperature sensors were mounted on special locations to monitor the cooling process. The short mock-up was cooled down to about 3.2 K after 15 h.

The short SCU was trained to increase the current loading ability. The maximum current in the mock-up coils reached 500 A within ten quenches [14]. A cryogenic hall probe was set in the undulator gap to measure the peak magnetic field on the axis. The relationship curve between the load current and the peak

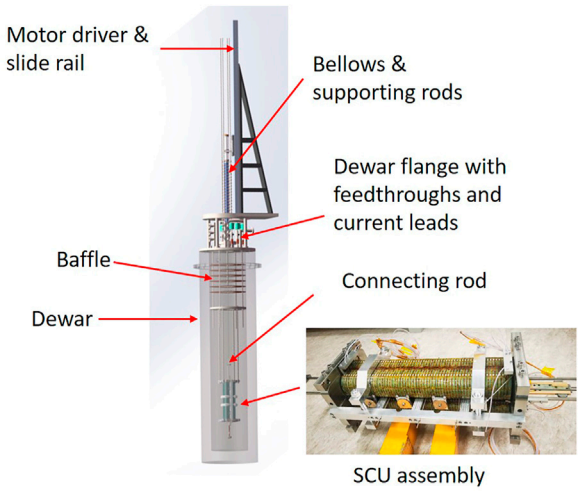

FIGURE 8
Vertical test system for the 0.5-m-long SCU.

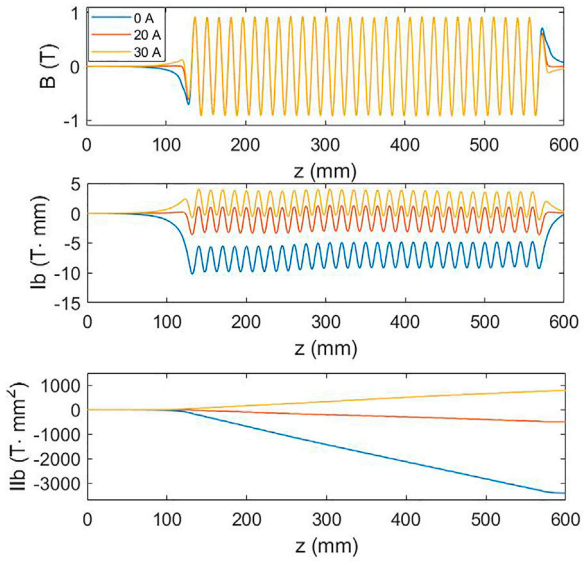

FIGURE 9
Magnetic field curves and the corresponding first and second field integrals at 400 A main current with 0 A, 20 A, and 30 A correction currents, respectively.

magnetic field was obtained, as given in Figure 7. The measured peak field reached 1 T at 460 A load current. In addition, the mock-up coils kept running at 450 A current for 5 h to verify the long-term stability.

4 0.5-m-long SCU

After the production of the short SCU mock-up, we produced a 0.5-m-long SCU prototype. The structure of the long SCU was kept the same as the short SCU. For the SCU, the magnetic field quality was directly determined based on the precision of manufacturing and fabrication.

The height of the magnet poles for each iron yoke was measured using a three-coordinate measuring instrument, which was then assembled together as a 0.5-m-long SCU. The pole height RMS error was 25 μm for the first magnet yoke and 9.8 μm for the second magnet yoke [15]. Due to the poor manufacturing accuracy, the first magnet yoke had bad pole height consistency. The second one was produced more precisely to meet the tolerance requirement. The two magnet yokes were clamped together in a frame to ensure good alignment. Several blocks made of stainless steel were inserted into the gap to maintain the gap distance. There were two side railways installed in the gap to guide a copper sledge for carrying hall probes to measure the magnetic field during the cryogenic test. The gap was set at 7 mm to match the size of the guide rails.

The 0.5-m-long SCU prototype was tested using a vertical test system [11], as shown in Figure 8. During the vertical test, the SCU was hung in a Dewar submerged in liquid helium to maintain the testing temperature at 4.2 K. The system was equipped with a motor-driven linear slide rail to pull the movable parts of the system. An L-shaped flange installed on the motor-driver slide was used to connect the bellows and pass the hall signals *via* the feed-through. The bottom of the bellows was connected to the Dewar flange. The travel of the bellows must be longer than the 1.5-m-long undulator. The bellows were specially designed to be supported by four external guide rods to avoid heavy bending during compression. A traction tube inside the bellows was used to connect the hall sledge and top flange of the bellows.

After quench training, the load current in the coils achieved 480 A, and the peak magnetic field reached 1 T at 450 A. We repeated the measurement four times to calculate the RMS errors of the peak magnetic field and half period length, which were <5 G and <10 μ m, respectively.

Correction coils were wound in the 0.5-m-long SCU to correct the first and second magnet field integrals. The correction coils were loaded with different currents to test the ability. Figure 9 shows the magnetic fields and the corresponding first and second integrals at 400 A main current with 0 A, 20 A, and 30 A correction currents, respectively. When the correction current was 20 A, the offset of the center part of the first magnet field integral shifted closer to the beam axis. Accordingly, the second integral was optimized from −3400 T·mm^2 to −487 T·mm^2. However, since the correction currents were not appropriately set, the magnetic field integrals were increased again.

The simulation results also indicated that the center part of the magnetic field induced by the correction coils was small but not negligible. This can affect the phase error of the magnetic field, which is an important parameter to assess the field quality. The optical phase is determined by the phase slip between the electron beam and the emitted photon as given in Eq. 3.

$$\varphi(z) = \frac{2\pi}{\lambda_u(1+0.5K^2)}\left\{z + \left(\frac{e}{mc}\right)^2 \int_{-\infty}^{z}\left(\theta + \int_{-\infty}^{z_1} B_y(z_2)dz_2\right)^2 dz_1\right\} - \frac{2\pi z}{\lambda_u}, \tag{3}$$

where K is the deflection parameter, e is the electron charge, m is the electron mass, c is the light velocity, λ_u is the undulator period

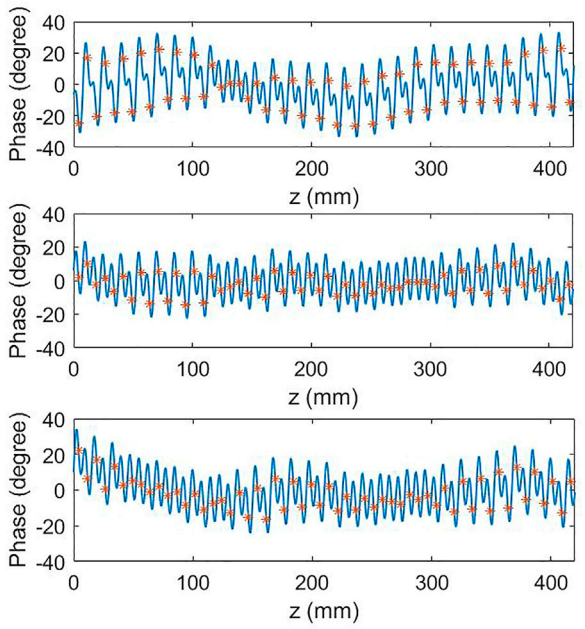

FIGURE 10
Phase maps for 400 A main current with 0 A (top), 20 A (middle), and 30 A (bottom) correction currents. The red markers indicate the phases on each undulator pole center.

length, and θ is the launch angle to compensate for the initial kick at the entrance of the undulator.

The magnetic field of a real undulator is not a pure cosine function. The end field part, so-called fringe field, is much different from the regular peaks. Normally, the first three ending poles are regarded as the ending poles to be excluded in the phase calculation [16]. The phase error is calculated as the RMS error of the phase on each undulator pole. Figure 10 shows the pole phase curves of the 0.5-m-long SCU at 400 A main current and three different correction currents. The corresponding phase errors were 14.8°, 6.1°, and 8.2° for 0 A, 20 A, and 30 A correction currents, respectively. With a suitable correction current, the phase errors of the SCU are also corrected.

5 1.5-m-long SCU

The R&D project aims to produce a 1.5-m-long SCU, which was achieved recently. The 1.5-m-long SCU was manufactured and assembled with the same scheme as the 0.5-m-long SCU. The gap of the 1.5-m-long SCU was set at 9.5 mm in order to fit the vacuum chamber installed in between the gap, when tested horizontally in the cryostat [17]. The two SCU yokes were also mounted on the end plates and clamped tightly on the gap plugs. The pole height RMS error of the two magnet yokes were under 10 μm.

This prototype went through two rounds of the vertical test. During the first test, the load current reached 426 A after more than 40 quenches. However, the magnetic field measurement results showed a relatively bad field quality due to the large phase error,

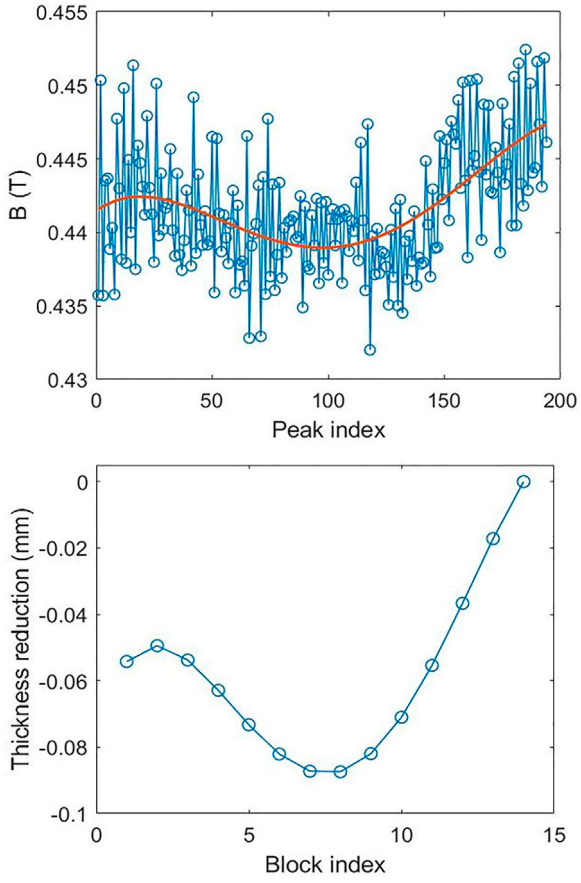

FIGURE 11
Absolute peak field distribution including the fitting curve (top) and the reduced thickness of the blocks (bottom).

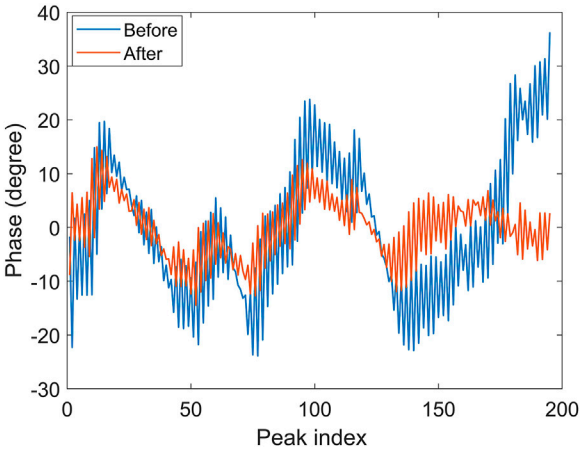

FIGURE 12
Phase maps for the 1.5-m-long SCU at 300 A main current before and after the gap adjustment.

which was larger than the required tolerances of 10° for the project. In this case, the local field needs to be modified based on the peak magnetic fields. The local field can be changed at the places where the

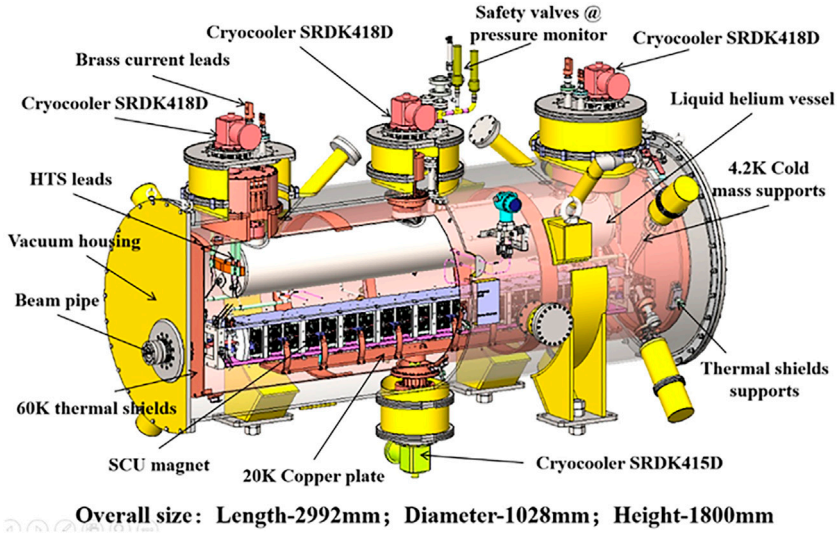

FIGURE 13
Schematic representation of the 1.5-m-long SCU test cryostat.

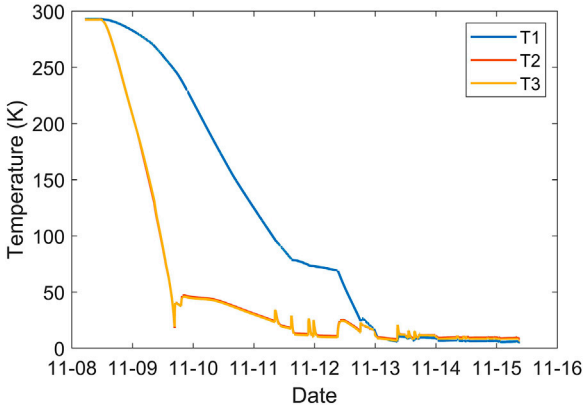

FIGURE 14
Cooling curves of the 1.5-m-long SCU in the cryostat. T1 for the magnet core; T2 and T3 for the two current leads.

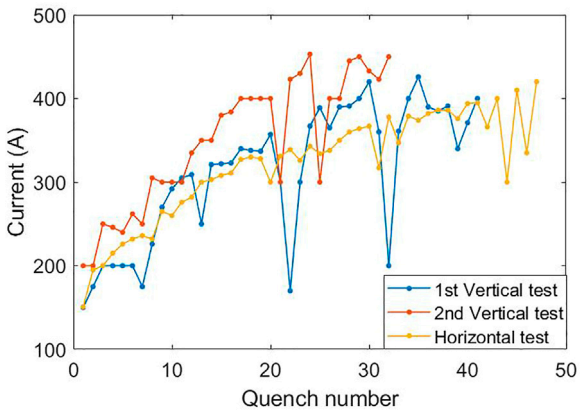

FIGURE 15
Quench currents of the 1.5-m-long SCU during the vertical and the horizontal tests.

gap plugs are located. The peak field at each plug pair was obtained from the fitting curve of the peak fields. Then, the thickness of the blocks that is to be reduced was calculated according to the simulation results as described in Section 2. The absolute peak field distribution and the reduced thickness of the blocks are given in Figure 11.

After the gap adjustment, the SCU was vertically tested again. The phase error was reduced significantly. Figure 12 shows the phase distributions at the pole centers before and after the gap adjustment at 300 A main current with a suitable correction current for each measurement. After the gap adjustment, the phase RMS error was reduced from 18.7° to 6.0°. Furthermore for the measurement at 400 A main current, the phase error was calculated to be 8.3° with a suitable correction current.

SCUs should be installed in a cryostat to be operated in accelerators. We designed a large cryostat to test the 1.5-m-long SCU under a horizontal installation condition as shown in Figure 13. This cryostat was equipped with four G-M-type two-stage cryocoolers, three at the top and one at the bottom. The thermal shields were cooled to about 60 K by the first stages of the four cryocoolers. The LHe vessel was connected to the second-stage cryocoolers at the top. The beam vacuum chamber in the undulator gap was cooled down to 20 K by the second stage of the bottom cryocooler. The SCU was cooled by the LHe flow, which was driven by the thermosiphon cooling loops, through the iron core channel. The cooling curves of the magnet core and the low temperature ends of the two current leads are shown in Figure 14. The three curves represent the temperature at the magnet core and the two current

leads. It took about 7 days to cool the magnet down to the target temperature of 4.2 K.

During the horizontal test, the SCU still needs quench training to load the high current because the fabrication structure was far different from the vertical system that results in a band quench memory. Figure 15 gives the quench curves of the 1.5-m-long SCU for the vertical and horizontal tests. The horizontal test went through 48 quenches to reach a load current of 420 A. After the quench, the temperature of the magnet core rose about 9 K and took much more time to recover due to the weaker cooling ability of the LHe flow compare to the LHe immersion during the vertical test. After the quench training, the 1.5-m-long SCU was stably operated over a long time with a high load current. The future focus is to develop a horizontal magnetic field measurement system. The SCU needs to be adjusted based on the measurement result to achieve a good field quality.

6 Summary

This paper reviews the progress of NbTi planar SCU development at the IHEP. The project started by producing several short mock-up coils to verify the feasibility of the producing technologies. These short SCUs were tested in a free LHe cryostat to reach the maximum current loading ability. After the quench training, the current in the coils achieved 500 A, and the peak magnetic field exceeded 1 T at a 6.5 mm gap.

The second stage of the project was manufacturing a 0.5-m-long SCU prototype. The long SCU structure and the coil winding scheme were kept the same as the short mock-up. After fabrication, the SCU was cryogenically tested using a vertical test system by hanging it in a Dewar submerged in liquid helium. The magnetic field measurement system for the vertical test had a repeated accuracy of <5 G for the peak field and <10 μm for the half period length. The correction coils had the ability in both corrections: magnetic field integrals and phase error. The phase error was optimized to 6.1° by applying 20 A correction current at 400 A main current.

Manufacturing a 1.5-m-long SCU was the final target of our R&D project. Currently, a prototype has been produced and cryogenically tested. The SCU was vertically tested twice. After the first test, we applied the gap adjustment method to change the local field for optimizing the phase error, which was reduced below 9° with 400 A main current during the second vertical test. Recently, this 1.5-m-long SCU was installed in a large cryostat and was successfully cooled down to the target temperature of 4.2 K. The maximum load current reached 420 A, and the SCU can stably operate in the cryostat at a high current for a long time. The measurement system to be used in the cryostat is under development. Based on the measurement result, the SCU can be adjusted under the horizontal condition to meet the requirement of the magnetic field quality in the cryostat.

Data availability statement

The raw data supporting the conclusion of this article will be made available by the authors, without undue reservation.

Author contributions

JW: magnet design and simulation, experimental setup and data analysis, and writing—original manuscript and revision. YL: conceptualization, supervision, and reviewing. XY: mock-up coil manufacture and testing and reviewing. XZ: cryostat design and manufacture and reviewing. XB: quench protection system design and testing. ZC: magnet assembly, measurement, and reviewing.

Acknowledgments

The authors thank their colleagues for the valuable suggestions to their project during the SCU production and the vertical test. They also acknowledge the support of the National Natural Science Foundation of China (E1113R5C10 and E029A5M111).

Conflict of interest

The authors declare that the research was conducted in the absence of any commercial or financial relationships that could be construed as a potential conflict of interest.

Publisher's note

References

1. Bahrdt J, Gluskin E. Cryogenic permanent magnet and superconducting undulators. *Nucl Instrum Methods Phys Res Sect A* (2018) 908:149–68. doi:10.1016/j.nima.2018.03.069

2. Bahrdt J, Ivanyushenkov Y. Short period undulators for storage rings and free electron lasers. *J Phys Conf Ser* (2013) 425:032001. doi:10.1088/1742-6596/425/3/032001

3. Zhang K, Calvi M. Review and prospects of world-wide superconducting undulator development for synchrotrons and fels. *Supercond Sci Technol* (2022) 35:093001. doi:10.1088/1361-6668/ac782a

4. Huang CS, Jan JC, Chang CS, Chen SD, Chang CH, Uen TM. Development trends for insertion devices of future synchrotron light sources. *Phys Rev ST Accel Beams* (2011) 14:044801. doi:10.1103/physrevstab.14.044801

5. Casalbuoni S, Glamann N, Grau A, Holubek T, Saez de Jauregui D, Bauer S, et al. Superconducting undulators: From development towards a commercial product. *Synchrotron Radiat News* (2018) 31:24–8. doi:10.1080/08940886.2018.1460171

6. Kasa M, Anliker J, Fuerst Q, Hasse I, Kesgin Y, Shiroyanagi E, et al. Superconducting undulators for the advanced photon source upgrade. *Proc Ipac2019* (2019). 1884–6. doi:10.18429/JACoW-IPAC2019-TUPRB095

7. Ivanyushenkov Y, Harkay K, Abliz M, Boon L, Borland M, Capatina D, et al. Development and operating experience of a short-period superconducting undulator at the Advanced Photon Source. *Phys Rev ST Accel Beams* (2015) 18:040703. doi:10.1103/physrevstab.18.040703

8. Xu JP, Zhou Q, Yin L, Ding Y, Wang S, Li M, et al. Development of a superconducting undulator prototype at the SSRF. *IEEE Trans Appl Supercond* (2017) 27:1–4. doi:10.1109/tasc.2016.2632758

9. Dassault System. *Opera: Electromagnetic and electromechanical simulation* (2021). Available at: https://www.3ds.com/products-services/simulia/products/opera/.

10. Zhang X, Xu M, Yang X, Bian X, Chen Z, Wei J, et al. Development of liquid helium-free cryostat for a superconducting undulator. *Nucl Instrum Methods Phys Res Sect A* (2023) 1049:168037. doi:10.1016/j.nima.2023.168037

11. Chen Z, He P, Li Y, Yang X, Wei J, Zhang X, et al. Magnetic field measurement system in vertical status for superconducting undulator cooled in Dewar. *JINST* (2022) 17:T09008. doi:10.1088/1748-0221/17/09/t09008

12. Casalbuoni S, Gerstl S, Glamann N, Grau A, Holubek T, Saez de Jauregui D, et al. Test of short mockups for optimization of superconducting undulator coils. *IEEE Trans Appl Supercond* (2015) 24:1–5. doi:10.1109/tasc.2013.2295921

13. Karasev YV, Pantsyrny VI, Polikarpova MV, Lukianov PA, Potanina LV, Baumgartner T, et al. $J_c(B, T)$ characterization of commercial NbTi stands for the ITER poloidal field coils by transport and magnetization methods. *IEEE Trans Appl Supercond* (2013) 23:6001304. doi:10.1109/tasc.2013.2243811

14. Wei J, Yang X, Zhang X, Chen Z, Bian X, Xu M, et al. Development and cryogenic test of superconducting undulator mock-up coils at ihep. *Nucl Instrum Methods Phys Res Sect A* (2022) 1034:166822. doi:10.1016/j.nima.2022.166822

15. Wei J, Li Y, Yang X, Chen Z, Zhang X, Bian X. Development and magnetic field measurement of a 0.5-m-long superconducting undulator at IHEP. *J Synchrotron Rad* (2022) 29:997–1003. doi:10.1107/s1600577522006166

16. Li Y. *Definition and calculation of the optical phase to the undulator*. European XFEL Report (2011). No.WP71-2011-19.

17. Chen Z, Yang X, Wei J, Zhang X, Bian X, Li Y, et al. Vertical measurement and on-line correction of the magnetic field for a 1.5-m-long superconducting undulator. *Nucl Instrum Methods Phys Res Sect A* (2023) 1047:167826. doi:10.1016/j.nima.2022.167826

frontiers | Frontiers in Physics

TYPE Review
PUBLISHED 12 April 2023
DOI 10.3389/fphy.2023.1166179

OPEN ACCESS

EDITED BY
Nicholas Walker,
Helmholtz Association of German Research Centres (HZ), Germany

REVIEWED BY
Jacek Sekutowicz,
Helmholtz Association of German Research Centres (HZ), Germany
Mathieu Omet,
High Energy Accelerator Research Organization, Japan

*CORRESPONDENCE
R. Xiang,
r.xiang@hzdr.de

SPECIALTY SECTION
This article was submitted to Interdisciplinary Physics, a section of the journal Frontiers in Physics

RECEIVED 14 February 2023
ACCEPTED 27 March 2023
PUBLISHED 12 April 2023

CITATION
Xiang R, Arnold A and Lewellen JW (2023), Superconducting radio frequency photoinjectors for CW-XFEL. *Front. Phys.* 11:1166179. doi: 10.3389/fphy.2023.1166179

Superconducting radio frequency photoinjectors for CW-XFEL

R. Xiang[1]*, A. Arnold[1] and J. W. Lewellen[2]

[1]Helmholtz Zentrum Dresden Rossendorf, Dresden, Germany, [2]SLAC National Accelerator Laboratory, Menlo Park, CA, United States

A dependable and consistent electron source is a crucial requirement for the achievement of high-power free electron lasers (FELs). Over the past two decades, it has been demonstrated that photoinjectors based on SRF technology (SRF guns) are suitable for continuous wave (CW) beam generation. SRF guns possess both the high accelerating field gradients of normal conducting RF photoinjectors and the low power dissipation thanks to mature SRF cavity technology, and therefore have the potential to provide the high-brightness, high-current beams required for CW-XFELs. After the demonstration of the first SRF gun in Dresden-Rossendorf, several SRF gun programs based on different approaches have achieved promising progress and even succeeded in routine operation. SRF guns are expected to play an important role in XFEL facilities in the near future. In this paper, we give an overview of design concepts, important parameters and development status of the worldwide SRF gun projects.

KEYWORDS

superconducting RF, photoinjector, continues wave, FEL, low emittance, SRF gun

1 Introduction

Superconducting radio frequency photoinjectors (SRF guns) have advantages for operating in continuous wave (CW) mode and generating the high-brightness and high-current beams required by CW X-ray free electron laser (XFEL) [1, 2] and energy recovery linac (ERL) facilities [3, 4]. Similar to the normal conducting rf guns, SRF guns are able to provide higher gradients on the cathode surface than DC guns, increasing the achievable surface current density and reducing the thermal emittance contribution for a given bunch charge; higher beam voltages help to mitigate space-charge effects as the beam travels from the gun to the next accelerator cavity. Concurrently, SRF guns have an outstanding vacuum environment for sensitive cathodes and potentially lower RF jitter compared to CW normal conducting (NC) photoinjectors [5].

From a technical perspective, an CW injector based on SRF technology is a complex device that not only presents challenges common to other types of high-brightness beam sources and superconducting accelerators, but also introduces new issues in both realms. In common with other injectors, in order to produce low emittance beams required by XFEL facilities, SRF guns must have high accelerating gradients, effective emittance compensation, precise synchronization between cathode drive laser and RF, application-appropriate photocathodes, proper laser pulse shaping, and so on. As with other SRF-based accelerators, an SRF gun utilizes superconducting RF cavities and cryostats, with requisite need for precise frequency control, field stabilization, etc. In addition to these issues, the geometry of SRF photoinjectors can introduce additional complexities regarding cleaning the SRF surface, RF power conduction along the cathode support, RF power coupling, and emittance compensation, all of which require new solutions. But the most

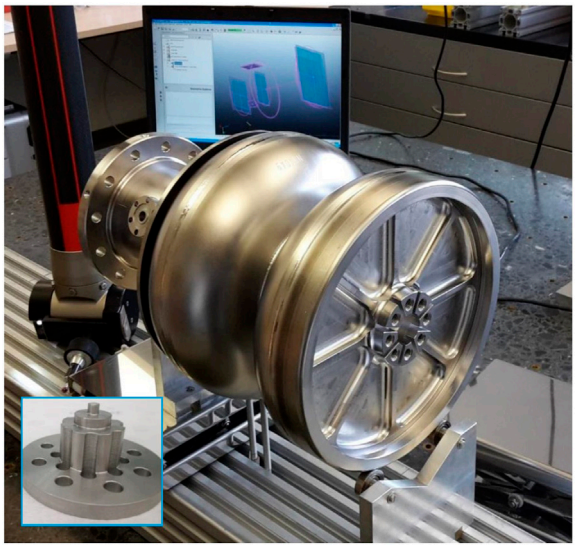

FIGURE 1
The cavity and cathode plug for DESY SRF gun.

consistently challenging aspect of SRF gun design has been cathode integration into an SRF structure.

In the last 20 years, SRF gun projects made excellent progress [6, 7]. All of them are based on the mature superconducting (SC) pure niobium cavity technology, with either high-frequency cavities based on the 1.3 GHz TESLA shape, or low frequency quarter wavelength resonator (QWR). The former is able to reach a higher field on axis and thus higher energy gain for the electrons, but the QWR cavity can produce a longitudinally homogeneous (DC-like) field profile. Two SRF guns are currently in user operation (HZDR SRF Gun-II) [8] or generate routine beams for experiments (BNL CeC SRF gun [9]). Furthermore, five gun projects have made promising R&D progress (DESY, SLAC, HZB, KEK and PKU) [10–14]. Among them, the DESY SRF gun and LCLS-II HE SRF gun are specially designed for CW-XFEL application. This overview paper focuses on the recent progress on these projects and compares their performance as potential injectors for CW-XFELs.

2 SRF guns developed for CW-FELS

2.1 DESY SRF gun (elliptical cavity with SC cathode)

A future upgrade of the European XFEL foresees High-Duty-Cycle (HDC) operation [15]. The first choice for the required CW injector is an SRF gun with high gradient [10], which is a 1.6 cell L-band cavity with a superconducting photocathode (lead-coated or nanostructured) directly installed in the cavity back wall (see Figure 1).

The elliptical L-band cavity allows the gun to operate at high accelerating gradient comparable to a NC RF L-band gun, which helps to generate the low emittance beam required by the CW-XFEL. In recent years, the DESY SRF Gun project has invested considerable effort in the treatment and modification of cavities and made significant progress. All recent prototypes achieved ~55 MV/m peak on-axis gradients and the back wall is mechanically stable enough to withstand the high Lorenz force at this field [16]. With this gradient, the transverse emittance of 100 pC bunch change should be under 1 μm. The special feature of this design is that there is no provision for cathode transport and exchange *in situ*; the cathode exchange must be performed when the cavity is warmed up and in a clean room. The advantage of this design is removal of particulate contamination risk from the cathode exchange in a cold cavity. However, the integrated cathode needs to be extremely robust and exhibit a reasonable long lifetime to ensure the continuous user's beam time. Meanwhile, after the cathode is installed into cavity, the cavity needs to be re-cleaned, which is a big challenge for the cathode robustness. If the cathode material migrates from the cathode surface onto the cavity wall, the particles might spoil the cavity and degrade drastically the achieved maximum RF field. Furthermore, another challenge of this design is the superconducting photocathode itself. Lead (Pb) coated on Nb substrate is chosen as one possibility because of its relatively high critical temperature. The treatment and photoemission of this material have been studied by the group of J. Smedley and T. Rao at BNL [17], later by R. Barday at HZB [18], and recently by J. Lorkiewicz at NCBJ [19]. After laser cleaning the QE of lead can reach 10^{-4} level at 258 nm. However, compared to the normal conducting photocathodes with QE values of 0.1%–10%, the low QE of lead cathode will increase the requirements for the cathode drive laser as well as the optical elements, and heating from the laser could potentially pose limitations to the maximum achievable average current.

Alternative photocathodes for the DESY SRF gun are in planning, e.g., metallic cathode (niobium or copper) with surface nanostructuring to improve the QE by plasmonic states [20]. Such cathodes are expected to be robust to established SRF cleaning procedures [21]. However, the intrinsic emittance and its optimization of the nanostructured cathode remain to be investigated.

Presently, the DESY SRF gun project is still under R&D. Before performing the first beam tests, the next essential step is to determine the acceptable range of cathode laser power through a series of measurement.

2.2 LCLS-II HE SRF gun (QWR cavity with NC cathode)

The LCLS-II-HE project [1] will double the beam energy of the LCLS-II linac, from 4 to 8 GeV. To fully realize the benefits of this energy upgrade, including saturated lasing at 20-keV X-ray energy, a factor-of-two lower beam emittance is required than that expected from the existing LCLS-II injector. As part of addressing this gap, an SRF Gun R&D program encompassing low mean transverse energy (MTE) cathode research, and high gradient QWR cavity development, has been started. SLAC has partnered with the Facility for Rare Isotope Beams (FRIB) at Michigan State University (MSU), Argonne National Laboratory (ANL) and Helmholtz-Zentrum Dresden Rossendorf (HZDR) to build a gun prototype (see Figure 2) [14]. The aim is to demonstrate stable CW

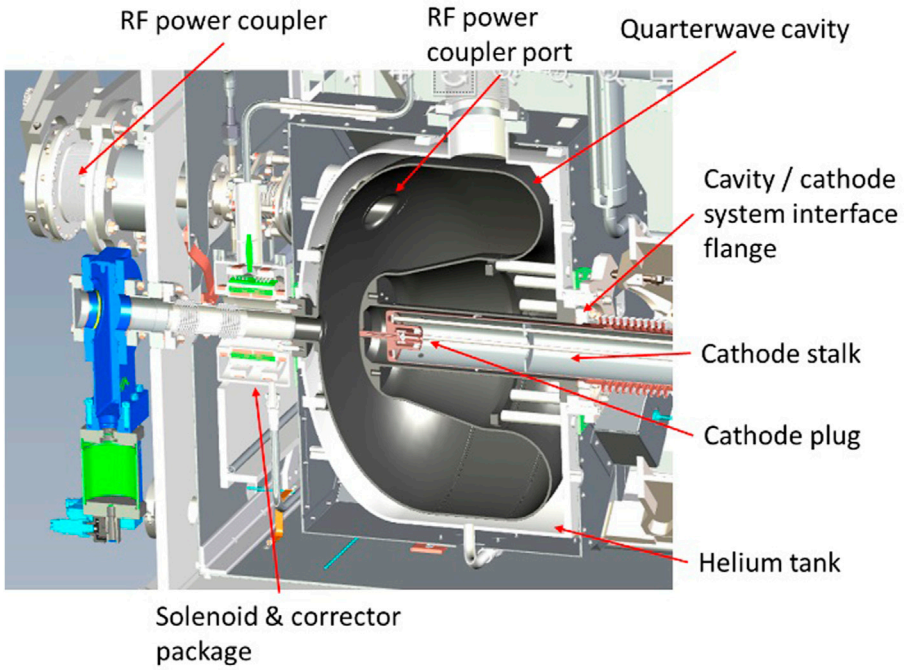

FIGURE 2
Design concept of LCLS-II HE SRF gun cavity with the cathode stalk [14].

operation at a cathode gradient of 30 MV/m. The first RF tests will be performed on a "blank" cavity (no provision for inserting a cathode plug) in 2023. A second, "prototype" QWR SRF gun cavity will be fabricated and tested with an on-cathode gradient of up to 30 MV/m with a full cathode system in place, but no active photocathode deposited on the cathode plug, towards the end of 2024. Finally, the intent is to fabricate a "production" gun, incorporating lessons-learned from the fabrication and test of the "blank" and "prototype" structures.

The new gun is based around a "squat" QWR cavity profile, and a normal conducting photocathode in an rf choke, with an overall design inspired by, and drawing lessons-learned, from the NPS [22] and WiFEL designs [23]. In comparison, the SLAC/MSU QW SRF gun has a reduced cathode - anode distance and a thinner exit beam tube; this reduces the final beam energy, but retains most of the advantages of the "DC-like" beam transit through the gap, as exhibited by the VHF-type CW NCRF guns [24]. Also, the RF main coupler is placed on the downstream wall of the cavity ("anode plate") rather than along the beamline. The RF frequency is 185.7 MHz (1/7 of 1300 MHz). The new gun should generate a beam with kinetic energy >1.6 MeV, bunch charge of 100 pC and, given a suitable photocathode, a transverse emittance <0.1 μm.

To reach the required low transverse emittance, a high-QE photocathode with a low mean transverse energy (MTE) < 0.2 eV is planned to be used. Combined with a small laser spot, the initial transverse emittance can be lower than 0.1 μm. The nominal design calls for using an "S20" photocathode (a Cs_3Sb layer deposited on an underlying Na_2KSb photocathode), illuminated at ~500 nm (green). This represents both a challenge and an unknown, since there are no reported results of this cathode operating at 30 MV/m. Before more experimental experience about high-gradient performance–field emission and lifetime, as well as emittance–is available, such cathodes should not be used in the production gun. Metallic cathodes, such as copper, can be considered as the commissioning photocathode for the prototype gun.

Contrary to the DESY SRF gun with SC cathode, the SLAC/MSU gun is intended to use high-QE normal conducting (NC) photocathode, thus the photocathode drive laser can be simpler. However, the SLAC/MSU gun needs a more complex cathode system. A specially designed cathode stalk is under development at MSU. In addition to acting as an RF choke to reduce the RF loss in the cathode system, the cathode stalk is electrically and mechanically isolated from the SRF cavity. This allows to suppress multipacting between the cathode stalk and the gun with a DC bias. Mechanically, the stalk provides for fine adjustment of the cathode position to reach the best working point, and allows for the cathode to be maintained at either room or cryogenic (~50 K) temperature [25]. The photocathode structure and the load-lock system adopt the HZDR design, which should ensure the particle-free and warm exchange ability.

This gun is a very promising injector for the SLAC XFEL project. The challenge for both the cavity and cathode is the high gradient of 30 MV/m on cathode and the low dark current requirement <10 nA during operation. For the future operation, reliable cathode exchange is another key point, as is the identification of a photocathode capable of meeting strict requirements for MTE, quantum efficiency, lifetime and field emission/dark current.

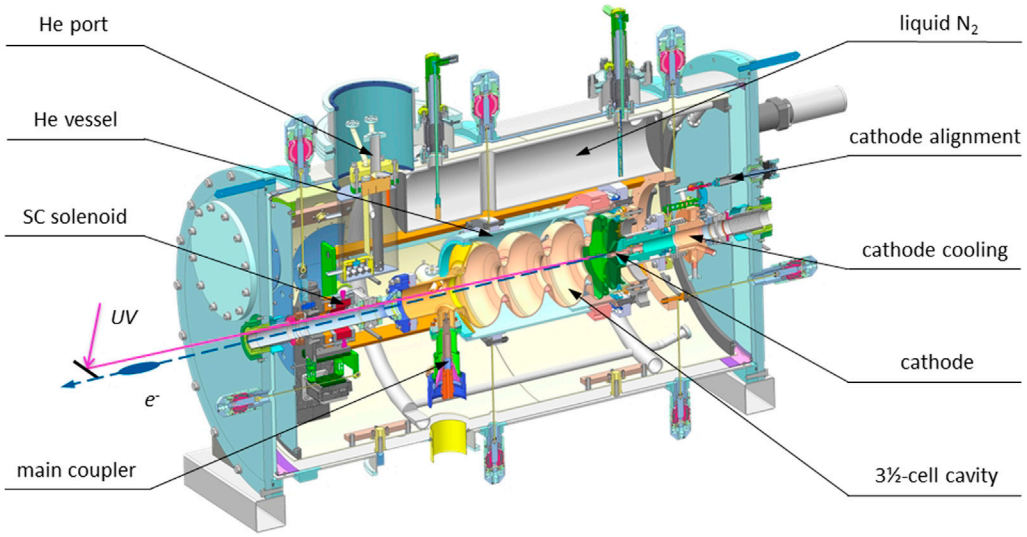

FIGURE 3
A cross-section view of the HZDR SRF gun-II cryostat.

3 Other SRF guns with potential as CW-XFEL injectors

3.1 Elliptical cavities with RF chokes (HZDR, KEK, HZB)

3.1.1 HZDR SRF gun

Although the HZDR SRF gun was not developed as an injector for CW-XFEL, it represents a practical and successful CW SRF gun design. HZDR SRF gun-I was the first SRF gun worldwide that injected beams into an accelerator for CW IR-FEL production [26], and the Gun-II is the first one in user operation for CW super radiation THz source [8].

As shown in Figure 3, the cryostat of Gun-II includes the 3½ cell 1.3 GHz cavity and choke cell in the He vessel, the RF coupler, the SC solenoid and the cathode holding system. From 2017 to 2020 this gun was operated with a Mg cathode and since 2020 with Cs_2Te cathode driven at 262 nm. The bunch charge injected into the ELBE linac can be up to 250 pC with repetition rates of 50–250 kHz. The drive laser is adjusted to a short rms pulse length of 2.3 ps. The accelerating gradient E_{acc} is 8 MV/m, with a corresponding field on the cathode of 14 MV/m, limited by the field emission and liquid He power consummation in the SRF cavity. The beam kinetic energy after an acceleration gap of 0.5 m can be as high as 4 MeV, which simplifies the beam transport to linac.

The successful operation of HZDR SRF gun benefits from its special cathode structure. The cavity gradient has not obviously degraded even though the cathode has been exchanged dozens of times. The cavity was recovered even after a Cs_2Te cathode overheated and evaporated in the cavity in 2017.

Up to now, the main task of HZDR SRF gun has been to provide high bunch charge with sub-ps pulse lengths for the THz beamline at ELBE [27]. Thus, there are no systematic theoretical studies or demonstration experiments performed, which can prove the capability of this design to generate low emittance beam with moderate bunch charge, for example, 100 pC. One possible disadvantage as an XFEL injector might be its solenoid design. Both the large distance of 70 cm from the SC solenoid to the cathode and the coil design itself are not optimized for low emittance applications.

3.1.2 HZB SRF gun

The HZB-SRF gun is designed for the bERLinPro ERL project, which originally requires a very high CW beam current of 100 mA. The latest version is a 1.4-cell cavity with a choke cell, normal conducting bi-antimonite cathode and a SC solenoid at the cavity exit (see Figure 4) [11].

After the first successful beam test with a copper cathode in 2017, the cavity performance was found severely degraded due to the cathode unexpectedly overheating. Moreover, careful inspection of the cavity revealed surface damage close to the cathode opening to be the source of the measured dark current. A repair program was developed and a second gun cavity was built. Unfortunately, during the final high-pressure rinsing at the manufacturer, the cavity received unexpected damage again. By applying a combination of mechanical grinding, buffered chemical polishing, HF rinsing and an optimized high-pressure water rinsing both cavities could be brought back to nominal performance, without any field emission up to 30 MV/m peak on-axis field. Since end of 2022, the SRF gun has been reassembled in the cleanroom, and the cryo-module setup and integration has started in the bERLinPro accelerator hall during early 2023. It is planned to start commissioning of bERLinPro's injector line only with the SRF gun operating, and to create the first beam with the 50 MHz photocathode laser system to measure the possible parameter space of this setup. Afterwards the injector will be completed by adding the booster, so that the full injector performance can be studied from short pulse low charge to high current and high charge.

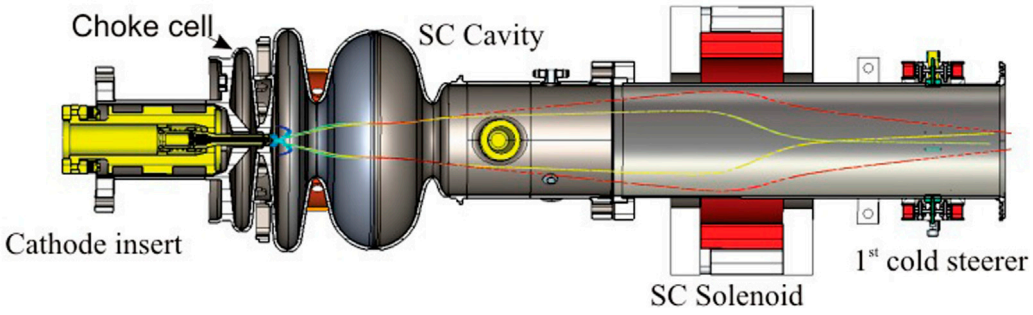

FIGURE 4
The cross section of the bERLinPro SRF gun cavity with an inserted cathode [11].

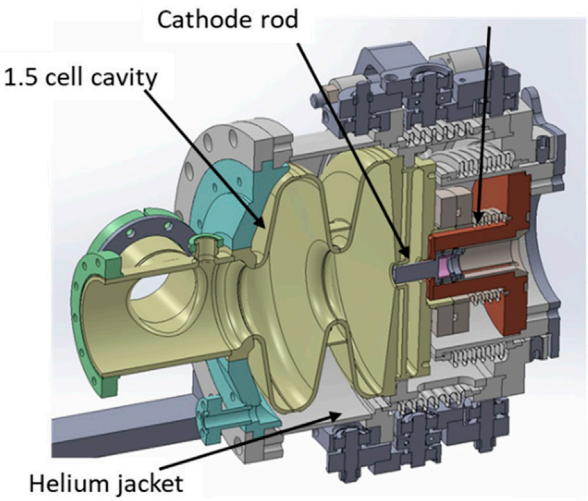

FIGURE 5
Cross section of the KEK SRF gun cavity with a cathode plug [12].

Compared to the HZDR design, the HZB SRF gun has a bigger exit tube to let higher order modes (HOM) propagate to the HOM damper, thus its solenoid must also have a larger bore, which is reducing spherical aberration of the magnet. In addition, because of its 1.4 cell cavity, its SC solenoid sits closer to the cathode to provide early focusing. And the special solenoid holder based on a hexapod enables fine axis adjustment to minimize dipole- and quadrupole-field errors from misalignment of the solenoid magnet.

3.1.3 KEK SRF gun

The KEK SRF gun, still in the R&D phase, was developed as a source for the compact energy recovery linac (cERL) at KEK [3]. It consists of a 1.5 cell SC gun cavity with a choke cell (see Figure 5). The gun incorporates several unique design features. The cathode is cooled with liquid He. The cathode laser can illuminate the photocathode (bi-alkali antimonite) from the backside through a transparent superconductor substratum [28]. The vertical tests have been successfully performed at KEK, receiving a maximum surface peak electric field of ~75 MV/m without cathode and over 60 MV/m with a niobium cathode plug [12]. Following the successful vertical test, the next step will be to install the gun cavity with the cathode rod in the horizontal cryostat and commence beam commissioning. This process was initiated at KEK in the last few years and will be continued at MSU in 2023.

The obtained high gradient can help to obtain low emittance. Nevertheless, one concern is the cathode performance at such high gradient. Furthermore, the design of a transparent superconducting cathode plug coated with bi-alkali antimonite photo-emitter is very challenging, and the low operation temperature is not ideal for bi-alkali antimonite photocathode.

3.2 Elliptical cavities with NC cathodes in DC gun (PKU)

PKU's SRF gun has a unique hybrid design, combining a compact DC gun with a 1.3 GHz cavity. This simplifies the cavity design and minimizes contamination risk from photocathode operation and exchange. However, a main concern is the limited electric field gradient on the cathode surface (~6 MV/M) lower than that of the other SRF gun designs (>10 MV/m).

The last version of DC-SRF gun with 3.5 cell reached mA-level current in the pulsed mode operation in 2014 [29]. In 2021 the installation of the updated version DC-SRF-II has been finished, which aimed especially to improve the transverse emittance by increasing the electric field gradient on the cathode surface. The DC voltage is increased to 100 kV, with a corresponding field on cathode surface of 6 MV/m. A 1.5-cell SRF cavity with E_{acc} of 13–14 MV/m is adopted in this new version (see Figure 6) [30]. A K_2CsSb photocathode is driven by a temporally- and spatially-shaped drive laser. The beam optics are also carefully designed for optimized emittance compensation [31]. The gun is intended to produce bunch charge of 100 pC with rms emittance as low as 0.33 μm, and repetition rate of 1 MHz. Commissioning of the new gun was successful. The gun was operated with the expected RF field gradient of 13 MV/m CW, with dark current < 1 pA; the normalized emittance of the delivered electron beam was measured as 0.85 μm @ 100 pC [13].

One of the design tasks of this DC-SRF-II is a potential injector for CW-XFEL. The advantages of this design include separation of cathode and SRF cavity, reducing the potential for contamination of

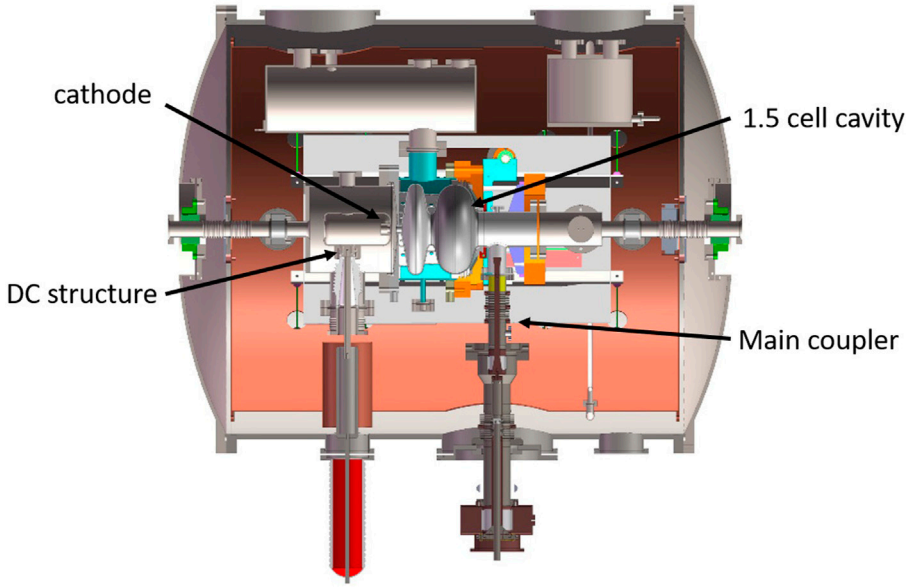

FIGURE 6
Design concept of the new PKU DC-SRF gun with 1.5 cell cavity and a cathode in the DC gap.

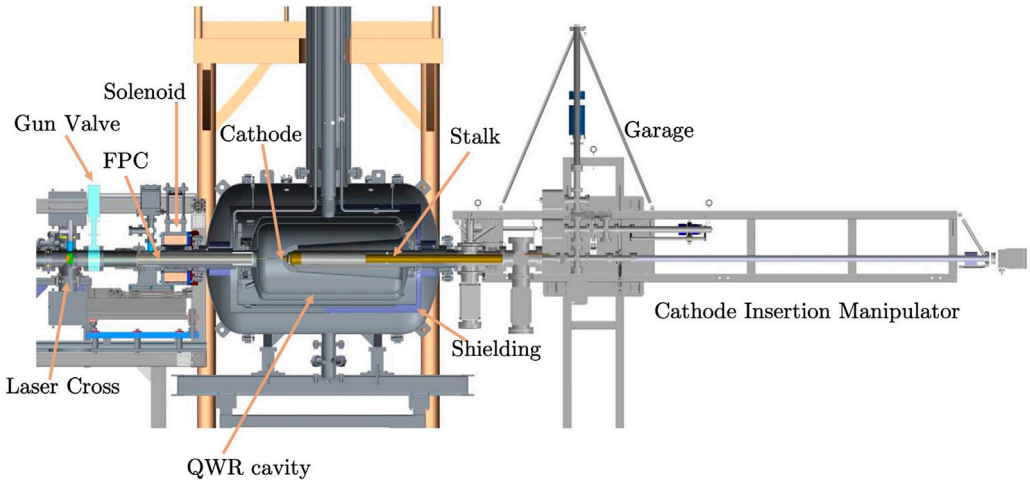

FIGURE 7
Assembly overview of the BNL QWR SRF gun and cathode insertion system [35].

cathode to cavity, cathode overheating, and multipacting due to migration of cathode material. No complex cathode choke structure is required, but a complicated high voltage part must be operated in the cryostat. Meanwhile, although the RF leakage through the hole on the cavity back wall has been excluded, the free drift space between the DC gap and the cavity may increase the problem of space charge effects at low beam energies. Additionally, no published reports exist on the analysis of the solenoid field utilized in this project, nor on the dipole and quadrupole correctors for the solenoid field. These factors are crucial for achieving a low emittance injector, highlighting the need for further investigation and documentation in this topic.

3.3 QWR cavity with NC cathode in choke filer (BNL)

The BNL SRF gun was built for the Coherent electron Cooling (CeC) proof of principle experiment at the Relativistic Heavy Ion Collider (RHIC), and has been in routine operation since 2016 [32].

TABLE 1 Summary of SRF guns' parameters.

Name	DESY SRF gun	LCLS-II HE SRF gun	HZDR SRF Gun-II	BNL CeC SRF gun	PKU DC-SRF-II	HZB bERLinPro SRF gun	KEK SRF gun #2
Aim	XFEL	XFEL	THz-FEL	e– cooler	FEL	ERL	ERL
Cavity type	1.6 TESLA	QWR	3.5 TESLA	QWR	1.5 TESLA	1.4 TESLA	1.5 TESLA
RF freq. (MHz)	1300	185.7	1300	113	1300	1300	1300
Operation temp. (K)	2	4	2	4	2	2	2
Gradient E_{acc} (MV/m)	>21	26*	8	~21 (E_{peak})	13	16	~16
$E_{cathode}$ (MV/m)	>40	30*	14	~15	6	24-27	52.5
Kinetic energy (MeV)	>4*	1.8*	4	1.25(CeC) −1.7		2.5-3	2
Current (μA)		100*	62.5	140	100		
Dark current (nA)		<10* (captured @ 100 MeV)	100	<1	10^{-3}	4.5@9.5 MV/m w.o. cath	
Cathode	Pb or nanostructured metal	Green	Mg, Cs_2Te	CsK_2Sb	CsK_2Sb	CsK_2Sb	CsK_2Sb (SC)
Cathode temp. (K)	2	50 or 300	80	300	36	80	2
Laser wavelength (nm)	UV or other	532	262	532	519	521-523	532 (plan)
Rep. Rate (kHz)	100-1000	-up to 1 MHz	50-250	78	1000	Up to 1.3 GHz	1.3 GHz (plan)
Pulse length rms (ps)		20	2.3	400 (CeC)	20	3-12	3*
Bunch charge (pC)	20-100*	100*	50–250	100-20000	100	77*	80*
Transv. rms emit. (μm)	0.2-0.4*	0.1*	1.3–6.3	0.15 μrad@100 pC	0.85	<1 *	1*
Energy spread (keV)			5-25	0.5	2.75	1.7*@1.7 MeV	2*
Status	R&D	R&D	user operation	operation	demonstrated	R&D	R&D

(*Design Value).

The gun consists of a 112 MHz quarter wavelength resonator (QWR) and a room temperature K_2CsSb cathode cooled with water (see Figure 7). The typical cathode lifetime for the high bunch charge (~nC) operation is one to 2 months [33]. Intensive multipacting studies have been performed for this gun, resulting in a procedure for crossing the multipacting barriers from zero to the operational voltage 1.2 MV [34].

The BNL 112 MHz SRF gun has shown its outstanding performance as a high current CW operation injector [9]. The gun demonstrated the ability to deliver low emittance electron bunches, e.g., 0.15 mm-mrad slice emittance for 100 pC, albeit the bunch length of 400 ps (required by CeC application) before compression is about twenty times longer than the pulse length required by the XFEL. The low electron energy at the gun exit (1.25 MeV) also mandates a careful beam transport design.

One concern for long-term user facility operation is cavity performance degradation over time, especially due to the cathode exchange. Special care is needed when manipulating the insertion mechanism to correctly install the cathode, as incorrect manipulation could lead to unexpected field emission and new multipacting barriers [35]. Though the He conditioning technique has proven to be an effective method for cavity restoration, the cathode lock and exchange system still poses a potential risk to the facility's operating lifetime. Therefore, it is essential to implement additional measures to minimize the risks associated with cathode exchange and ensure the smooth operation of the facility in the long run.

4 Photocathode integration into SRF guns

Providing a stable beam with high current and low emittance for CW-XFEL facility, requires high accelerating gradients on the photocathode, high QE, low mean transverse energy (MTE), and long lifetime. A big challenge for SRF guns is how to best place the selected cathode in the fields in the SRF cavity. In NC RF guns, direct

electrical and mechanical contact between the cathode and cavity is typically done *via* an RF spring, but for SRF guns this approach is problematic due to particle generation and, potentially, the need to keep the cathode at a substantially higher temperature than the gun cavity. Several concepts of cathode assembly and insertion have been successfully applied in the SRF guns [36], but this remains one of the major challenges to SRF gun development and operation.

4.1 SC cathodes on the cavity back wall

Intuitively a superconducting cathode is well-matched to the SC RF cavity. The superconducting cathode material (for example, Pb or Nb) can be directly coated or sealed onto the cavity back wall [37, 38], or the well cleaned cavity back wall can be used as photocathode [39]. The advantage of this method is that the cavity and cryostat design can be simplified because no special cathode assembly or RF choke structure is required. However, for applications demanding high average beam current, such as most CW-XFELs, the low quantum efficiency presents the risk of overheating the cathode and cavity from the required laser power, and the high work functionrequires challenging high-power UV drive lasers.

Using this method has a significant drawback - the SRF gun needs to be moved back to the cleanroom if the cathode needs to be replaced. This can result in increased machine downtime, high maintenance costs, and a new risk of cavity contamination when either the entire SRF cavity needs to be replaced or the cavity needs to be cleaned again.

4.2 RF choke for utilizing normal conducting photocathodes

To operate high-QE normal conducting photocathode in a SC RF gun, a thermal isolation between the NC cathode and SC cavity, for example, a vacuum gap, must be induced. Even if the cathode material can be operated effectively at 2–4 K, the cathode substrate itself presents the risk of dissipating too much RF power and quenching the cavity. Therefore, the design of the SC cavity and cryostat becomes more complex. Cathode holders (stalks) are usually designed as RF chokes in order to minimize the RF loss in this vacuum gap. Various RF choke designs suitable for the 1.3 GHz elliptical cavity guns [3, 8, 11] and for the QWR cavity guns [9, 14, 23]have been reported.

Because of the isolation from the SRF gun body, the photocathode can operate at different temperatures, cooled with liquid helium (KEK SRF gun), liquid nitrogen (HZDR, HZB SRF gun), low- or room-temperature He gas (SLAC SRF gun) or with water (BNL SRF gun). This unique variable provides scientists a possibility to obtain the lowest mean transverse energy (MTE) as well as a good QE of the photocathode by controlling the working temperature.

The multipacting phenomena is an inevitable problem, especially given the sensitivity of high-QE photocathodes to the vacuum environment. In the area of cathode, if the cathode is electrically isolated from the SC cavity, a DC bias can be applied on the cathode, which helps to suppress the possible MP resonance [25, 40] between the cathode stalk and body of the gun. Multipacting within the gun itself is still a concern, but this can be addressed both by the initial cavity design and by conditioning the cavity prior to photocathode insertion.

4.3 DC gap for normal conducting cathodes

As introduced in Section 3.2, a NC cathode can be integrated to the SRF cavity through a DC gap. Compared to the other RF choke designs, the main advantages of this design are greatly reduced chance of contamination from cathode to the SC cavity, and no RF heating of cathode. But this design sacrifices the electrical field strength on cathode surface. Meanwhile, the free drift space between the DC gap and the cavity back wall enhances the difficulty of space charge control and thus the following emittance compensation. Nevertheless, this approach continues to be intriguing for the low-medium bunch charge CW photoinjector.

5 Summary and outlook

Benefitting from the fast development of both SC RF cavity and photocathode technology, SRF photoinjectors are becoming rather promising as potential electron sources for CW-XFEL facilities. Over the last several years SRF guns made excellent progress, even realizing routine operation (see parameters overview in Table 1). The transverse emittance of 100 pC bunch charge can reach sub-μm level in simulation and even in experiments. Different from the NC RF guns, the solenoids for the SRF guns have to be placed outside the cavity area, but a suitable solenoid design can still efficiently improve the emittance. The idea to compensate the transverse emittance with an additional TE mode exited in the cavity might be an applicable solution to the long-distance limitation [41].

Besides the first-rate niobium cavity quality and delicate cryostat design, proper cathode system design is a key for successful gun operation. Various solutions for cathode integration have shown to be reliable, and new design concepts continue to emerge. CsK_2Sb has shown its good lifetime in SRF guns, and it is believed the best candidate as low emittance photocathode required by the low emittance beam for XFELs. Present efforts to improve gun performance include increasing the cavity gradient/cathode field in operation while maintaining low dark current, as well as to further improve the robustness and safety of selected photocathodes.

Author contributions

RX wrote the first draft of the manuscript. JL und AA modified the manuscript. All authors contributed to manuscript revision, read, and approved the submitted version.

Acknowledgments

Many thanks to the colleagues, who provided materials on their projects for this review: I. Petrushina (BNL, SBU), E. Vogel (DESY), A. Neumann (HZB), T. Konomi (FRIB), and S. Huang (PKU).

Conflict of interest

The authors declare that the research was conducted in the absence of any commercial or financial relationships that could be construed as a potential conflict of interest.

Publisher's note

References

1. Raubenheimer TO. The LCLS-II-HE, A high energy up-grade of the LCLS-II. In: Proc. 60th ICFA Advanced Beam Dynamics Workshop on Future Light Sources (FLS'18); 5-9 March 2018; Shanghai, China (2018). p. 6–11.

2. Decking W. A MHz-repetition-rate hard X-ray free-electron laser driven by a superconducting linear accelerator. *Nat Photon* (2020) 14(6):391–7. doi:10.1038/s41566-020-0607-z

3. Konomi T, Honda Y, Kako E, Kobayashi Y, Michizono S, Miyajima T, et al. Development of high intensity, high brightness CW SRF gun in KEK. In: Oral talk for 19th International Conference on RF Superconductivity (SRF 2019); 30 June-5 July 2019; Dresden, Germany (2019).

4. Abo-Bakr M. Status report of the berlin energy recovery linac project BERLinPro. In: Proc. 9th Int. Particle Accelerator Conf. (IPAC'18); 29 Apr - 4 May 2018; Vancouver, Canada (2018).

5. Qian H, Vogel E. Overview of CW RF guns for short wavelength FELs. In: 39th International Free-Electron Laser Conference (FEL2019); August 26-30, 2019; Hamburg, Germany (2019).

6. Arnold A, Teichert J. Overview on superconducting photoinjectors. *Phys Rev Spec Top - Acc Beams* (2011) 14(2):024801. doi:10.1103/physrevstab.14.024801

7. Xiang R. Review of superconducting radio frequency gun. In: 12th Int. Particle Accelerator Conf.(IPAC'21); 24 - 28 May 2021; Campinas, Brazil (2021).

8. Teichert J, Arnold A, Ciovati G, Deinert JC, Evtushenko P, Justus M, et al. Successful user operation of a superconducting radio-frequency photoelectron gun with Mg cathodes. *Phys Rev Acc Beams* (2021) 24(3):033401. doi:10.1103/physrevaccelbeams.24.033401

9. PetrushinaI I, Litvinenko1 VN, Jing Y, Ma J, Pinayev I, Shih K, et al. High-brightness continuous-wave electron beams from superconducting radio-frequency photoemission gun. *Phys Rev Lett* (2020) 124(24):244801. doi:10.1103/physrevlett.124.244801

10. Vogel E, Barbanotti S, Brinkmann A, Buettner T, Iversen J, Kay J, et al. Status of the all superconducting gun cavity at DESY. In: 19th Int. Conf. RF Superconductivity (SRF'19); 30 Jun - 05 Jul 2019; Dresden, Germany (2019).

11. Neumann A, Böhlick D, Bürger M, Echevarria P, Frahm A, Glock H-W, et al. The berlinpro srf photoinjector system - from first Rf commissioning to first beam. In: 9th International Particle Accelerator Conference (IPAC2018); 29 Apr - 4 May 2018; Vancouver, BC, Canada (2018).

12. Konomi T, Honda Y, Kako E, Kobayashi Y, Michizono S, Miyajima T, et al. Development of high intensity, high brightness, CW SRF gun with Bi-alkali photocathode. In: 19th Int. Conf. RF Superconductivity (SRF'19); 30 Jun - 05 Jul 2019; Dresden, Germany (2019).

13. Huang S, Ouyang D, Wang F, Jiao F, Zhu F, Wang G, et al. Continuous-wave operation of a low-emittance DC-SRF photocathode gun (WEAO3). In: 40th International Free Electron Laser Conference (FEL2022); August 22-26 2022; Trieste, Italy (2022).

14. Lewellen J, Adolphsen C, Coy R, Ge L, Ji F, Murphy M, et al. Status of the SLAC/MSU SRF gun development project. In: North American Particle Accelerator Conference 2022; 7-12 August 2022; Albuquerque, New Mexico, USA (2022).

15. DESY. TS4I | SRF photoinjector test stand Ts4i (2023). Available at: https://ts4i.desy.de/motivation/index_eng.html.

16. van der Horst B, Klinke D, Muhs A, Schmökel M, Sekutowicz J, Sievers S, et al. Development and adjustment of tools for supercondcuting rf gun cavities. In: 20th Int. Conf. on RF Superconductivity SRF2021; 28 June-2 July 2021; East Lansing, MI, USA (2021).

17. Smedley J, Rao T, Sekutowicz J. Lead photocathodes. *Phys Rev ST Accel Beams* (2008) 11:013502. doi:10.1103/physrevstab.11.013502

18. Barday R, Burrill A, Jankowiak A, Kamps T, Knobloch J, Kugeler O, et al. Characterization of a superconducting Pb photocathode in a superconducting rf photoinjector cavity. *Phys Rev Spec Topics-Accelerators Beams* (2013) 16(12):123402. doi:10.1103/physrevstab.16.123402

19. Lorkiewicz J, Nietubyć R, Diduszko R, Sekutowicz J, Kosińska A, Mirowski R, et al. Coating in ultra-high vacuum cathodic-arc and processing of Pb films on Nb substrate as steps in preparation of Nb-Pb photocathodes for radio-frequency, superconducting e-guns. *Vacuum* (2020) 179:109524. doi:10.1016/j.vacuum.2020.109524

20. Li RK, To H, Andonian G, Feng J, Polyakov A, Scoby CM, et al. Surface-plasmon resonance-enhanced multiphoton emission of high-brightness electron beams from a nanostructured copper cathode. *Phys Rev Lett* (2013) 110:074801. doi:10.1103/physrevlett.110.074801

21. Bazyl EVD. *Interviewee,* personal communication (2023).

22. Harris JR, Ferguson KL, Lewellen JW, Niles SP, Rusnak B, Swent RL, et al. Design and operation of a superconducting quarter-wave electron gun. *Phys Rev Spec Topics-Accelerators Beams* (2011) 14(5):053501. doi:10.1103/physrevstab.14.053501

23. Legg R, Bisognano J, Bissen M, Bosch R, Eisert D, Fisher M, et al. Status of the Wisconsin srf gun. In: Proceedings of IPAC2012; May 2-25, 2012; New Orleans, Louisiana, USA (2012).

24. Schmerge JF, Brachmann A, Dowell D, Fry A, Li RK, Li Z, et al. The LCLS-II injector design. In: Proceedings of the 2014 International Free-Electron Laser Conference; 25-29 August 2014; Basel, Switzerland (2014).

25. Konomi T, Hartung W, Kim S, Miller S, Morris D, Popielarski J, et al. Design of the cathode stalk for the LCLS-II-HE low emittance injector. In: 5th North American Particle Accel. Conf. (NAPAC2022); August 6-12, 2022; Albuquerque, NM, USA (2022).

26. Teichert J, Arnold A, Büttig H, Justus M, Kamps T, Lehnert U, et al. Free-electron laser operation with a superconducting radio-frequency photoinjector at ELBE. *Nucl Instrum Methods Phys Res Sect A* (2014) 743:114–20. doi:10.1016/j.nima.2014.01.006

27. Lu P, Arnold A, Teichert J, Vennekate H, Xiang R. Simulation of ELBE SRF gun II for high-bunch-charge applications. *Nucl Instr Methods Phys Res A* (2016) 830:536–44. doi:10.1016/j.nima.2016.05.087

28. Konomi T, Honda Y, Kako E, Kobayashi Y, Michizono S, Miyajma T, et al. Development of SRF gun applying new cathode idea using a transparent superconducting layer. In: 59th ICFA Advanced Beam Dynamics Workshop on Energy Recovery Linacs (ERL17); 18-23 June 2017; Geneva, Switzerland (2017).

29. Quan S, Hao J, Lin L, Zhu F, Wang F, Feng L, et al. Stable operation of the DC-SRF photoinjector. *Nucl Instr Methods Phys Res Section A: Acc Spectrometers, Detectors Associated Equipment* (2015) 798:117–20. doi:10.1016/j.nima.2015.07.025

30. Liu YQ, Chen M, Huang S, Lin L, Liu KX, Quan SW, et al. Engineering design of low-emittance DC-SRF photocathode injector. In: 39th Free Electron Laser Conference (FEL2019); August 26-30, 2019; Hamburg, Germany (2019).

31. Tan T, Jia H, Zhao S, Li T, Wang T, Liu Z, et al. Sub-micron normalized emittance measurement for a MeV continuous-wave electron gun. *Nucl Instr Methods Phys Res Section A: Acc Spectrometers, Detectors Associated Equipment* (2023) 1045:167552. doi:10.1016/j.nima.2022.167552

32. Litvinenko V, Altinbas Z, Anderson R, Belomestnykh S, Boulware C, Brown K, et al. Commissioning of FEL-based coherent electron cooling system. In: 38th Int. Free Electron Laser Conf. (FEL'17); 20-25 August 2017; Santa Fe, NM, USA (2017).

33. Wang E, Litvinenko VN, Pinayev I, Gaowei M, Skaritka J, Belomestnykh S, et al. Long lifetime of bialkali photocathodes operating in high gradient superconducting radio frequency gun. *Scientific Rep* (2021) 11(1):4477–9. doi:10.1038/s41598-021-83997-1

34. Petrushina I, Litvinenko VN, Pinayev I, Smith K, Narayan G, Severino F. Mitigation of multipacting in 113 MHz superconducting rf photoinjector. *Phys Rev Acc Beams* (2018) 21(8): 082001. doi:10.1103/physrevaccelbeams.21.082001

35. Petrushina I, Jing Y, Litvinenko VN, Ma J, Severino F, Narayan G, et al. First experience with He conditioning of a superconducting rf photoinjector. *Phys Rev Acc Beams* (2022) 25(9):092001. doi:10.1103/physrevaccelbeams.25.092001

36. Xiang R, Jan S. Review of recent progress on advanced photocathodes for superconducting RF guns. *Micromachines* (2022) 13(8):1241. doi:10.3390/mi13081241

37. Vogel E, Barbanotti S, Brinkmann A, Buettner T, Iversen J. Status of the all superconducting gun cavity at desy. In: 19th Int. Conf. on RF Superconductivity; 30 Jun - 05 Jul 2019; Dresden, Germany (2019).

38. Hannon F, Andonian G, Harris L. A plasmonic niobium photocathode for srf gun applications. In: 10th Int. Particle Accelerator Conf. IPAC2019; 19 - 24 May 2019; Melbourne, Australia (2019).

39. Liu A, Kostin R, Jing C, Avrakhov P. Optimization of an srf gun design for uem applications. In: North American Particle Acc. Conf (NAPAC2019); 1—6 September 2019; Lansing, MI, USA (2019).

40. Tulu ET, van Rienen U, Arnold A. Systematic study of multipactor suppression techniques for a superconducting rf gun. *Phys Rev Acc Beams* (2018) 21(11):113402. doi:10.1103/physrevaccelbeams.21.113402

41. Janssen D, Volkov V. Emittance compensation in a superconducting rf photoelectron gun by a magnetic rf field. In: Proceedings of EPAC 2004; 5-9 July 2004; Lucerne, Switzerland (2004).

frontiers | Frontiers in Physics

TYPE Review
PUBLISHED 19 April 2023
DOI 10.3389/fphy.2023.1150809

OPEN ACCESS

EDITED BY
Winni Decking,
Helmholtz Association of German Research Centres (HZ), Germany

REVIEWED BY
Houjun Qian,
Zhangjiang Laboratory, China
Dmitry Bazyl,
Helmholtz Association of German Research Centres (HZ), Germany

*CORRESPONDENCE
F. Zhou,
zhoufeng@slac.stanford.edu

SPECIALTY SECTION
This article was submitted to Interdisciplinary Physics, a section of the journal Frontiers in Physics

RECEIVED 25 January 2023
ACCEPTED 01 March 2023
PUBLISHED 19 April 2023

CITATION
Zhou F, Adolphsen C, Dowell D and Xiang R (2023), Overview of CW electron guns and LCLS-II RF gun performance. *Front. Phys.* 11:1150809. doi: 10.3389/fphy.2023.1150809

Overview of CW electron guns and LCLS-II RF gun performance

F. Zhou[1]*, C. Adolphsen[1], D. Dowell[1] and R. Xiang[2]

[1]SLAC National Accelerator Laboratory, Menlo Park, CA, United States, [2]Helmholtz-Zentrum Dresden Rossendorf, Dresden, Germany

Various continuous-wave (CW) electron gun technologies are reviewed, including DC, superconducting radio frequency RF (SRF), hybrid DC-SRF and normal-conducting RF. Also, the SLAC Linac Coherent Light Source II (LCLS-II) normal-conducting RF gun and injector are described, and the performance to date, including the bunch emittance achieved and the dark current observed, is presented.

KEYWORDS

CW, DC gun, SRF gun, NC RF gun, LCLS-II, emittance, dark current

1 Introduction

X-ray free electron lasers (XFELs) [1–4] have proven to be a revolutionary tool for scientific studies of material properties. However, existing XFEL facilities typically operate at repetition rates below a few hundred Hertz (Hz) due to power handling limitations of their normal-conducting guns and accelerator structures. To push to photon science Frontier, MHz rate beams are needed with continuous-wave (CW) radiofrequency (RF) operation. One of the major challenges for such MHz XFELs is to find a CW electron gun technology that can produce high-brightness electron bunches.

CW gun R&D has been pursued worldwide since the 1980s. The gun technologies include DC [5–8], Superconducting RF (SRF) [9–18], hybrid DC-SRF [19] and normal-conducting (NC) RF [20, 21]. This paper first surveys these technologies and then discusses the design and performance of the NC RF gun and injector at the SLAC Linac Coherent Light Source II (LCLS-II). Finally, the performance of representative guns is summarized.

2 CW gun development

Significant progress has been made for each gun technology noted above [22–24]. The labs that have been involved are listed below and more information is provided in the following subsections.

DC gun
- Cornell University in the United States of America [5, 6].
- Daresbury Laboratory in the United Kingdom [8].
- JAEA/KEK in Japan [7].

Hybrid DC-SRF gun
- Peking University in China [19].

SRF gun with 1.3 GHz Elliptical Cells
- Helmholtz-Zentrum Dresden-Rossendorf (HZDR) in Germany [11].
- Helmholtz-Zentrum Berlin (HZB) in Germany [12].
- DESY in Germany [13].

- KEK in Japan [14].

SRF gun with 100–200 MHz Quarter-Wave Resonator (QWR) cavity

- Wisconsin University in the US [15].
- BNL in the US [16].
- SLAC/MSU/HZDR [17, 18].

NC gun (185.7 MHz)

- LBNL in the US [20, 21].

A version of the LBNL NC gun is currently being used at LCLS-II and will be used at the Shanghai XFEL facility [25]. The SLAC/MSU/HZDR 185.7 MHz SRF gun is currently being developed for use in a low projected emittance (~0.1 μm) injector that has been proposed for the high energy upgrade of LCLS-II (LCLS-II-HE).

2.1 DC guns

The DC guns have been developed for high current Energy Recovery Linac (ERL) applications. The Cornell DC gun is the most advanced and can routinely operate with a 400 kV cathode-to-anode potential, which produces a ~4.4 MV/m gradient at the photocathode. It has successfully produced 75 mA low-emittance beams, which is a world's record for average current [5]. Green light photocathodes (e.g., K_2CsSb, NaKSb) are typically used and the dark current is generally negligible.

At Cornell, 100 pC bunches with an emittance of about 0.4 μm [6] have been produced with ten's-of-ps-long flattop-like laser pulses. However, because the flattop-like laser pulses were obtained through stacking ps-level short pulses, a small intensity modulation on the flattop is generated, which can be significantly amplified after the ~100 times bunch compression required for XFELs, thereby compromising the longitudinal phase space [26]. Thus, smooth Gaussian temporal laser pulses are typically used for XFELs although the transverse emittance is not optimum compared to that achievable with a stacked laser pulse.

The 400 kV gun voltage is near the high voltage limit without major advances in high voltage insulator and electrode materials. The relatively low gradient on the cathode and the low gun energy that results limit the ultimate electron peak current after bunch compression. Preliminary simulations [27] have shown that the peak bunch current is notably limited after two stages of bunch compression due to the highly non-linear energy spread.

2.2 Superconducting RF guns

SRF guns are promising candidates for CW operation with at least 30 MV/m of gradient at the photocathode and energy gains of a few MeV. There are two main categories of SRF guns in use: one uses 1.3 GHz elliptical cells, for example, those developed by HZDR, HZB, KEK and DESY, while the other uses 100–200 MHz single-cell QWR cavities, and have been, or are being developed by U. of Wisconsin, BNL and a SLAC/MSU/HZDR collaboration.

Among the first category of guns, the DESY 1.6 cell SRF-Gun has a metallic photocathode (niobium plug coated with lead, which becomes superconducting below 7.2 K) that attaches to the cavity half-cell shorting plate. Thus, no *in-situ* photocathode exchange is possible and no loadlock system is required. The quantum efficiency of the lead photocathode is about 2 orders lower than that for the semiconductor photocathodes used in most CW guns, which imposes a challenge for MHz-rate electron beam operation. The

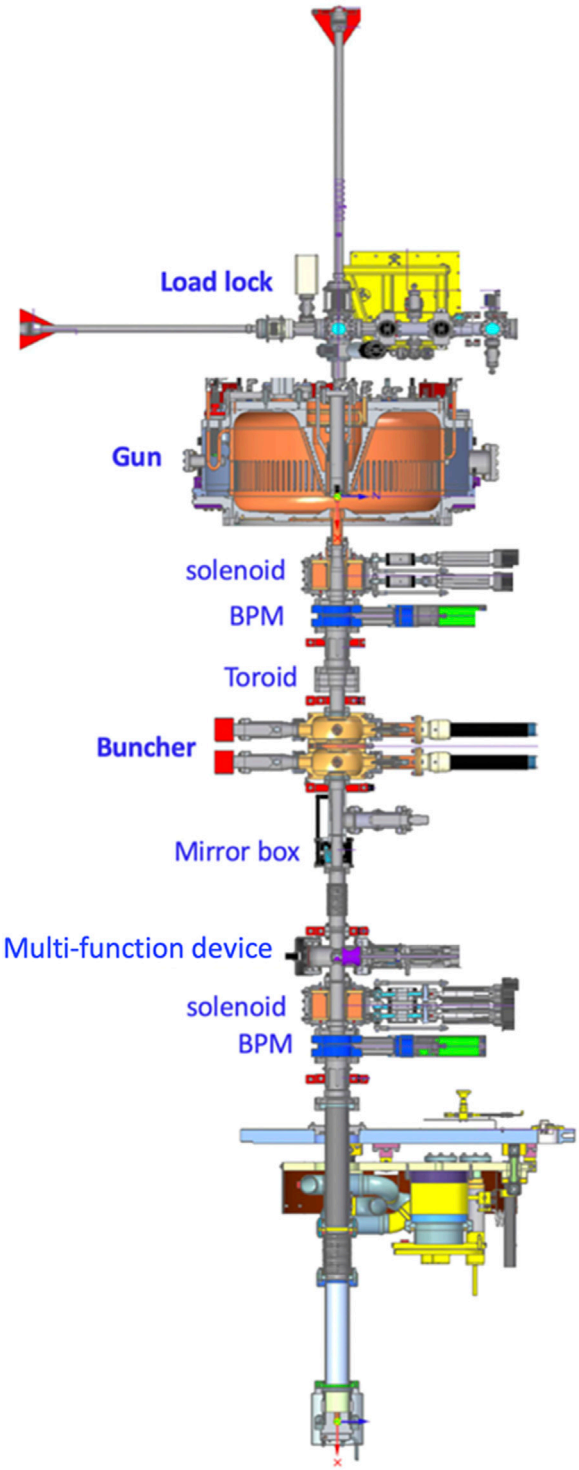

FIGURE 1
Schematic of LCLS-II electron source.

TABLE 1 LCLS-II gun and injector parameters.

Parameters	Nominal
Gun energy (keV)	650–750
Gun gradient on the photocathode (MV/m)	17.5–19.5
Cs_2Te photocathode QE (%)	>0.5
Drive laser pulse: Gaussian shape, FWHM (ps)	15–20
Maximum bunch repetition rate (MHz)	0.93
Bunch charge (pC)	20–100
Maximum average beam current (μA)	30
Injector final energy (MeV)	>90
Normalized emittance (μm, rms) @ 50–100 pC	<0.5
RMS bunch length (mm)	<1

gun has achieved a 40 MV/m gradient at the photocathode based on vertical test [13, 24].

The HZDR, HZB and KEK guns use removable semiconductor photocathodes that are thermally isolated from the niobium cavity and include a choke cell to limit RF leakage into the gap between the cathode stalk that holds the photocathode and the niobium. Their cryostats contain a superconducting solenoid magnet for emittance compensation, and there is an upstream load-lock system for warm photocathode exchange.

The HZDR 1.3 GHz SRF gun with a Mg photocathode began routine operation in 2017 as part of an accelerator for Tera Hertz (THz) RF production [11]. Cs_2Te photocathodes were tested in 2020 [28] but strong QE degradation occurred soon after CW RF operation began. Currently, the gun is operating in CW mode with a 14 MV/m of gradient at the photocathode for the user program, and typically produces bunch charges of 200 pC at 50–100 kHz. The bunch transverse emittance is ~3 μm and the rms bunch length is 300 fs after the linac and chicane, which meets the THz program requirements. The L-Band gun has the potential to provide a higher gradient at the photocathode, but it is currently gradient limited due to cavity contamination from a photocathode failure in 2017.

BNL developed their QWR SRF gun for an electron cooling project. The gun consists of a 112 MHz QWR cavity with a warm photocathode, which can be exchanged via a load-lock system under ultra-low vacuum pressure. The gun is typically operated with a photocathode gradient of 15–18 MV/m. A low intrinsic emittance green light photocathode (K_2CsSb) is used, whose lifetime benefits from the low vacuum pressure afforded by the cryogenic environment. An emittance of about 0.3 μm has been demonstrated for 100 pC bunches but with a very long bunch length (~400 ps), more than 100 times longer than that required for XFELs.

The SRF guns have common challenges including.

- Complex/fragile photocathode exchange systems, which can readily cause gun contamination/degradation during photocathode insertion into the gun body
- Non-optimal emittance compensation
- Much lower-than-expected gradient on the photocathode with the photocathode inserted.

The need to keep the photocathode plugs from contacting the cold cavity walls creates complexity for the SRF gun design and operation. The compatibility of SRF cavities with insertable photocathodes remains a challenge for robust SRF gun operation, particularly when frequent photocathode exchanges are required, which can introduce particulates. Also, semiconductor photocathodes pose a contamination risk from the diffusion/sputtering of their chemical components during operation. Contaminants can create field emission on the cavity surface that results in significant performance degradation due to dark current generation and enhanced secondary electron emission. BNL finds that *in-situ* helium processing helps recover from such degradation [29] although the cleaning process is not-trivial.

A solenoid magnet is typically used just downstream of the gun as part of a compensation process to reduce space charge related emittance growth. SRF guns have a notable drawback in this regard as the magnetic field on the niobium cavity surfaces must be kept lower than the critical magnetic field. As a result, the solenoid must be located farther away from the cathode in an SRF gun cavity, which can compromise emittance compensation compared to a NC gun. This distance is longer for 3.5-cell 1.3 GHz SRF guns than for a QWR SRF gun, which is disadvantageous for producing the sub-micron emittance bunches required for XFELs [30, 31].

To date, SRF guns have not routinely demonstrated e-beam operation with >20 MV/m gradient on photocathode. Multipacting and particle-contaminant-induced field emission are the major factors limiting the gradient. However, there are ongoing SRF gun R&D programs that are pursuing higher than 30 MV/m of gradients on the photocathode for e-beam operation [12–14, 17, 18].

2.3 Hybrid DC-SRF gun

A DC-SRF gun has been under development by Peking University for about 3 decades. It has evolved to combine a 100 kV DC cell (5 MV/m of gradient on the photocathode) and a 1.3 GHz, 13 MV/m, 1.5-cell SRF cavity. They are connected by a drift tube that is about 1 cm long, and the resulting energy gain is 2.2 MeV. With the DC cell, the photocathode is moved out from the cryogenically cooled cavity, which lessens the compatibility issues noted above. The emittance compensation solenoid is in a warm beamline section that is about 0.5 m downstream of the cavity. K_2CsSb photocathodes are used, and recently sub-micron emittances have been achieved with 50–100 pC bunches generated by stacked laser pulses [19]. The dark current is small (pA level) and the bunch length has yet to be measured.

2.4 NC RF guns

High-frequency (>1 GHz), high gradient NC RF guns are being used to produce high-brightness beams for pulsed XFELs. The average power loss density in such cavities limits the practical repetition rate to less than 1 kHz. By decreasing the RF frequency to hundreds MHz, the size of the cavities increases with a beneficial reduction of the power density, allowing higher duty RF operation [32, 33].

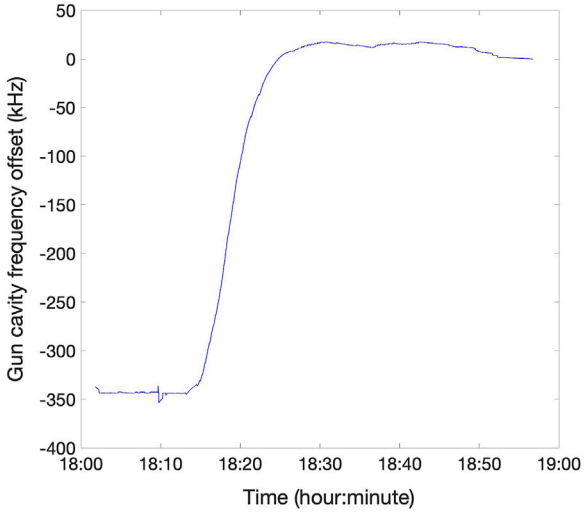

FIGURE 2
Example of the gun cavity frequency evolution during initial turn-on.

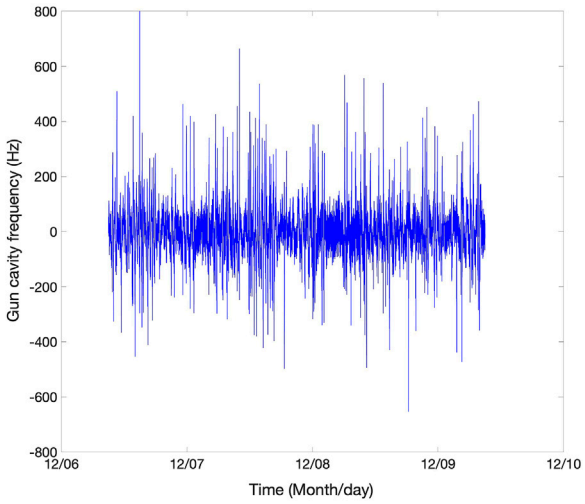

FIGURE 3
Example of the gun frequency regulation over a several-day period.

In 2006, a LBNL team proposed and later developed [20, 34] a 186 MHz CW QWR NC RF gun for high repetition rate XFELs. The power load on the cavity walls at the nominal 20 MV/m of gradient on photocathode is removed by conventional cooling techniques. Good vacuum (~10^{-10} Torr) is achievable and long lifetime operation with Cs_2Te photocathodes has been demonstrated, but practical lifetimes with K_2CsSb photocathodes have yet to be realized. An emittance of 0.25 μm has been achieved with 20 pC bunches [21] but μA level dark current has been an issue [35]. Given the good performance with Cs_2Te photocathodes, the gun design was adopted for LCLS-II.

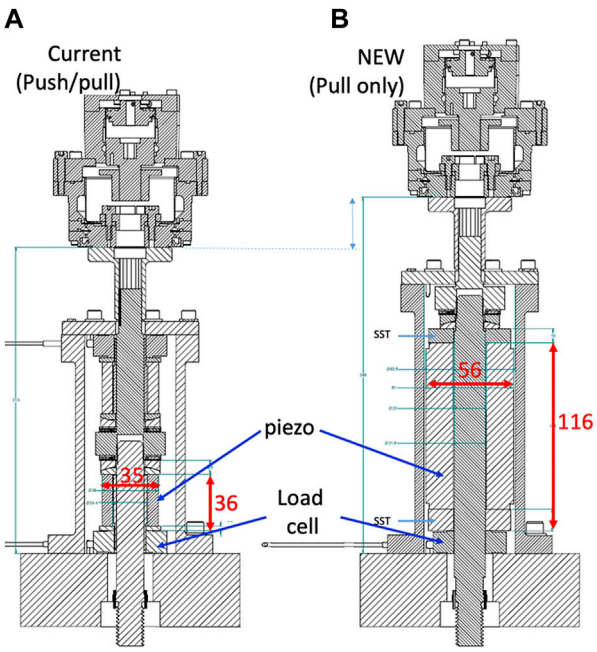

FIGURE 4
New gun tuner design with a larger piezo **(B)** and the original design **(A)**.

3 LCLS-II gun systems

This section provides an overview of the LCLS-II CW electron injector and summarizes the beam performance and the dark current measurements and mitigations.

3.1 Layout and parameters

The LCLS-II electron source, which comprises the first 3 m of the injector, was designed and built by the LBNL following their decade-long advanced photoinjector experiment (APEX) program to develop a 186 MHz NC, CW electron gun [20, 21, 34, 35]. For the LCLS-II project, modifications to the gun design were made based on lessons learned and specific LCLS-II requirements.

Figure 1 shows a schematic layout of the electron source, which includes a 185.7 MHz QWR-style CW NC RF gun, a 1.3 GHz two-cell NC cavity for compressing the bunch length, and two solenoid magnets for beam focusing and emittance compensation. Beam diagnostics include two beam position monitors (BPMs), a current monitor (toroid), and a newly installed multi-function insertion device that contains 4 circular collimators with different aperture sizes, an yttrium-aluminum-garnet (YAG) screen, and a YAG screen with a central hole. Electrons lost on the circular collimator plates are detected by a pico-ammeter, which serves to monitor gun dark current. A load lock for photocathode exchange is located upstream of the gun and mirror box is located 1.1 m downstream of the photocathode for injecting 257.5-nm-wavelength laser pulses. Cs_2Te photocathodes produced at SLAC are being used for bunch charge generation.

Following the electron source is 1) a standard LCLS-II cryomodule, which has eight 9-cell cavities to boost the electron

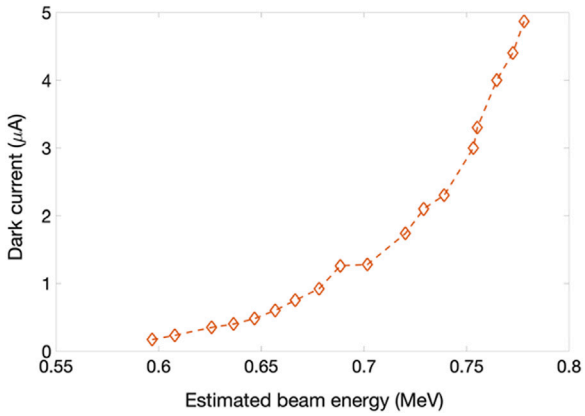

FIGURE 5
LCLS-II RF gun dark current 3 m from the cathode *versus* the gun energy gain.

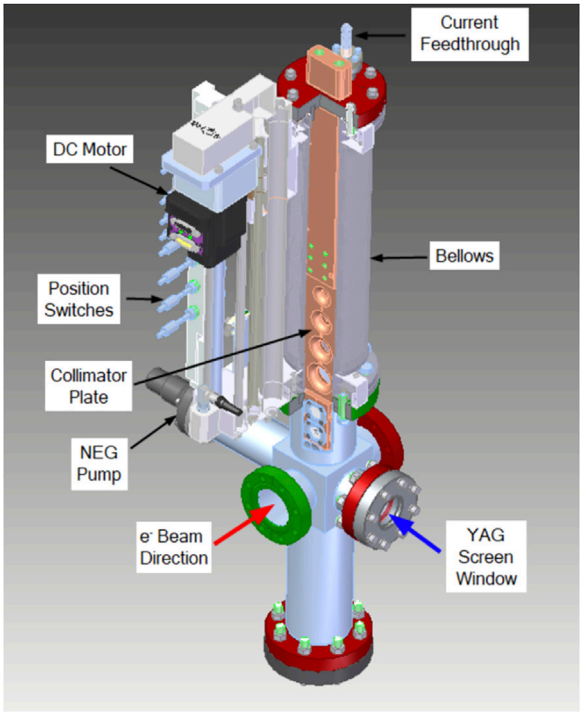

FIGURE 6
Ladder-like multi-function beamline insertion device that includes four circular collimators and two YAG screens.

energy to more than 90 MeV, 2) an emittance station including four matching quads and a screen, 3) a laser heater chicane that increases the bunch slice energy spread to suppress micro-bunching, 4) two cavity-based average current monitors to measure electron beam current and dark current, and 5) a dedicated off-axis beamline for emittance and bunch length measurements. The LCLS-II electron source and injector parameters are summarized in Table 1.

3.2 NC RF gun and buncher systems

The single-cell gun cavity is designed for CW RF operation at 185.7 MHz, the seventh subharmonic of the 1.3 GHz superconducting linac frequency. The cavity has an R/Q of 198.2 Ω, a Q_0 of 29,923, and two RF power coupling ports with a combined coupling coefficient of 1.1. The design gun voltage gain is 750 kV, but the gun is typically run with a voltage gain of ~650 kV, corresponding to a photocathode gradient of ~17.5 MV/m. The RF connection to each of the two-gun ports consists of an air-to-vacuum window followed by a 90° bend that terminates in a loop coupler, all implemented in coaxial waveguide. The bend keeps dark current from the gun interior from directly hitting the vacuum window. In each feed line, three permanent solenoid magnets are installed in the short section between the RF coupler and the vacuum window to suppress multipacting. Light detectors that view the rf windows and gun body will shut off the RF in the event of an arc, but none has occurred yet.

Each gun port is powered by a 60 kW solid state amplifier (SSA). The SSA output power is very stable in open loop, about 0.01% rms in amplitude and 0.1° rms in phase on a 1-s timescale [36]. The SSAs are installed in the SLAC linac gallery, and 6.125-inch rigid coaxial waveguide is used to transport the RF power from the SSAs to the gun in the linac tunnel. Although the SSA transistors are back terminated, high-power isolators are included in the transport lines in the gallery. For non-ionizing radiation safety, the gallery waveguide is pressurized at a few pounds per square inch, which requires the use of coaxial air barriers. The RF will shut off if there is a drop in pressure inside the waveguide.

The gun vacuum is maintained by six non-evaporable getters (NEGs) and six combined NEGs and ion pumps that are located around the outer cavity radius and connect to a cylindrical structure that is cut off to the RF. A vacuum pressure in the low 10^{-9} Torr scale, and a partial pressure of less than 10^{-11} Torr for specific harmful molecules like oxygen, are required to achieve reasonably long lifetimes of the Cs_2Te photocathodes used in the gun. The gun is cooled *via* five separate water circuits that connect to the SLAC 30 °C low-conductance water system. The combined flow is about 40 gallons-per-minute, and the flow through the anode plate was adjusted so the steady-state cavity frequency was in a range that did not overstress the mechanical tuners.

The RF buncher [37] is a two-cell, *p*-mode, 1.3 GHz NC cavity with R/Q = 340 Ω and Q_o = 25,700. It has four input power couplers with a combined coupling coefficient of unity. The cavity adds an energy chirp to the bunches and the resulting velocity variation compresses the bunch length by a factor of 3–5. Each input coupler is powered by an independent SSA. For the nominal combined input of power of 7.6 kW, the integrated buncher field voltage is measured to be about 200 kV.

3.3 Gun and buncher frequency tuners

With the large size of the gun cavity, there is a substantial frequency change due to RF heating, about 250 kHz, which is much larger than the 6 kHz cavity half-bandwidth. A system of four mechanical tuners is used to pull the anode plate outward to adjust the cavity frequency. For each tuner, a DC motor rotates a shuttle that screws onto a bolt connected to the anode plate. When the gun warms up, the anode plate bows outward, and the reactive force on the shuttle disk is transferred through a piezo actuator and load cell to a thick plate that is attached to the outer rim of the gun anode. The load cells provide a measure of the

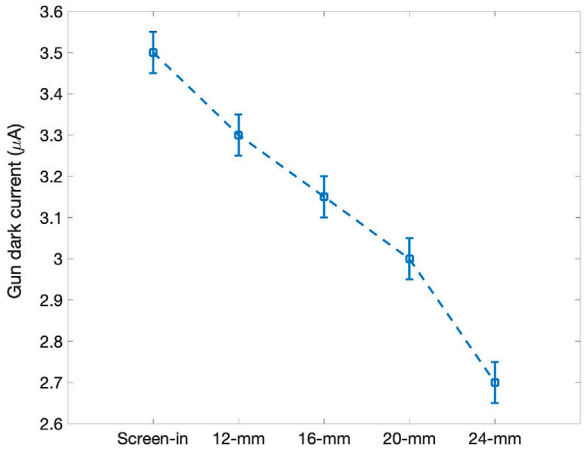

FIGURE 7
Dark current measured 1.5 m from the cathode with different LEB collimator sizes. For the 'Screen-In' case, a thin YAG screen intercepts the full current.

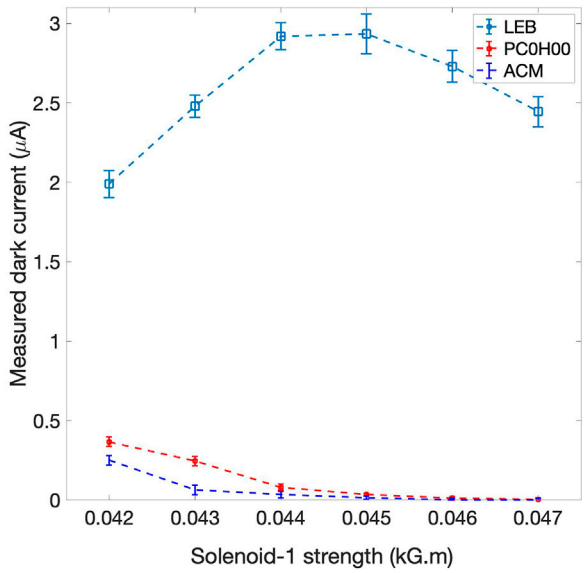

FIGURE 8
Measured dark current at the 20-mm LEB collimator and the PC0H00 collimator, and the dark current transported through an ACM as function of the strength of Solenoid-1.

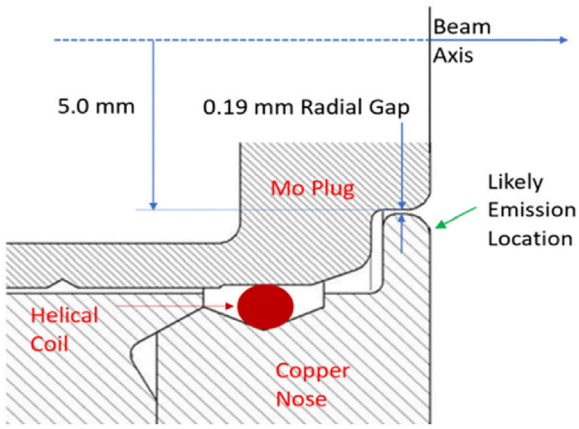

FIGURE 9
Cross section of the molybdenum cathode plug when inserted into the copper cathode nose. The likely dark current emission region is indicated.

applied force. During the warm-up period, the Low Level RF system first employs a self-excited loop controller to track the cavity frequency until the anode temperature begins to stabilize, then the tuners are used to set and maintain the cavity frequency near the nominal 185.714 MHz value. Figure 2 shows an example of the initial gun cavity frequency evolution when the RF duty factor was ramped to near 100%.

The frequency feedback system uses a two-tiered control loop in which a high-level feedback loop adjusts the tuner load cell set points based on the detuning relative to the nominal frequency, and four low-level feedback loops regulate the four tuner loads to their set point values. This control is critical as there is a subsequent −100 kHz frequency drift over a 4-h time period due to the slow heating of the outer cavity wall, which otherwise would pull the anode plate inward. During this period, the duty cycle is increased to 100% and cavity frequency is then computed based on the phase difference between the forward and probe signal RF. This control procedure typically regulates the frequency to within ±200 Hz of the nominal value, which is ~ ± 3% of the cavity half-bandwidth. However, there are occasional larger frequency jumps when one of the tuner screws overcomes a frictional barrier. Figure 3 shows an example of the frequency regulation over a several-day period.

The four piezo actuators were originally meant to be used for fine frequency control, but they were damaged by radiation. Further investigation revealed that the piezos are readily radiation damaged when several hundred volts are applied for control. Upgrades to the tuner piezo system are underway, which should allow them to be used to improve the frequency regulation. Figure 4 shows schematics of the current and new tuners. The new piezo ceramic is 116 mm long and has a 56 mm outer diameter [38], making it considerably stronger than the original ceramic, which is 36 mm long with a 35 mm outer diameter. The new piezos are expected to require only one-fifth of the voltage of the original ones for same force generation, which should significantly extend their lifetimes.

The process for buncher cavity frequency tracking during warm-up and subsequent frequency locking is similar to that for the gun except the cavity frequency is controlled by adjustments to the temperature of the cooling water, which is provided by a closed-loop chiller. The RF heating detunes the cavity by about 600 kHz, much larger than its 50 kHz half-bandwidth. The cavity frequency is regulated to within 2 kHz of the nominal 1.3 GHz frequency using a PID temperature controller where the setpoint changes are proportional to the measured frequency offset.

3.4 Beam measurements

During the past year, the Cs_2Te photocathodes used in the gun are ones produced at SLAC, which have an initial QE of about 5%. Low charge (<1 pC) emittance measurements indicate the intrinsic emittance of Cs_2Te photocathodes is about 1 μm/mm-rms [39] with a 258 nm UV laser, which is close to that expected.

The laser pulses at the photocathode are shaped to be roughly uniform in their transverse profile although the emittance can be likely

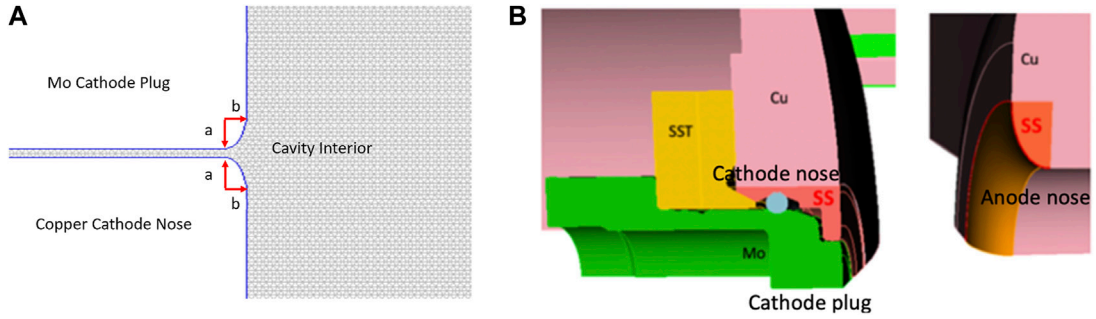

FIGURE 10
Improvements to the spare gun **(A)** elliptical shaped (b/a=0.17) edges on the cathode plug and nose, **(B)** stainless steel (SS) inserts at the cathode and anode openings.

TABLE 2 Representative CW gun parameters and challenges.

Parameters	DC gun (cornell)	Multi-cell SRF gun (HZDR)	Quarter-wave SRF gun (BNL)	DC-SRF gun (peking U.)	LCLS-II NC RF gun (SLAC)
Gun energy	0.4 MeV	3.5 MeV	1–1.5 MeV	2.2 MeV	0.65 MeV
Gradient on photocathode	4.4 MV/m	14 MV/m	18 MV/m	5 MV/m	17.5 MV/m
Photocathode exchange	Easy	Difficult	Difficult	Easy	Easy
General operation	Less difficult	Difficult	Difficult	Less difficult	Less difficult
Emittance compensation	Optimum	Compromised	Compromised	Compromised	Optimum
Laser wavelength	Green	UV	Green	Green	UV
Laser temporal shape	Stacked Flattop	Gaussian	Gaussian	Stacked Flattop	Gaussian
Photocathode	NaKSb, K_2CsSb	Mg, Cs_2Te	K_2CsSb	K_2CsSb	Cs_2Te
Demonstrated emittance	~0.4 μm @ 100 pC	>2 μm @ 200 pC	~0.3 μm @ 100 pC	~0.85 μm @ 100 pC	~0.5 μm @ 50 pC
Bunch length rms	3 ps	3 ps	400 ps	-	<3 ps
Dark current	pA level	pA level	pA level	pA level	μA level

improved using a truncated Gaussian profile [40]. A smooth Gaussian-like temporal laser shape is used as it is much easier to generate than a smooth flat pulse. However, efforts are underway to generate flat pulses as they should yield a lower emittance after space charge compensation.

The bunch emittance is measured using the conventional quadrupole-scan technique. The bunch sizes are measured at the first screen after the cryomodule, which currently increases beam energy to 80 MeV. The gun is currently operated with lower voltage gain (650 kV) than the design value (750 kV) to reduce dark current. Simulations suggest that the emittance is not compromised at this lower voltage. Trim-quad (both normal and skew quads) coils that are embedded in the two main solenoids play an important role in correcting for high-order fields in the solenoids and in the 1.3 GHz SRF cavity power couplers [41, 42]. Adjustment of these trim-quads are seen to improve the bunch shape and results in a lower emittance. Currently, the buncher is operated with a voltage gain of about 200 kV and a phase such that the bunches arrive −30° from the zero-crossing.

The emittance compensation process is particularly sensitive to the settings of the first and third cavities in the cryomodule: the second cavity is not powered by design. After optimization of the various parameters, an emittance of about 0.5 μm has been routinely achieved so far for 50 pC bunches, which is somewhat larger than the ~0.4 μm simulated values.

The bunch length is measured with the well-known RF zero-phasing technique [43]. A large bunch energy chirp is added by operating the seventh cryomodule cavity near the zero crossing. This streaks the bunch in the off-axis diagnostics line where there a large vertical dispersion, and the bunch length is inferred from the vertical bunch size as measured on a screen. Bunch length values of about 1 mm rms have been measured, which are close to expectation. Systematic optimization of the emittance and bunch length is still in progress.

3.5 Dark current measurements and mitigation

The CW NC RF gun generates several μA of dark current that appears to originate from localized areas on the rim of the cathode plug hole, which is 10 mm in diameter [35, 39]. Figure 5 shows the

dark current measured 3 m from the cathode as function of beam energy (the cryomodule was not installed at this time). Such large dark current, if transported through the 4 GeV SRF linac to the XFEL undulators, will degrade the permanent magnets used in these devices.

As the dark current is well separated from the photobeam transversely [39], a circular collimator was installed to intercept it while the electron energy is low (<1 MeV) and thus the radiation produced is minimized. For this purpose, a ladder-like multi-function insertion device was designed and installed 1.5 m from the cathode [44]. This device includes four circular collimators with different aperture sizes (referred to as 'LEB' collimators), a YAG screen, and a YAG screen with a central hole to allow beam halo measurements (see Figure 6).

An operator can remotely insert any one of the four LEB collimators, whose aperture sizes are 12, 16, 20 and 24 mm. The holes are machined in a 1.5 cm thick copper bar. The collimating function works well with the 20 mm aperture, which is sufficient to block the majority of the dark current while having a negligible impact on the photobeam. The copper bar is electrically isolated and connected to a pico-ammeter to monitor the intercepted current. Figure 7 shows an example of the measured dark current for different collimator settings when the gun energy gain was about 650 keV. More than 85% of the dark current is blocked with the 20 mm collimator.

The remainder of the dark current is accelerated through the cryomodule where it incurs losses due to the large energy spread it develops. It is further attenuated by a 12-mm diameter circular collimator (denoted 'PC0H00') located just downstream of cryomodule. The dark current loss on this collimator is estimated from the temperature rise of the water used to cool it. The transmitted dark current is measured downstream with an RF-cavity-based average current monitor (ACM). Figure 8 shows the dark current loss and transmission as a function of the strength of the solenoid magnet just after the gun (Solenoid-1). This solenoid affects the transverse separation of the dark current and photobeam at the LEB collimator and hence the effectiveness of the collimation there. As the Solenoid-1 strength is usually larger than 0.0435 kG-m for optimum emittance, only 10s nA of dark current make it through the ACM. This current is further attenuated by downstream collimators. Dark current tracking simulations are being performed to better optimize the collimation [45].

Figure 9 shows the region on the copper cathode nose where the dark current is believed to originate. The electric field there is about 24% higher than that at the center of the plug [39]. At SLAC, a spare gun is being built that includes improvements for dark current reduction. One change is to make the cathode and anode opening edges elliptically shaped instead of round, and another is to add stainless steel (SS) inserts near the cathode and anode openings (see Figure 10) [46]. Using a minor-to-major axis ratio of 0.17 for the cathode plug and nose edges reduces the electric field enhancement from 24% to 10%. The SS inserts should increase the gradient of dark current onset. The spare gun fabrication is expected to be completed by the end of 2023.

4 Summary

This paper has reviewed the four major CW gun technologies being developed for FELs and ERLs. Each technology has its advantages and disadvantages. The Cornell DC gun has produced 100 pC bunches with about 0.4 μm emittance although the longitudinal phase space may not be suitable for XEFL applications. As for ones using SRF technology, the BNL QWR SRF gun has achieved a 0.3 μm emittance with 100 pC bunches but with a bunch length more than 100 times longer than that required for XFELs, the HZDR SRF gun has routinely operated for a THz user program but has not yet demonstrated sub-micron emittance. And the DESY SRF gun with a superconducting lead photocathode can operate at higher gradients but the quantum efficiency is very low ($<1 \times 10^{-3}$). With a unique hybrid design, the Peking University DC-SRF gun has produced sub-micron emittance bunches, but the bunch length has yet to be characterized. Recently the LCLS-II NC RF-gun-based injector has routinely achieved 0.5 μm emittance for 50 pC bunches with the desired bunch length, and dark current mitigations that were implemented have been effective. Table 2 summarizes representative CW gun achieved parameters and challenges.

Author contributions

FZ drafts the paper and contributes to LCLS-II gun measurements, CA contributes to SRF section and LCLS-II gun analyses, DD contributes to LCLS-II gun analyses, and RX contributes to SRF section.

Funding

This work is supported by DOE under Grant Nos. DE-AC02-76SF00515.

Acknowledgments

We thank the LCLS-II injector commissioning team as well as the LBNL APEX group for their technical contributions and support, particularly X. Liu for excellent engineering support. We also thank S. Huang for providing supporting materials.

Conflict of interest

The authors declare that the research was conducted in the absence of any commercial or financial relationships that could be construed as a potential conflict of interest.

The reviewer DB declared a shared affiliation with the author RX at the time of review.

Publisher's note

References

1. Emma P, Akre R, Arthur J, Bionta R, Bostedt C, Bozek J, et al. First lasing and operation of an ångstrom-wavelength free-electron laser. *Nat Photon* (2010) 4:641–7. doi:10.1038/nphoton.2010.176

2. Ackermann W, Asova G, Ayvazyan V, Azima A, Baboi N, Bähr J, et al. Operation of a free-electron laser from the extreme ultraviolet to the water window. *Nat Photon* (2007) 1, 336–42. doi:10.1038/nphoton.2007.76

3. Tanaka H, Status report on the commissioning of the Japanese XFEL at SPRING-8, In: Proceedings of the 2nd International Particle Accelerator Conference (2011) San Sebastián, Spain (EPS-AG, Spain). 21.

4. Braun H, Commissioning of the Swiss FEL. In: Proceedings of the 8th International Particle Accelerator Conference (IPAC 2017); Copenhagen. Geneva: JACoW (2017).

5. Gulliford C, Bartnik A, Bazarov I, Cultrera L, Dobbins J, Dunham B, et al. Demonstration of low emittance in the Cornell energy Recovery linac injector prototype. *Phys Rev AB* (2013) 16:073401. doi:10.1103/physrevstab.16.073401

6. Bartnik A, Gulliford C, Bazarov I, Cultera L, Dunham B. Operational experience with nanocoulomb bunch charges in the Cornell photoinjector. *Phys Rev AB* (2015) 18: 083401. doi:10.1103/physrevstab.18.083401

7. Yamamoto N, Nishimura N. High voltage threshold for stable operation in a dc electron gun. *APL* (2016) 109:014103. doi:10.1063/1.4955180

8. Saveliev YM, Holder D, Muratori B, Smith S, Results from ALICE (ERLP) DC photoinjector gun commissioning. In: Proceedings of EPAC08, Genoa, Italy; Geneva. JACOW, Geneva (2008).

9. Chaloupka H, A proposed superconducting photoemission source of high brightness, *NIM-A* (1989) 285:327.

10. Teichert J, Arnold A, Lu P, Michel P, Murcek P, Vennekate H, First beam characterization of SRF gun II with a copper photocathode, In: Proceedings of ERL 2015; New York. Stony Brook, New York. Available at: https://accelconf.web.cern.ch/erl2015/papers/tuidlh1038.pdf (2015). 42.

11. Teichert J, Arnold A, Ciovati G, Deinert JC, Evtushenko P, Justus M, Successful user operation of a superconducting radio-frequency photoelectron gun with Mg cathodes, *PRAB* (2021) 24:033401. doi:10.1103/PhysRevAccelBeams.24.033401

12. Kamps T, Bohlick S, Buchel A, Burger M, Echevarria P, Frahm A, Setup and status of an SRF photoinjector for energy recovery linac application, In: Proceedings of IPAC2017; Copenhagen, Denmark. JACOW, Geneva (2017). 865.

13. Vogel E, Sekutowicz J, Barbanotti S, Hartl I, Jensch K, Klinke D, SRF gun development at DESY, In: Proceedings of LINAC2018; Beijing, China. JACOW, Geneva (2018). 105–8.

14. Konomi T, Honda Y, Kako E, Kobayashi Y, Michizono S, Miyajima T, Development of high intensity, high brightness, CW SRF gun with Bi-Alkali photocathode, In: Proceedings of SRF2019; Dresden, Germany. JACOW, Geneva (2019). 1219.

15. Bisognano J, Bissen M, Bosch R, Efremov M, Eisert D, Fisher M, Wisconsin SRF electron gun commissioning in Proceedings of NA-PAC2013 (2013) Pasadena, California (JACOW, Geneva), 622.

16. Petrushina I, Litvinenko VN, Jing Y, Ma J, Pinayev I, Shih K, et al. High-brightness continuous-wave electron beams from superconducting radio-frequency photoemission gun. *PRL* (2020) 124:244801. doi:10.1103/PhysRevLett.124.244801

17. Kim S, Adolphsen C, Ge L, Hartung W, Ji F, Kelly M, et al. Design of a 185.7MHz superconducting RF photo-injector quarter-wave resonator for the LCLS-II-HE low emittance injector, In: Proceedings of NA-PAC2022; Albuquerque, NM: JACOW, Geneva (2022). 245. doi:10.18429/JACoW-NAPAC2022-MOPA85

18. Ji F, Adolphsen C, Mayes C, Raubenheimer T, Coy R, Xiao L, et al. Beam dynamics studies on a low emittance injector for LCLS-II-HE, In: Proceedings of NA-PAC2022; Albuquerque, NM: JACOW, Geneva (2022). 619. doi:10.18429/JACoW-NAPAC2022-WEPA02

19. Huang S, Liu K, Zhao K, Chen J Continuous-wave operation of a low-emittance DC-SRF photocathode gun, In: Proceedings of FEL2022; Trieste, Italy: JACOW, Geneva (2022).

20. Sannibale F, Filippetto D, Papadopoulos CF, Staples J, Wells R, Bailey B, et al. Advanced photoinjector experiment photogun commissioning results. *PRAB* (2012) 15: 103501. doi:10.1103/physrevstab.15.103501

21. Sannibale F, Filippetto D, Qian H, Mitchell C, Zhou F, Vecchione T, et al. High-brightness beam tests of the very high frequency gun at the Advanced Photo-injector EXperiment test facility at the Lawrence Berkeley National Laboratory. *Rev Scientific Instr* (2019) 90(3):033304. doi:10.1063/1.5088521

22. Zhou F. Review of CW electron guns. In: Proceedings of FLS2018; Shanghai, China (2018).

23. Sannibale F. Overview of electron source development for high repetition rate FEL facilities. In: Proceedings of NA-PAC2016; Chicago, Illinois. JACOW, Geneva (2016). 445.

24. Qian H, Vogel E. Overview of CW RF guns for short wavelength FELs: Proceedings of FEL2019: Hamburg, Germany. JACOW, Geneva (2019). 290. doi:10.18429/JACoW-FEL2019-WEA01

25. Wang Z, Gu Q, Zhao M, Injector physics design at SHINE. In: Proceedings of IPAC2019; Melbourne, Australia. JACOW, Geneva (2019).1801. doi:10.18429/JACoW-IPAC2019-TUPRB053

26. Mitchell C, Qiang J, Venturini M, Emma P, Sensitivity of the microbunching instability to irregularities in cathode current in the LCLS-II beam delivery system. In: Proceedings of NAPAC2016; Chicago, IL, USA. JACOW, Geneva (2016). 1171.

27. Wang L, *Internal talk*. Private communication, SLAC, Menlo Park, California, USA (2016).

28. Xiang R, Arnold A, Ma S, Michel P, Murcek P, Schaber J, Study on QE evolution of Cs2Te photocathodes in the ELBE SRF gun-II, In: Proceedings of IPAC2022; Bangkok, Thailand. JACOW, Geneva (2022). 2617. doi:10.18429/JACoW-IPAC2022-THPOPT022

29. Petrushina I, Jing Y, Litvinenko V, Ma J, Pinayev I, Wang G, First experience with He conditioning of a superconducting rf photoinjector, *PRAB* (2022) 25:092001. doi:10.1103/PhysRevAccelBeams.25.092001

30. Vennekate H, Arnold A, Lu P, Murcek P, Teichert J, Xiang R. Emittance compensation schemes for a superconducting rf injector. *PRAB* (2018) 21:093403. doi:10.1103/physrevaccelbeams.21.093403

31. Ma S, Arnold A, Ryzhov A, Murcek P, Zwartek P, Schaber J, superconducting solenoid field measurement and optimization. In: Proceedings of IPAC2021; Campinas, Brazil. JACOW, Geneva (2021). 2425. doi:10.18429/JACoW-IPAC2021-TUPAB387

32. Dowell D. First-principles many-body study of the electronic and optical properties of CsK2Sb, a semiconducting material for ultra-bright electron sources. *APL* (1993) 63(15):2035.

33. Nguyen D, Moody N, Andrews H, Blome G, Castellano LJ, Heath CE, End-point energy measurements of field emission current in a continuous-wave normal-conducting rf injector. *PRAB* (2011) 14:030704. doi:10.1103/PhysRevSTAB.14.030704

34. Wells R, Ghiorso W, Staples J, Huang TM, Sannibale F, Kramasz TD. Mechanical design and fabrication of the VHF-gun, the Berkeley normal-conducting continuous-wave high-brightness electron source. *Rev Sci Instr* (2016) 87:023302. doi:10.1063/1.4941836

35. Huang R, Filippetto D, Papadopoulos C, Qian H, Sannibale F, Zolotorev M, Dark current studies on a normal-conducting high-brightness very-high-frequency electron gun operating in continuous wave mode. *PRAB* (2015) 18:013401. doi:10.1103/PhysRevSTAB.18.013401

36. Adolphsen C, Benwell A, Brown G, Dunning M, Gilevich S, Grouev K, et al. Initial operation of the LCLS-II electron source. In: Proceedings of the 19th International Conference on RF Superconductivity (SRF 2019); Dresden, Germany. Geneva: JACoW (2019). p. 891. doi:10.18429/JACoW-SRF2019-THP026

37. Virostek S, Sannibale F, Staples J, The RF and mechanical design of a compact, 2.5 kW, 1.3 GHz resonant loop coupler for the APEX buncher cavity. In: Proceedings of the 8th International Particle Accelerator Conference (IPAC2017); Copenhagen, Denmark. JACoW, Geneva (2017). p. 4380.

38. Liu X. *private communication*. SLAC, Menlo Park, California, USA (2021).

39. Zhou F, Adolphsen C, Benwell A, Brown G, Dowell D, Dunning M, et al. Commissioning of the SLAC linac coherent light source II electron source. *PRAB* (2021) 24:073401. doi:10.1103/physrevaccelbeams.24.073401

40. Zhou F, Brachmann A, Emma P, Gilevich S, Huang Z Impact of the spatial laser distribution on photocathode gun operation. *PRAB* (2012) 15:090701. doi:10.1103/PhysRevSTAB.15.090701

41. Dowell D, Zhou F, Schmerge J Exact cancellation of emittance growth due to coupled transverse dynamics in solenoids and rf couplers. *PRAB* (2018) 21:010101. doi:10.1103/PhysRevAccelBeams.21.010101

42. Zhou F, Dowell D, Li R, Raubenheimer T, Schmerge J, Mitchell C LCLS-II injector beamline design and RF coupler correction. In: Proceedings of FEL2015; Daejeon, Korea. JACOW, Geneva (2015). 77.

43. Emma P, Woodley M. *LCLS-II tn 18-01* (2018).

44. Liu X, Adolphsen C, Santana M, Xiao L, Zhou F Design and operation experience of a multi-collimator/YAG screen device on LCLS II low energy beamline. In: Proceedings of NA-PAC 2022; Albuquerque, NM. JACOW, Geneva (2022). 631. doi:10.18429/JACoW-NAPAC2022-WEPA08

45. Dowell D, Hindi M, van der Geer SB, de Loos MJ Combining Particle Tracking with Electromagnetic Radiation Showers: Merging GPT and Geant4 with Visualization (2023). Available at: https://arxiv.org/abs/2212.07993.PRAB, 2023.

46. Xiao L, Adolphsen C, Cedillo A, Jongewaard E, Liu X, Ng CK Spare gun multi-physics analysis for LCLS-II. In: Proceedings of IPAC2021; Campinas, SP, Brazil. JACOW, Geneva (2021). 1688. doi:10.18429/JACoW-IPAC2021-TUPAB127

frontiers | Frontiers in Physics

TYPE Original Research
PUBLISHED 03 May 2023
DOI 10.3389/fphy.2023.1154735

OPEN ACCESS

EDITED BY
Bo Liu,
Chinese Academy of Sciences, China

REVIEWED BY
Helmut Burkhardt,
European Organization for Nuclear Research (CERN), Switzerland
Simone Di Mitri,
Elettra Sincrotrone Trieste, Italy
Si Chen,
Chinese Academy of Sciences, China

*CORRESPONDENCE
Yi Jiao,
jiaoyi@ihep.ac.cn

RECEIVED 31 January 2023
ACCEPTED 17 April 2023
PUBLISHED 03 May 2023

CITATION
Zhang C and Jiao Y (2023), Design and optimization of a compact quasi-isochronous 180-deg transport arc with suppressed CSR-induced emittance growth.
Front. Phys. 11:1154735.
doi: 10.3389/fphy.2023.1154735

Design and optimization of a compact quasi-isochronous 180-deg transport arc with suppressed CSR-induced emittance growth

Chengyi Zhang and Yi Jiao*

Key Laboratory of Particle Acceleration Physics and Technology, Institute of High Energy Physics, Chinese Academy of Sciences (CAS), University of Chinese Academy of Sciences, Beijing, China

Preserving the beam quality of a high-brightness electron beam is a noteworthy issue when delivering the electron bunch through a beam transfer line. In a beam transfer line with a large deflection angle, e.g., a 180-deg transport arc comprised of a large amount of dipoles, emission of coherent synchrotron radiation (CSR) can lead to transverse emittance dilution. In addition, the longitudinal dispersion may cause undesirable bunch length variation. Both effects can degrade beam quality. Nevertheless, design and optimization of a 180-deg transport arc that can be well applied to practical applications is a challenging problem, considering the practical nonlinear effects of a real lattice and the contributions of transient CSR at the dipole edges and CSR in the subsequent drifts. In this study, we present the design and optimization of a compact 180-deg transport arc comprised of multi-triple-bend achromat (TBA) cells, aiming at suppressing the CSR-induced emittance growth and avoiding bunch length variation simultaneously. The TBA cells and optics along the arc are adjusted to suppress the CSR-induced emittance growth and bunch length variation cell by cell, after which a multi-objective optimization of the arc is conducted. Practical considerations including lattice nonlinear effects and a full one-dimensional CSR model (including transient CSR and CSR in drifts) are taken into account.

KEYWORDS

CSR, emittance growth compensation, bunch length, triple-bend achromat, transport arc, MOPSO optimization

Introduction

Since the development of the high-gain theory of free-electron lasers (FELs) and the advent of high-gain infrared (IR) and ultraviolet (UV) FELs [1–4], the production of high average FEL power has received considerable critical attention. As an industrial application, the need to apply high-power FELs to extreme ultraviolet (EUV) lithography [5] has obviously made energy recovery linac (ERL)-based FELs an appealing choice. ERLs are inherently continuous wave (CW) devices and are able to serve multiple FELs. In FEL spreaders or ERL turnaround arcs, preserving the beam quality can be a critical issue when delivering a high-brightness beam with typically picosecond (ps) or sub-ps bunch length, high peak current up to a few kilo-amperes (kA), and micrometer (μm) or sub-μm normalized horizontal emittance [6, 7]. However, in such an arc comprised of multiple dipoles, the emission of coherent synchrotron radiation (CSR) can degrade the beam quality

by causing emittance dilution [8–12], thus decreasing beam brightness, which may limit FEL output power [13]. Longitudinally, CSR can also give rise to microbunching instability (MBI) [14–19]. In addition, the longitudinal dynamics can be affected by longitudinal dispersion functions via the correlation of the longitudinal bunch coordinate z and momentum deviation δ of a particle [20–23], resulting in undesirable bunch length variation. In the high-brightness beam transport line/arc design, suppression of the CSR-induced emittance growth is highly desirable, while preserving the bunch length simultaneously to maintain high beam quality.

To control the impact of CSR on beam emittance, approaches such as the beam envelope matching method [10] and optical balance method [11] have been proposed, which are based on single or multiple double-bend achromats (DBAs). For the sake of making an isochronous cell, a triple-bend achromat (TBA) cell might be a promising candidate, as the first-order longitudinal dispersion function R_{56} can be easily canceled [22, 23]. As for suppressing CSR in a TBA cell, it has been reported that [22] a kind of TBA design could yield both first-order isochronicity, i.e., $R_{56} = 0$, and minimized steady-state CSR (denoted as ss-CSR hereafter)-induced emittance growth. Moreover, the study in Ref. [23] has demonstrated that in a TBA cell with periodic optics, the CSR-induced emittance growth and the longitudinal dispersion up to high orders can be minimized simultaneously when the horizontal transfer matrix entries between the first two dipoles in the TBA follow $[m_{11}, m_{21}\ (\mathrm{m}^{-1})] \approx (-2, 0)$.

As for preserving the bunch emittance in an arc comprised of multiple cells, the related studies mainly focus on two aspects of applications: one is arc compressors that are used to compress the bunch length and bend the beam simultaneously [6, 13, 25–27]; the other is isochronous transport arcs that are not expected to involve with bunch compression. In isochronous transport arc designs, the beam envelope matching method is commonly used to numerically minimize the emittance growth [10, 28]. Nevertheless, the design and optimization of an arc suitable for transporting a high-brightness beam is worthy of further studies, considering practical issues like the nonlinear effects of a real lattice and full 1D CSR effects in addition to ss-CSR, i.e., including transient CSR (denoted as tr-CSR) and CSR in the subsequent drifts (denoted as dr-CSR) [29, 30]. Practically, the transfer line/arc optics can be related to not only the first-order transfer map but also the high-order terms, which can produce nonlinear effects, e.g., chromatic and geometric aberrations [21, 31–33]. As the horizontal coordinate x and longitudinal coordinate z can be correlated with δ via some of the high-order terms, e.g., T_{166}, T_{266}, and T_{566}, such nonlinear effects may also give rise to emittance growth and bunch length variation. Preservation of bunch emittance and bunch length with such practical issues taken into account can be a challenging problem, especially for an arc comprised of multiple cells, which may require numerical methods to effectively obtain optimized design schemes.

In this study, we demonstrate the feasibility of designing a multi-TBA cell-based compact quasi-isochronous 180-deg arc suitable for transporting high-brightness beams with minimized CSR-induced emittance growth by applying the theoretical work in Ref. [23] to multiple cells.

TABLE 1 Input bunch parameters at the entrance of the arc in ELEGANT simulations.

Parameter	Value (unit)
Beam energy	1 GeV
Bunch charge	200 pC
Bunch length	15 μm
Transverse normalized emittance	1 μm rad
Relative rms energy spread	0.05%
Peak current	~1.5 kA

In the following sections, first, the arc design is described. Then, the numerical scans and optimization processes and the corresponding simulation results are presented. By comparing some representative optimization results, the possible correlation between CSR-induced emittance growth and MBI gain is discussed. The design strategy and the numerical scans and optimization processes may be helpful as a starting point for practically optimized transport arc designs.

Arc design

In this section, we describe the design goal of the transport arc and introduce the design of the TBA unit cell that forms the arc.

The design goal of the transport arc is to maintain the beam quality while achieving a large bending angle of 180 deg within a compact footprint, i.e., the survey length is about 40 m. To maintain the beam quality of a high-brightness beam, the arc is expected to be (quasi)-isochronous to avoid undesirable bunch length variation and CSR-immune for emittance preservation. A TBA cell is used as the basic unit cell of the transport arc, and we consider a center-symmetric design with three identical dipoles. With the goal of designing a compact 180-deg arc, dipole parameters and the length of the TBA single cell are carefully analyzed. Through a great deal of tests, the parameters of the dipole magnets are settled, i.e., the dipole lengths are $L_B = 0.4$ m and the bending angles are $\theta = 4^\circ$. Thus, it requires a total of 15 cells to form an arc. The length of a single cell is about 4.2 m to accommodate the survey requirement. The total arc length is about 63 m.

The TBA unit cell is designed according to the theoretical CSR-cancellation condition in a quasi-isochronous TBA [23], which is derived with only ss-CSR and linear transfer map of the lattice being considered. The dipole parameters are set at the aforementioned values. Between the dipoles, four families of quadrupoles are used to match the achromatic condition while adjusting m_{11}, m_{21}, and Twiss functions simultaneously. Specifically, in this design, the values of m_{11} and m_{21} are set to be −1.998 and −0.012, respectively, where we have used the accurate values of these two matrix elements derived using the accurate first-order transfer matrix of a sector dipole [24].

For the single cell, horizontal Twiss parameters at the TBA entrance, i.e., initial α_{x0} and β_{x0} are scanned in search of an optimal matching beam envelope for the orientation of a nonzero net CSR kick for a practical TBA, as mentioned in Ref. [10].

Although the theoretical condition in Ref. [23] reports a TBA with periodic optics, we further scan to find the optimal Twiss parameters for better CSR minimization in a practical cell instead of directly adopting the periodic optics solution. The TBA cell is tested using ELEGANT [34], employing the initial bunch parameters of a high-brightness beam listed in Table 1. For the case with ss-CSR and the first-order transfer map being considered, the relative normalized horizontal emittance growth $\Delta\varepsilon_n/\varepsilon_n$ is as low as 0.67% for a single TBA cell with periodic Twiss parameters of $\alpha_{x0} = 0$ and $\beta_{x0} = 4.96$ m, whereas it is found that $\Delta\varepsilon_n/\varepsilon_n$ can be further suppressed to 0.61% for a single TBA cell with the initial Twiss parameters of $\alpha_{x0} = 0.3$ and $\beta_{x0} = 1.3$ m, which are deviated from the periodic Twiss parameters. The TBA unit cell design is also tested with a transfer map up to the third order, with tr-CSR and dr-CSR included. The simulation results show that $\Delta\varepsilon_n/\varepsilon_n$ is suppressed to 1.52% with the aforementioned periodic Twiss parameters. And $\Delta\varepsilon_n/\varepsilon_n$ can be further suppressed to 1.38% with the initial Twiss parameters of $\alpha_{x0} = 0.4$ and $\beta_{x0} = 1$ m, which are also deviated from the periodic Twiss parameters and are different from the optimal Twiss parameters with ss-CSR and the first-order transfer map being considered.

Although the differences in $\Delta\varepsilon_n/\varepsilon_n$ seem tiny and the TBA single cell design is physically CSR-immune using all the abovementioned sets of Twiss parameters, the results somewhat indicate the dependence of the CSR-induced emittance growth on the lattice optic, as mentioned in Refs [10, 12, 26]. Moreover, the results indicate that $\Delta\varepsilon_n/\varepsilon_n$ is generally larger when the lattice nonlinear effects and tr-CSR and dr-CSR are included.

An arc design is obtained based on the TBA unit cell. The resulting schematic of the arc is shown in Figure 1. Considering the optics dependence of CSR-induced emittance suppression, in the following, we consider a practical single-pass transfer arc with non-periodic optics. To flexibly control the arc optics, for the in-between sections of the unit cells, two quadrupoles are used from cell-1~3 and three quadrupoles are used from cell-3~15. Moreover, two families of sextupoles are inserted between the dipoles in cell-2~15 the dipoles, which will not influence the linear lattice optics but will affect the high-order terms of the transfer map (e.g., T_{166}, T_{266}, and T_{566}) [31]. Such an arc will be adjusted and optimized in the following section with the full 1D CSR model and lattice nonlinear effects taken into account.

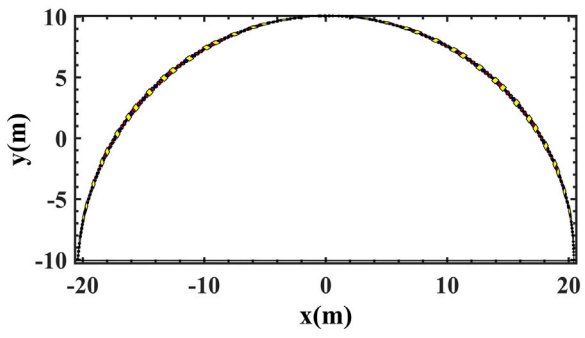

FIGURE 1
Schematic diagram of a multi-TBA-based 180-deg transport arc.

Optimization and results

For the sake of practical consideration, in this section, adjustments based on numerical scans and optimization of the TBA-based transport arc are performed considering full 1D CSR and the lattice transfer map up to the third order. Cell-by-cell adjustments based on numerical scans are first conducted and then multi-objective particle swarm optimization (MOPSO) of the adjusted arc design is performed.

First, the design setting of each TBA cell, i.e., $m_{11,i}$ and $m_{21,i}$ (where i represents the ith cell), and the corresponding optimal Twiss parameters are scanned based on the ELEGANT simulation results using the parameters listed in Table 1. In this step, the impact of lattice nonlinear effects together with tr-CSR and dr-CSR on linear optics settings is considered in the scans, while the high-order terms of the transfer map are not specially controlled. Only the quadrupoles and drifts are adjusted to change m_{11} and m_{21}. The sextupole strengths are coarsely tuned. Considering the impact of the aforementioned lattice nonlinear effects and tr-CSR and dr-CSR, the optimal design settings of the TBA cells might deviate from the theoretical result of a single unit cell. Moreover, the optimal Twiss parameters for each cell can be different considering that the bunch phase space distributions might have been changed under the influence of CSR and lattice nonlinear effects. Thus, the adjustments are conducted cell by cell. Specifically, we vary the settings of m_{11} and m_{21} for a certain cell in the vicinity of the theoretical result. For a specific setting of m_{11} and m_{21}, the optimal Twiss parameters are also scanned in search of the minimal $\Delta\varepsilon_n/\varepsilon_n$ value and relative bunch length variation $|\Delta\sigma_z/\sigma_z|$ (both values are obtained with ELEGANT simulations) that can be achieved for this setting of the cell.

In search of optimal $m_{11,i}$ and $m_{21,i}$ for each TBA cell, we scan the setting of m_{11} and m_{21} in the vicinity of the theoretical setting (denoted as $m_{11}^{\star}$ and $m_{21}^{\star}$ hereafter). Through a large number of tests, it is found that the optimal β_x function seems to be very sensitive to the variation in $m_{11,i}$; thus, a scan of optimal $m_{11,i}$ is conducted within a small range close to $m_{11}^{\star}$. The scanning range of $m_{11,i}/m_{11}^{\star}$ is set to be [0.99, 1.01] and the range of $m_{21,i}/m_{21}^{\star}$ is [0.95, 1.3], with the scanning steps all being 0.01. To find the optimal Twiss parameters (α_{xi} and β_{xi}) for each cell, for each setting of m_{11} and m_{21}, the scan of the initial Twiss parameters is conducted with α_{xi} ranging from 10 to 30 and β_{xi} ranging from 1 m to 20 m.

After the numerical scan of cell-1, the real bunch distribution can be obtained with ELEGANT. To proceed, using this distribution, the numerical scan of cell-2 is conducted. Similar processes are performed for the 15 cells. After such scans, an arc design is obtained (denoted as Solution-Scan hereafter). The ELEGANT simulation results of this design show that the final emittance at the arc exit is approximately 7.64 μm rad and the final bunch length is approximately 12.96 μm, i.e., $\Delta\varepsilon_n/\varepsilon_n$ and $|\Delta\sigma_z/\sigma_z|$ are approximately 6.64% and 13.6%, respectively. The scanning results show that the optimal $m_{11,i}$ for each cell is exactly the theoretical value $m_{11}^{\star}$. The optimal $m_{21,i}$ settings of the cells are different. For some cells, the scanned optimal $m_{21,i}$ deviates from

m_{21}^{*}, with the largest deviation being about 24%. It is noted that the obtained arc with the adjusted $m_{11,i}$ and $m_{21,i}$ may not yield a minimum total R_{56}. This is because the theoretical conditions of $\Delta\varepsilon_n = 0$ and $R_{56} = 0$ can be conflicting to some extent, as mentioned in Ref. [23]. Moreover, when the value of R_{56} is close to zero, the contributions of high-order longitudinal dispersion functions, e.g., T_{566} and U_{5666}, can become dominant. Thus, in the following optimization, $|\Delta\sigma_z/\sigma_z|$ is considered as a whole with first- and high-order longitudinal dispersion functions up to the third order being taken into account instead of simply pursuing $R_{56} = 0$.

It is found that the emittance growth of Solution-Scan is still large with a relatively large bunch length variation. This may result from the contributions of the lattice nonlinear effects, which can also give rise to emittance growth and bunch length variation [21, 31–33]. Moreover, CSR-induced energy spread can be distribution-dependent [28], which indicates that it might be very hard to suppress the emittance growth in the last few cells of the arc where the bunch distributions are distorted under the influence of CSR and lattice nonlinear effects. For example, $\Delta\varepsilon_n/\varepsilon_n$ of each cell is controlled below 1% for cell-1~5 and below 10% for cell-5~8. However, in the last seven cells, $\Delta\varepsilon_n/\varepsilon_n$ for each cell is generally close to 30%. So it seems that to obtain a minimum emittance growth of an arc comprised of multiple cells, it might be better to optimize the arc design as a whole compared to scanning and adjusting the arc cell by cell.

Second, to explore the possibility of finding an arc design scheme with minimized CSR-induced emittance growth, we adopted the widely used MOPSO [35] method to perform a global optimization of the arc. The MOPSO method is suitable for handling multi-objective optimization problems in the accelerator design (see, e.g., [36–39]). It provides a way to optimize a problem by iteratively improving the candidate solutions according to a criterion of the solution quality quantized as the "fitness value," which is also referred to as the "objective function". Each candidate is referred to as a particle that possesses a position in the n-dimensional space defined by n variables. Each particle moves randomly but is influenced by "pbest" and "gbest". "Pbest" represents the best fitness value the individual has hitherto achieved, and "gbest" represents the best fitness value that the whole group has experienced. The solutions are ranked in accordance with their fitness values. By adjusting the variables to a certain bounded range, the candidate solutions are updated iteratively while searching for optima [40–42].

For the optimization variables, considering the basic need for isochronicity and CSR-induced emittance suppression, the $m_{11,i}$ and $m_{21,i}$ are fixed to the scanned optimal values and only the in-between sections of the 15 cells are optimized. Specifically, the strengths of quadrupoles and lengths of drifts of the in-between sections are considered to be variables. The lengths of all quadrupoles are fixed to be 0.15 m. Apart from these, the strengths of the sextupoles inside the TBA cells are set to be variables with the lengths being fixed to 0.1 m. In addition, the initial Twiss parameters at the arc entrance, i.e., α_{x0}, β_{x0} and α_{y0}, β_{y0} are set to be variables. Totally, there are 126 variables, including 40 quadrupoles strengths, 28 sextupoles strengths, 54 drift lengths and four Twiss parameters. The corresponding setting is regarded as a seed in the optimization. All the 126 variables are adjusted within the preset ranges, e.g., the drift lengths range from 0.01 to 0.5 m, the strengths of quadrupoles vary within ±60 m^{-2}, and the strengths of the sextupoles vary within

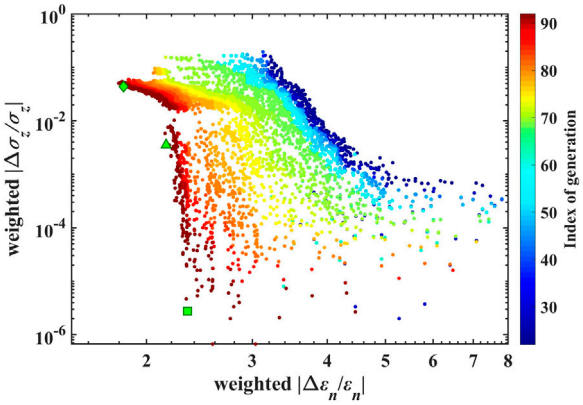

FIGURE 2
Convergence trend of the objective functions (weighted $|\Delta\varepsilon_n/\varepsilon_n|$ and weighted $|\Delta\sigma_z/\sigma_z|$ obtained with ELEGANT using the initial beam parameters of a high-brightness beam listed in Table 1) in the optimization of a 180-deg transport arc with tr-CSR, dr-CSR, and the lattice transfer map up to the third order being considered. Only the last 70 generations are shown in this figure. The solutions are marked using a green diamond, a triangle, and a square corresponding to Solution-OPT-I~III.

±3 × 10^3 m^{-3}. The initial Twiss parameters vary in the range of [−50, 50] for $\alpha_{x,y0}$ and [0.1 m, 100 m] for $\beta_{x,y0}$.

The two objective functions are set to be the absolute values of the following: the weighted relative CSR-induced emittance growth $\Delta\varepsilon_n/\varepsilon_n$ and the weighted relative bunch length variation $\Delta\sigma_z/\sigma_z$ obtained with ELEGANT using the initial bunch parameters listed in Table 1. By imposing constraints, the optimization is conducted with practical considerations. For example, the transverse $\beta_{x,y}$ functions along the arc are controlled to a reasonable range of 0.1–1,000 m, and the survey length of the arc is constrained to be approximately 40 m. If any of the constraints is violated during the optimization, the objective functions are multiplied by a factor larger than 1, which is referred to as the "weight factor." These weight factors are used to measure the degree that a specific variable setting accommodates for the optimization constraints [36–39].

By adding fluctuations to Solution-Scan, 600 initial seeds are generated and optimized. After evolving over 200 generations, the optimization results have become convergent, especially for those solutions with small relative emittance growths, e.g., $\Delta\varepsilon_n/\varepsilon_n < 2.4$. The last 70 generations are presented in Figure 2.

The figure shows that in the selected variable ranges, $|\Delta\sigma_z/\sigma_z|$ can be optimized to the order of 10^{-6}, while it seems that $|\Delta\varepsilon_n/\varepsilon_n|$ can only be minimized to approximately 1.8. As an illustration, three representative frontier solutions in the optimization are selected and compared in detail. The related comparisons and discussions are presented in the following section.

Comparison of the optimized ARC designs

In this section, we further look into the corresponding arc designs of several representative frontier solutions of the MOPSO with full 1D

TABLE 2 Horizontal and longitudinal dispersion functions of TBA arc designs.

Parameter (unit)	Solution-Scan	Solution-OPT-I	Solution-OPT-II	Solution-OPT-III
$\Delta\varepsilon_n/\varepsilon_n$	6.644	1.798	2.158	2.341
$\lvert\Delta\sigma_z/\sigma_z\rvert$ (%)	13.59	5.04	0.34	2.67×10^{-4}
R_{16} (m)	-1.151×10^{-7}	-2.570×10^{-8}	-3.435×10^{-8}	-3.654×10^{-8}
R_{26} (rad)	1.179×10^{-7}	-7.955×10^{-8}	-1.055×10^{-7}	-1.132×10^{-7}
T_{166} (m)	−0.039	−0.151	−0.156	0.137
T_{266} (rad)	−1.146	6.642×10^{-3}	0.158	0.160
T_{566} (m)	0.0998	0.0321	0.0109	0.0136
U_{5666} (m)	−0.508	−2.115	−1.675	−1.688

CSR and high-order terms of the lattice transfer map being considered. To clearly show the advancement of the optimized arc designs, the specific horizontal and longitudinal dispersion functions and parameters of the quadrupoles and sextupoles of the selected representative designs in MOPSO are compared with the design Solution-Scan. Then, MBI gains of the designs are compared, while the contribution of tr-CSR and dr-CSR is also discussed.

Three frontier solutions in the MOPSO results are selected (marked in Figure 2): one has a relatively small $\Delta\varepsilon_n/\varepsilon_n$ value which is approximately 1.8 (marked using a green diamond, denoted by Solution-OPT-I), one has a relatively small $|\Delta\sigma_z/\sigma_z|$ value (marked using a green square, denoted by Solution-OPT-III), and one is located between the two previous solutions (marked using a green triangle, denoted by Solution-OPT-II). In the following section, the corresponding arc designs of the three solutions are carefully compared with Solution-Scan.

Comparison of the horizontal and longitudinal dispersion functions

The related horizontal and longitudinal dispersion functions of Solution-Scan and Solution-OPT-I~III are listed in Table 2. The R_{56} values of these designs are all same, i.e., 2.923×10^{-3} m. Thus, they are not specifically listed in the table.

The optimized arc designs of Solution-OPT-I~III generally yield smaller $\Delta\varepsilon_n/\varepsilon_n$ and $|\Delta\sigma_z/\sigma_z|$ values than those of Solution-Scan, which may be the result of the mitigation of the high-order dispersion effects. Table 2 shows that compared with Solution-Scan, the optimized arc designs of Solution-OPT-I~III yield relatively small second-order horizontal and longitudinal dispersion functions, i.e., T_{166}, T_{266}, and T_{566}. As mentioned previously, the aberrations caused by leaking of transverse dispersion can lead to emittance growth [21, 31–33]. Furthermore, high-order longitudinal dispersions can result in bunch length variation [21, 23].

Then, we focus on Solution I~III. Table 2 indicates that the emittance growth of a certain design is related to second-order horizontal dispersion functions, while the bunch length variation is related to high-order longitudinal dispersion functions. For Solution-OPT-I with the smallest $\Delta\varepsilon_n/\varepsilon_n$ value among the three solutions, T_{166} and T_{266} are lower than the other two solutions, especially for T_{266}, which is two orders of magnitude lower. For Solution-OPT-II and -III with smaller $|\Delta\sigma_z/\sigma_z|$ values, T_{566} and U_{5666} values are smaller than those of Solution-OPT-I.

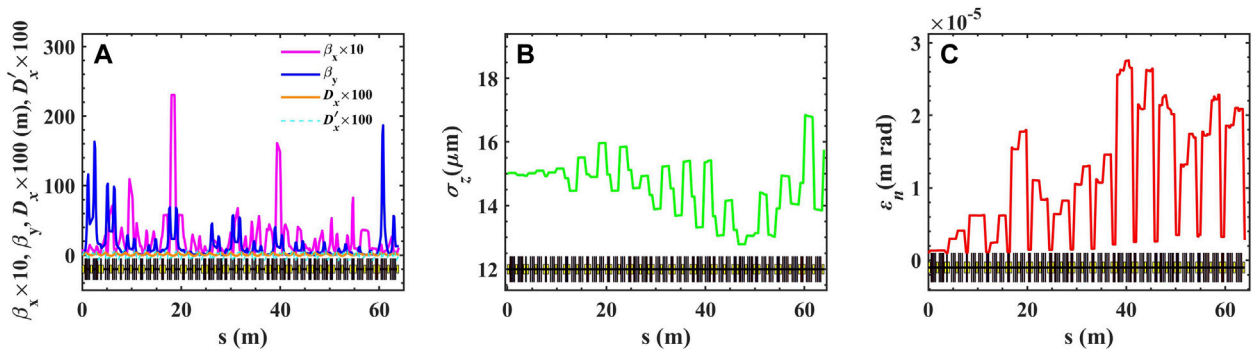

FIGURE 3
Simulation results of the related parameters along the corresponding arc of Solution-OPT-I considering full 1D CSR model and the lattice transfer map up to the third order: **(A)** optics functions; **(B)** bunch length; **(C)** normalized horizontal emittance. The results are obtained with ELEGANT using the high-brightness beam parameters listed in Table 1.

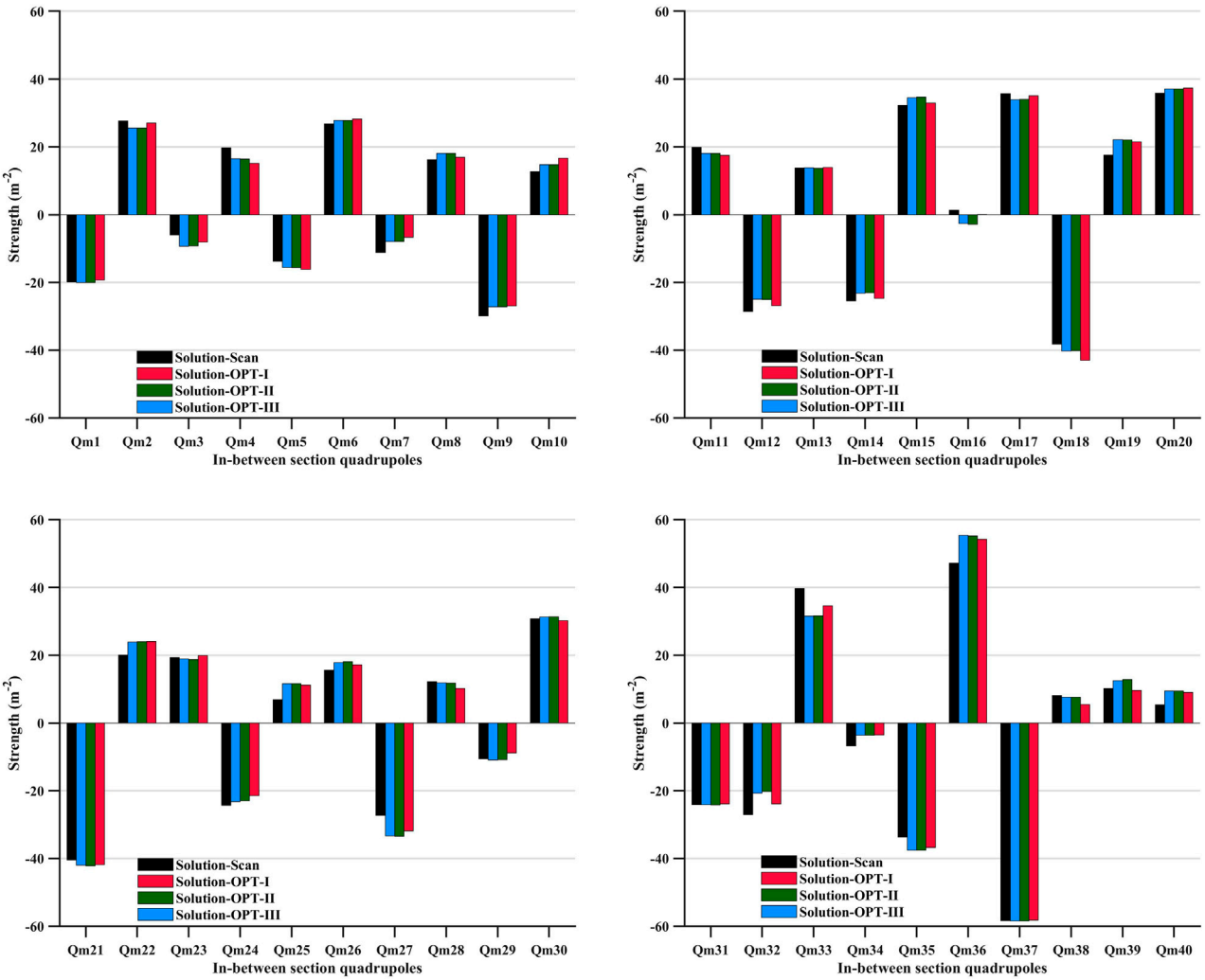

FIGURE 4
Comparison of the strengths of 40 quadrupoles in the in-between section of Solution-Scan and Solution-OPT-I ~III.

In Figure 3, the ELEGANT simulation results of optics functions, bunch lengths, and the normalized horizontal emittance along the corresponding arc of Solution-OPT-I are presented as an example.

Comparison of lattice element parameters

For Solution-Scan and Solution-OPT-I~III, we compare the strengths of 40 quadrupoles in the in-between sections and the strengths of 28 sextupoles in the TBA cells. For Solution-Scan, the sextupoles are not specially adjusted; thus, they are not included in the comparison. The results are shown in Figures 4, 5, respectively.

It appears that the strengths of 40 quadrupoles are not notably different except for Qm-16 (in the section between cell-5 and cell-6) and Qm-33 (in the section between cell-11 and cell-12), which indicates that first-order transfer maps of the four solutions are close to each other. However, it seems that the strengths of 28 sextupoles of Solution-OPT-I~III are different. Specifically, the sextupole strengths in Solution-OPT-I are remarkably different from those in Solution-OPT-II and -III. Some of the sextupoles in Solution-OPT-I even have opposite signs compared with those in Solution-OPT-II and -III, which are as follows: S-1 (in cell-2), S-11 and S-12 (in cell-7), S-13 and S-14 (in cell-8), and S-25 (in cell-14) (six of 28 sextupoles). This means that some of the focusing sextupoles change to defocusing sextupoles (or *vice versa*) in Solution-OPT-I compared with Solution-OPT-II and -III, which may result in differences between horizontal and longitudinal dispersion functions, as listed in Table 2.

Comparison of the MBI gains

The MBI gains of Solution-Scan and Solution-OPT-I~III are compared using the semi-analytical tool Volterra [17, 19], and the results are shown in Figure 6. The results indicate that the CSR-

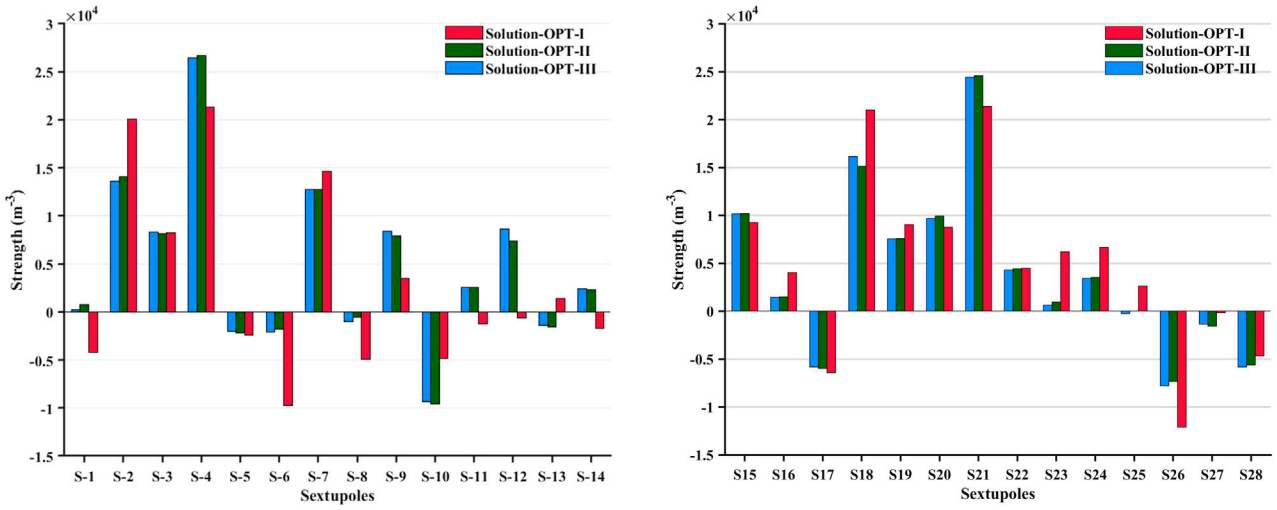

FIGURE 5
Comparison of the strengths of 28 sextupoles in Solution-OPT-I ~III.

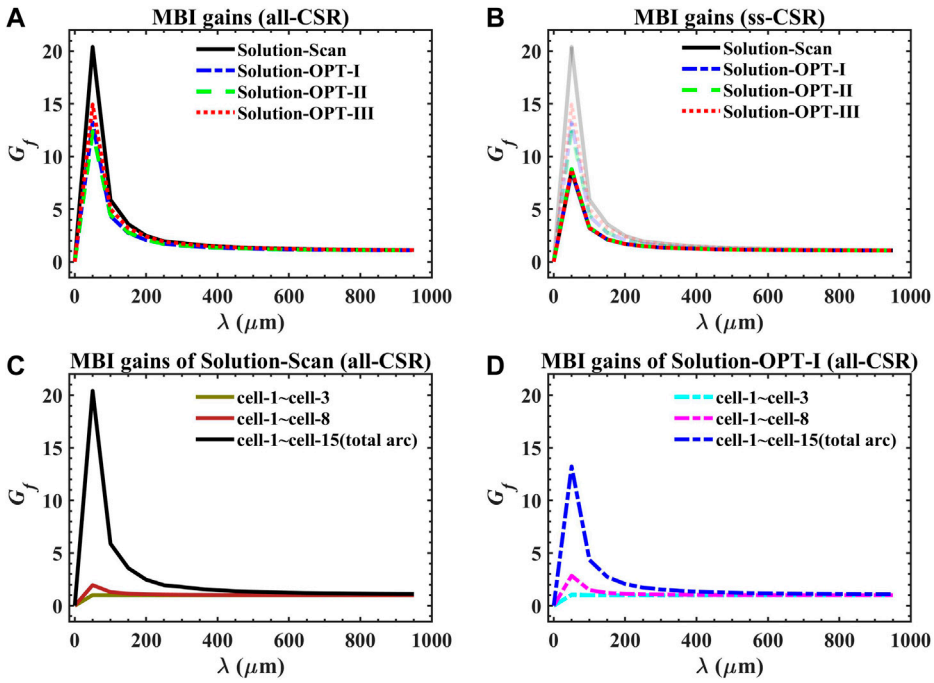

FIGURE 6
MBI gains of Solution-Scan and Solution-OPT-I ~III under different conditions **(A)** all-CSR considered; **(B)** only ss-CSR considered (the results with all-CSR considered are shown together, but light colored); **(C)** The MBI gains of cell-1~cell-3, cell-3~cell-8 and the total arc of Solution-Scan with all-CSR considered; **(D)** The MBI gains of cell-1~cell-3, cell-3~cell-8 and the total arc of Solution-OPT-I with all-CSR considered.

induced emittance growth at the exit of the arc might be correlated with the MBI gain. This can be understood through the CSR suppression condition proposed in Ref. [23], which is based on the assumption of the Gaussian bunch distribution. If the bunch distribution is no longer Gaussian, such a condition may not correspond to the minimized CSR-induced emittance growth and even lose efficacy. This suggests that the MBI gain might serve as an *indicator* that shows the degree of longitudinal phase space distortion [18, 19].

As can be seen from Figure 6A, compared with Solution-Scan, CSR-induced MBI gains are suppressed for Solution-OPT-I~III, which indicates the mitigation of the MBI effects. Moreover, Figure 6C and Figure 6D show that the MBI effect becomes more significant as the

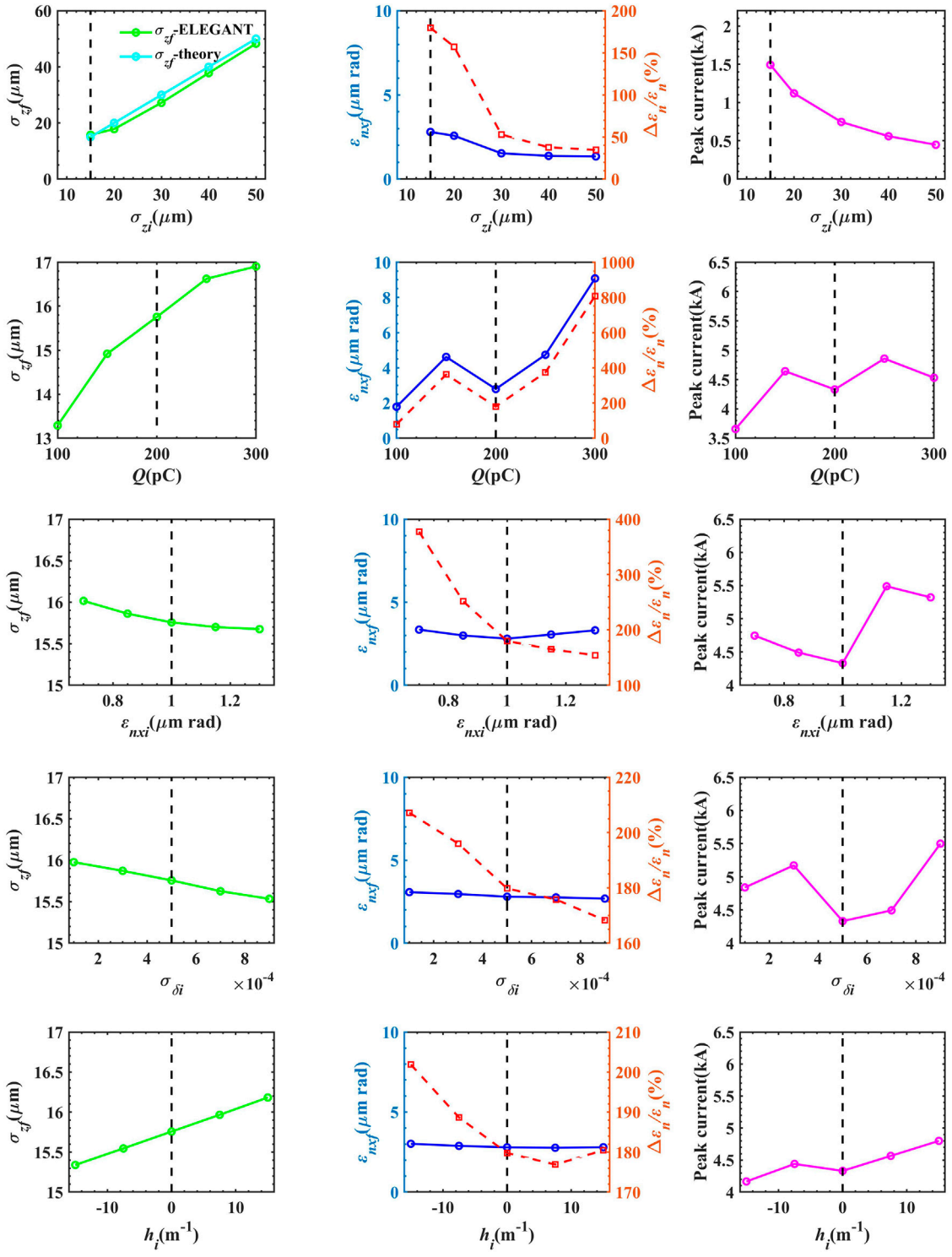

FIGURE 7
Results of the sensitivity tests of the dependence of σ_{zf}, ε_{nxf}, and $\Delta\varepsilon_n/\varepsilon_n$ and the peak current on the initial bunch parameters of the corresponding arc of Solution-OPT-I.

bunch passes through more cells, which indicates that the longitudinal phase space distribution is distorted more significantly. Thus, in the last few cells in the arc, it might be more difficult to preserve the emittance for such a distorted bunch.

We further look into the MBI gains of the designs with only ss-CSR included. It is found that tr-CSR and dr-CSR significantly contribute to MBI gain for a certain arc design, as mentioned in Ref. [18]. As can be seen from Figure 6B, MBI gains for Solution-Scan and Solution-OPT-

I~III are very close to each other with only ss-CSR being considered [which are overlapped in Figure 6B], and they are notably lower than the case with tr-CSR and dr-CSR being included.

Initial bunch parameter sensitivity tests

To identify the range of parameters that allows feasibility of such an arc for transporting a high-brightness beam, in this section, the sensitivity tests on the initial bunch parameters are conducted for the corresponding arc designs of Solution-OPT-I as an example. The initial bunch parameters vary in the ranges close to the parameters listed in Table 1. The test results show that the emittance growth of this design is not sensitive to the initial uncorrelated energy spread or energy chirp. Nevertheless, the emittance growth is closely related to the initial bunch length, bunch charge, and initial bunch emittance.

The results of univariate tests on the relevant input beam parameters (i.e., initial bunch length σ_{zi}, bunch charge Q, initial horizontal emittance ε_{nxi}, initial uncorrelated energy spread $\sigma_{\delta i}$, and energy chirp h_i) are shown in Figure 7.

As can be seen from the figures, σ_{zf} and ε_{nxf} are not sensitive to $\sigma_{\delta i}$ or h_i, with the largest difference of $\Delta\varepsilon_n/\varepsilon_n$ being below 40% when varying $\sigma_{\delta i}$ in the range of $[0, 1 \times 10^{-3}]$ and h_i in the range of $[-15\ \mathrm{m}^{-1}, 15\ \mathrm{m}^{-1}]$. It is noted that insensitivity to h_i is important, as a compressed bunch typically has an energy chirp. If isochronicity is not satisfactorily guaranteed, the bunch length of a chirped bunch will have a significant variation, which might couple with the CSR effect and result in severe bunch quality degradation [6, 23].

Nevertheless, it appears that the emittance growth of this design changes significantly with the varying σ_{zi}, Q, and ε_{nxi} values. Specifically, the $\Delta\varepsilon_n/\varepsilon_n$ value becomes larger when the σ_{zi} value is smaller, Q value is larger, and ε_{nxi} value is smaller. The reason is that the CSR-induced rms energy spread σ_{CSR} has scale relationships with σ_{zi} and Q as $\sigma_{CSR} \propto \sigma_{zi}^{-4/3}$ and $\sigma_{CSR} \propto Q$ [8, 29, 30]. Thus, the σ_{CSR} value becomes larger when the σ_{zi} value becomes smaller and the Q value becomes larger, which also indicates more significant CSR effects. In addition, a bunch with a smaller ε_{nxi} value indicates that the horizontal bunch size is smaller for the same initial Twiss parameters, which might give rise to stronger CSR effects.

Conclusion and discussion

In this study, based on the theoretical CSR-cancellation condition of a quasi-isochronous TBA cell proposed in Ref. [23], the design and optimization of a TBA-based 180-deg transport arc is presented. The optimal design setting of $m_{11,i}$ and $m_{21,i}$ for each cell is first scanned, and the optics along the arc are adjusted. The scanning results indicate that the optimal $m_{11,i}$ values are close to the theoretical value in Ref. [23], while $m_{21,i}$ values show relatively large deviations when a full 1D CSR model and a high-order lattice transfer map are considered. The optimal Twiss parameters of each cell are different and deviated from the periodic optics functions.

Then, the arc is optimized by adopting the MOPSO method, aiming at suppressing the CSR-induced emittance growth and avoiding bunch length variation simultaneously. The optimization results show that in the selected variable ranges, for a high-brightness beam with parameters of 1 GeV, 200 pC, 15 μm, and 1 μm rad, the final emittance can be controlled to approximately 2.8 μm rad ($\Delta\varepsilon_n/\varepsilon_n \sim 1.8$) and $|\Delta\sigma_z/\sigma_z|$ can be suppressed to about 5%. Moreover, it has been tested that the obtained arc design is not sensitive to the initial uncorrelated energy spread or energy chirp, which is suitable for transporting a high-brightness beam that typically has an energy chirp. In addition, such a TBA-based 180-deg transport arc can serve as a turnaround arc in ERL-based facilities. It has been tested that for a typical initial beam with parameters of 100 pC, 600 μm, and 0.5 μm rad, the $\Delta\varepsilon_n/\varepsilon_n$ value is below 1% and the bunch length remains almost unchanged. In addition, the obtained arc has a compact footprint, with the survey length being approximately 40 m.

It is found that in our tests, the CSR-induced emittance growth and MBI gain are correlated to some extent. Particularly, for the last few cells in the arc, an exploded MBI gain often indicates a severely distorted longitudinal phase space distribution of the bunch [18, 19]. The theoretical CSR-cancellation condition may not work well or even lose efficacy for such a distorted bunch, and hence, the arc design may yield an imperfectly canceled or even uncontrollable emittance growth. This gives us a hint that simply pursuing CSR-induced emittance growth suppression might not be an effective way to obtain optimal design schemes. Instead, emittance growth and MBI gain suppression should be considered comprehensively. For example, MBI gain can be adopted as a weight factor in the MOPSO of the CSR-induced emittance growth.

The design strategy and numerical scans and optimization processes presented in this paper may hopefully serve as a starting point for designing a compact transport arc. Future research could continue to explore the possibility of further global optimization, with the CSR-induced emittance growth and MBI gain suppression being considered comprehensively.

Also, it is noted that the suppression conditions of the CSR-induced emittance growth and MBI effects can be different, i.e., a certain design with suppressed MBI gain does not definitely ensure a suppressed CSR-induced emittance growth and *vice versa* [18]. It can be a rather complex problem to take both issues into account. And such problem may only be optimized through numerical optimizations. First, high-order longitudinal dispersion functions can make a contribution to the MBI gain [18, 19]. Apart from R_{56}, z can be correlated with δ through high-order longitudinal dispersion functions, which can also distort the bunch longitudinal phase space distribution [18, 21, 23]. Moreover, the MBI suppression condition can be related to the Twiss parameters (see, e.g., Ref. [18]). This means that the requirements of suppressing the CSR-induced emittance growth and MBI gain might conflict with each other. In addition, as illustrated previously, tr-CSR and dr-CSR can have a significant impact on the MBI gain [18].

Apart from this, optimized design schemes can be further explored to mitigate the lattice nonlinear effects. For example, multi-poles can be adopted in cells (e.g., sextupoles [21] and octupoles [43]). Moreover, further global optimizations based on the parameter ranges of actual hardware and start-to-end simulations are worthy of being studied further. Following similar designs and numerical scans and optimization processes as presented in this paper, it would be feasible to achieve optimized practical arc design schemes.

Data availability statement

The raw data supporting the conclusion of this article will be made available by the authors, without undue reservation.

Author contributions

CZ: conceptualization, methodology, visualization, software, investigation, data curation, formal analysis, and writing—original draft. YJ: validation, resources, writing—review and editing, and supervision. All authors contributed to the article and approved the submitted version.

Funding

This work was supported by the National Natural Science Foundation of China (Nos 11922512 and 12275284) and the Youth Innovation Promotion Association of Chinese Academy of Sciences (No. Y201904).

Conflict of interest

The authors declare that the research was conducted in the absence of any commercial or financial relationships that could be construed as a potential conflict of interest.

Publisher's note

References

1. Pellegrini C. The history of X-ray free-electron lasers. *EPJ H* (2021) 37:659–708. doi:10.1140/epjh/e2012-20064-5

2. Ackermann W, Asova G, Ayvazyan V, Azima A, Baboi N, Bähr J, et al. Operation of a free-electron laser from the extreme ultraviolet to the water window. *Nat Photon* (2007) 1:336–42. doi:10.1038/nphoton.2007.76

3. Emma P, Akre R, Arthur J, Bionta R, Bostedt C, Bozek J, et al. First lasing and operation of an ångstrom-wavelength free-electron laser. *Nat Photon* (2010) 4:641–7. doi:10.1038/nphoton.2010.176

4. Ishikawa T, Aoyagi H, Asaka T, Asano Y, Azumi N, Bizen T, et al. A compact x-ray free-electron laser emitting in the sub-Ångstr′om region. *Nat Photon* (2012) 6:540–4. doi:10.1038/nphoton.2012.141

5. Schneidmiller E, Vogel V, Weise H, Yurkov M. Potential of the FLASH free electron laser technology for the construction of a kW-scale light source for next-generation lithography. *J Micro-nanolithography Mems Moems* (2012) 11:021122–1. doi:10.1117/1.JMM.11.2.021122

6. Akkermans JAG, Di Mitri S, Douglas D, Setija ID. Compact compressive arc and beam switchyard for energy recovery linac-driven ultraviolet free electron lasers. *Phys Rev Accel Beams* (2017) 20(8):080705. doi:10.1103/PhysRevAccelBeams.20.080705

7. Di Mitri S, Spampinati S. Microbunching instability study in a linac-driven free electron laser spreader beam line. *Phys Rev Accel Beams* (2017) 20(12):120701. doi:10.1103/PhysRevAccelBeams.20.120701

8. Derbenev YS, Rossbach J, Saldin EL, Shiltsev VD. *Microbunch radiative tail-head interaction, DESY, Hamburg, Germany*. Rep. TESLA-FEL 95-05 (1995). doi:10.3204/PUBDB-2018-04128

9. Hajima R. A first-order matrix approach to the analysis of electron beam emittance growth caused by coherent synchrotron radiation. *Jpn J Appl Phys* (2003) 42:L974–6. doi:10.1143/JJAP.42.L974

10. Hajima R. Emittance compensation in a return arc of an energy-recovery linac. *Nucl Instrum Methods Phys Res Sect A* (2004) 528(1–2):335–9. doi:10.1016/j.nima.2004.04.063

11. Di Mitri S, Cornacchia M, Spampinati S. Cancellation of coherent synchrotron radiation kicks with optics balance. *Phys Rev Lett* (2013) 110:014801. doi:10.1103/PhysRevLett.110.014801

12. Jiao Y, Cui X, Huang X, Xu G. Generic conditions for suppressing the coherent synchrotron radiation induced emittance growth in a two-dipole achromat. *Phys Rev ST Accel Beams* (2014) 17:060701. doi:10.1103/PhysRevSTAB.17.060701

13. Di Mitri S, Cornacchia M. Transverse emittance-preserving arc compressor for high-brightness electron beam-based light sources and colliders. *Europhys Lett* (2015) 109:62002. doi:10.1209/0295-5075/109/62002

14. Heifets S, Stupakov G, "Beam instability and microbunching due to coherent synchrotron radiation", in *Proc.19th IEEE particle accelerator conference* (PAC 2001), Chicago, Illinois, 18–22. 2001, paper TPPH081, pp.1856-1858.

15. Huang Z, Kim K-J. Formulas for coherent synchrotron radiation microbunching in a bunch compressor chicane. *Phys Rev Accel Beams* (2002) 5:074401. doi:10.1103/PhysRevSTAB.5.074401

16. Venturini M. Microbunching instability in single-pass systems using a direct two-dimensional Vlasov solver. *Phys Rev Accel Beams* (2007) 10:104401. doi:10.1103/PhysRevSTAB.10.104401

17. Tsai C-Y, Douglas D, Li R, Tennant C. Linear microbunching analysis for recirculation machines. *Phys Rev Accel Beams* (2016) 19:114401. doi:10.1103/PhysRevAccelBeams.19.114401

18. Tsai C-Y, Di Mitri S, Douglas D, Li R, Tennant C. Conditions for coherent-synchrotron-radiation-induced microbunching suppression in multibend beam transport or recirculation arcs. *Phys Rev Accel Beams* (2017) 20:024401. doi:10.1103/PhysRevAccelBeams.20.024401

19. Tsai C-Y, Derbenev YS, Douglas D, Li R, Tennant C. Vlasov analysis of microbunching instability for magnetized beams. *Phys Rev Accel Beams* (2017) 20:054401. doi:10.1103/PhysRevAccelBeams.20.054401

20. England RJ, Rosenzweig JB, Andonian G, Musumeci P, Travish G, Yoder R. Sextupole correction of the longitudinal transport of relativistic beams in dispersionless translating sections. *Phys Rev ST Accel Beams* (2005) 8:012801. doi:10.1103/PhysRevSTAB.8.012801

21. Charles TK, Paganin DM, Latina A, Boland MJ, Dowd RT. Current-horn suppression for reduced coherent-synchrotron-radiation-induced emittance growth in strong bunch compression. *Phys Rev Accel Beams* (2017) 20(3):030705. doi:10.1103/PhysRevAccelBeams.20.030705

22. Venturini M. Design of a triple-bend isochronous achromat with minimum coherent-synchrotron-radiation-induced emittance growth. *Phys Rev Accel Beams* (2016) 19(6):064401. doi:10.1103/PhysRevAccelBeams.19.064401

23. Zhang C, Jiao Y, Tsai C-Y. Quasi-isochronous triple-bend achromat with periodic stable optics and negligible coherent-synchrotron-radiation effects. *Phys Rev Accel Beams* (2021) 24:060701. doi:10.1103/PhysRevAccelBeams.24.060701

24. Zhang C, Jiao Y, Tsai C-Y, "Theoretical analysis of the conditions for an isochronous and CSR-immune triple-bend achromat with stable optics", in *Proceedings of the 12th international particle accelerator conference (IPAC 2022)*, Campinas, SP, Brazil (JACOW, Geneva, Switzerland, 2022), pp. 786–9.

25. Douglas DR, Benson SV, Li R, Roblin Y, Tennant CD, Krafft GA, et al. "Control of synchrotron radiation effects during recirculation with bunch compression", in *Proceedings of the 6th international particle accelerator conference* (IPAC 20215, Richmond, VA, USA (JACOW, Geneva, Switzerland, 2015), pp. 1910–2.

26. Di Mitri S. Feasibility study of a periodic arc compressor in the presence of coherent synchrotron radiation. *Nucl Instrum Methods Phys Res Sect A* (2016) 806:184–92. doi:10.1016/j.nima.2015.10.015

27. Zhang C, Jiao Y, Liu W, Tsai C-Y. Suppression of the coherent synchrotron radiation induced emittance growth in a double-bend achromat with bunch compression. *Phys Rev Accel Beams* (2023). (Accepted).

28. Shimada M, Yokoya K, Suwada T, Enomoto A. Lattice and beam optics design for suppression of CSR-induced emittance growth at the KEK-ERL test facility. *Nucl Instrum Methods Phys Res Sect A* (2007) 575:315–20. doi:10.1016/j.nima.2007.02.095

29. Stupakov G, Emma P. *CSR wake for a short magnet in ultra-relativistic limit"* Proceedings of the EPAC (2002). p. 1479–81. doi:10.2172/799089

30. Khan DZ, Raubenheimer TO. Approximated expressions for the coherent synchrotron radiation effect in various accelerator scenarios. *Phys Rev Accel Beams* (2021) 24(8):080701. doi:10.1103/PhysRevAccelBeams.24.080701

31. Björklund Svensson J, Charles TK, Lundh O, Thorin S. Third-order double-achromat bunch compressors for broadband beams. *Phys Rev Accel Beams* (2019) 22(10):104401. doi:10.1103/PhysRevAccelBeams.22.104401

32. Sun Y. Second-order achromat design based on FODO cell. *Phys Rev ST Accel Beams* (2011) 14(6):060703. doi:10.1103/PhysRevSTAB.14.060703

33. Lindstrøm CA, Adli E. Design of general apochromatic drift-quadrupole beam lines. *Phys Rev Accel Beams* (2016) 19(7):071002. doi:10.1103/PhysRevAccelBeams.19.071002

34. Borland M. Simple method for particle tracking with coherent synchrotron radiation. *Phys Rev ST Accel Beams* (2001) 4(7):070701. doi:10.1103/PhysRevSTAB.4.070701

35. Coello Coello CA, Lechuga MS. Mopso: A proposal for multiple objective particle swarm optimization. In: *Proc. 2002 congress on evolutionary computation (CEC'02)*. Honolulu, HI, USA (2002). p. 1051–6. doi:10.1109/CEC.2002.1004388

36. Pang X, Rybarcyk LJ. Multi-objective particle swarm and genetic algorithm for the optimization of the LANSCE linac operation. *Nucl Instrum Methods Phys Res Sect A* (2014) 741:124–9. doi:10.1016/j.nima.2013.12.042

37. Huang X, Safranek J. Nonlinear dynamics optimization with particle swarm and genetic algorithms for SPEAR3 emittance upgrade. *Nucl Instrum Methods Phys Res Sect A* (2014) 757:48–53. doi:10.1016/j.nima.2014.04.078

38. Jiao Y, Xu G. Optimizing the lattice design of a diffraction-limited storage ring with a rational combination of particle swarm and genetic algorithms. *Chin Phys C* (2017) 41(2):027001. doi:10.1088/1674-1137/41/2/027001

39. Xu J, Yang P, Liu G, Bai Z, Li W. Constraint handling in constrained optimization of a storage ring multi-bend-achromat lattice. *Nucl Instrum Methods Phys Res Sect A* (2020) 988:164890. doi:10.1016/j.nima.2020.164890

40. Akbari R, Ziarati K. A rank based particle swarm optimization algorithm with dynamic adaptation. *J Comput Appl Math* (2011) 235(8):2694–714. doi:10.1016/j.cam.2010.11.021

41. Li J, Feikes J, Goslawski P, Ries M, "Particle swarm optimization algorithm applied in online commissioning at the MLS and BESSY II", in *Proceedings of the 8th international particle accelerator conference (IPAC 2017)*, Copenhagen, Denmark (JACOW, Geneva, Switzerland, 2017), pp. 3700–3.

42. Tharwat A, Schenck W. A conceptual and practical comparison of PSO-style optimization algorithms. *Expert Syst Appl* (2021) 167:114430. doi:10.1016/j.eswa.2020.114430

43. Sudar N, Nosochkov Y, Bane K, Zhang Z, Ding Y. Octupole based current horn suppression in multistage bunch compression with emittance growth correction. *Phys Rev Accel Beams* (2020) 23(11):112802. doi:10.1103/PhysRevAccelBeams.23.112802

frontiers | Frontiers in Physics

TYPE Review
PUBLISHED 25 May 2023
DOI 10.3389/fphy.2023.1172368

OPEN ACCESS

EDITED BY
Sam Vinko,
University of Oxford, United Kingdom

REVIEWED BY
Markus Kuster,
European X-Ray Free Electron Laser, Germany
Enrico Allaria,
Elettra Sincrotrone Trieste, Italy

*CORRESPONDENCE
Haixiao Deng,
denghx@sari.ac.cn
Bo Liu,
bo.liu@zjlab.org.cn

RECEIVED 23 February 2023
ACCEPTED 12 May 2023
PUBLISHED 25 May 2023

CITATION
Liu T, Huang N, Yang H, Qi Z, Zhang K, Gao Z, Chen S, Feng C, Zhang W, Luo H, Fu X, Liu H, Faatz B, Deng H, Liu B, Wang D and Zhao Z (2023), Status and future of the soft X-ray free-electron laser beamline at the SHINE.
Front. Phys. 11:1172368.
doi: 10.3389/fphy.2023.1172368

Status and future of the soft X-ray free-electron laser beamline at the SHINE

Tao Liu[1], Nanshun Huang[2], Hanxiang Yang[3], Zheng Qi[1], Kaiqing Zhang[1], Zhangfeng Gao[1], Si Chen[1], Chao Feng[1], Wei Zhang[1], Hang Luo[1], Xiaoxi Fu[1], He Liu[3], Bart Faatz[1], Haixiao Deng[1]*, Bo Liu[1]*, Dong Wang[1] and Zhentang Zhao[1]

[1]Shanghai Advanced Research Institute, Chinese Academy of Sciences, Shanghai, China, [2]Zhangjiang Lab, Chinese Academy of Sciences, Shanghai, China, [3]University of Chinese Academy of Sciences, Beijing, China

The Shanghai High repetition rate XFEL and Extreme light facility (SHINE) is under construction and aims at generating X-rays between 0.4 and 25 keV with three FEL beamlines at repetition rates of up to 1 MHz. The soft X-ray FEL beamline, FEL-II, will be ready for commissioning in 2025. It is designed to cover the photon energy from 0.4 to 3 keV, in which the baselines of the FEL operation modes are self-amplified spontaneous emission (SASE), self-seeding, echo-enabled harmonic generation (EEHG), and polarization control. Therefore, a high repetition-rate external seed laser, large period length modulator, soft X-ray monochromator, planar undulator, and elliptically polarized undulator have been adopted in the FEL-II beamline. Several potentials such as an ultra-short pulse mode and a multi-color mode are also foreseeable without significant equipment changes in the follow-up operation. A dual-period undulator design is suggested for the echo-enabled harmonic generation (EEHG) commissioning, and it has great potential to break through the unreachable energy of the fully coherent X-ray in the future. The FEL-II beamline will deliver SASE radiation and fully coherent radiation in all the wavelengths of interest.

KEYWORDS

SHINE, FEL, x-ray, SASE, self-seeding, external seeding, harmonic lasing, polarization

1 Introduction

Free-electron lasers (FELs) [1] hold a great capability to generate high intensity, ultra-short, tunable coherent radiation pulses [2, 3], opening up new frontiers of ultra-fast and ultra-small science at atomic length scales [4–6]. High gain FELs have been in operation for users with the great success of several operational facilities around the world, such as FLASH [7], LCLS [8], SACLA [9], FERMI [10], PAL-XFEL [11], European-XFEL ([12]), SwissFEL [13], and SXFEL [14, 15]. The spectral range of these FEL facilities is usually operating in the X-ray regime, which basically chooses self-amplified spontaneous emission (SASE) [16, 17] and external/self-seeding FELs [18–23] as the baseline operation modes. A SASE FEL has the advantages of a simple setup, technological maturity, and excellent transverse coherence, while it typically lacks temporal coherence. External/self-seeding FELs perfectly respond to the problem and provide nearly Fourier-transform limited pulses in the X-ray regime, which mainly includes high-gain harmonic generation (HGHG) [18, 19, 24], echo-enabled harmonic generation (EEHG) [20, 21, 25–30], and soft and hard X-ray self-seedings [22,

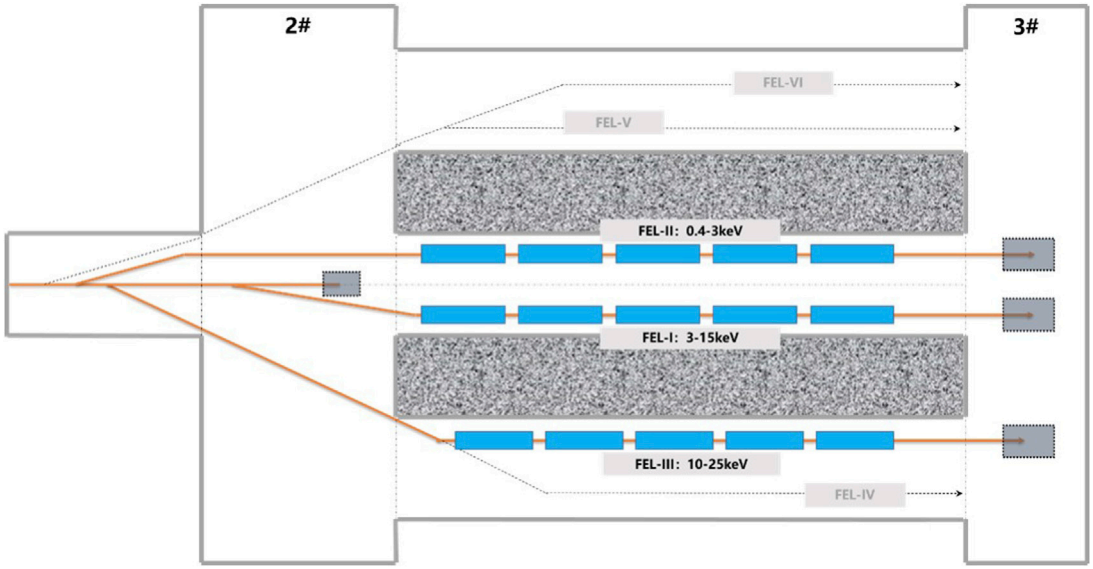

FIGURE 1
Layout of the undulator system at the SHINE (top view). The undulator system, which is 400 m in total length in the underground tunnel, is located between the upstream switchyard system (shaft 2#) and the downstream beam dump beamline (shaft 3#). The FEL-I and FEL-II beamlines are in the same tunnel, while the FEL-III is in the other tunnel. The blue boxes are undulator sketches and the grey area denotes a concrete wall. Some areas are reserved for facility development in the future.

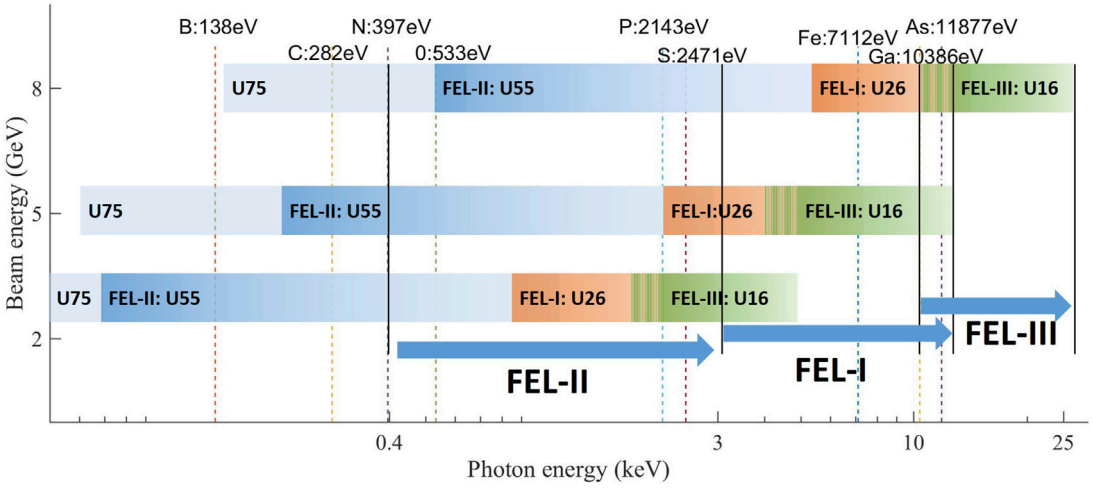

FIGURE 2
Photon energy coverage of the three undulator beamlines at the SHINE with the nominal beam parameter at the beam energy of 3 GeV, 5 GeV, and 8 GeV, respectively.

23, 31–36]. To further extend the FEL output performance and increase the flexibility of FEL facilities, more advanced FEL modes, such as cascading seeding, the fresh bunch technique, and polarization control have been demonstrated in FEL facilities and supported FEL user experiments.

The Shanghai High repetition rate XFEL and Extreme light facility, abbreviated as SHINE, aims to join the exclusive XFEL club as one of the most advanced user facilities by delivering femtosecond X-ray pulses with up to one million pulses per second. The SHINE is designed to deliver photons between 0.4 keV and 25 keV at a repetition rate as high as 1 MHz using a superconducting linear accelerator (LINAC) [37]. It consists of an 8 GeV CW superconducting RF Linac, 3 undulator beamlines, 3 X-ray beamlines, and 10 experimental stations in phase-I, and started its construction in April 2018. In this article, we briefly describe the three undulator beamline scheme designs shown in Figure 1, and mainly focus on the soft X-ray FEL beamline, i.e., FEL-II with several advanced FEL operation modes and a flexible schematic design.

In front of the undulator beamlines at the SHINE, the nominal electron beam properties are as follows: the maximum electron beam energy is 8 GeV, the peak current is approximately 1500 A with a bunch charge of 100 pC, the normalized transverse emittance is 0.4–0.5 mm·mrad, the sliced energy spread is approximately 0.01%, and the maximum repetition rate is up to 1 MHz. For each undulator beamline of the SHINE, the photon energy coverage with different operating beam energies is presented in Figure 2. There are two hard X-ray FEL beamlines, FEL-I and FEL-III.

The FEL-I is designed to cover the photon energy range of 3–15 keV. The baseline FEL operation modes are SASE and self-seeding with horizontal polarization, in which the normal planar undulator with a 26 mm undulator period, 1.05 T maximum magnetic peak field, and a 4 m segment length will be used. The output FEL photon is approximately $1 \times 10^{10} - 5 \times 10^{11}$ per pulse with a pulse duration of ~30 fs (FWHM) and up to a 1 MHz repetition rate and will be delivered to the end-stations, including the Hard X-ray Scattering and Spectroscopy End-station (HSS), the Coherent Diffraction End-station for Single Molecules and Particles (CDS), and the Station of Extreme Light (SEL).

The FEL-III is designed to cover the photon energy range of 10–25 keV, in which the superconducting planar undulator (vertical) with a 16 mm undulator period, 1.583 T maximum magnetic peak field, and a 4 m segment length is the first option. The baseline FEL modes of the FEL-III are SASE and hard X-ray self-seeding. It is a challenging task to develop a 4 m-length superconducting undulator with a maximum 1.583 T magnetic peak field. Hence, the alternative scheme design of the FEL-III that adopts an in-vacuum undulator with a 16 mm period length (IVU16) is also on standby to support FEL performance with a maximum 1.25 T magnetic peak field. The output FEL photon is approximately $2 \times 10^{9} - 8 \times 10^{10}$ with a pulse duration of ~30 fs (FWHM) and a repetition rate of up to 0.1 MHz, and will be delivered to the end-stations, including the Hard X-ray Spectroscopy End-station (HXS), the Serial Femtosecond Crystallography End-station (SFX), the Coherent Diffraction Imaging-Imaging End-station for Materials (CDE-IEM), and the High Energy Density physics end-station (HED).

The FEL-II is the beamline that delivers the softest radiation of all FEL beamlines and is designed to cover the photon energy range from 0.4 to 3 keV. Actually, if required by scientific users, FEL radiation with photon energy as low as 0.08 keV is also achievable. The output radiation will be delivered to the downstream four serial experimental stations, namely, the Soft X-ray Scattering and Spectroscopy end-station (SSS), the Coherent Diffraction imaging End-station-Imaging End-station for Biomaterials (CDE-IEB), the Atomic, Molecular and Optical science end-station (AMO), and the Spectrometer for Electronic Structure end-station (SES). For the scientific objectives of the four end-stations, they aspire to cover the photon energy range from 0.2 to 3 keV, with a pulse energy of 10–300 μJ, pulse duration of less than 50 fs, and a maximum repetition rate of ≥100 kHz. The SES hopes to cover photon energy as low as 0.1 keV for the Angle Resolved PhotoEmission Spectroscopy experiment (ARPES). The AMO and IEB have higher expectations for the single-shot pulse energy and IEB and SES even hope for fully coherent radiation and circularly polarized radiation.

The FEL-II is the most diversified FEL beamline of the three FEL beamlines and includes SASE, self-seeding, EEHG, polarization control, and several more advanced FEL modes. It is worth mentioning that some of the advanced FEL modes have been commissioned and demonstrated at the Shanghai soft X-ray Free-Electron Laser facility (SXFEL), including HGHG, EEHG, HGHG-HGHG cascading, EEHG-HGHG cascading, harmonic lasing, polarization control, and fast-switch [14, 15, 30, 38]. Furthermore, the soft X-ray monochromator for self-seeding has been also arranged at the SXFEL and online for further testing. Given the arrangement of the whole project, the FEL-II will be the first undulator beamline which will start beam transportation and FEL commissioning in the spring of 2025.

2 Baseline design of the FEL-II

The design of the FEL-II undulator beamline aims to realize and exceed the regular SASE FEL operation to offer a fully coherent FEL pulse and several novel modes of operation for scientific users such as ultra-short pulse, polarization control, and fast switch. The baseline FEL operation modes consist of SASE, self-seeding, external seeding, and polarization control. In order to match these, a unique feature of this beamline is that it selects several kinds of undulator types, including main radiation undulator, modulation undulator, dual-period undulator, and elliptically polarized undulator (EPU). Considering the complexity and flexibility, the undulator module has been optimized to improve the performance of the baselines and several advanced FEL modes, and the layout is shown in Figure 3. The period length of the main radiator is 55 mm with 32 modules and a module length of 4 m, of which the first 14 modules are dual-period undulators with a switchable period of 75 mm (abbr. U55 and U75/55). The modulator period in the front of the beamline is 180 mm, which satisfies the FEL resonant condition with an approximately 260 nm seed laser at the electron beam energy range of 5–8 GeV. The EPU period is 55 mm (EPU55) with the plan of the Apple-X type, which is located downstream of the main radiators U55s as an afterburner for polarization control. There are five chicanes inserted, of which the first three are used for EEHG operation in the modulator section and the last two are used for self-seeding operation. Beyond the baseline design above, harmonic lasing, fresh bunch, ultra-short pulse, and polarization fast switch are also under construction.

2.1 SASE

The standard SASE configuration is the most general and popular FEL mode and has been adopted widely in the world. We present the following numerical simulation results using a Gaussian beam with the nominal beam parameter, a single SASE pulse spectrum in the time domain, and a frequency domain evaluated with a representative 1.24 keV photon energy, i.e., the 1.0 nm wavelength in Figure 4. The saturation peak power is nearly 10 GW and the pulse energy is nearly 300 μJ. The pulse length is about 28 fs (FWHM), and the radiation bandwidth is 0.31% (FWHM). It corresponds to a time-bandwidth product of 260, which is 600 times larger than that of the transform-limit pulse

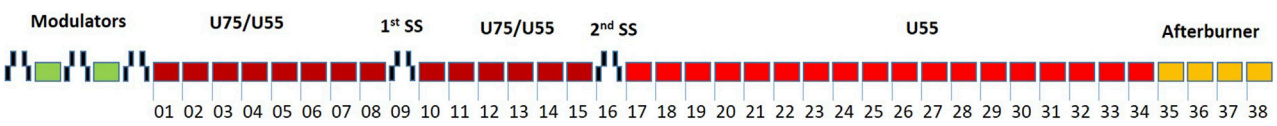

FIGURE 3
The FEL-II schematic layout at the SHINE. Three chicanes (black) and two modulators (green) are in the front, the following parts are two dual-period undulator sections (14*U75/55, claret) and two self-seeding chicanes (ss, black), then there is a long main radiator section (18*U55, red), and the last four undulators are elliptically polarized (EPUs) for afterburner (orange).

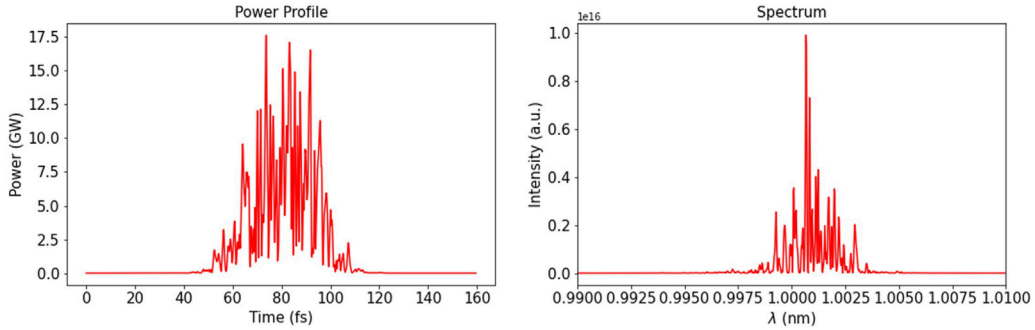

FIGURE 4
Simulation results for the SASE scheme at 1.24 keV: radiation pulse in the time domain (left) and single-shot spectrum (right).

TABLE 1 SASE FEL performance of different photon energies in the FEL-II.

Specifications	Values						
Photon energy (keV)	0.4	0.6	0.9	1.24	2	2.5	3
Peak power (GW)	12.5	11.2	13.0	9.6	8.8	7.6	6.0
Pulse length (fs)	25	29	27	28	27	25	26
Bandwidth (%, FWHM)	0.39	0.41	0.35	0.31	0.24	0.23	0.22
Pulse energy (μJ)	371	412	349	274	203	129	76
Source size (μm, FWHM)	109	94	83	75	65	61	59
Divergence (μrad, FWHM)	27.8	20.0	14.3	11.2	7.4	6.3	6.0

with a Gaussian profile. The FEL spot size near the saturation point is 75 μm (FWHM) and the divergence angle is 11 μrad (FWHM), which means the transverse coherence of the M2 factor is 1.9. Meanwhile, we can calculate that the FEL pulse contains 2.5 × 10^{12} photons, corresponding to the peak brightness of 8.9 × 10^{31} (photons/s/mm^2/$mrad^2$/0.1%BW) and the average brightness of 2.2 × 10^{24} (photons/s/mm^2/$mrad^2$/0.1%BW) at 1 MHz repetition rate. The undulator tapering technique application after FEL saturation can significantly improve the FEL power and pulse energy further [39]. For the FEL-II, the undulator module quantity is enough for the undulator tapering, therefore pulse energy larger than 500 μJ and even to the 1 mJ level is possible for 1.24 keV. To illustrate the performance in the SASE mode, the FEL properties in the SASE mode for 0.4 keV, 0.6 keV, 0.9 keV, 2.0 keV, 2.5 keV, and 3.0 keV photon energies are also given, as shown in Table 1. It is worth mentioning that, in order to increase the delivery and acceptance efficiency downstream for the lower photon energy radiation, e.g., 0.4 keV, FEL pulse optimization with a smaller divergence would be a more valuable objective.

2.2 Self-seeding

The X-ray radiation based on the SASE configuration is coherent spatially but lacks temporal coherence. The temporal and spectrum profiles exhibit a relatively wide bandwidth at the 0.1% level and a multi-spike structure characteristic of the SASE process due to the initial shot noise in the electron beam. The temporal coherence of SASE can be improved with the seeding technique that generates a narrow bandwidth pulse that is nearly Fourier transform-limited. External seeding and self-seeding technologies are configured in the FEL-II, which are used to cover the different photon energies. The self-seeding mode of the FEL-II is designed with a photon energy range of 0.6–1.5 keV and output spectral bandwidth of less than 0.02%. The layout of the soft X-ray self-seeding scheme (SXSS) is shown in Figure 5, which includes a two-stage self-seeding for sideband elimination, heat loading reduction, and high repetition rate operation.

Figure 6 illustrates the simulated self-seeding performances of 1.24 keV using a Gaussian beam. The saturation peak power is up to 15 GW with 390 μJ pulse energy. The spectrum bandwidth equals to 0.024% (FWHM), and the temporal duration is approximately 50 fs

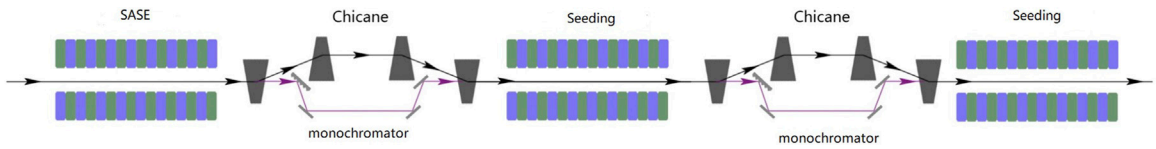

FIGURE 5
Soft X-ray self-seeding schematic design for the FEL-II. The two-stage self-seeding scheme is presented here. The two same self-seeding systems including an electron by-pass chicane and photon monochromator are inserted in the undulator beamline and separate 32 main radiators into three sections, i.e., the SASE section, and the 1st and 2nd seeding sections.

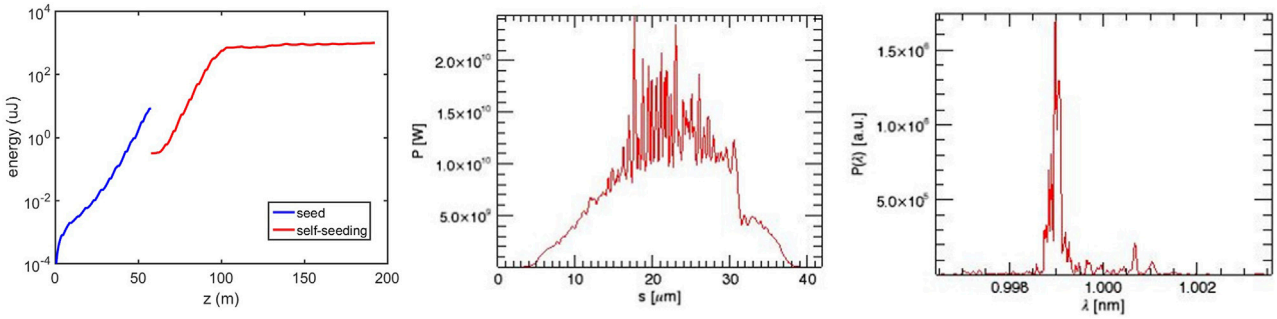

FIGURE 6
Simulation results for the SXSS scheme at 1.24 keV: the SXSS FEL pulse energy growth along the undulators beamline (left), output FEL pulse in the time domain (middle), and single-shot spectrum (right).

(FWHM), which gives a time-bandwidth product of 3.6, approximately 8 times larger than that of the transform-limited pulse with a Gaussian profile. The typical spot size and diffraction angle of the X-ray source are approximately 100 μm (FWHM) and 5.5 μrad (FWHM), respectively. With all the numbers, one can calculate that, the peak brilliance of FEL-II transmission-based self-seeding is 1.9×10^{33} (photons/s/mm^2/$mrad^2$/0.1%BW), at the photon energy of 1.24 keV. In order to suppress the side effect and mitigate the heat-loading on the granting, the two-stage SXSS mode can be operated.

For the SXSS mode with the granting-based photon monochromator, the SXSS system combined with a chicane is inserted in the undulator section with a 4 m length. The system includes two mirror boxes located at the two wings of the chicane and uses the configuration of LCLS as a reference [32, 40]. The front spectral box located between the first two dipoles of the chicane, consists of a cylindrical VLS grating and a plane mirror. The incidence of the VLS granting is fixed at 89°. The central wavelength adjustment depends on the off-axis rotation of the plane mirror. The rear mirror box located between the last two dipoles of the chicane consists of two cylindrical mirrors for the radiation spot focusing and radially optical path returning. The system is quite compact with a 4 m length, and the maximum delay time is approximately 1.5 ps, which is a challenge for mechanical design.

As mentioned above, the resolution is expected to be larger than 5,000 at the range of 0.6–1.5 keV, and we adopt a blazed grating and an alternative holographic grating, covering the different photon energy, respectively. In order to further understand self-seeding, research and development has carried out on the monochromator system. At the end of 2022, the front box of the monochromator system based on the blazed grating has been installed at the beamline of the SXFEL facility and tested online. The test result presented a resolution larger than 5,300 at 520 eV. More detailed and systematic research is still ongoing.

2.3 EEHG

Besides the self-seeding technique, the external seeding technique is also employed in the FEL-II. The FEL radiation performances based on the external seeding technique, for example, temporal coherence, stability, and wavelength, are usually determined by the UV seed laser. Single-stage HGHG and EEHG are two basic operation modes. Different from the HGHG with relatively low harmonic up-conversion, the EEHG allows the up-conversion to higher harmonics and is capable of achieving higher than 50th harmonics. Theoretically, the 90th harmonics and even higher than 100th harmonics are possible to be produced, but it is difficult to achieve this experimentally due to the electron beam collective effects such as coherent synchrotron radiation (CSR), incoherent synchrotron radiation (ISR), and intra beam scattering (IBS). At the SXFEL facility, the 47th EEHG harmonic lasing has been demonstrated and passed the national acceptance, and the 54th harmonic lasing and the 61st harmonic signal have also been achieved during the commissioning. Thus, the

TABLE 2 Designed EEHG main parameters of the FEL-II.

Parameter	Value	Unit
Modulator period length	180	mm
Modulator total length	2.16	m
Seed laser wavelength	240–266	nm
Seed laser pulse duration (FWHM)	150	fs
Seed laser repetition rate	≥10	kHz
Seed laser pulse energy (rms)	≥400	μJ
Seed laser spot size (FWHM)	0.2	mm

baseline design for the EEHG mode at the FEL-II is to generate fully coherent radiation at the photon energy up to 0.25 keV (5.0 nm, 54th harmonic), and the realization of 0.4 keV (3 nm, 90th harmonics) is still desirable in the future.

The modulator and the UV seed laser parameters of the FEL-II for the EEHG design and simulation are listed in Table 2. The seed laser is able to induce an energy modulation in beam longitudinal phase space with a maximum of 8 times the modulation amplitude of the beam slice energy spread, which basically satisfies the HGHG and EEHG operation requirements. The modulator has 12 periods with a total length of 2.16 m, which is optimized as approximately 3 times the FEL gain length of the 266 nm radiation. The 10 fs slippage length within the modulator ensures that the fresh-slice-based EEHG-HGHG cascading configuration depending on an ultra-short seed laser is possible for operation in the future.

Using a Gaussian beam, Figure 7 illustrates the performances of the 6 nm and 3 nm outputs at the FEL-II for the EEHG mode with the harmonic number of 43 and 85, respectively. The EEHG-43 results show that a radiation peak power of up to 9.6 GW can be reached with a pulse energy larger than 180 μJ. The pulse duration is approximately 20 fs (FWHM), and the spectrum is quite narrow with a single spike and bandwidth of 0.065% (FWHM), corresponding to a time-bandwidth product of approximately 0.64, which is about 1.5 times larger than that of the transform-limit pulse with a Gaussian profile. In addition, the EEHG-85 results show that the radiation power can reach 9.8 GW and the pulse energy is approximately 170 μJ. The pulse duration is approximately 20 fs (FWHM), and the relative spectral bandwidth is 0.033% (FWHM), corresponding to a time-bandwidth product of about 0.65. It is worth noting that the micro-bunching instability contributed by the beam collective effects degrades the output performances partly, which has been analyzed before, but not presented here [41, 42].

The radiation undulator used for the EEHG operation is mainly the dual-period undulator U75/U55. As shown in Figure 2, the relatively lower harmonics operation depends on U75 with lower beam energy and while U55 is mainly used for the higher harmonics. It is worth noting that the EEHG source point is much earlier than the other FEL operation modes inevitably. For the beamline and end station, increasing the acceptance and tolerance of the optical design has to be taken into consideration. We also tried to enlarge the electron beam size in the undulator to reduce the radiation divergence. Simultaneously, the undulator taper technique which is usually used to increase the FEL pulse energy, will be used to stretch the spot waist longitudinally. In order to improve the delivery efficiency further due to the optical diffraction, the aperture of the vacuum pipe and the undulator gap are expanded and limited to larger than the FEL-I design. In addition, the injection and extraction of the seed laser is also a challenging task that is still ongoing. Up to now, we have optimized the lattice and shortened the

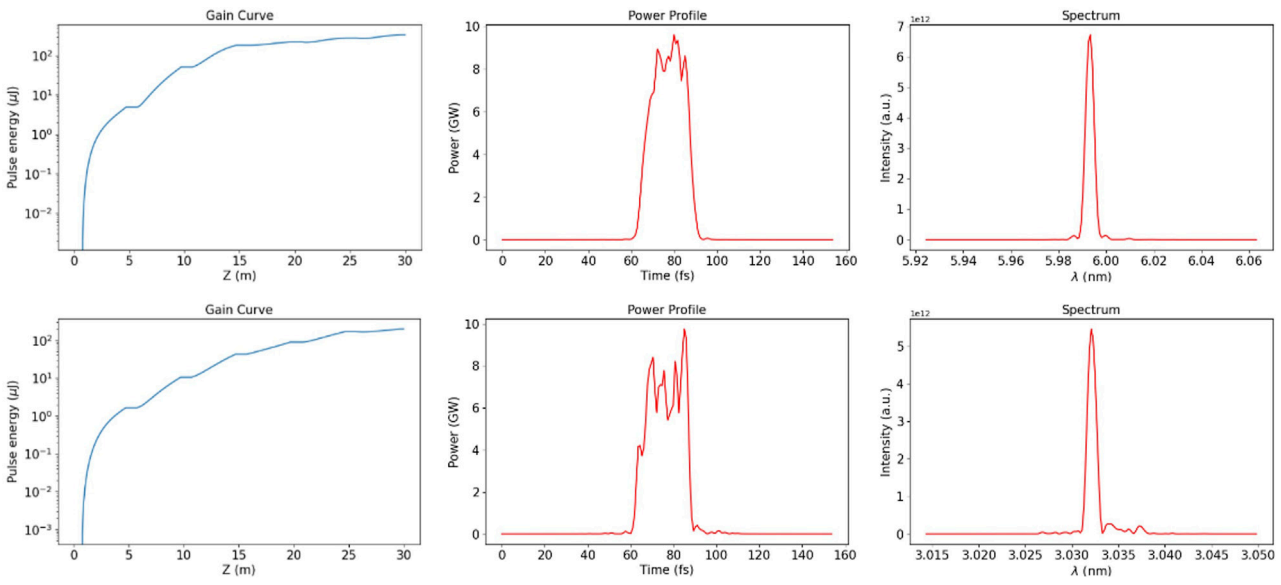

FIGURE 7
Simulation results of the 43rd and 85th harmonics of EEHG in the FEL-II: FEL pulse energy growth along the undulator (left), saturation FEL pulse (middle), and single-shot spectrum (right). The upper panel shows the 43rd harmonics, i.e., 6 nm wavelength, and the lower panel shows the 85th harmonics, i.e., 3 nm wavelength.

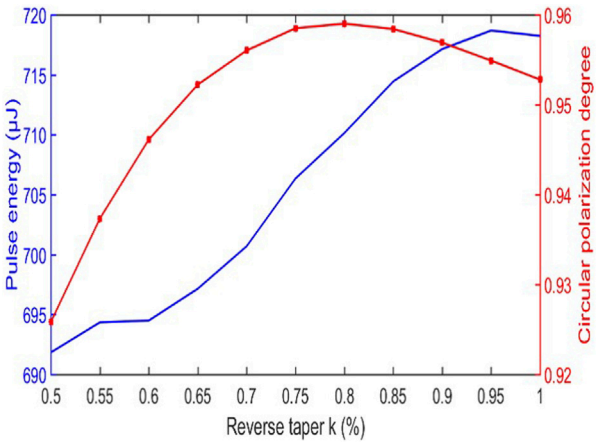

FIGURE 8
EPU afterburner performances at the FEL-II.

distance from laser injection to extraction further facing the challenge.

2.4 Afterburner

The main undulators adopt the plane-type undulator technique since it is more mature in terms of short periods, high magnetic field strength, and magnetic field error control. This is a benefit for FEL gain and reduces the cost of the device. However, the plane-type undulator provides a fixed polarization state which limits the user community. In order to obtain circularly polarized FEL radiation, a cross-plane undulator or an elliptically polarized undulator (EPU) might be the representative options. Consequently, we plan to install several EPU undulators in the form of afterburners downstream of the plane-type undulator section, so that the pre-clustered beam can emit near-saturated FEL radiation through the EPU undulators.

Polarized radiation based on EPU with a 55 mm undulator period length is designed to cover the same range of the SASE in the FEL-II with adjustable polarization. In order to ensure a relatively large photon energy range and flexibility, the advanced Apple-X type is taken into consideration. Figure 8 illustrates the polarization switch performances of 1.24 keV output, in which the reverse-taper technique is adopted. The reverse taper undulators are optimized to get maximum FEL power and high helicity purity. The maximum circular polarization is achieved with a reverse taper value of 0.8%, where the pulse energy is 720 μJ with about 96% degree of polarization.

3 Advanced FEL operation modes

In the previous section, the baseline configurations of the FEL-II undulator beamline, including SASE, self-seeding, EEHG, and polarization control were presented. However, our design work foresees physical and technical solutions which will allow significant performance enhancements without significant changes to the infrastructure and hardware. Several potentials such as ultra-short, coherent X-ray coverage expansion, multi-color, polarization fast-switch, high-power FEL, and high-brightness SASE are under consideration for the future. It is worth noting that different FEL operation modes will require different beam properties, therefore, more flexibility of the schematic design at the FEL-II is still under consideration to allow further development.

3.1 Ultra-short pulse

Besides the baseline configuration of X-ray pulses with several tens of fs pulse duration, the users also require femtosecond level (even to attosecond) X-ray pulses for time-resolved studies of atomic and molecular processes. According to current progress in normal conducting FELs, the main feasible methods for ultra-short pulse generation are low charge mode, emittance spoiler foil, dechirper, and enhanced SASE (ESASE) technique [43–48].

The method of low charge mode has been extensively applied in many FEL facilities. Due to relaxed space charge effects, the electron beam can be compressed to the fs level in low charge mode. For the SHINE, the operation modes based on the 10 pC beam and 20 pC beam have been taken into consideration. FEL simulations show that the FEL pulse with a pulse duration of less than 10 fs and peak power at the GW level is feasible. The second method uses an emittance spoiler in the second bunch compressor. It is worth stressing that the thermal loading of the spoiler foil determines the maximum operational repetition rate. The third method uses a dechirper in the front of the undulator, where transverse wake and longitudinal wake would induce the fresh slices and change the pulse length for lasing. Further, multi-time slice slippages by utilizing the small chicane in-between undulators would improve the FEL peak power to 10–100 GW-level after saturation. In addition, the ESASE technique could also compress the bunch length to the fs level. ESASE employs an ultra-short infrared laser pulse to manipulate the beam's longitudinal phase space and imprint a very strong current enhancement on a small fraction of the electron beam. At the SHINE, with a currently available laser of 15 fs (FWHM) duration, 1.6 μm central wavelength, and 100 GW peak power, the peak current of the electron beam can be enhanced by approximately 7 times. These current spikes will generate ultra-short radiation pulses with a pulse duration of approximately 200 as and a peak power of about 70 GW in a 50 m long undulator in simulation. When using a shorter laser pulse with a 3 fs (FWHM) pulse duration, we can get a single spike X-ray pulse from the ESASE. The peak power exceeds 30 GW after a 40 m long undulator. The longitudinal coherence has also been improved due to the short pulse duration. The ultra-short ESASE radiation pulse is naturally locked to the optical laser, thus allowing a pump-probe experiment to be performed with high temporal resolution.

3.2 Harmonic lasing

The SHINE is constructed to cover the photon energy from 0.4 keV to 25 keV based on SASE mode, which is also capable to be

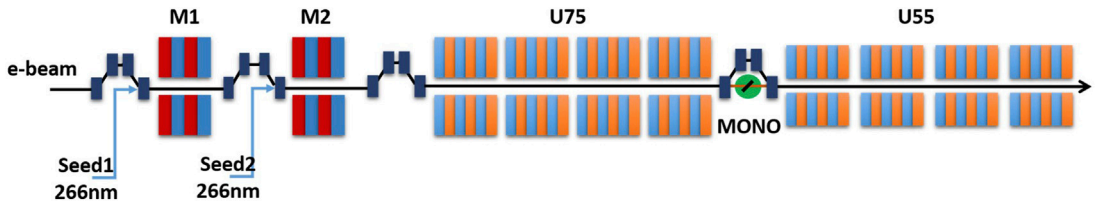

FIGURE 9
Advanced FEL configurations for coherent X-ray full coverage at the FEL-II. It mainly consists of the EEHG section (two seed lasers, two modulators, and three chicanes), U75 section, self-seeding section, and U55 section.

less than 0.4 keV for the requirements of scientific research. However, the energy range of the fully coherent FEL modes is less than the SASE mode. It should be noted that there are two energy gaps that can not be covered, one of which is the approximate 1.5–4.5 keV range between SXSS and HXSS modes, and another one is the approximate 0.25–0.6 keV range between EEHG and SXSS modes. Several advanced FEL configurations can be attempted in the FEL-II beamline and are promising to cover the energy gaps. The higher harmonics up-conversion to 90th of the single-stage EEHG is relatively difficult to realize.

However, due to the configuration of the different undulator periods, harmonic lasing is a better way to expand the coherent X-ray coverage range. Usually, harmonic lasing is used for SASE-dependent harmonic lasing schemes based on two different undulator periods [49–51]. In order to expand the coherent X-ray coverage range, EEHG harmonic cascading can be operated at 0.25–0.6 keV, and self-seeding harmonic lasing can cover 1.5–4.5 keV [52]. Consequently, the full coverage of the coherent X-ray FEL can be expected due to the flexible infrastructure.

As shown in Figure 2, for the 5 GeV operation, the single stage EEHG with the 75 mm-period undulator easily generates the FEL output with a wavelength of 5–10 nm (≤0.25 keV), and the 2-3rd harmonic lasing with the 55 mm-period undulator is expected to cover the wavelength of 2–5 nm, i.e., 0.25–0.6 keV. For the SXSS harmonic lasing, the pure 55 mm-period undulator covers the coherent hard X-ray photon energy gap. Figure 2 tells us that the 55 mm-period undulator can cover photon energy of 0.54–6.0 keV for the 8 GeV operation. Therefore, the undulators upstream are used for the SXSS operation and generate the FEL output with a photon energy of 0.54–1.5 keV, and the 2-3rd harmonic lasing with the undulator downstream can cover the photon energy of 1.5–4.5 keV. In the simulation, we have seen a quasi-coherent X-ray generation within the two energy gaps connecting with the reverse taper technique, and the current setup has already offered the requirement of the harmonic lasing schemes.

3.3 EEHG-HGHG cascading

For the external seeding technique of the FEL-II at the SHINE, the baseline design is the EEHG operation with the highest harmonics of approximately 50. For the FEL simulation, higher harmonics are possible based on single-stage EEHG or EEHG-HGHG cascading. At the SXFEL facility, the EEHG-HGHG cascading scheme has been demonstrated experimentally [38]. For the single-stage EEHG, the 54th harmonics, i.e., 5nm, has been demonstrated and the higher harmonics commissioning is ongoing. Therefore, to cover the photon energy between 0.25 and 0.6 keV, and meet the needs of users, the advanced EEHG-HGHG cascading mode is an option with the fresh bunch technique. Figure 9 presents the current schematic layout which only requires a minor improvement for the EEHG-HGHG cascading operation. The first-stage EEHG will generate the FEL pulse with a 3–9 nm wavelength in U75s, which is the seed of the second-stage HGHG to generate the FEL pulse with a 1–3 nm wavelength in U55s. Figure 10 presents the EEHG-HGHG cascading simulation results, where the wavelength of the first-stage EEHG is 3 nm as a harmonic up-conversion of approximately 90 and the second-stage HGHG is 1 nm as a harmonic up-conversion of 3. The final output peak power of the 1 nm wavelength X-ray pulse is approximately 8 GW and the pulse energy is more than 100 μJ with a spectrum close to Fourier-transform-limited. For this scheme, a flat-top distribution of the current profile for the electron beam is required. The key point is an fs level time jitter which impacts the stability of the output FEL power significantly [42].

3.4 Multi-color

In the past few years, several techniques for multi-color operation and spectral control of X-ray FELs have been developed worldwide. The key to achieving multi-color pulse generation is easily understood from the basic principles of FEL operation. The multi-color experiment usually employs de-chirpers, chicanes, and, of course, the central wavelengths of the FEL pulses can be independently tuned by simply changing the gaps of the undulator [53–62]. All the components will be established at the facility, thus it is very convenient for delivering multi-color and/or multi-pulse to the experimental stations. Because of the long undulator, one can display the powerful ability of multi-color operation at the SHINE.

3.5 HB-SASE

The high-brightness SASE (HB-SASE) technique can be applied to significantly improve the temporal coherence of SASE [63]. By inserting a series of small chicanes between the undulator segments of SASE, the slippage length between the FEL

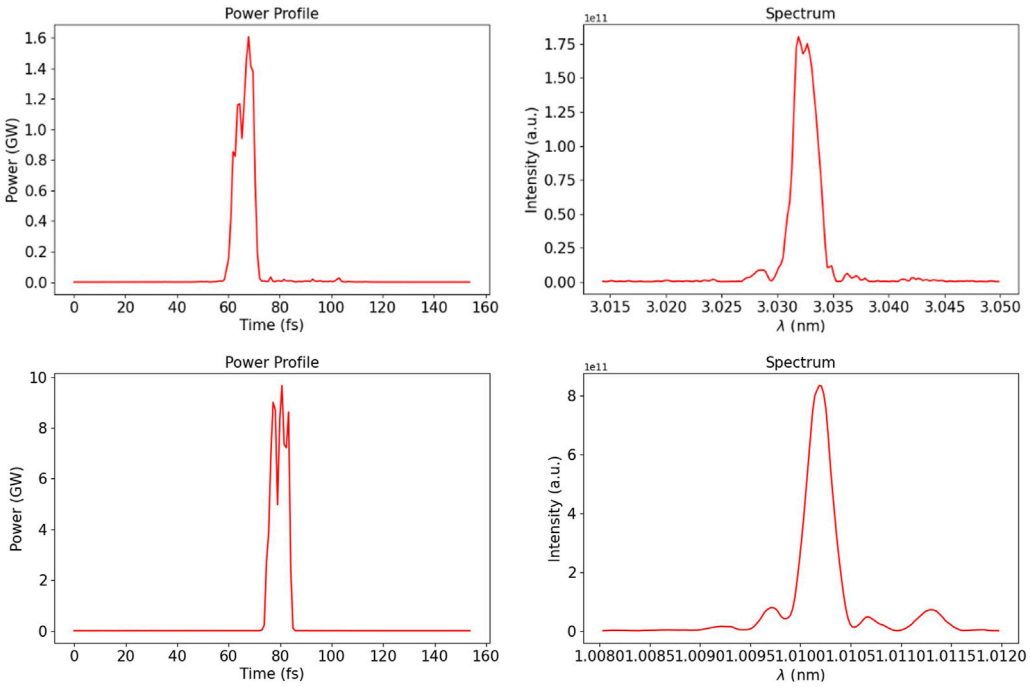

FIGURE 10
EEHG-HGHG cascading simulation results. The top two are the first-stage 90th EEHG with 3 nm wavelength and the bottom two are the second-stage 3rd HGHG with 1 nm wavelength.

radiation and electron bunch can be artificially increased, giving a corresponding increase in coherence length and a narrowing output bandwidth. The HB-SASE technique does not require an external seeding source or X-ray photon optics and is applicable at any wavelength and repetition rate. In the SHINE design, the length of each undulator module is 5 m, and a delay sequence based on prime number increases is used. The delay induced by the first small chicane is approximately 36 nm, which is a little longer than the slippage length in one undulator module. The simulation shows that the peak power of the HB-SASE is comparable with the normal SASE. The longitudinal phase distribution of the HB-SASE is smoother, which results in a much narrower bandwidth of approximately 0.003%, approximately 20 times narrower than that of the normal SASE case.

3.6 Others

There are still several other advanced FEL operation modes on the way one of which is a high-power SASE a high-power SASE scheme. The basic method adopts the dechirper to kick the beam slice and generate multi-stage slippage between the beam slice and the FEL pulse, which could increase the FEL peak power to several times the saturation power. We are also working on the polarization fast-switch based on a fast-switch phase shifter. The fast-switch phase shifter with a length of less than 3 m and a 0.5 MHz switch frequency will be inserted between the four EPU undulators to continuously switch between the different polarization states. Simulation results show that two different polarization FEL pulses with higher than 90% polarization degree are theoretically achievable.

4 Summary

In summary, this article presents the physical design of the FEL-II undulator beamline at the SHINE, which is the first high repetition rate based hard X-ray FEL facility in China. The SHINE completed an international review of the physical design at the end of 2022, and this work in detail is presented first as a manuscript. We mainly introduce the FEL-II, which is the most diversified undulator beamline compared to the FEL-I and the FEL-III.

The baseline design mainly consisting of SASE, self-seeding, external seeding, and polarization control, will provide X-ray FEL pulses beyond the photon energy range from 0.4 to 3.0 keV with a repetition rate up to 1 MHz. Furthermore, the FEL-II is also designed to provide more flexible FEL output properties towards ultra-short pulse, coherent X-ray coverage expansion, multi-color, and so on. This beamline aims to be one of the most advanced FEL beamlines in the world and meet the needs of more scientific users. As the softest X-ray beamline of the SHINE, the commissioning and operation of the FEL-II beamline will be started firstly, and the comprehensive advance in engineering construction is urgent and important in the coming years. The research and development program, including the prototype construction of the undulator, the magnet device, and the

beam measurement device, will be completed in 2023. After this, effective serial production and installation may start by 2024. After the installation, the FEL commissioning of the FEL-II beamline will start, and realize the first lasing by June 2025.

Author contributions

All authors contributed to the article and approved the submitted version. The first author TL wrote most of the manuscript and contributed to the physical design of all FEL schemes. NH, HY, and ZG contributed to the different scheme designs and simulations. ZQ, KZ, SC, CF, WZ, HaL, XF, HeL, and BF partially contributed to the scheme design, simulation, test, and manuscript writing. The corresponding authors HD and BL took the head in the accelerator and FEL scheme design, reviewed the manuscript, and supervised the work. DW and ZZ were in charge of the whole project design and construction.

Funding

This work was partially supported by the National Natural Science Foundation of China (11905277, 12125508, 11935020, 11975300 and 12122514), the CAS Project for Young Scientists in Basice Research (YSBR60 and YSBR42), Youth Innovation Promotion Association CAS (2023302), Program of Shanghai Academic/Technology Research Leader (21XD1404100), Natural Science Foundation of Shanghai (23ZR1471300), and Shanghai Pilot Program for Basic Research—Chinese Academy of Science, Shanghai Branch (JCYJ-SHFY-2021-010).

Acknowledgments

The authors would like to thank the whole FEL team in SARI for their excellent contributions to the FEL-II physical design and preparation at the SHINE.

Conflict of interest

The authors declare that the research was conducted in the absence of any commercial or financial relationships that could be construed as a potential conflict of interest.

Publisher's note

References

1. Madey JMJ. Stimulated emission of bremsstrahlung in a periodic magnetic field. *J Appl Phys* (1971) 42:1906–13. doi:10.1063/1.1660466

2. Huang Z, Kim K-J. Review of x-ray free-electron laser theory. *Phys Rev ST Accel Beams* (2007) 10:034801. doi:10.1103/PhysRevSTAB.10.034801

3. Huang N, Deng H, Liu B, Wang D, Zhao Z. Features and futures of x-ray free-electron lasers. *The Innovation* (2021) 2. doi:10.1016/j.xinn.2021.100097

4. Bostedt C, Boutet S, Fritz DM, Huang Z, Lee HJ, Lemke HT, et al. Linac coherent light source: The first five years. *Rev Mod Phys* (2016) 88:015007. doi:10.1103/RevModPhys.88.015007

5. Young L, Kanter EP, Krässig B, Li Y, March AM, Pratt ST, et al. Femtosecond electronic response of atoms to ultra-intense x-rays. *Nature* (2010) 466:56–61. doi:10.1038/nature09177

6. Chapman HN. Femtosecond x-ray protein nanocrystallography. *Nature* (2010) 470:73–7. doi:10.1038/nature09750

7. Ackermann W, Asova G, Ayvazyan V, Azima A, Baboi N, Bähr J, et al. Operation of a free-electron laser from the extreme ultraviolet to the water window. *Nat Photon* (2007) 1:336–42. doi:10.1038/nphoton.2007.76

8. Emma P, Akre R, Arthur J, Bionta R, Bostedt C, Bozek J, et al. First lasing and operation of an ångström-wavelength free-electron laser. *Nat Photon* (2010) 4:641–7. doi:10.1038/nphoton.2010.176

9. Ishikawa T, Aoyagi H, Asaka T, Asano Y, Azumi N, Bizen T, et al. A compact x-ray free-electron laser emitting in the sub-ångström region. *Nat Photon* (2012) 6:540–4. doi:10.1038/nphoton.2012.141

10. Allaria E, Appio R, Badano L, Barletta WA, Bassanese S, Biedron SG, et al. Highly coherent and stable pulses from the fermi seeded free-electron laser in the extreme ultraviolet. *Nat Photon* (2012) 6:699–704. doi:10.1038/nphoton.2012.233

11. Kang H-S, Min C-K, Heo H, Kim C, Yang H, Kim G, et al. Hard x-ray free-electron laser with femtosecond-scale timing jitter. *Nat Photon* (2017) 11:708–13. doi:10.1038/s41566-017-0029-8

12. Decking W, Abeghyan A, Abramian P, Abramsky A, Aguirre A, Albrecht C, et al. A mhz-repetition-rate hard x-ray free-electron laser driven by a superconducting linear acceleratorn. *Nat Photon* (2020) 14:391–7. doi:10.1038/s41566-020-0607-z

13. Prat E, Abela R, Aiba M, Alarcon A, Alex J, Arbelo Y, et al. A compact and cost-effective hard x-ray free-electron laser driven by a high-brightness and low-energy electron beam. *Nat Photon* (2020) 14:748–54. doi:10.1038/s41566-020-00712-8

14. Zhao Z, Wang D, Gu Q, andMing Gu LY, Leng Y, Liu B. Status of the sxfel facility. *Appl Sci* (2017) 7:607. doi:10.3390/app7060607

15. Liu B, Zhang W, Fang W, Wang Z, Zhou Q, Leng Y, et al. The sxfel upgrade: From test facility to user facility. *Appl Sci* (2021) 12:176. doi:10.3390/app12010176

16. Kondratenko A, Saldin E. Generation of coherent radiation by a beam of relativistic electrons in an undulator. *Sov Phys - Tech Phys (Engl Transl.); (United States* (1981) 26:8.

17. Bonifacio R, Pellegrini C, Narducci L. Collective instabilities and high-gain regime in a free electron laser. *Opt Commun* (1984) 50:373–8. doi:10.1016/0030-4018(84)90105-6

18. Yu LH. Generation of intense uv radiation by subharmonically seeded single-pass free-electron lasers. *Phys Rev A* (1991) 44:5178–93. doi:10.1103/PhysRevA.44.5178

19. Yu L-H, Babzien M, Ben-Zvi I, DiMauro LF, Doyuran A, Graves W, et al. High-gain harmonic-generation free-electron laser. *Science* (2000) 289:932–4. doi:10.1126/science.289.5481.932

20. Stupakov G. Using the beam-echo effect for generation of short-wavelength radiation. *Phys Rev Lett* (2009) 102:074801. doi:10.1103/PhysRevLett.102.074801

21. Xiang D, Stupakov G. Echo-enabled harmonic generation free electron laser. *Phys Rev ST Accel Beams* (2009) 12:030702. doi:10.1103/PhysRevSTAB.12.030702

22. Geloni G, Kocharyan V, Saldin E. A novel self-seeding scheme for hard x-ray fels. *J Mod Opt* (2011) 58:1391–403. doi:10.1080/09500340.2011.586473

23. Amann J, Berg W, Blank V, Decker F-J, Ding Y, Emma P, et al. Demonstration of self-seeding in a hard-x-ray free-electron laser. *Nat Photon* (2012) 6:693–8. doi:10.1038/nphoton.2012.180

24. Liu B, Li WB, Chen JH, Chen ZH, Deng HX, Ding JG, et al. Demonstration of a widely-tunable and fully-coherent high-gain harmonic-generation free-electron laser. *Phys Rev ST Accel Beams* (2013) 16:020704. doi:10.1103/PhysRevSTAB.16.020704

25. Xiang D, Colby E, Dunning M, Gilevich S, Hast C, Jobe K, et al. Demonstration of the echo-enabled harmonic generation technique for short-wavelength seeded free electron lasers. *Phys Rev Lett* (2010) 105:114801. doi:10.1103/PhysRevLett.105.114801

26. Xiang D, Colby E, Dunning M, Gilevich S, Hast C, Jobe K, et al. Evidence of high harmonics from echo-enabled harmonic generation for seeding x-ray free electron lasers. *Phys Rev Lett* (2012) 108:024802. doi:10.1103/PhysRevLett.108.024802

27. Hemsing E, Dunning M, Garcia B, Hast C, Raubenheimer T, Stupakov G, et al. Echo-enabled harmonics up to the 75th order from precisely tailored electron beams. *Nat Photon* (2016) 10:512–5. doi:10.1038/nphoton.2016.101

28. Zhao ZT, Wang D, Chen JH, Chen ZH, Deng HX, Ding JG, et al. First lasing of an echo-enabled harmonic generation free-electron laser. *Nat Photon* (2012) 6:360–3. doi:10.1038/nphoton.2012.105

29. Ribic PR, Abrami A, Badano L, Bossi M, Braun H-H, Bruchon N, et al. Coherent soft x-ray pulses from an echo-enabled harmonic generation free-electron laser. *Nat Photon* (2019) 13:555–61. doi:10.1038/s41566-019-0427-1

30. Feng C, Deng H, Zhang M, Wang X, Chen S, Liu T, et al. Coherent extreme ultraviolet free-electron laser with echo-enabled harmonic generation. *Phys Rev Accel Beams* (2019) 22:050703. doi:10.1103/PhysRevAccelBeams.22.050703

31. Feldhaus J, Saldin E, Schneider J, Schneidmiller E, Yurkov M. Possible application of x-ray optical elements for reducing the spectral bandwidth of an x-ray sase fel. *Opt Commun* (1997) 140:341–52. doi:10.1016/S0030-4018(97)00163-6

32. Ratner D, Abela R, Amann J, Behrens C, Bohler D, Bouchard G, et al. Experimental demonstration of a soft x-ray self-seeded free-electron laser. *Phys Rev Lett* (2015) 114. doi:10.1103/PhysRevLett.114.054801

33. Nam I, Min C-K, Oh B, Kim G, Na D, Suh YJ, et al. High-brightness self-seeded x-ray free-elctron laser covering the 3.5kev to 14.6kev range. *Nat Photon* (2021) 10:435–41. doi:10.1038/s41566-021-00777-z

34. Liu S, Decking W, Kocharyan V, Saldin E, Serkez S, Shayduk R, et al. Preparing for high-repetition rate hard x-ray self-seeding at the European x-ray free electron laser: Challenges and opportunities. *Phys Rev Accel Beams* (2019) 22:060704. doi:10.1103/PhysRevAccelBeams.22.060704

35. Inoue I, Osaka T, Hara T, Tanaka T, Inagaki T, Fukui T, et al. Generation of narrow-band x-ray free-electron laser via reflection self-seeding. *Nat Photon* (2019) 13:319–22. doi:10.1038/s41566-019-0365-y

36. Huang N-S, Liu Z-P, Deng B-J, Zhu Z-H, Li S-H, Liu T, et al. The ming proposal at shine: Megahertz cavity enhanced x-ray generation. *Nucl Sci Tech* (2023) 34:2210–3147. doi:10.1007/s41365-022-01151-6

37. Zhao Z, Wang D, Yang Z, Yin L. Sclf: An 8-gev cw scrf linac-based x-ray fel facility in shanghai. *Int Free Electron Laser Conf* (2018) 2018. doi:10.18429/JACoW-FEL2017-MOP055

38. Feng C, Liu T, Chen S, Zhou K, Zhang K, Qi Z, et al. Coherent and ultrashort soft x-ray pulses from echo-enabled harmonic cascade free-electron lasers. *Optica* (2022) 9:785–91. doi:10.1364/OPTICA.466064

39. Kroll N, Morton P, Rosenbluth M. Free-electron lasers with variable parameter wigglers. *IEEE J Quan Elect* (1981) 17:1436–68. doi:10.1109/JQE.1981.1071285

40. Cocco D, Abela R, Amann J, Chow K, Emma P, Feng Y, et al. The optical design of the soft x-ray self seeding at lcls. *Proc SPIE* (2013) 8849. doi:10.1117/12.2024402

41. Zhou K, Feng C, Wang D. Feasibility study of generating ultra-high harmonic radiation with a single stage echo-enabled harmonic generation scheme. *Nucl Instr Methods Phys Res Section A: Acc Spectrometers, Detectors Associated Equipment* (2016) 834:30–5. doi:10.1016/j.nima.2016.07.021

42. Yang H, Yan J, Zhu Z, Deng H. Optimization and stability analysis of the cascaded eehg-hghg free-electron laser. *Nucl Instr Methods Phys Res Section A: Acc Spectrometers, Detectors Associated Equipment* (2022) 1039:167065. doi:10.1016/j.nima.2022.167065

43. Reiche S, Musumeci P, Pellegrini C, Rosenzweig J. Development of ultra-short pulse, single coherent spike for sase x-ray fels. *Nucl Instr Methods Phys Res Section A: Acc Spectrometers, Detectors Associated Equipment* (2008) 593:45–8. doi:10.1016/j.nima.2008.04.061

44. Ding Y, Brachmann A, Decker F-J, Dowell D, Emma P, Frisch J, et al. Measurements and simulations of ultralow emittance and ultrashort electron beams in the linac coherent light source. *Phys Rev Lett* (2009) 102:254801. doi:10.1103/PhysRevLett.102.254801

45. Emma P, Bane K, Cornacchia M, Huang Z, Schlarb H, Stupakov G, et al. Femtosecond and subfemtosecond x-ray pulses from a self-amplified spontaneous-emission–based free-electron laser. *Phys Rev Lett* (2004) 92:074801. doi:10.1103/PhysRevLett.92.074801

46. Ding Y, Behrens C, Coffee R, Decker F-J, Emma P, Field C, et al. Generating femtosecond x-ray pulses using an emittance-spoiling foil in free-electron lasers. *Appl Phys Lett* (2015) 107:191104. doi:10.1063/1.4935429

47. Zholents AA. Method of an enhanced self-amplified spontaneous emission for x-ray free electron lasers. *Phys Rev ST Accel Beams* (2005) 8:040701. doi:10.1103/PhysRevSTAB.8.040701

48. Duris J, Li S, Driver T, Champenois EG, MacArthur JP, Lutman AA, et al. Tunable isolated attosecond x-ray pulses with gigawatt peak power from a free-electron laser. *Nat Photon* (2019) 14. doi:10.1038/s41566-019-0549-5

49. Schneidmiller EA, Yurkov MV. Harmonic lasing in x-ray free electron lasers. *Phys Rev ST Accel Beams* (2012) 15:080702. doi:10.1103/PhysRevSTAB.15.080702

50. Schneidmiller EA, Faatz B, Kuhlmann M, Rönsch-Schulenburg J, Schreiber S, Tischer M, et al. First operation of a harmonic lasing self-seeded free electron laser. *Phys Rev Accel Beams* (2017) 20:020705. doi:10.1103/PhysRevAccelBeams.20.020705

51. Prat E, Reiche S. Compact coherence enhancement by subharmonic self-seeding in X-ray free-electron laser facilities. *J Synchrotron Radiat* (2018) 25:329–35. doi:10.1107/S1600577518000395

52. Zhang K, Qi Z, Feng C, Deng H, Wang D, Zhao Z. Extending the photon energy coverage of an x-ray self-seeding fel via the reverse taper enhanced harmonic generation technique. *Nucl Instr Methods Phys Res Section A: Acc Spectrometers, Detectors Associated Equipment* (2017) 854:3–10. doi:10.1016/j.nima.2017.02.039

53. Ciocci F, Dattoli G, Pagnutti S, Petralia A, Sabia E, Ottaviani PL, et al. Two color free-electron laser and frequency beating. *Phys Rev Lett* (2013) 111:264801. doi:10.1103/PhysRevLett.111.264801

54. Lutman AA, Coffee R, Ding Y, Huang Z, Krzywinski J, Maxwell T, et al. Experimental demonstration of femtosecond two-color x-ray free-electron lasers. *Phys Rev Lett* (2013) 110:134801. doi:10.1103/PhysRevLett.110.134801

55. Hara T, Inubushi Y, Katayama T, Sato T, Tanaka H, Tanaka T, et al. Two-colour hard x-ray free-electron laser with wide tunability. *Nat Commun* (2013) 4:2919. doi:10.1038/ncomms3919

56. Lutman AA, Maxwell TJ, MacArthur JP, Guetg MW, Berrah N, Coffee RN, et al. Fresh-slice multicolour x-ray free-electron lasers. *Nat Photon* (2016) 10:745–50. doi:10.1038/nphoton.2016.201

57. Guetg MW, Lutman AA, Ding Y, Maxwell TJ, Huang Z. Dispersion-based fresh-slice scheme for free-electron lasers. *Phys Rev Lett* (2018) 120:264802. doi:10.1103/PhysRevLett.120.264802

58. Reiche S, Prat E. Two-color operation of a free-electron laser with a tilted beam. *J Synchrotron Radiat* (2016) 23:869–73. doi:10.1107/S1600577516007189

59. Dijkstal P, Malyzhenkov A, Reiche S, Prat E. Demonstration of two-color x-ray free-electron laser pulses with a sextupole magnet. *Phys Rev Accel Beams* (2020) 23:030703. doi:10.1103/PhysRevAccelBeams.23.030703

60. Qin W, Ding Y, Lutman AA, Chao Y-C. Matching-based fresh-slice method for generating two-color x-ray free-electron lasers. *Phys Rev Accel Beams* (2017) 20:090701. doi:10.1103/PhysRevAccelBeams.20.090701

61. Chao Y-C, Qin W, Ding Y, Lutman AA, Maxwell T. Control of the lasing slice by transverse mismatch in an x-ray free-electron laser. *Phys Rev Lett* (2018) 121:064802. doi:10.1103/PhysRevLett.121.064802

62. Feng C, Deng H. Multicolour emission. *Nat Photon* (2016) 10:695–6. doi:10.1038/nphoton.2016.204

63. McNeil BWJ, Thompson NR, Dunning DJ. Transform-limited x-ray pulse generation from a high-brightness self-amplified spontaneous-emission free-electron laser. *Phys Rev Lett* (2013) 110:134802. doi:10.1103/PhysRevLett.110.134802

frontiers | Frontiers in Physics

TYPE Original Research
PUBLISHED 14 June 2023
DOI 10.3389/fphy.2023.1181862

OPEN ACCESS

EDITED BY
Nicholas Walker,
Helmholtz Association of German Research Centres (HZ), Germany

REVIEWED BY
Feng Zhou,
Stanford University, United States
Lutz Winkelmann,
Helmholtz Association of German Research Centres (HZ), Germany

*CORRESPONDENCE
Guorong Wu,
wugr@dicp.ac.cn
Zhigang He,
zghe@dicp.ac.cn
Wei Liu,
liuw@mail.iasf.ac.cn

†These authors have contributed equally to this work and share first authorship

RECEIVED 08 March 2023
ACCEPTED 31 May 2023
PUBLISHED 14 June 2023

CITATION
Zhang B, Li X, Liu Q, Zhu Z, Zhang W, He Z, Liu W, Wu G and Yang X (2023), High repetition-rate photoinjector laser system for S^{3}FEL.
Front. Phys. 11:1181862.
doi: 10.3389/fphy.2023.1181862

High repetition-rate photoinjector laser system for S^{3}FEL

Baichao Zhang[1†], Xiaoshen Li[2†], Qi Liu[2], Zexiu Zhu[2], Weiqing Zhang[1,2], Zhigang He[1,2]*, Wei Liu[2,3]*, Guorong Wu[1,2]* and Xueming Yang[1,2,4]

[1]State Key Laboratory of Molecular Reaction Dynamics, Dalian Institute of Chemical Physics, Chinese Academy of Sciences, Dalian, China, [2]Institute of Advanced Science Facilities, Shenzhen, China, [3]School of Science, Sun Yat-Sen University, Shenzhen, China, [4]Department of Chemistry and Shenzhen Key Laboratory of Energy Chemistry, Southern University of Science and Technology, Shenzhen, China

The photoinjector laser system of Shenzhen Superconducting Soft X-Ray Free Electron Laser (S^{3}FEL) is reported in this paper. This laser system operates at up to 1 MHz and produces more than 50 μJ infrared (IR) laser pulses. With a customized fourth harmonic generation (FHG) module, more than 2 μJ ultraviolet (UV) laser pulses were obtained. The power standard deviations of the IR laser and the UV laser are 0.093% and 0.395% respectively. While the pulse energy standard deviations are 1.087% and 1.746% correspondingly. We implemented the pulse stacking scheme to generate flat-top pulses. With four birefringent uniaxial crystals, the Gaussian pulses were converted to flat-top shape, featuring 10 ps pulse width and 0.5 ps rising and falling edges. A cut-Gaussian transverse profile with very sharp rising and falling edges can be produced after the spatial pulse shaper.

KEYWORDS

FEL, high repetition, photoinjector laser, pulse shaper, power stability, energy stability

1 Introduction

S^{3}FEL is a CW free electron laser facility in plan phase. This high repetition rate soft-X-ray super-conducting free-electron laser facility consists of a 2.5 GeV CW superconducting linear accelerator and four initial undulator lines, which aims at generating X-Rays between 40 eV and 1 keV at rates up to 1 MHz. Photoinjectors are often exploited as the initial electron source for many FEL facilities, like for instance FLASH [1], SPARC [2], LCLS [3], LCLS-II [4], SwissFEL [5], FERMI [6], SHINE [7] and European XFEL [8]. Photoinjector is a device that produces high-quality electron beams by using drive laser to extract electrons from the cathode material. The basic properties of the electron beams, such as the stability of the produced charge and the emittance of the electron beams, are influenced by the pulse parameters of the drive laser [9]. Temporally and spatially shaping of the laser pulses should be performed in order to obtain minimal increase of transverse emittance at acceleration of electron beams [10–13]. The photoinjector laser system is a very crucial part and has a significant impact on performances of FELs. In this paper, we describe the S^{3}FEL photoinjector laser system, including the IR front end laser, UV conversion unit and temporal-spatial pulse shaping unit. In order to be operating at a high repetition rate (adjustable up to 1 MHz), Cs_2Te photocathode will be used to produce the initial electron bunches because of high quantum efficiency (~ 10%)[14, 15]. For efficient emission of electron bunches, UV laser pulses should be exploited to illuminate the photocathode [16, 17], for instance fourth harmanic of Yb:fiber laser [4] and Nd:YLF laser [8]. According to design specifications of the S^{3}FEL, 0.2 μJ UV laser pulse with sharp temporal and spatial

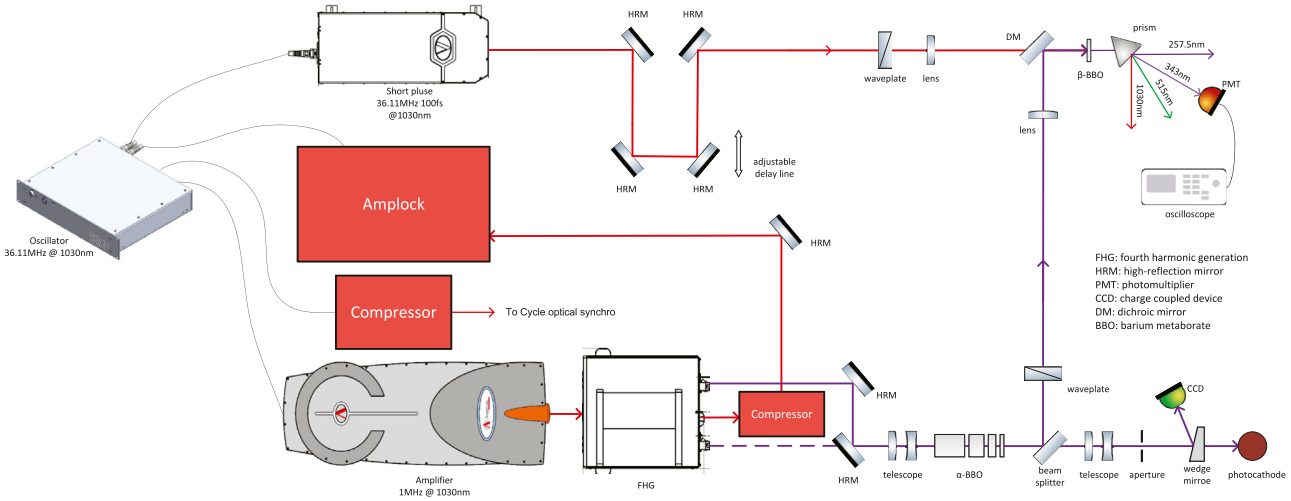

FIGURE 1
Layout of the photoinjector laser system.

edges is required to generate 200 pc charge and its pulse width should be between 10 and 60 ps. We use a commercial ytterbium-doped fiber laser (Tangerine from Amplitude) as the front end laser which can be operating at repetition rate up to 1 MHz and produce up to 50 μJ pulse energy. After the FHG module, 257.5 nm laser pulses with 2 μJ pulse energy are produced. For good UV beam quality, the efficiency of FHG is about 4% by controlling the thickness of the nonlinear crystals and the pulse width of IR laser.

2 Performance of the laser system

The layout of the photoinjector laser system is presented in Figure 1. The laser system consists of oscillator, short pulse module (to cross-correlator), compressor (to Cycle optical synchro module), slow drift locking module (Amplock), IR fiber amplifier, FHG module, temporal and spatial pulse shapers and the corresponding diagnostics setup.

The oscillator is a customized ytterbium-doped fiber laser operating at 36.11 MHz, which has four output ports. One port serves as the seed of the IR fiber amplifier, the second one is compressed to transform-limited pulse and ready for optical-to-optical locking. The third one and the output from the IR fiber amplifier are launched to the Amplock for slow drift compensation. The fourth one is nonlinearly amplified and compressed down to sub-100 fs, so that it could increase measurement resolution of UV laser pulse duration. The oscillator is phase-locked to a 216.66 MHz RF reference signal (6th harmonic of the 36.11 MHz). The integrated timing jitter is 122 fs in the range between 10 and 10 MHz (measured by Keysight E5052B SSA @4188.76 MHz). While the oscillator is free running, the integrated timing jitter is 558 fs in the range between 10 and 10 MHz. In the future, the oscillator will be phase-locked to an optical synchro module via two-color balanced optical cross-correlation (TCBOC). The short pulse module featuring 100 mw output power and 100 fs pulse width is exploited to measure temporal pulse shape of the UV laser via optical cross-correlation. The Amplock module is used to control the timing drift between the amplifier and the oscillator via optical cross-correlation. The standard deviation of the timing drift is 13.49 fs over 8 h. The IR fiber amplifier is comprised of fiber stretcher, fiber preamplifier, pulse picker, programmable spectral phase and amplitude shaper, fiber amplifier (tangerine). The IR front-end can produce 50 μJ, 1030 nm laser pulses with adjustable repetition rate up to 1 MHz and adjustable pulse duration from 267 fs to 10 ps by changing the compression grating pair distance. Spectrum (measured by Ocean Optics HR4000) and minimal pulse width (measured by APE PulseCheck 150) of the IR laser beam are shown in Figure 2. Spectral width (FWHM) is approximately 7.5 nm and minimal pulse width is about 267 fs. The angular deviation of the IR laser beam, in the horizontal and vertical direction, were measured to be 8.62 μrad and 5.45 μrad, respectively. The IR laser beam quality factor, M square (M^2), is less than 1.2 (measured by Dataray S-WCD-LCM-UV, Dataray, America) and spot ellipticity is 94%.

The IR laser beam directly accesses the FHG module, as presented in Figure 1. For efficient IR to UV conversion, two second harmonic generation (SHG) stages are exploited to convert 1030 nm laser to 515 nm and further to 257.5 nm. The overall conversion efficiency is strongly dependent on the laser beam diameter and the thickness of nonlinear crystals. For higher UV conversion efficiency, smaller beam diameter and thicker nonlinear crystal can be exploited. But this will deteriorate the UV laser beam quality and result in narrower spectrum. Meanwhile, high UV power would reduce the FHG nonlinear crystal lifetime owing to two-photon absorption. According to the design specifications, around 2 W UV laser is sufficient for the S^{3}FEL. So we take a tradeoff between the UV conversion efficiency and UV beam quality/crystal damage. The first SHG is achieved via a beta barium borate (β-BBO) crystal with 2.5 mm thickness. In the second SHG, a thinner β-BBO crystal with 0.5 mm thickness is employed, which would reduce thermal load of the FHG nonlinear crystal. When the IR laser is fully compressed (shown in Figure 2) by changing the distance of compression gratings, the conversion efficiencies of the two SHG stages are around 55% and 8%, respectively. The nonlinear crystals are placed in a closed chamber with a filtered air circulation system to

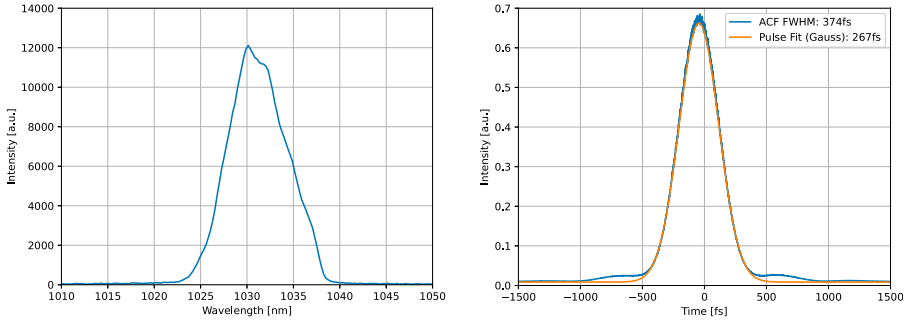

FIGURE 2
Spectrum (left) and pulse width (right) of the IR laser beam.

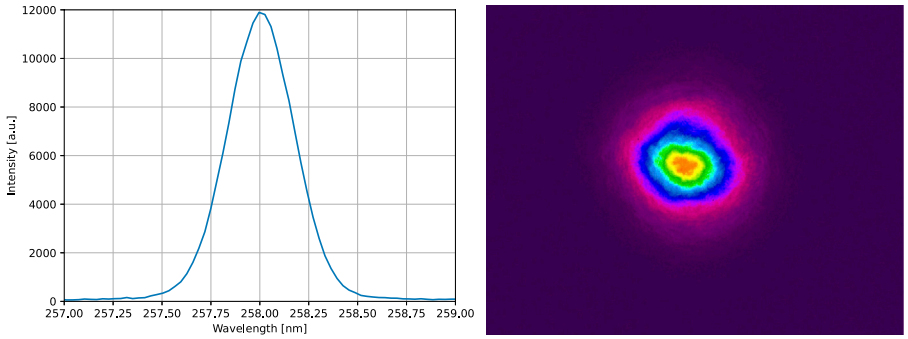

FIGURE 3
Spectrum (left) and beam profile (right) of the FHG laser beam.

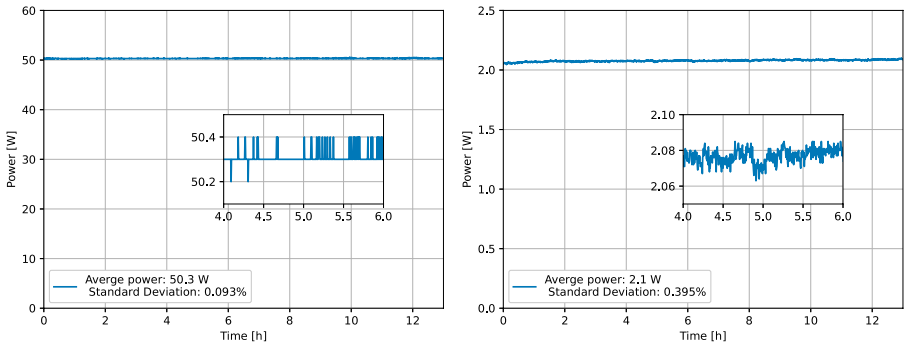

FIGURE 4
The power stability of the IR laser (left) and the UV laser (right).

extend nonlinear crystals lifetime. The spectrum (spectrometer customized from Ocean Optics with 0.02 nm resolution) and beam profile (measured by ophir SP920) of the UV laser beam (operating at 1 MHz) are shown in Figure 3. Spectral width (FWHM) of the UV laser is approximately 0.4 nm which can support 245 fs transform limited laser pulse. There is no significant deterioration in the transverse beam profile due to thinner FHG nonlinear crystal. The beam profile can be preserved for approximately 3 weeks for 24/7 operation. Over time, scattering spots would be observed around the beam spot. The UV laser pulse energy would drop by approximately 20% when the repetition rate is adjusted from 1 MHz to 1 KHz due to less thermal load. One microjoule is enough for our application. There is a energy attenuator consisting of a half waveplate and a polarizer before the electron gun. The laser energy on the photocathode can remain constant by adjusting the attenuator when the repetition rate changes.

2.1 Power stability and pulse energy stability

In order to measure the power stability of the IR laser and the UV laser, output powers of the IR front-end and the FHG module were directly measured (Gentec UP25N-100H-H9-D0) over 12 h, respectively. The measured results are presented in Figure 4. The average output power of the IR laser is approximately 50 W (at 1 MHz) and standard deviation is approximately 0.093% over 12h, as shown in Figure 4 (left). When the power of the IR laser is set to 45 W by rotating the half wave plate inside the FHG module, the average power of the UV laser is approximately 2.1 W and standard deviation is approximately 0.395%, as shown in Figure 4 (right). The overall conversion efficiency from IR laser to UV laser is about 4.67%.

Pulse energy stability of drive laser is also very important for FELs because electron beam parameters are affected by drive laser pulse energy. A photodetector (Thorlabs DET10A2), featuring 350 MHz bandwidth and 200nm–1100 nm wavelength, was used to receive the IR laser or the UV laser. An oscilloscope (Keysight Infiniium MXR404A), featuring 16GSa/s sampling rate and 200Mpts memory depth, was exploited to measure the voltage signal from the

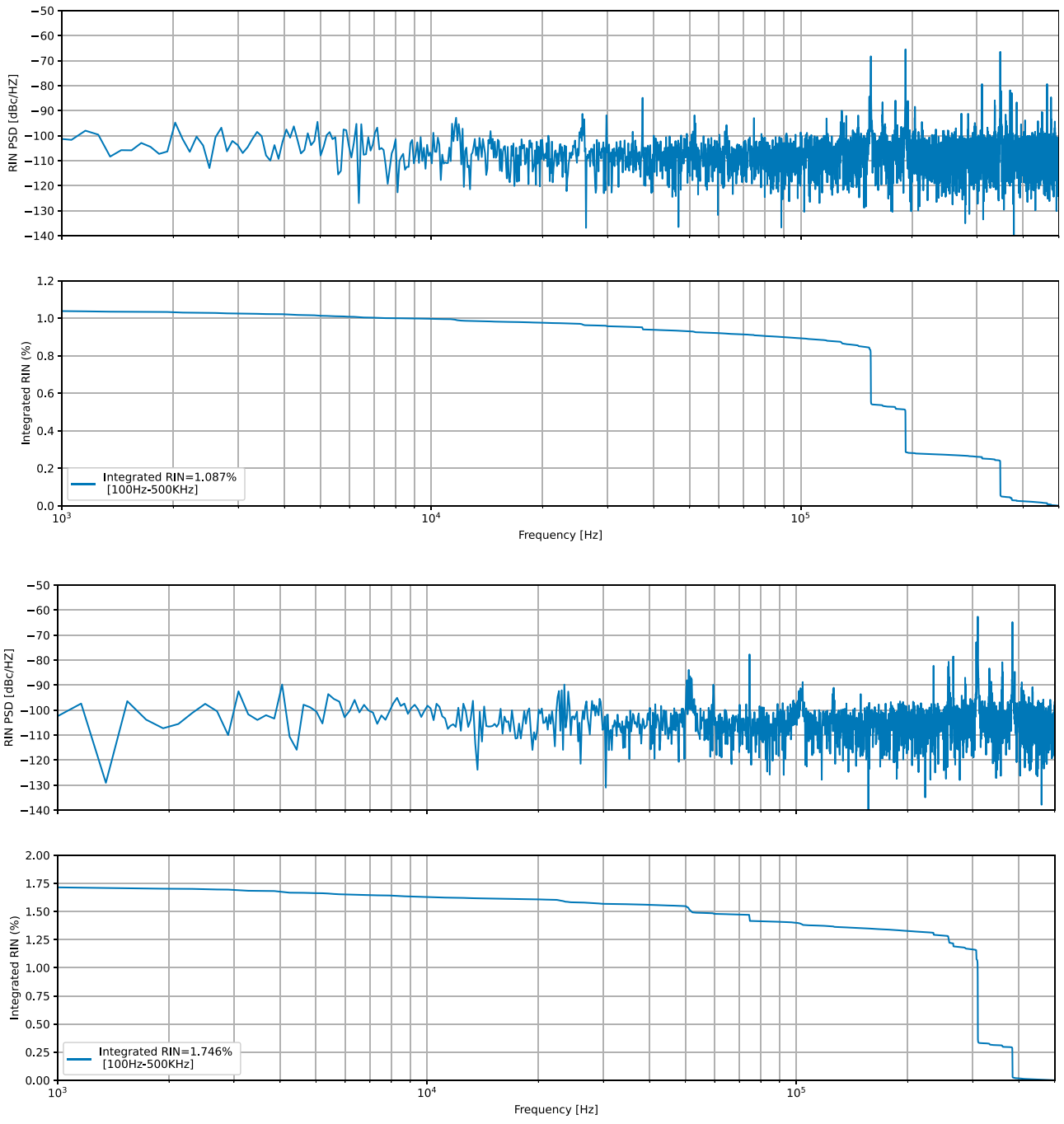

FIGURE 5
Relative Intensity Noise (RIN) of the IR (top) and the UV laser beam (bottom).

photodetector. The capture time of the oscilloscope is 12.5 ms (200Mpts/16GSa/s), which means 12,500 laser pulses (@1 MHz) can be recorded one time. The pulse energy of every laser pulse can be obtained by taking peak values of the measured voltage signal. Relative intensity noise power spectral density (RIN PSD) of pulse energy can be obtained via scipy.signal.periodogram function [18]. Relative intensity noise can be obtained by integrating the RIN PSD [19], the results are presented in Figure 5. From Figure 5 (top), we can know that the integrated RIN of the IR laser from 100 Hz to 500 KHz is 1.087% and the RIN is mainly distributed in the 100 KHz–400 KHz domain. This intensity noise should come from the oscillator because the PSD changes when another oscillator is used. Relaxation oscillation and pump power fluctuation of the oscillator may mainly contribute to the noise in this frequency range [20]. The integrated RIN of the UV laser from 100Hz to 500 KHz is 1.746%, which is almost twice of the IR laser. The RIN of the UV laser is mainly distributed in the 300 KHz–400 KHz domain, as shown in Figure 5 (bottom). When the overall conversion efficiency from IR laser to UV laser reaches 8%, the integrated RIN of the UV laser would be reduced to 1.112% due to the saturation effect of nonlinear processes. But this would deteriorate the UV laser beam quality and reduce FHG nonlinear crystal lifetime. In the future, the FHG module will be redesigned and an acousto-optic modulator (AOM) will be introduced between the two SHG nonlinear crystals to suppress the RIN of the UV laser. The AOM also acts as the fast optical shutter to protect the FEL facility when a failure occurs.

2.2 Temporal shaping

Temporal shaping of the laser involves controlling the duration and temporal profile of the laser pulses, which is important for optimizing the electron beam properties and FEL performance. In this work, we employed the typical pulse stacking for temporal shaping. Pulse stacking is a technique used to generate laser pulses with a flat-top temporal profile. This is achieved by splitting the amplified pulses into sub-pulses, delaying each sub-pulse by a controlled amount, and then recombining them to create a train of pulses with a uniform flat-top profile [21]. As shown in Figure 1, the temporal pulse shaper consists of four alpha-barium borate (α-BBO) crystals (with thickness 11.58, 5.79, 2.90, and 1.45 mm) which have large birefringence over a broad transparent range of 190–3500 nm. These crystals are cut with their optical axes parallel to their optical surfaces and anti-reflection coated at 257.7 nm. The transmission efficiency of the pulse shaper is approximately 64% owing to the linear and nonlinear absorption. The group refractive index for o-wave and e-wave is n_{go} = 2.071 and n_{ge} = 1.823 @257.5 nm [22, 23]. So, the group velocity mismatch (GVM) is 0.846 ps/mm. The temporal intensity distribution of the UV laser is measured via optical cross-correlation, as shown in Figure 1. A β-BBO crystal with 0.1 mm thickness is used as the nonlinear crystal to generate differential frequency signal (343 nm) and a PMT is used to receive the signal. A python program was developed to control the delay line (one step 3 μm) and read signal from the PMT. The temporal intensity of the UV laser can be obtained from the recorded positions of the delay line and the signals from the PMT. The temporal intensity distribution of the incident UV laser pulse is presented in Figure 6 (left), the pulse width is approximately 1 ps. The pulse shape is not perfect Gaussian, possibly due to the presence of second-order and higher-order dispersion. After the temporal pulse shaper, a nearly flat-top laser pulse with 10ps pulse width can be obtained, as shown in Figure 6 (right).

2.3 Spatial shaping

Spatial shaping of the UV pulses involves controlling the intensity profile of the laser beam in the transverse plane, which is important for generating a uniform electron beam. The 257.5 nm DUV laser used in the S^{3}FEL photoinjector incorporates a pinhole that used to generate apodized beam by the so called hard-cut method. The pinhole would be imaged onto the photocathode via the image relay system. This ensures that the laser beam has a uniform intensity distribution across the photocathode. A camera placed in the equivalent position to the photocathode plane can be used to monitor laser beam position and

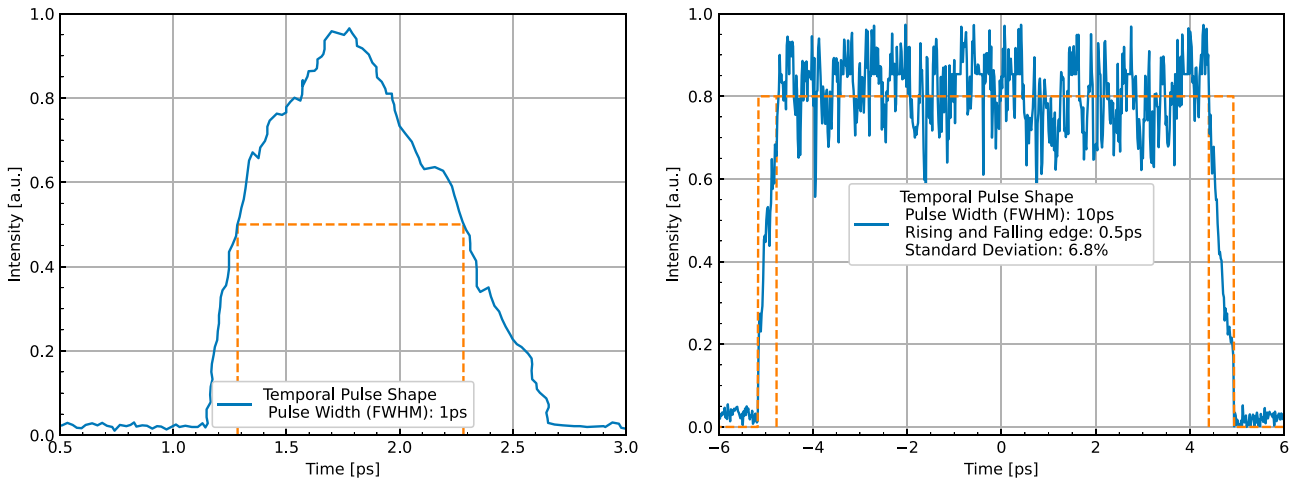

FIGURE 6
Temporal intensity distribution of the incident laser (left) and the output laser (right).

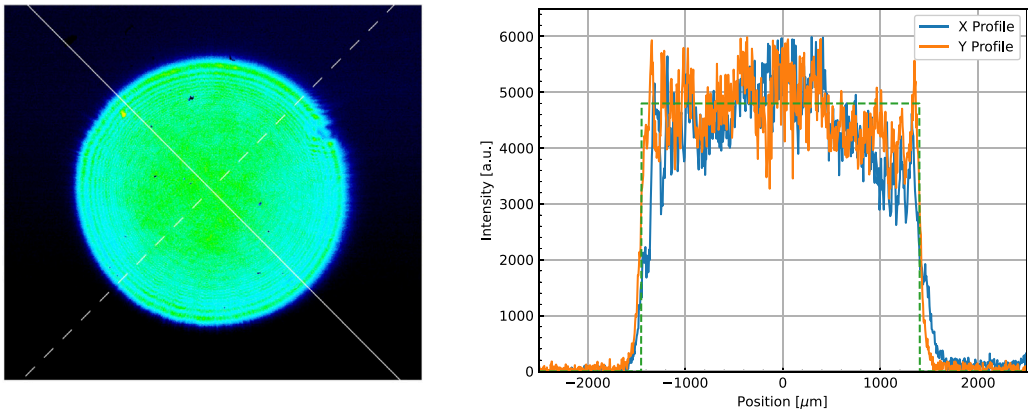

FIGURE 7
Laser beam transverse profile (left) and XY direction profile (right) after the spatial pulse shaper.

spatial distribution on the photocathode. The resulted laser beam profile recorded by the camera is presented in Figure 7. The laser beam has very sharp rising edge and falling edge which would improve the electron beam emittance. The position of the pinhole can be adjusted to ensure its image is exactly on the photocathode.

3 Conclusion

The photoinjector laser system for S^{3}FEL was established and tested. The main amplifier delivers 1 MHz, 50 uJ IR laser pulses and is tightly synchronized with RF reference and ready for locking with optical reference. With fourth harmonic generation, we generate the 257.5 nm UV laser with more than 2 W average power and good long-term performance. By pulse stacking and apodization method, we generate flat-top beam both in time and spatial domain. In the future, for longer UV temporal shaping (> 20 ps), the pulse will be directly stretched by grating pair. A cut-Gaussian transverse profile was obtained via an aperture directly which would be improved by using adaptive optics, such as digital micromirror device (DMD). Particular efforts will be made to reduce the RIN of the UV laser by inserting an AOM into the redesigned FHG module. This system will be optimized to meet the 24/7 operation requirements of the S^{3}FEL facility in the future.

Data availability statement

The raw data supporting the conclusion of this article will be made available by the authors, without undue reservation.

Author contributions

All authors listed have made a substantial, direct, and intellectual contribution to the manuscript and approved it for publication.

Funding

This work is supported by the National Natural Science Foundation of China (12175324) and Shenzhen Commission of Development and Reform Research funding (ZDKJ20200106001).

Conflict of interest

The authors declare that the research was conducted in the absence of any commercial or financial relationships that could be construed as a potential conflict of interest.

Publisher's note

All claims expressed in this article are solely those of the authors and do not necessarily represent those of their affiliated organizations, or those of the publisher, the editors and the reviewers. Any product that may be evaluated in this article, or claim that may be made by its manufacturer, is not guaranteed or endorsed by the publisher.

References

1. Ackermann W, Asova G, Ayvazyan V, Azima A, Baboi N, Bähr JW, et al. Operation of a free-electron laser from the extreme ultraviolet to the water window. *Nat Photon* (2007) 1:336–42. doi:10.1038/nphoton.2007.76

2. Cianchi A, Alesini D, Bacci A, Bellaveglia M, Boni R, Boscolo M, et al. High brightness electron beam emittance evolution measurements in an rf photoinjector. *Phys Rev ST Accel Beams* (2008) 11:032801. doi:10.1103/PhysRevSTAB.11.032801

3. Akre R, Dowell D, Emma P, Frisch J, Gilevich S, Hays G, et al. Commissioning the linac coherent light source injector. *Phys Rev ST Accel Beams* (2008) 11:030703. doi:10.1103/PhysRevSTAB.11.030703

4. Gilevich S, Alverson S, Carbajo S, Droste S, Edstrom S, Fry A, et al. The LCLS-II photoinjector drive laser system. In: Conference on lasers and electro-optics. In: 2020 Conference on Lasers and Electro-Optics (CLEO); 10-15 May 2020; San Jose, CA, USA (2020).

5. Schietinger T, Pedrozzi M, Aiba M, Arsov V, Bettoni S, Beutner B, et al. Commissioning experience and beam physics measurements at the SwissFEL injector test facility. *Phys Rev Accel Beams* (2016) 19:100702. doi:10.1103/PhysRevAccelBeams.19.100702

6. Penco G, Allaria E, Badano L, Cinquegrana P, Craievich P, Danailov M, et al. Optimization of a high brightness photoinjector for a seeded FEL facility. *J Instrumentation* (2013) 8:05015. Available from. doi:10.1088/1748-0221/8/05/p05015

7. Zhao Z, Wang D, Yang Z, Yin L. SCLF: An 8-GeV CW SCRF linac-based X-ray FEL facility in shanghai. In: Proceedings, 38th International Free Electron Laser Conference, FEL2017; 20-25 August 2017; Santa Fe, NM, United States (2018).

8. Decking W, Abeghyan S, Abramian P, Abramsky A, Aguirre A, Albrecht C, et al. A MHz-repetition-rate hard X-ray free-electron laser driven by a superconducting linear accelerator. *Nat Photon* (2020) 14:391–7. doi:10.1038/s41566-020-0607-z

9. Zhen Z, Yuantao D, Zhirong H, Feng Z. Multiplexed photoinjector optimization for high repetition rate free electron lasers. *Front Phys* (2023) 11, 11. doi:10.3389/fphy.2023.1166216

10. Gacheva EI, Zelenogorskii VV, Andrianov AV, Krasilnikov M, Martyanov M, Mironov S, et al. Disk Yb:KGW amplifier of profiled pulses of laser driver for electron photoinjector. *Opt express* (2015) 23(8):9627–39. doi:10.1364/oe.23.009627

11. Li Y, Lewellen JW. Generating a quasiellipsoidal electron beam by 3D laser-pulse shaping. *Phys Rev Lett* (2008) 100:074801. doi:10.1103/PhysRevLett.100.074801

12. Bazarov IV, Ouzounov DG, Dunham BM, Belomestnykh SA, Li Y, Liu X, et al. Efficient temporal shaping of electron distributions for high-brightness photoemission electron guns. *Phys Rev ST Accel Beams* (2008) 11:040702. doi:10.1103/PhysRevSTAB.11.040702

13. Sheehy B. ERL R&D: Laser and laser light transport (2010). BNL-90921-2010-IR. Available from: https://www.osti.gov/biblio/1013444 (Accessed March 1, 2023).

14. Xiang R, Teichert J. Photocathodes for high brightness photo injectors. *Phys Proced* (2015);77:58–65. (Accessed March 1, 2023). doi:10.1016/j.phpro.2015.11.010

15. Lederer S, Hansen H, Schreiber S. Photocathodes at flash. In: 33rd International Free Electron Laser Conference; August 22-26, 2011; Shanghai, China (2016).

16. Schreiber S, Michelato P, Monaco L, Pagani C, Sertore D. Photocathode studies at flash. In: Proceedings of EPAC08; June 23 - 27, 2008; Genoa, Italy (2008).

17. Lederer S, Michelato P, Monaco L, Sertore D. Cathode issues at the flash photoinjector. In: Proceedings of FEL08; May 13-15, 2008; Gyeongju, Korea (2008).

18. Smit-create, end olith, yotarok, WarrenWeckesser, BassCoder2808. Data From: scipy.signal.periodogram (2019). Available from: https://docs.scipy.org/doc/scipy/reference/generated/scipy.signal.periodogram.html (Accessed March 1, 2023).

19. Keller U. *Ultrafast lasers: A comprehensive introduction to fundamental principles with practical applications*. 1st ed. Cham: Springer (2022).

20. Koechner W. *Solid-state laser engineering*. 5th ed. Berlin, Heidelberg: Springer (2013).

21. Will I, Klemz G. Generation of flat-top picosecond pulses by coherent pulse stacking in a multicrystal birefringent filter. *Opt Express* (2008) 16(19):14922–37. doi:10.1364/oe.16.01492

22. Smith AV. How to select nonlinear crystals and model their performance using SNLO software. In: JW Pierce editor. *International society for optics and photonics*. Bellingham, Washington USA: SPIE (2000). p. 62–9. Nonlinear Materials, Devices, and Applications. doi:10.1117/12.379931

23. CASTECH. Alpha-barium borate (2002). Available from: https://www.castech.com/product/%CE%B1-BBO--Alpha-Barium-Borate-90.html (Accessed March 1, 2023).

frontiers | Frontiers in Physics

TYPE Original Research
PUBLISHED 21 June 2023
DOI 10.3389/fphy.2023.1170175

OPEN ACCESS

EDITED BY
Subrata Das,
National Institute for Interdisciplinary Science and Technology (CSIR), India

REVIEWED BY
Alexander Scheinker,
Los Alamos National Laboratory (DOE), United States
Igor Pogorelsky,
Brookhaven National Laboratory (DOE), United States

*CORRESPONDENCE
Andrea Bellandi,
andrea.bellandi@desy.de

RECEIVED 20 February 2023
ACCEPTED 30 May 2023
PUBLISHED 21 June 2023

CITATION
Bellandi A, Branlard J, Schlarb H and Schmidt C (2023), Feedforward resonance control for the European X-ray free electron laser high duty cycle upgrade.
Front. Phys. 11:1170175.
doi: 10.3389/fphy.2023.1170175

Feedforward resonance control for the European X-ray free electron laser high duty cycle upgrade

Andrea Bellandi*, Julien Branlard, Holger Schlarb and Christian Schmidt

Deutsches Elektronen-Synchrotron DESY, Hamburg, Germany

The High Duty Cycle (HDC) upgrade is a proposed improvement to the existing European X-ray Free Electron Laser (EuXFEL) to extend the pulsed RF duty factor from the actual value of around 1% to more than 5% up to Continuous Wave (CW). To implement this upgrade, the loaded quality factor (Q_L) of the superconducting cavities will increase by more than one order of magnitude. This will result in shrinking the cavity bandwidth to values as low as a few Hertz. Since the Lorentz Force Detuning (LFD) experienced during the accelerating field buildup is of hundreds of Hertz, the Low-Level RF (LLRF) system has to accurately track and control the cavity resonance frequency to obtain the desired accelerating gradient. Moreover, ponderomotive instabilities have to be suppressed to achieve stability during beam acceleration. Since LFD is a repetitive disturbance in cavity frequency, the correction to its effects can be implemented as a feedforward compensation on the piezoelectric tuners of the cavity. Initial results on the simulation of feedforward resonance control in the HDC regime are discussed in this proceeding.

KEYWORDS

particle accelerators, LLRF, superconducting RF, free electron laser, control systems

1 Introduction

The European X-ray Free Electron Laser (EuXFEL) is a hard X-ray FEL based on superconducting TESLA-type cavities operating in pulsed mode [1, 2]. The proposed High Duty Cycle (HDC) upgrade would make the operation of the machine in Continuous Wave (CW) mode possible, with a final beam energy of 8 GeV [3]. Due to the requirements of the experimental community, the EuXFEL HDC upgrade will also enable a Long Pulse (LP) mode of operation. In such a mode of operation, the experiments will benefit from beam energies higher than 10 GeV and, at the same time, produce a number of bunches per second comparable to machines operated in CW [4]. The LP mode is realized by extending the duty factor of the EuXFEL pulse flattop from 0.65% to 5–50%. For this mode of operation, it is planned to use the same RF amplifiers as for the CW mode and not increase the cryogenic heat load compared to the continuous case. The use of either a CW or LP mode on EuXFEL will be scheduled depending on the requirements of the experimental campaign. From the Low-Level RF (LLRF) perspective, the most significant change is the requirement to drive the RF superconducting accelerating cavities with a *loaded quality factor* (Q_L) of $6 \cdot 10^7$, one order of magnitude higher than the current value of $4.6 \cdot 10^6$. This change is required to lower the cavity RF power consumption to the kilowatt level [5, 6]. Such a change will result in an RF half bandwidth ($f_{1/2}$) of 10.8 Hz. Due to this change, the superconducting cavities will be an order of magnitude more sensitive to mechanical

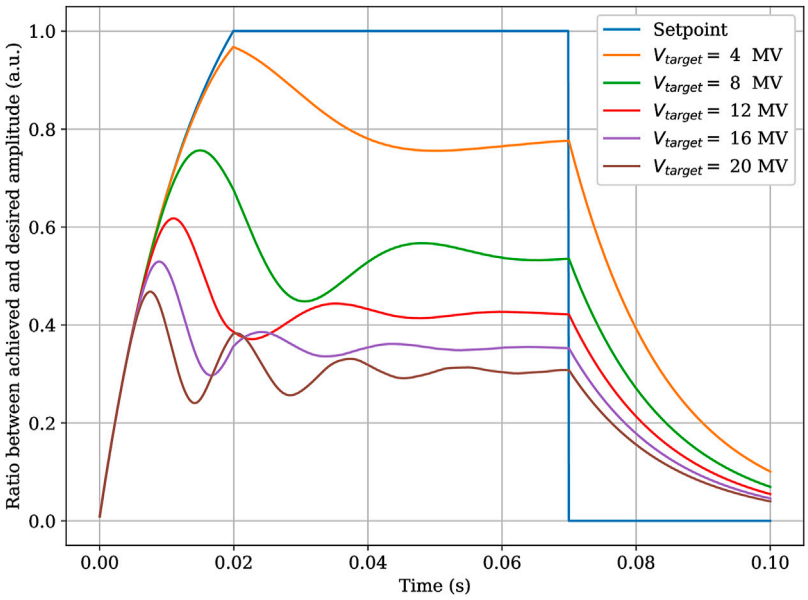

FIGURE 1
Simulation of the ratio between the target and achieved V_{acc} without any active detuning compensation. The effect of LFD-generated ponderomotive instabilities increases at higher gradients. The cavity parameters are taken from Czarski et al. [7].

disturbances. These disturbances originate from external (microphonics) and internal Lorentz Force Detuning (LFD) vibrations. A particular concern is the LFD-generated ponderomotive instabilities when driving the resonators at their maximum foreseen accelerating voltage (V_{acc}) of 20 MV. Considering a static LFD value k_{lfd} normalized to the active electrical length of the TESLA cavity (1.038 m) of up to 1.5HzMV^{-2}, the ratio between the LFD and the cavity half bandwidth will be.

$$-\frac{k_{lfd}V_{acc}^2}{f_{1/2}} = 55.3. \tag{1}$$

As explained in Schulze [8], such a value for $\frac{k_{lfd}V_{acc}^2}{f_{1/2}}$ would make the accelerating system affected by the monotonic instability. Such an effect would prevent the RF accelerating field build up inside the cavity as shown in Figure 1 [9].

Therefore it is of extreme importance to first develop a detuning-correcting method to drive the field of the cavities at a level where closed-loop operation is possible and, at the same time, not do not exceed the RF power budget of (6 kW) foreseen for the HDC upgrade. Once such a condition is realized, the residual field error will be then regulated by the RF feedback controller which operates at faster timescales compared to typical mechanical disturbances. Such scheme is necessary to realize a field regulation of 0.01% on amplitude and 0.01 deg on phase required by the EuXFEL experiments [10]. The detuning control method has to be implemented in a reliable and automated way due to its criticality in the correct operation of the accelerator. For this, the LLRF system must control the piezoelectric cavity tuners to compensate for LFD-generated effects [10, 11]. To simulate the control algorithms, an accurate mechanical model of the accelerating cavity is needed. Previous work already proved the feasibility of implementing an LFD-compensating scheme for gradients up to 14MVm^{-1} [12].

In this paper, the mechanical system model used in the simulations is given in Section 2. A feedforward control approach is presented in Section 3. Additionally, simulations using the Iterative Learning Control (ILC) algorithm are presented in Section 4 [13]. Such an algorithm is already in use in particle accelerators for RF and beam trasient compensation [14–17]. The advantage of using ILC is that repetitive un-modeled detuning disturbances can be rejected in an adaptive way. A challenge of using ILC for detuning compensation in high Q_L cavities is the presence of strong nonlinearities and hysteretic behaviour that might worsen the convergence properties of the algorithm. Therefore, in this paper, some simple modifications on the ILC algorithm were studied to limit the effect of ponderomotive instabilities. The final considerations are given in Section 5.

2 System model

The dynamics of the detuning in superconducting cavities can be described as the result of the excitation of a series of second-order mechanical resonances. These mechanical resonances can be either excited by the radiation pressure by the accelerating field or by external microphonics disturbances

$$\begin{aligned}
\dot{\Delta\mathbf{f}}^{(\mu)} &= \mathbf{A}^{(\mu)}\Delta\mathbf{f}^{(\mu)} + \mathbf{B}^{(\mu)}u(t) + \mathbf{E}^{(\mu)}V_{acc}^2(t) + \mathbf{F}^{(\mu)}\nu^{(\mu)}(t),\\
\Delta\mathbf{f}^{(\mu)} &= \begin{bmatrix}\Delta f^{(\mu)}(t)\\ \Delta\dot{f}^{(\mu)}(t)\end{bmatrix}, \quad \mathbf{A}^{(\mu)} = \begin{bmatrix}0 & 1\\ -\left(\omega^{(\mu)}\right)^2 & -\dfrac{\omega^{(\mu)}}{Q^{(\mu)}}\end{bmatrix},\\
\mathbf{B}^{(\mu)} &= \begin{bmatrix}0\\ \delta^{(\mu)}\left(\omega^{(\mu)}\right)^2\end{bmatrix}, \quad \mathbf{E}^{(\mu)} = \begin{bmatrix}0\\ k_{lfd}^{(\mu)}\left(\omega^{(\mu)}\right)^2\end{bmatrix},\\
\mathbf{F}^{(\mu)} &= \begin{bmatrix}0\\ \left(\omega^{(\mu)}\right)^2\end{bmatrix},\\
\dot{\Delta\mathbf{f}}^{(\mu)} &= \frac{d\Delta\mathbf{f}^{(\mu)}}{dt}.
\end{aligned} \tag{2}$$

Where μ is the mechanical mode index, $\Delta f^{(\mu)}$ is the detuning contribution of the mode, $\omega^{(\mu)}$, $Q^{(\mu)}$ and $\delta^{(\mu)}$ are the angular resonance frequency, quality factor and coupling with the piezoelectric actuator. $u(t)$ is the piezoelectric input variable, controllable by the LLRF system, while $v^{(\mu)}(t)$ is the microphonic noise. $v^{(\mu)}(t)$ might be not synchronized with the accelerator timing. In general, an effective resonance control system requires driving $u(t)$ so the detuning Root Mean Square (RMS) is smaller than the half bandwidth

$$\Delta f_{RMS} = \left(\sum_{\mu} \Delta f^{(\mu)} \right)_{RMS} < f_{1/2}, \tag{3}$$

To minimize the RF power required to drive the cavity at a certain accelerator voltage [5].

In this work, we ignore the problem of rejecting unsynchronous detuning originating from $v^{(\mu)}(t)$ since the repetitive LFD-generated disturbance is around two orders of magnitude higher [18]. The compensation of the unsynchronized part of $v^{(\mu)}(t)$ will be addressed in future studies.

3 Feedforward control

During the nominal operation of EuXFEL HDC, the accelerating field $V_{acc}(t)$ will be required to have a well-defined periodic structure repeated in time with a repetition rate of 1 Hz. Such a *pulse* will have three distinct regions. These are the filling, flattop, and decay regions [19]. In the HDC upgrade, the filling region will last 20 ms. The flattop region length will be between 50 ms and 500 ms depending on the resulting dynamic heat load and cryogenic capacity [20]. The reference trajectory $V_{ref}(t)$ is then defined

$$V_{ref}(t) = \begin{cases} V_{flat} \dfrac{1 - e^{-2\pi f_{1/2}(t - t_{fill})}}{1 - e^{-2\pi f_{1/2}(t_{flat} - t_{fill})}} & \text{for} \quad t_{flat} > t \geq t_{fill} \quad \text{(filling)} \\ V_{flat} & \text{for} \quad t_{decay} > t \geq t_{flat} \quad \text{(flattop)} \\ V_{flat} e^{-2\pi f_{1/2}(t - t_{decay})} & \text{for} \quad t \geq t_{decay} \quad \text{(decay)} \end{cases} \tag{4}$$

Where t_{fill}, t_{flat}, t_{decay} are the starting times for the filling, flattop, and decay regions, V_{flat} is the desired accelerating voltage at flattop. Since Eq. 4 describes the desired field, it can be inserted in Eq. 2 to find the radiation pressure-induced detuning excitation and, consequently, the function for $u(t)$ that achieves a perfect disturbance compensation. To do this $\omega^{(\mu)}$, $Q^{(\mu)}$ and $\delta^{(\mu)}$ have to be determined. Alternatively, a transfer function approach can be used by measuring the step response to V_{acc}^2 variations. However, the characterization of cavity mechanical parameters is still matter of study and the presence of high quality factor mechanical resonances complicates the identification process. A more simplistic approach is to use a zero-order approximation of Eq. 2, by setting the time derivatives to zero. Then it is possible to solve the equations the actuator drive $u_0(t)$

$$u_0(t) = \frac{k_{lfd} V_{ref}^2(t)}{\sum_{\mu} \delta^{(\mu)}}. \tag{5}$$

Eq. 5 can be used in the simulations to see if it is sufficient to prevent the occurrence of ponderomotive instabilities.

Figure 2 shows the shape of the feedforward piezoelectric tuner drive of Eq. 5.

Figure 3 shows a simulation of an accelerating cavity when the zero-order feedforward correction is used. The LFD effects are significantly reduced compared to Figure 1 even though the dynamics of the cavity is not taken into account in the feedforward signal compitation. The sharp transition between the different pulse regions produces the residual excitation of the mechanical resonances.

4 Iterative learning control

The correction of the residual mechanical oscillations resulting from the use of Eq. 5 and unmodeled detuning disturbances in TESLA-like cavities is challenging using white-box approaches [21]. Therefore, an adaptive gray-box ILC method is used. The idea is that future RF pulses can be corrected adaptively using the detuning information acquired in past pulses. An ILC-like method is already implemented at EuXFEL [22]. However, the difference in pulse length and Q_L with respect to the HDC upgrade makes it unsuitable in LP mode due to the absence of strong nonlinear ponderomotive effects. For the simulation tests in LP mode, a modified discrete Arimoto-like update law

$$\Delta u_{k+1}(n) = \sum_{q=-\infty}^{\infty} Q(q) \left[\Delta u_k(n-q) + \gamma \Delta f_k(n+d-q) \right], \tag{6}$$

Is chosen. In the above formulation, the classical Arimoto algorithm was changed to take into account the time-delay in the step response that originate from the high quality factor mechanical resonances. The adaptive correction component $\Delta u_k(n)$ is summed with Eq. 5 to give the piezo driving signal for a pulse identified with k. n is the sample within the pulse. The simulations use a sample rate of 5 kHz. Such a sample rate is roughly ten times the highest resonance frequency of the set of parameters used in the simulations [7]. d is the sample delay and is chosen by

$$d = \arg_n \max |h(n)|, \tag{7}$$

with $h(n)$ the impulse response of Eq. 2. For the set of parameters used in the simulations $d = 3$. The controller gain γ is empirically found to be $\simeq -0.15$ by looking at the value that gives the fastest algorithm convergence. $Q(q)$ is a second order lowpass filter with a bandwidth of 1 kHz synthetized and applied using the routines *butter* and *sosfiltfilt* of the package *SciPy* [23]. $Q(q)$ prevents the growth of high-frequency noise at increasing k. A benefit of the method of Eq. 6 is the low computational complexity. A mechanical model-aware ILC might give better results in terms of disturbance rejection. However it would require further theoretical study. The reduction in detuning resulting from the application of Eq. 6 is simulated for a cavity driven at 20 MV for the following cases.

- Static detuning of 0 Hz (tuned)
- Static detuning of −5.4 Hz ($-f_{1/2}/2$) (under-tuned)
- Static detuning of 5.4 Hz ($f_{1/2}/2$) (over-tuned)
- Gaussian microphonics with a standard deviation of 0.5 Hz

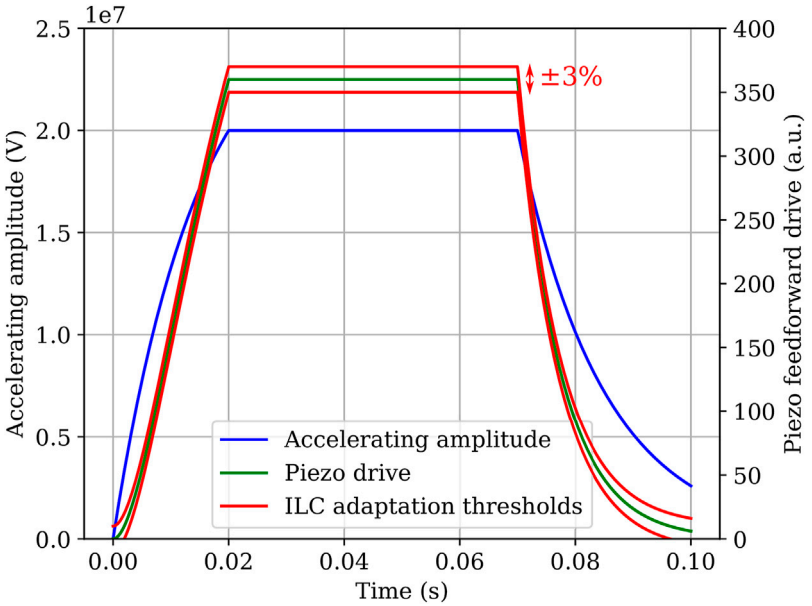

FIGURE 2
Accelerating voltage pulse structure at 20 MV and piezo feedforward drive generated using Eq. 5. Additionally, the learning thresholds for the clipped ILC algorithm are shown. The ILC correction magnitude is constrained to be within ± 3% the feedforward value at flattop.

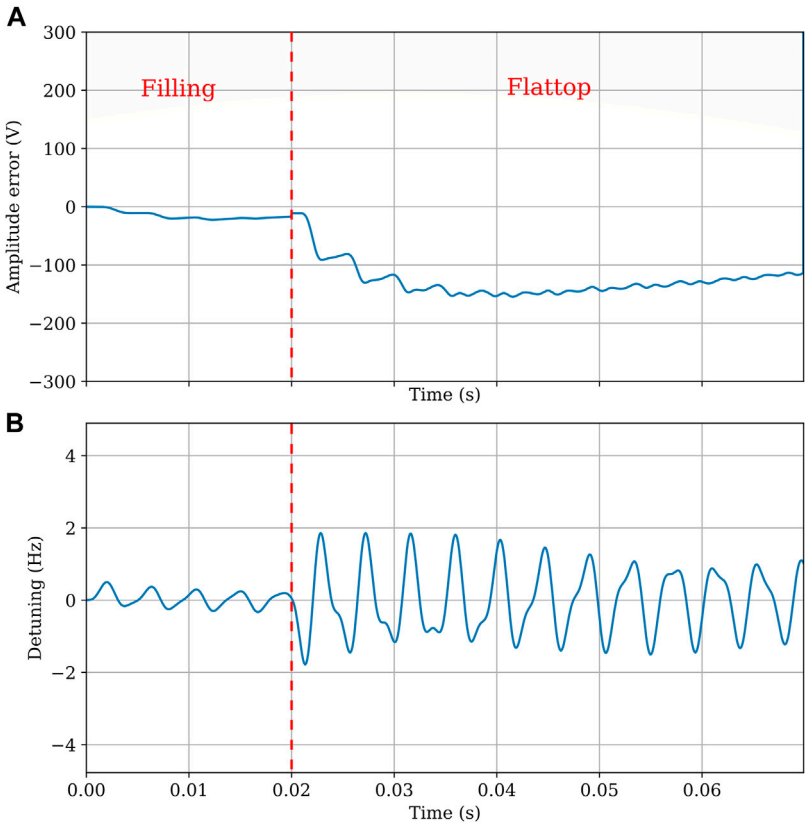

FIGURE 3
Simulation of the accelerating voltage error **(A)** and detuning **(B)** when the zero-order piezo feedforward is applied. The cavity system is simulated with an open RF loop. The simulation shows that in the flattop, an amplitude error of 200 V over an accelerating field of 20 MV. $\delta^{(\mu)}$ = 0.33 Hz. The residual detuning oscillation is ±2 Hz.

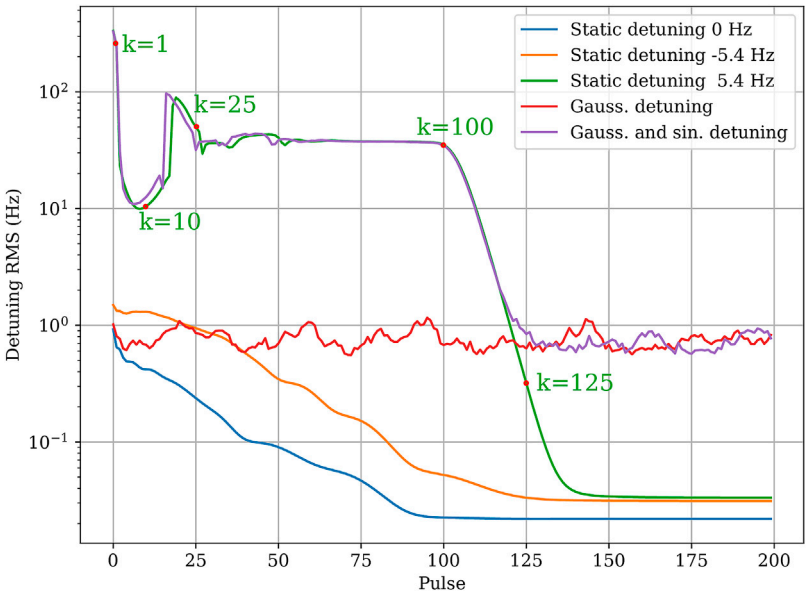

FIGURE 4
Detuning RMS in the *filling* and *flattop* region as a function of the pulse number for different types of detuning disturbances. The system is adapted using the ILC algorithm of Eq. 6.

- Gaussian microphonics with a standard deviation of 0.5 Hz plus a sinuisoidal component with a frequency of 50 Hz and an amplitude 5 Hz

The detuning disturbances of the above list are chosen to be similar to the ones observed in working particle accelerators and test facilities [18].

Figure 4 shows the convergence of the modified Arimoto ILC. For the tuned and under-tuned case, the detuning converges monotonically to values of 0.02 – 0.03 Hz RMS. The uncorrelated microphonics contributions dominate the detuning RMS for the trace affected by gaussian noise. Therefore, in this case, the ILC cannot decrease the pulse detuning noticeably. Still, the detuning remains in the order of 1 Hz RMS, fulfilling the requirement of Eq. 3. The most interesting cases are the over-tuned simulation and the one affected by sinusoidal microphonics. The initial detuning RMS is over 300 Hz and stays constant at a level of 40 Hz for both cases between $k = 25$ and $k = 100$. Then the detuning RMS starts decreasing and reaches a value of 1 Hz at $k = 120$. The explanation for this behaviour is that the simulated cavity, when over-tuned due to static detuning or microphonics, experiences a *static drop* [8] that detunes positively the cavity by several hundred Hertz. Therefore the ILC learns an invalid correction for the trace points affected by the static drop.

After the ILC under-tunes the cavity enough to prevent the static drop from happening, it has to 'unlearn' the invalid part of the correction for the RMS detuning value to decrease again (Figure 5). At a repetition rate of 1 Hz, the tuning might reach acceptable RMS levels only after 2 min. This delay would complicate the machine setup operations because the operators would need to wait until the algorithm converges to continue the accelerator commissioning. A possible improvement is to modify Eq. 6 to constrain the values in the ILC correction table within a pre-determined range

$$\Delta u_{k+1}(n) = \sum_{q=-\infty}^{\infty} Q(q)\,\mathrm{clip}\left(-\Delta u_{learn}, \Delta u_{learn}, \Delta u_k(n-q) + \gamma \Delta f_k(n+d-q)\right), \tag{8}$$

Where

$$\mathrm{clip}(a,b,x) = \begin{cases} a & \text{for} \quad a > x \\ x & \text{for} \quad b > x \geq a \\ b & \text{for} \quad x \geq b \end{cases} . \tag{9}$$

Δu_{learn} determines the maximum learning range for the ILC algorithm. Therefore, even in the case of a static drop, the controller does not learn an excessive tuning correction. From the simulations, $\Delta u_{learn} = 10$ is enough for the final correction to be represented in the tables. Using Eq. 8, a much faster convergence is achieved for the over-tuned case and the one affected by sinusoidal microphonics. For pulses with $k > 3$, a detuning ≈ 1 Hz RMS is achieved for both cases. No significant differences to the simulations performed with the original ILC algorithm were found for the other cases.

5 Final remarks

This article presented a study of a possible feedforward detuning compensation scheme for superconducting cavities. The simulation of the compensation of the ponderomotive instabilities in TESLA cavities driven at $V_{acc} = 20$ MV and $Q_L = 6 \cdot 10^7$ was possible by using a simple zero-order approximation. Additionally, the use of an Arimoto-like ILC algorithm allowed the compensation of the disturbances generated by the residual un-modeled mechanical dynamics in the presence of microphonics and ponderomotive instabilities. Clipping the values of the ILC controller not only allowed reaching an acceptable detuning root mean square values after just 3 s of operation but limited the amplitude of

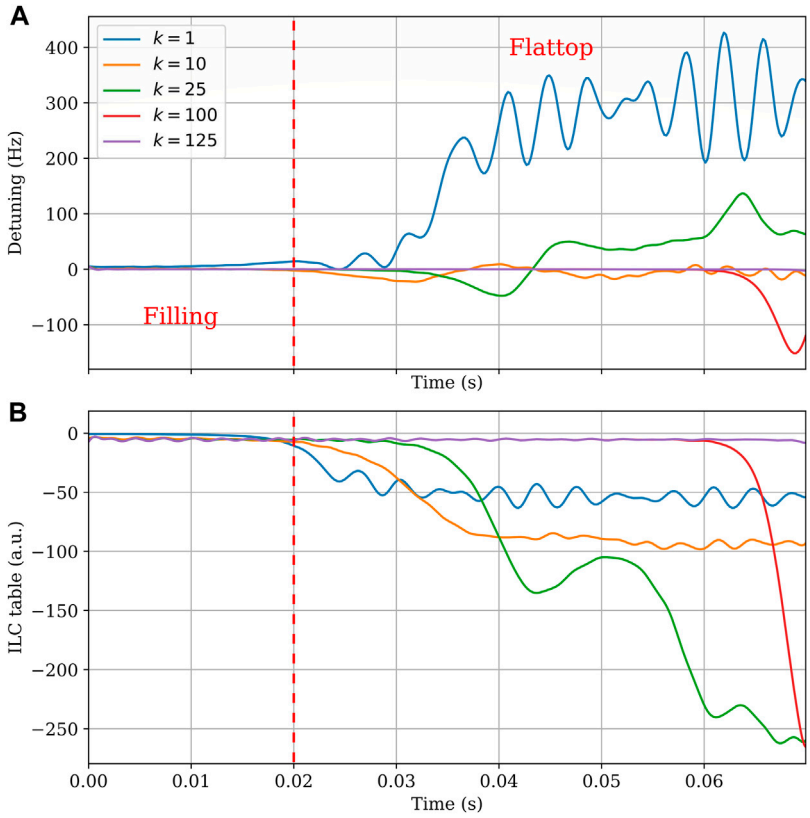

FIGURE 5
Detuning **(A)** and ILC table **(B)** at different values of *k* for the first version of the ILC algorithm. The simulation is performed with a static predetuning of 5.4 Hz. The evaluated *k* corresponds to the ones highlighted in Figure 4. As can be seen in plot **(B)**, due to the presence of the monotonic instability, the ILC algorithm learns initially an incorrect state. Such an incorrect state requires around 125 ILC iteration to be cleared.

the piezo driving signal within ± 3% the value already provided by the static feedforward correction of Eq. 5. Since real piezoelectric tuners can be damaged when driven at high voltage values, such a technique could help increase the lifespan of these actuators. The approach of limiting or stopping the correction learning of adaptive controller when an anomalous condition is met is already in used at European XFEL for RF. These results show for the first time the feasibility of performing resonance control in high-duty cycle pulsed mode superconducting accelerators even when the cavity bandwidth is of few Hertz. Further research will concentrate on using a more accurate model-aware feedforward compensation scheme to minimize the mechanical excitation between pulse region transitions. Also, the ILC will need a more sophisticate exception handling mechanism to avoid learning invalid corrections during other anomalous conditions, like cavity quenches or amplifier trips, that might happen during operations. The presented compensation methods will be experimentally tested in the forthcoming year at DESY module superconducting test facilities.

Data availability statement

The raw data supporting the conclusion of this article will be made available by the authors, without undue reservation.

Author contributions

AB contributed to the idea, design, and simulation of the feedforward and ILC control scheme for resonance control in long pulse mode of operation. JB and HS contributed to the requirements of the resonance controller for the European XFEL HDC upgrade. CS contributed with consulting on the use of the ILC technique. All authors contributed to the article and approved the submitted version.

Funding

This work is supported by the Helmholtz institute and by European XFEL GmbH.

Conflict of interest

The authors declare that the research was conducted in the absence of any commercial or financial relationships that could be construed as a potential conflict of interest.

Publisher's note

References

1. Aune B, Bandelmann R, Bloess D, Bonin B, Bosotti A, Champion M, et al. Superconducting TESLA cavities. *Phys Rev Spec Topics-Accel Beams* (2000) 3:092001. doi:10.1103/physrevstab.3.092001

2. Brinkmann R. *The european XFEL project*, 6. FEL (2006). p. 24.

3. Sekutowicz J, Ayvazyan V, Barlak M, Branlard J, Cichalewski W, Grabowski W, et al. Research and development towards duty factor upgrade of the European X-Ray Free Electron Laser linac. *Phys Rev Spec Topics-Accel Beams* (2015) 18:050701. doi:10.1103/physrevstab.18.050701

4. Brinkmann R, Schneidmiller E, Sekutowicz J, Yurkov M Prospects for CW and LP operation of the European XFEL in hard X-ray regime. *Nucl Instr Methods Phys Res Section A: Acc Spectrometers, Detectors Assoc Equip* (2014) 768:20–5. doi:10.1016/j.nima.2014.09.039

5. Padamsee H *RF superconductivity: Science, technology, and applications*. John Wiley & Sons (2009).

6. Neumann A, Anders W, Kugeler O, Knobloch J Analysis and active compensation of microphonics in continuous wave narrow-bandwidth superconducting cavities. *Phys Rev Spec Topics-Accel Beams* (2010) 13:082001. doi:10.1103/physrevstab.13.082001

7. Czarski T, Pozniak KT, Romaniuk RS, Simrock S Tesla cavity modeling and digital implementation with fpga technology solution for control system development. In: Photonics Applications in Astronomy, Communications, Industry, and High-Energy Physics Experiments II, 5484. SPIE (2004). p. 111–29.

8. Schulze D (1972). *Ponderomotive stability of RF resonators and resonator control systems*. Tech. rep.,. FR Germany: Kernforschungszentrum Karlsruhe, Inst. fuer Experimentelle Kernphysik.

9. Bellandi A, Branlard J, Eichler A, Pfeiffer S Integral resonance control in continuous wave superconducting particle accelerators. *IFAC-PapersOnLine* (2020) 53:361–7. doi:10.1016/j.ifacol.2020.12.186

10. Branlard J, Ayvazyan G, Ayvazyan V, Grecki M, Hoffmann M, Jezynski T, et al. The European XFEL LLRF system. *IPAC* (2012) 12:55–7.

11. Bosotti A, Paparella R, Albrecht C Development of an acceptance test procedure for the xfel sc cavity tuners. In: Proceedings, 23rd Conference, PAC'09 (2009).

12. Cichalewski W, Sekutowicz J *Long pulse operation of the E-XFEL cryomodule* (2022). JACoW IPAC2022, TUPOST018. doi:10.18429/JACoW-IPAC2022-TUPOST018

13. Moore KL *Iterative learning control for deterministic systems* (2012).

14. Kichhoff S, Schmidt C, Lichtenberg G, Werner H An iterative learning algorithm for control of an accelerator based free electron laser. In: 2008 47th IEEE Conference on Decision and Control (2008). p. 3032–7. doi:10.1109/CDC.2008.4739064

15. Pfeiffer S, Lichtenberg G, Schmidt C, Schlarb H Tensor techniques for iterative learning control of a free-electron laser. In: 2012 IEEE International Conference on Control Applications (2012). p. 160–5. doi:10.1109/CCA.2012.6402643

16. Qiu F, Michizono S, Matsumoto T, Miura T, Wibowo SB, Liu N Development of iterative learning and disturbance observer-based llrf control system for international linear collider. In: Proceedings of the 14th Annual Meeting of Particle Accelerator Society of Japan (2017). p. 490–2.

17. Shahriari Z, Dumont GA, Fong K Current-iteration non-causal iterative learning control for beam loading cancellation in particle accelerators. In: 2019 8th International Conference on Systems and Control (ICSC) (2019). p. 170–5. doi:10.1109/ICSC47195.2019.8950532

18. Bellandi A, Branlard J, Cruz JD, Aderhold S, Benwell A, Brachmann A, et al. *Narrow bandwidth active noise control for microphonics rejection in superconducting cavities at LCLS-II* (2022). arXiv preprint arXiv:2209.13896.

19. Simrock S, Geng Z *Low-level radio frequency systems*. Springer Nature (2022).

20. Walker N, Decking W, Branlard J, Sekutowicz J High-duty-cycle operations scenarios at the European XFEL accelerator Frontiers in Physics. In: *Global developments towards continuous-wave free-electron lasers* (2023).

21. Scheinker A Application of extremum seeking for time-varying systems to resonance control of rf cavities. *IEEE Trans Control Syst Technol* (2017) 25:1521–8. doi:10.1109/TCST.2016.2604742

22. Przygoda K, Butkowski L, Omet M, Hierholzer M, Grecki M, Branlard J, et al. Piezo controls for the European XFEL. In: 10th Int. Particle Accelerator Conf.(IPAC'19); 19-24 May 2019; Melbourne, Australia. Geneva, Switzerland: JACOW Publishing (2019). p. 3856–9.

23. Virtanen P, Gommers R, Oliphant TE, Haberland M, Reddy T, Cournapeau D, et al. SciPy 1.0: Fundamental algorithms for scientific computing in Python. *Nat Methods* (2020) 17:261–72. doi:10.1038/s41592-019-0686-2

frontiers | Frontiers in Physics

TYPE Original Research
PUBLISHED 22 June 2023
DOI 10.3389/fphy.2023.1204073

OPEN ACCESS

EDITED BY
Kazuya Hayata,
Sapporo Gakuin University, Japan

REVIEWED BY
Riccardo Meucci,
National Research Council (CNR), Italy
Patrick Krejcik,
Stanford University, United States

*CORRESPONDENCE
Sara Casalbuoni,
sara.casalbuoni@xfel.eu

RECEIVED 11 April 2023
ACCEPTED 01 June 2023
PUBLISHED 22 June 2023

CITATION
Casalbuoni S, Abeghyan S, Alanakyan L, Baader J, Barbanotti S, Decking W, Felice MD, Eckoldt H-J, Englisch U, Geloni G, Grattoni V, Grau A, Hauberg A, Helwich C, Hobl A, Jensch K, Karabekyan S, Civita DL, Lederer S, Lechner C, Lilje L, Liu S, Marchetti B, Potter A, Schnautz T, Schneidmiller E, Sinn H, Walter W, Wichmann R, Wohlenberg T, Yakopov G, Yakopov M, Zagorodnov I, Zimmermann R and Ziolkowski P (2023), Superconducting undulator activities at the European X-ray Free-Electron Laser Facility.
Front. Phys. 11:1204073.
doi: 10.3389/fphy.2023.1204073

Superconducting undulator activities at the European X-ray Free-Electron Laser Facility

Sara Casalbuoni[1]*, Suren Abeghyan[1], Levon Alanakyan[1], Johann Baader[1], Serena Barbanotti[2], Winfried Decking[2], Massimiliano Di Felice[1], Hans-Jörg Eckoldt[2], Uwe Englisch[1], Gianluca Geloni[1], Vanessa Grattoni[1], Andreas Grau[3], Axel Hauberg[2], Christian Helwich[2], Achim Hobl[4], Kay Jensch[2], Suren Karabekyan[1], Daniele La Civita[1], Sven Lederer[2], Christoph Lechner[1], Lutz Lilje[2], Shan Liu[2], Barbara Marchetti[1], Andrew Potter[5], Tobias Schnautz[2], Evgeny Schneidmiller[2], Harald Sinn[1], Wolfgang Walter[4], Riko Wichmann[2], Torsten Wohlenberg[2], Grigory Yakopov[1], Mikhail Yakopov[1], Igor Zagorodnov[2], René Zimmermann[2] and Pawel Ziolkowski[1]

[1]European X-ray Free-Electron Laser Facility, Schenefeld, Germany, [2]Deutsches Elektronen-Synchrotron, Hamburg, Germany, [3]Karlsruhe Institute of Technology, Karlsruhe, Germany, [4]Bilfinger Noell GmbH, Wurzburg, Germany, [5]University of Liverpool, Liverpool, England

For more than 5 years, superconducting undulators (SCUs) have been successfully delivering X-rays in storage rings. The European X-Ray Free-Electron Laser Facility (XFEL) plans to demonstrate the operation of SCUs in X-ray free-electron lasers (FELs). For the same geometry, SCUs can reach a higher peak field on the axis with respect to all other available technologies, offering a larger photon energy tunability range. The application of short-period SCUs in a high electron beam energy FEL > 11 GeV will enable lasing at very hard X-rays > 40 keV. The large tunability range of SCUs will allow covering the complete photon energy range of the soft X-ray experiments at the European XFEL without changing electron beam energy, as currently needed with the installed permanent magnet undulators. For a possible continuous-wave (CW) upgrade under discussion at the European XFEL with a lower electron beam energy of approximately 7–8 GeV, SCUs can provide the same photon energy range as available at present with the permanent magnet undulators and electron energies. This paper will describe the potential of SCUs for X-ray FELs. In particular, it will focus on the different activities ongoing at the European XFEL and in collaboration with DESY to allow the implementation of SCUs in the European XFEL in the upcoming years.

KEYWORDS

free-electron laser, future light source, superconducting undulator, hard X-rays, continuous-wave, magnetic measurements, instrumentation, photon science

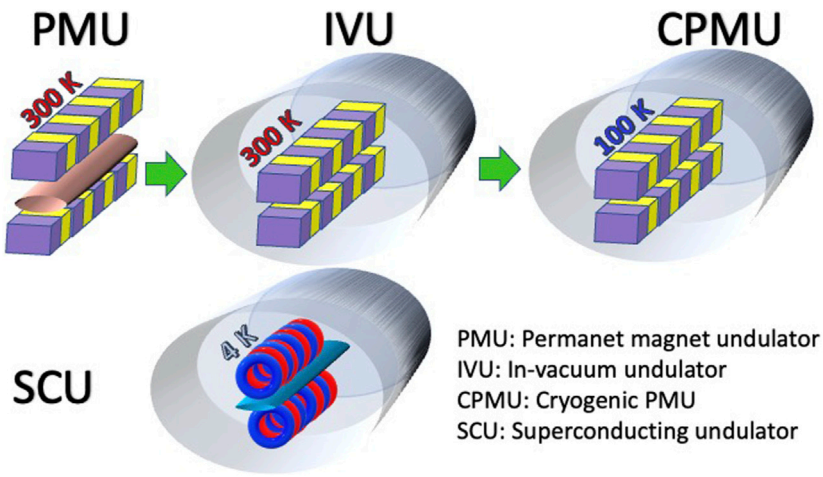

FIGURE 1
Top: sketches of the evolution of permanent magnet undulator technology to achieve a higher magnetic peak field on the magnetic axis. Bottom: a sketch of NbTi superconducting undulator technology, which allows to further improve the peak field on the magnetic axis with respect to the one that is PMU-based.

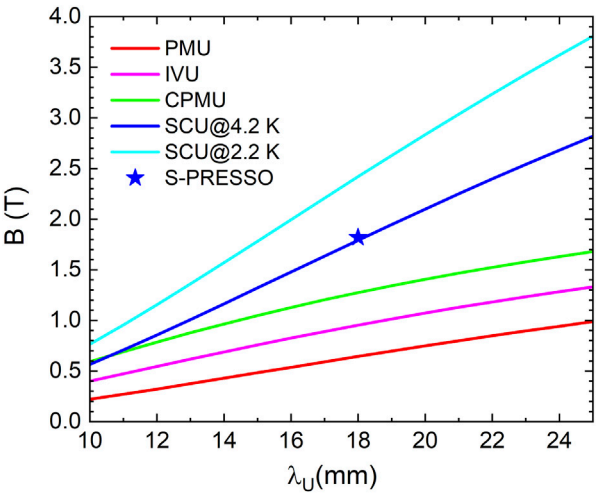

FIGURE 2
Comparison in terms of the magnetic field as a function of the undulator period at a beam stay clear/vacuum gap of 5 mm for different undulator technologies sketched in Figure 1. The peak field on the magnetic axis of S-PRESSO is also shown.

1 Introduction

Storage rings and free-electron lasers (FELs) make use of undulators to deliver highly brilliant photon beams to a vast user community. Undulators are special magnets consisting of an array of dipoles that produce a sinusoidal magnetic field. Undulators emit radiation at specific wavelengths λ_n:

$$\lambda_n = \frac{\lambda_U}{2n\gamma^2}\left(1+\frac{K^2}{2}\right); K = \frac{eB\lambda_U}{2\pi m_e c}, \quad (1)$$

where λ_U is the undulator period, $n = 1,2,3,...$ is an integer describing the harmonic number, and γ is the Lorentz factor. K is the "so-called" undulator parameter, e is the electron beam charge, B is the peak magnetic field on the axis, m_e is the electron mass, and c is the speed of light. Most of the undulators used nowadays are based on permanent magnet technology. As shown in Equation (1), in order to reduce the photon wavelength/increase the photon energy without increasing the electron beam energy at a fixed peak magnetic field on axis B, the undulator period λ_U needs to be reduced. On the other hand, for the same technology and geometry, by reducing λ_U, the peak magnetic field on axis B and, therefore, the tunability range (the available photon energy range) are also decreased.

Different efforts have been made in the past decades to reduce the period of the undulators while keeping a high magnetic field on axis B. Figure 1 shows the evolution of these efforts. On the top left is sketched a permanent magnet undulator (PMU) with the magnet arrays out of the vacuum chamber. The first step has been the inclusion of the magnetic arrays inside the electron beam vacuum chamber. In this way, the magnets are closer to the electron beam, which, therefore, is subject to a higher magnetic field. These are the "so-called" in-vacuum undulators (IVUs). The second step consisted in cooling the magnetic arrays in the IVUs. By cooling the magnets to approximately 100 K, their remanence increases and so does the peak field on the magnetic axis. These are the "so-called" cryogenic permanent magnet undulators (CPMUs). In order to further increase the peak field on the axis, superconducting magnet technology has been applied. Superconducting undulators (SCUs) have dipole arrays made of superconducting coils cooled down to approximately 4 K.

A comparison in terms of peak field on the magnetic axis between the aforementioned technologies is shown in Figure 2. A beam stay clear/vacuum gap of 5 mm has been considered. The curves reported in Figure 2 are obtained by the following parametrization curves. For the magnetic field on axis B (T) of

the PMUs and IVUs with, respectively, a magnetic gap g of 7 mm and 5.2 mm, the following function [1] is considered:

$$B = 3.381 \cdot \exp\left(-4.73 \cdot \frac{g}{\lambda_U} + 1.198 \cdot \left(\frac{g}{\lambda_U}\right)^2\right). \quad (2)$$

The magnetic field of the CPMUs with $g = 5.2$ mm is described by [2].

$$B = 3.502 \cdot \exp\left(-3.604 \cdot \frac{g}{\lambda_U} + 0.359 \cdot \left(\frac{g}{\lambda_U}\right)^2\right). \quad (3)$$

The one for the SCUs is described by [3].

$$B = \left(0.28052 + 0.05798 \cdot \lambda_U - 0.0009 \cdot \lambda_U^2 + 5.10^{-6} \cdot \lambda_U^3\right) \cdot \exp\left(-\pi \cdot \left(\frac{g}{\lambda_U} - 0.5\right)\right), \quad (4)$$

where λ_U and g are in mm and B is in T. The blue curve shown in Figure 2 for SCUs is valid by operating at a temperature of 4.2 K with a temperature margin of 1 K for both of the following cases: a) a magnetic gap of 6 mm applying ≈80% of the critical current and b) a magnetic gap of 6.5 mm applying ≈85% of the critical current. The last one, which is the case for S-PRESSO, the first SCU to be installed at the European XFEL, is described in Section 4. SCUs show potential to further increase their performance, as shown in the blue curve in Figure 2. This is possible by applying superconductors with higher critical temperatures and current densities, such as Nb_3Sn or high-temperature superconducting tapes or bulks. Both technologies are not mature yet. Another possibility is to work with the well-proven technology based on the NbTi wire using a cooling scheme, allowing it to reach lower temperatures (the cyan curve in Figure 2). Applying superfluid helium cooling schemes as performed for the Nb superconducting radio frequency (RF) cavities improves the peak field on the axis by 35%. The cyan curve in Figure 2 is obtained by multiplying the right term of Equation (4) by 1.35. Simulations made with FEMM (http://www.femm.info/wiki/HomePage) confirmed this parametrization for 10, 15, 18, 20, and 25-mm period length SCUs with a magnetic gap of 6 mm and a temperature margin of 1 K.

An additional advantage of NbTi SCUs with respect to permanent magnet-based undulators is radiation hardness, which has been demonstrated in NbTi magnets used in different colliders such as the Tevatron [4], HERA [5], and LHC [6] for several decades.

The choice of the undulator period is driven by the selected photon energy range and can be made once the electron energy is fixed. To cover an even larger photon energy range, it is possible to 1) vary the electron beam energy, which is performed, for example, at the European XFEL and 2) use undulators with period doubling. These possibilities complicate the parameter space, and for the sake of simplicity, they should be kept as options and not as guiding lines. It should also be remembered that the large tunability range of the photon energy presents challenges for both the optics and the experimental techniques.

SCUs offer elegant solutions, using the same winding body, to duplicate or triplicate the period length, which can further increase the photon energy tunability range considerably [7].

SCUs based on NbTi coils have been serving users since more than 5 years at the Advanced Photon Source (APS) [8] and the Karlsruhe Institute of Technology (KIT) light source [9]. SCUs are now commercially available from the company Bilfinger Noell GmbH (BNG). A long-term development carried out at KIT in collaboration with the industrial partner BNG has led to the successful commercialization of SCUs [10]. Recently, an SCU produced by BNG and measured by KIT has been installed in the Australian Light Source [11].

It is now time to implement SCUs in FELs. The potential of SCUs for X-ray FELs is addressed in the following section. Afterward, the plans for implementing SCUs at the European XFEL and the ongoing activities necessary to realize them are described.

2 Superconducting undulators for X-ray free-electron lasers

In terms of cost reduction, the main advantage of using short-period and strong magnetic field undulators, such as SCUs, for an FEL with respect to PMUs, is that, to reach a defined photon energy, it is possible to reduce the electron beam energy.

In the case of an undulator with a shorter period but keeping the same K value, the saturation length is shorter, and consequently, the length of the undulator line is shorter. For a green field facility, this would result in considerable savings in civil construction costs.

Advantages of SCU over PMUs include the following:

- SCUs allow for building more compact and, therefore, less expensive FELs.
- For a given electron beam energy, SCUs allow to reach harder X-rays than PMUs, maintaining a larger tunability. This is because SCUs can reach higher peak fields for the same geometry.
- Due to the larger maximum peak magnetic field, SCUs offer wider photon energy tunability ranges than PMUs.

Currently, X-ray FELs use PMUs and IVUs. However, there are no plans, to the best of authors' knowledge, to install CPMUs, SHINE, LCLS, and European XFEL working on the implementation of SCUs [12]. The Chinese CW X-ray FEL SHINE plans a complete undulator line with SCUs [13]. The LCLS facility is planning to install a cryostat with two 1.5-m-long SCU coils with a cold intersection in between consisting of a superconducting phase shifter, a copper quadrupole, and an RF cavity BPM [14]

SCUs are part of the European XFEL facility development program. The development of SCUs will enable us to build the know-how inside the facility for the state-of-the-art technology and further improve the know-how technology to be later transferred to industries. The benefits of SCUs to the European XFEL strategic plan are manifold:

- The European XFEL has the highest electron beam energy among all the similar facilities worldwide [15]. SCUs with a period between 15 and 20 mm, and a vacuum gap (magnetic gap) of 6 mm (7 mm) offer the possibility to establishing an FEL source above 30 keV toward 100 keV, which is unprecedented to date [16,17].
- The European XFEL has two hard undulator lines and one soft X-ray undulator line. In order to enable the complete photon

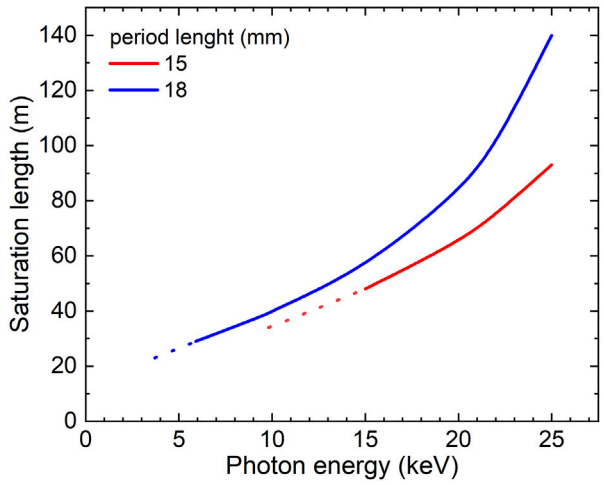

FIGURE 3
Saturation length for an SCU with an 18-mm period and B_{max} = 1.82 T (blue line) and for an SCU with a 15-mm period and B_{max} = 1.64 T (red line) as a function of the photon energy for an electron beam energy of 8 GeV, peak current = 5 kA, emittance = 0.4 mm mrad, energy spread = 3 MeV, and horizontal and vertical beta functions $\beta_x = \beta_y = 16$ m. The solid lines indicate the photon energies reachable with an SCU operating at 4.2 K, while the dotted lines are the photon energies reachable with an SCU operating at 2.2 K, both with a minimum temperature margin of 1 K.

energy range of 250 eV—3 keV for the experiments at the soft X-ray line with the present PMUs (period length = 68 mm; K_{max} = 9), the electron beam energy has to be lowered to 8.5 GeV. On the other hand, the harder X-ray experiments benefit from the high electron beam energy (up to 17.5 GeV). The state-of-the-art SCU technology offers a solution to this challenge and allows reaching the required tunability with similar period lengths, as the present PMUs (~ 70 mm).

- The European XFEL is currently running in the so-called burst mode, which provides trains with a maximum of 2,700 electron bunches spaced by 220 ns (4.5 MHz repetition rate) with a repetition rate of the trains of 10 Hz. A CW upgrade of the linac, similar to what will be supplied by SHINE and LCLS II, is under consideration. This upgrade includes a refurbishment of the cryogenic plant with the aim of approximately doubling its capacity and operation at a reduced electron beam energy of approximately 7–8 GeV. In order to cover a similar photon energy range as now covered with an electron beam energy of 17.5 GeV and the PMUs with a 40-mm period length, it would be necessary to use undulators with a shorter period length. SCUs with a period length between 15 and 20 mm will be able to cover the same photon energy range. Figure 3 shows the saturation length of SCUs with 18 mm and 15 mm period lengths as a function of the photon energy for an electron beam energy of 8 GeV, peak current = 5 kA, normalized emittance = 0.4 mm mrad, rms energy spread = 3 MeV, and horizontal and vertical beta functions $\beta_x = \beta_y = 16$ m. The solid lines indicate the photon energies reachable with an SCU operating at 4.2 K, while the dotted lines are those reachable with an SCU operating at 2.2 K, both with a 1-K temperature margin.

3 FESTA: a superconducting undulator afterburner for the European XFEL

The European XFEL has three undulator lines serving seven instruments. There are two hard X-ray lines and a soft X-ray line named SASE1, SASE2, and SASE3, respectively. By changing the electron energy range between 8.5 GeV and 17.5 GeV and/or the undulator gap, the undulator lines can be tuned to cover the following photon beam energy ranges: 3.6–25 keV (SASE1/2) and 0.25–3 keV (SASE3).

A total of six SCU modules are planned to be installed downstream of the SASE2 PMUs at the European XFEL. The Superconducting undulator PRE-SerieS mOdule (S-PRESSO) is the pre-series module for the Free-Electron laser SuperconducTing undulator Afterburner (FESTA). More details on the design of S-PRESSO can be found in the following section. The small-series production FESTA consists of five modules.

A sketch of the SASE2 undulator line at the European XFEL showing the position of the planned six SCU modules is presented in Figure 4. The length of each SCU module cryostat is 5 m, identical to the length of the installed PMUs. This allows us to use the same intersections (violet rectangle).

Each intersection contains a quadrupole magnet to focus the electron beam transversely below ≈30 μm, which is necessary for the FEL process to take place; a beam position monitor and a beam loss monitor for electron beam diagnostics; air coils to trim the vertical and horizontal first and second field integrals of the undulators; and a phase shifter to compensate the phase advance of the emitted photons with respect to the electron beam. In the PMU lines, the intersections are 1.1 m long. An RF valve will be placed at the intersection separating the last PMU and the first SCU. The intersections interfacing with the SCUs also need to host RF bellows. The RF bellows permit vertical and horizontal alignment of the SCUs with beam and length compensation for the thermal shrinkage of the SCU modules after cooldown. Each SCU module will sit on four cam movers that are remotely controllable.

All SCU modules will be cooled with cryocoolers, following a cryogen-free conduction-cooled scheme similar to the one developed by the KIT/Bilfinger Noell collaboration. We are planning to use six cryocoolers per SCU module. Each SCU module contains two 2-m-long SCU coils with superconducting corrector coils co-wound at the last grooves of the iron yoke and two pairs of vertical and horizontal iron-free coils located between the main coils with a superconducting phase shifter between them (see the upper plot in Figure 4). The layout of each module is planned to be the same as the S-PRESSO module, and it is described in the following section.

Each intersection also contains an absorber to screen the downstream undulator from the radiation produced by the upstream undulators. The PMU vacuum chambers are elliptical with horizontal and vertical axes of 15 mm and 8.6 mm, respectively. The absorbers in the PMU line have a diameter of 8 mm. The SCU vacuum chamber has a racetrack shape with horizontal and vertical axes of 10 mm and 5 mm, respectively. Therefore, absorbers with a diameter of 4 mm are planned.

Simulations were run to estimate the heat load on the six SCU modules. The simulations were performed using BDSIM [18], a

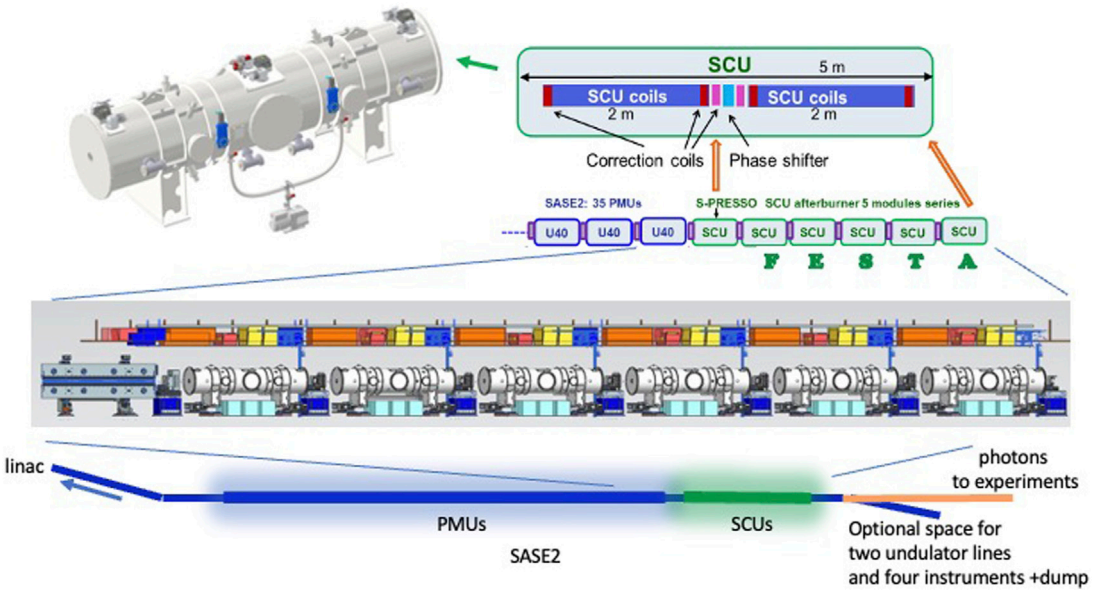

FIGURE 4
Layout of the SASE2 undulator line (bottom) indicating the downstream side (middle) with S-PRESSO and the planned FESTA SCU modules [16]. On the top, a sketch of each SCU module is shown with a 3D model of the cryostat.

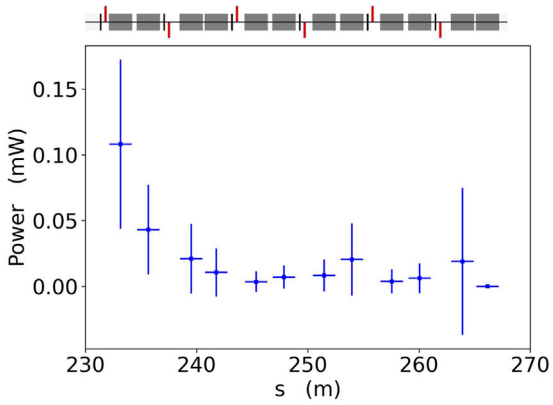

FIGURE 5
Power from the synchrotron radiation and its scattered particles deposited in the SCU coils of the six modules as a function of the longitudinal coordinates considering 4 mm diameter copper absorbers in the intersection between the last PMU and the first SCU and in between the SCUs.

tracking code that also models the interactions between the particles and the beamline components. The simulation tracked the incoherent synchrotron radiation produced in SASE2 until after the SCU modules, simulated with SPECTRA. Some of this radiation is absorbed by copper absorbers and other beamline components during the simulation. The absorbers throughout SASE2 have an aperture of 8 mm. However, the absorber above the S-PRESSO module and all absorbers downstream of the S-PRESSO module have an aperture of 4 mm. The results of the simulation are used to estimate the rate at which energy is deposited into the SCU modules when the machine is running at full power. The results, reported in Figure 5, show that the maximum heat load is ≈ 0.1 mW, which does not affect the SCU module's operation.

A test 4-mm-diameter absorber has been installed downstream of the last PMUs of SASE2 in the winter shutdown of 2022/2023. The electron beam successfully passed through this test absorber. Radiation-sensitive detectors are placed downstream, and the effects of the radiation on the devices installed nearby are under investigation. The first results show low radiation levels.

The SCU coils are foreseen to have a period of 18 mm and a peak field on the axis of 1.82 T. We are mainly focusing on applications above 30 keV for electron beam energies > 16 GeV. S-PRESSO and FESTA can be operated by amplifying the first harmonic of the PMUs up to ≈40–50 keV. To reach higher photon energies, we planned to use the second harmonic bunching generated by the FEL process in the PMUs and amplify it with the fundamental of the SCUs. From first estimations, considering an electron beam energy of 16.5 GeV, a normalized emittance of 0.4 mm rad, and an initial energy spread of 3 MeV, the number of photons per pulse 30 fs long is $\geq 10^{10}$ up to ≈50 keV and $> 10^{9}$ at ≈ 60 keV [17]. Such values are up to two orders of magnitude larger than what can be reached in diffraction-limited storage rings such as the ESRF-EBS and APS-U [16]. Further studies, including wakefields, tapering, and optimized electron beam parameters, are foreseen. A promising way to generate brilliant photon beams at high energies is harmonic lasing [19]. A scheme using phase shifters and filters [20] for suppression of the fundamental is currently under numerical study. Experimental tests at low energies are also planned in the near future.

TABLE 1 Main parameters of S-PRESSO [16].

Period	18 mm
Peak field	1.82 T
K	3.06
Vacuum gap	5 mm
First field integral (x,y)	$< 4 \times 10^{-6}$ T m
Second field integral (x,y)	$< 10^{-4}$ T m^2
$\Delta K/K$ rms	< 0.0015
Roll-off at ±2 mm	$< 5 \times 10^{-5}$
Beam heat load	10 W

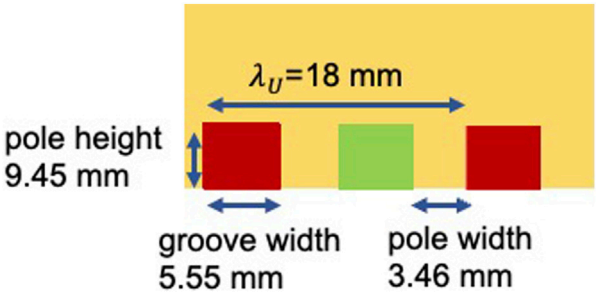

FIGURE 6
Sketch of the one-and-a-half period with dimensions of poles, grooves, and winding packages.

4 S-PRESSO: a pre-series module for FESTA

S-PRESSO is the pre-series module for FESTA. The technical requirements are reported in the study by [16] and summarized as follows. The main goals of S-PRESSO are to demonstrate the following:

- it is possible to contribute to the FEL process with such an SCU by reaching the needed accuracy in the alignment of the two 2-m-long SCU coils, and the mechanical manufacturing and assembly of the SCU coils;
- the feasibility of the implementation of such an SCU module in the accelerator in terms of interaction with the electron beam and space, utilities, and transport.

The contract of S-PRESSO has been assigned to Bilfinger Noell GmbH. The main parameters of the SCU coils of S-PRESSO are shown in Table 1. The peak fields on the axis and period have been chosen such that the fundamentals of the SCUs and SASE2 PMUs overlap at the high-photon-energy end of the SASE2 PMU tuning range. For example, for an electron beam energy of 16.5 GeV, the lowest photon energy of the fundamental of the SCUs is 25.3 keV and will overlap with the fundamental of the PMUs up to $K \approx 0.765$, corresponding to 50 keV. As mentioned in Section 2, for the CW upgrade, it will be necessary to lower the electron beam energy to 7–8 GeV. For an electron beam energy of 8 GeV, the lowest photon energy of the fundamental of the SCUs is 5.9 keV and will overlap with the fundamental of the PMUs up to ≈ 11.8 keV.

TABLE 2 Mechanical accuracies of the SCU coils [16].

Groove width	20 (μm)
Pole width	20 (μm)
Winding package position	40 (μm)
Pole height	40 (μm)

The main coils will be wound with a rectangular NbTi wire of 0.6 mm × 1 mm (bare dimensions). The wire has polyvinyl Formvar insulation with a thickness of 0.04 mm and 2,100 filaments with a diameter of 13 μm. All grooves are filled with 55 turns except the first and last three ones, which have a different winding scheme for end field compensation similar to the one used for the SCUs installed in the KIT and Australian light sources [10,11]. The geometry of a one-and-a-half period is shown in Figure 6.

The upstream and downstream SCU coils will be powered by two power supplies up to a maximum current of 900 A. With 900 A of operating current, 2D and 3D magnetic field simulations produce a peak magnetic field on the axis that slightly exceeds the required 1.82 T. At a nominal current of 900 A, the conductor has a temperature margin of 1 K by operating at 4.2 K. To reduce the power consumption during operation, the power supplies will be placed in the tunnel close to S-PRESSO.

For the correctors and phase shifters, nine power supplies with 30 A and 40 V are foreseen. These are standard power supplies developed by the Deutsches Elektonen-Synchrotron (DESY) and used for the room temperature correctors of EuXFEL and PETRA III. The correctors and phase shifter will operate at a current of 10 A with a large temperature margin > 3 K.

The needed mechanical accuracies are reported in Table 2. They have been set considering that for the half periods, the following limits on $K/2$ hold: $|\Delta K/K|_{rms} < 0.0015$ and $|\Delta K/K| < 0.006$. With the aforementioned restrictions on $K/2$, the pulse energy emitted by the six SCU modules is not significantly reduced [21]. FEL simulations show that the same requirements for mechanical accuracies are well-compatible with a complete SCU line with a 15-mm period length. Such mechanical accuracies reduce the mean FEL power at saturation length by less than 5% [22] and are, therefore, not notably harming the performance of the FEL process. In case that the magnetic field measurements show that the required mechanical accuracies/range of deviation of the undulator parameter are not reached in the manufacturing and assembly processes or are not maintained after cooldown, shim coils are foreseen.

The shim coils can be wound as racetracks (see the orange coil in Figure 7) with a thin NbTi wire with a diameter of 0.152 mm (insulated). Each shim coil wound around one pole can correct approximately 1% of the field with a current of 5 A. Using two neighboring shim coils with a pole in between and powered with 5 A, it is possible to correct up to 2% of the magnetic field. These values are sufficiently larger with respect to the maximum specified variations on the K-value. More configurations are studied and reported in [23]. A maximum of 11 power supplies of the same type as those for the corrector coils are foreseen for the shim coils.

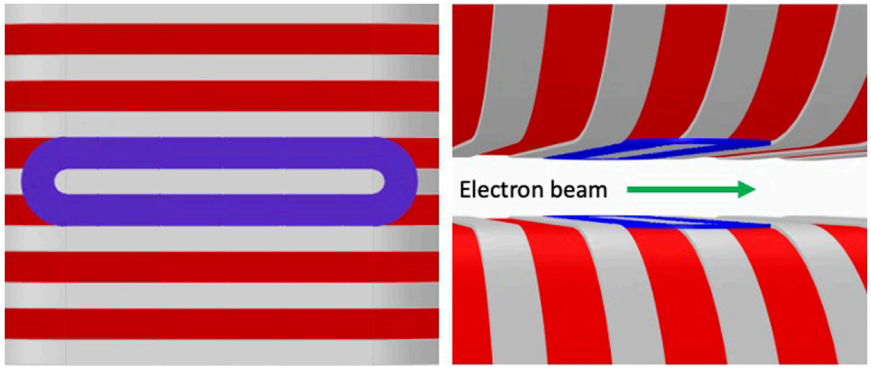

FIGURE 7
Sketch of a shim coil wound around one pole of the top and bottom SCU coils. Left: on the upper yoke. Right: on upper and lower yokes. Adapted from [29].

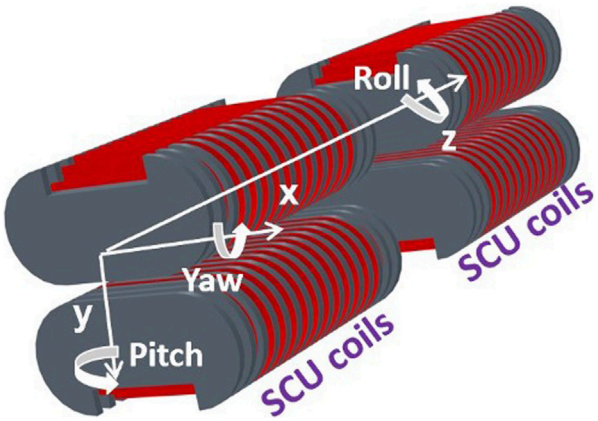

FIGURE 8
Sketch of the two SCU coils with the reference system defining the angles for the alignment constraints reported in Table 3 [29]. Reproduced under Creative Commons from Ref. [16].

TABLE 3 Alignment requirements for the SCU coils [16].

x	±200 μm
y	±50 μm
Pitch	< 0.1 mrad
Yaw	< 0.1 mrad
Roll	2 mrad

A misalignment between the two coils causes a correlated error in *K*-values along the magnetic axis. Calculations made by [22] show that for an SCU line, the two SCU coils in one module, as reported in Figure 8, need to be aligned with respect to each other within the values listed in Table 3. To fulfill the requirements on alignment, a rigid support structure, sustained by eight Ti rods, is designed to hold the SCU coils straight within 30 μm over a length of approximately 4.5 m. The magnetic gap is accessible at some places for coordinate measurement machine (CMM) measurements in assembled conditions. The alignment of the coils will be performed at room temperature and atmospheric pressure. The fiducialization procedure is foreseen to be performed as described in the study by [9].

A copper vacuum chamber separates the cold mass, placed in an insulation vacuum, from the electron beam vacuum. The racetrack chamber, with horizontal and vertical axes of 10 mm and 5 mm, respectively, will be 0.3 mm thick and will be made of copper with a residual-resistance ratio ≈100. The internal surface of the copper electron beam vacuum chamber must have a roughness $R_a < 0.8$ μm and an oxide layer thinner than 20 nm. In such conditions, the beam heat load due to resistive wall heating is always below 10 W for all relevant operation modes [16]. Geometric impedance will contribute to less than 0.1 W by keeping steps in the vacuum chamber cross-section < 0.1 mm. Synchrotron radiation will be screened by the copper absorbers placed in the upstream intersection (see Section 3).

A passive quench protection system in the form of cold rectifier diodes is foreseen. Each SCU single coil (top or bottom coil of one of the two SCU coils in the module) is protected by a set of six cold diodes, amounting to a total of 24 diodes for the two SCU coils. In case of a quench, the output of the power supply is deactivated via its interlock function, and the stored energy is dissipated within the coils and the diode racks. The quench detection is based on the balanced voltage principle. A quench is detected as soon as the difference between the voltages across the upper and lower coils increases above a certain threshold for longer than a given amount of time.

The cooling system is divided into two circuits: one for cooling the magnets and one for the vacuum chamber. S-PRESSO is cooled by six Gifford McMahon (GM) cryocoolers from Sumitomo: three are of type SRDE-412D4 with a cooling power of 1.25 W at 4 K and three are of type RDK-408S with a cooling power of 5.4 W at 10 K. The second stages of the three SRDE-412D4 cryocoolers are connected to the 4.2 K components, including the high-temperature superconducting current leads, while the three RDK-408S cryocoolers are connected to the electron beam chamber at approximately 10 K. The first stages of all six cryocoolers are used to intercept radiation on the thermal shield and the heat due to thermal conduction on the support rods, the electron beam chamber, and the resistive part of the current leads. The upstream and downstream

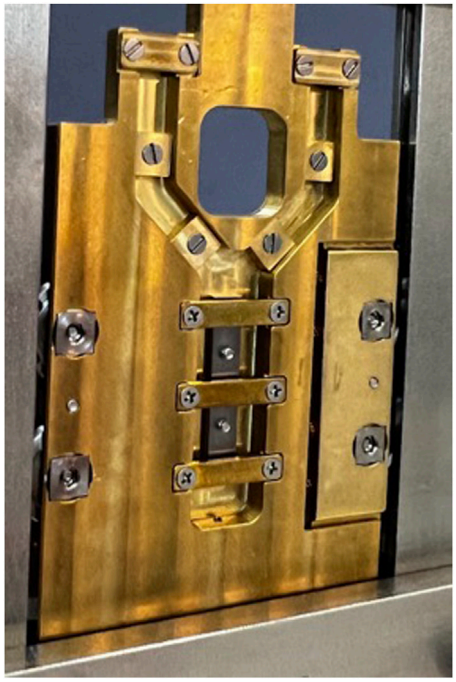

FIGURE 9
Sledge placed in precisely machined rails hosting the Hall probes to measure the magnetic field profile of planar SCU coils in SUNDAE1.

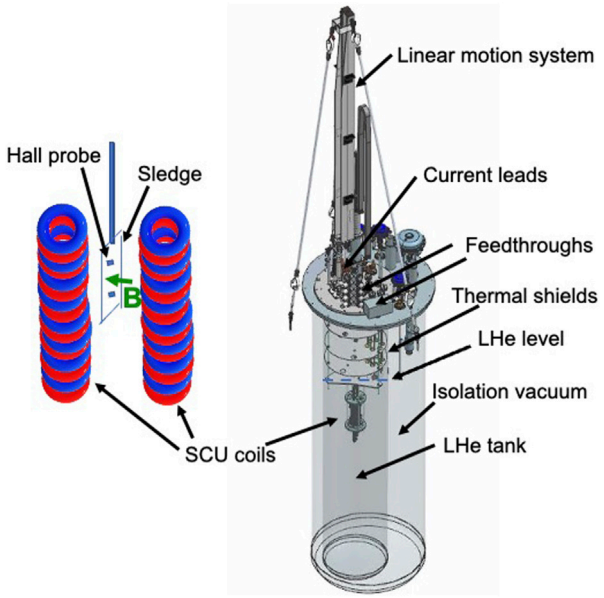

FIGURE 10
Model of SUNDAE1 (right) with a sketch of the sledge attached to a rod with Hall probes sliding along the magnetic field axis of the SCU coils (left).

SCU coils are powered by two power supplies through three current leads designed to operate at 900 A. This is of considerable advantage in terms of heat load and, therefore, needed cooling power compared to the normal design with four current leads carrying the operating current. The foreseen cooldown time is 7 days, and the warm-up time is 4 days.

5 SUNDAE test facilities

Two test facilities, SUNDAE1 [24] and SUNDAE2 [25] (Superconducting UNDulAtor Experiment), are under development to qualify the magnetic field properties of SCU coils. SUNDAE1 and SUNDAE2 are planned, keeping in mind the present needs for S-PRESSO and FESTA, and possible future upgrades of the European XFEL. SUNDAE1 is also foreseen to measure SCU test coils with novel winding schemes and superconducting wires and tapes carrying higher currents than NbTi, such as high-temperature superconducting (HTS) tapes (see Section 6). SUNDAE1 and SUNDAE2 are located at DESY in a hall with a cryoplant. Tests at 2 K are foreseen in SUNDAE1 and will be possible in SUNDAE2 with minor refurbishments of the helium distribution box. Measurements at 2 K might be of interest for possible future upgrades of the European XFEL, where complete SCU lines might be used. In such a case, cooling would be performed with a cryoplant instead of cryocoolers. To further improve the performance of the NbTi SCUs, similar solutions, as adopted for the superconducting RF cavity cryo-modules, could be used to cool the developed SCUs to 2 K (see Figure 2).

Both test stands will use their own in-house developed control systems, specifically based on Beckhoff Automation components and PLC software frameworks, as well as .NET applications. Data from the experiments will be stored in the InfluxDB database. Real-time visualization of time series will be performed via the Grafana web-based framework (see https://grafana.com/) connected to a database. Data analysis, such as calculating field integrals, will be performed via in-house developed software.

5.1 SUNDAE1

SUNDAE1 is a vertical cryostat to test SCU coils up to 2 m long in liquid and superfluid helium at 4 K and 2 K, respectively. The cryostat, previously used for tests of superconducting RF cavities, has a fixed helium level (≈2.4 m) and is being equipped with a new lid produced by the company Cryovac. The cryostat is directly connected to the cryoplant through a distribution box that can provide helium at two temperature levels: 4–5 K and 70–80 K. SUNDAE1 is additionally connected to pump stations to allow pumping of the helium bath down to ≈30 mbar (≈2 K). A liquid nitrogen supply line and a gas nitrogen return line are employed to cool the thermal shield and the magnet current leads.

SUNDAE1 is planned to perform training on the SCU coils and measure their magnetic field profile along the magnetic axis. The Hall probes will be mounted on a sledge moving along rails machined with high precision. The sledge is shown in Figure 9. The sledge is connected through a Ti rod to a linear motion system (see Figure 10) produced by Hositrad (https://www.hositrad.com/), with a single-axis vertical translator with a 2.4 m travel range and

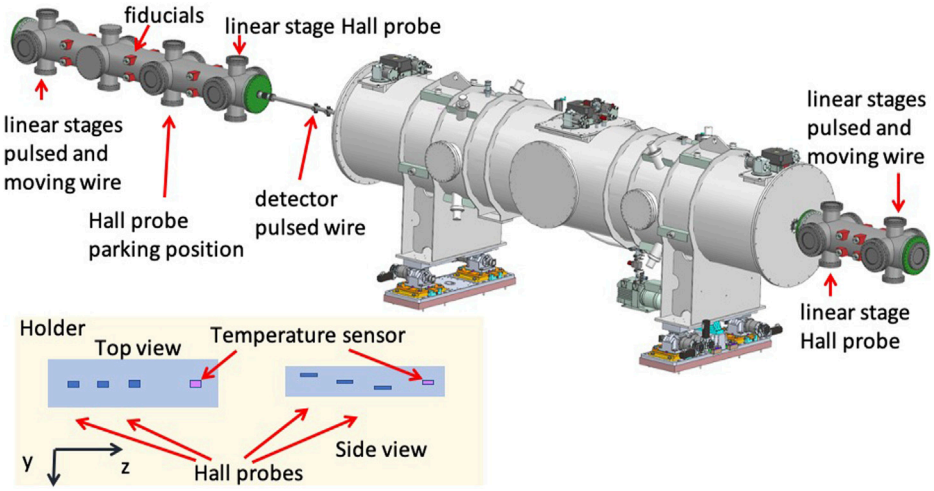

FIGURE 11
Model of SUNDAE2, including the UHV chambers with the magnetic measurement systems and S-PRESSO. Bottom left: top and side view of the holder for the three Hall probes (one 3-axis Hall magnetometer) and a temperature sensor.

resolution, accuracy, and repeatability of 1 μm. The rod is located in a bellows, allowing a long motion range. We foresee two Hall probes from Areopoc calibrated at KIT at 4.2 K. The calibration error of the Hall probes is ±0.1 mT.

The lid is equipped with four current leads to carry a maximum current of 1000 A, four current leads for 500 A, and 12 current leads for 20 A. Two bipolar power supplies with ± 1500 A and six power supplies with 20 A, with respective quench detectors, are being procured from JEMA (https://www.jemaenergy.com/). It is possible to power coils with a maximum current of 3000 A.

The temperature at the different stages of the current leads will be measured by Pt100 and Cernox temperature sensors and read out on five Lakeshore 224 monitors with 12 channels.

To locate possible quenches, five Cronosflex HISO-8 isolated amplifier modules (https://www.imc-tm.com/products/daq-systems/imc-cronosflex/overview/) with 40 channels (8 channels each) simultaneously readable with a maximum sampling rate of 2000 kS/s (max 50 kS/s per channel), to be connected to voltage taps on SCU coils, have been procured. The data acquisition is started by a trigger coming from a quench detector. A typical acquisition time scale is 1.5 s, including a pre-trigger time of 0.5 s. To read out the signals, the program imc STUDIO (https://www.imc-tm.com/products/measurement-software/imc-studio/overview/) is used.

The S-PRESSO and FESTA SCU coils, as well as the Helmholtz correction coils and phase shifter, will be tested in SUNDAE1. After quality assurance tests, they will be assembled in the final cryostat. Before the installation of S-PRESSO and FESTA modules in the tunnel, they will be characterized in SUNDAE2.

5.2 SUNDAE2

SUNDAE2 is a horizontal test stand to qualify SCU coils in their final cryostat. A sketch of SUNDAE2 is presented in Figure 11. The vacuum chambers at the two ends of the SCU modules are connected to the electron beam chamber.

A similar system, as in SUNDAE1, is foreseen for training the coils and performing quench analysis; this includes eight Cronosflex HISO-8 isolated amplifier modules with eight channels each for a total of 64 channels.

A stretched wire will be implemented. This will be used as a moving wire to measure the first and second field integrals and as a pulsed wire to measure the magnetic field longitudinal profile. The pulsed wire measurements will be dominated by dispersion. Such a measurement, in vacuum, on a magnetic length > 4 m with a period length as small as 18 mm, has never been performed before. A code was developed at the EuXFEL to correct for dispersion, finite pulse width, discretization errors, and sag [26]. Several steps to test the measurement technique are foreseen prior to the final characterization of S-PRESSO. The pulsed wire technique is extremely appealing for small apertures, as is the case for our SCU modules.

Given the extremely small dimensions of the S-PRESSO and FESTA module vacuum chambers, the Hall probe measurement is particularly challenging. Our approach is to use four Hall probes mounted on a ceramic holder tightly fitting the vacuum chamber. The longitudinal position of the Hall probes can be measured using an interferometer and a retroreflector placed on one side of the holder. The interferometer is planned to be installed on an optical table placed outside of the UHV chamber, close to the flange on the right side of Figure 11. The interferometer allows us to measure the relative longitudinal position with a precision of 1 μm. With such a holder, the transverse position of the Hall samples along the longitudinal axis cannot be determined with the required precision < 100 μm. The horizontal position is not critical since a good field region of ±2 mm is foreseen (see the roll-off in Table 1). To determine the magnetic field in the middle of the gap, three Hall probes need to be used at a distance along y of ≈100–200 μm, one from the other (see the reference system displayed in Figures 8, 11). In this way, considering the vertical transverse dependence of the magnetic field,

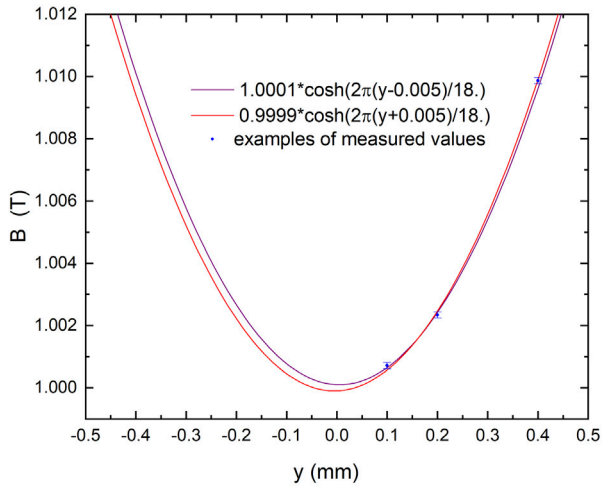

FIGURE 12
Typical measurement data set (blue dots) for the magnetic field at a specific longitudinal position. The two lines represent curves in Equation 5 with minimum and maximum fitting values for *B*.

$$B(y) = B\cosh\left(\frac{2\pi y}{\lambda_U}\right). \quad (5)$$

It will be possible to fit the measured field at each longitudinal position with Equation (5) and find the magnetic field value *B* at the minimum, corresponding to the middle of the gap. By measuring the field profile with the three Hall probes, it is possible to identify a set of three field measurements corresponding to the same longitudinal position. The distance in *y* between the three Hall probes can be determined by placing the holder with the Hall probes in a calibration setup. A room-temperature dipole is available at the European XFEL for this purpose. A goniometer with translation stages is being procured with a cold finger to hold the Hall probes. The typical calibration error obtained with Aeropoc Hall probes measured at KIT at 4.2 K, 30 K, and 77 K is ±0.4 mT. The expected error in determining *B* is approximately ±1mT, as shown in the example reported in Figure 12. To correct for possible deviations of the Hall probes' position from being perpendicular to the magnetic axis, we foresee including an embedded 3-axis Hall magnetometer MagVector™ MV2 from Metrolab (https://www.metrolab.com/products/magvector-mv2/). Along axis z, the Hall probes will be at different temperatures. These will be determined during the first cooldown using a temperature sensor placed on the same holder as the Hall probes (see Figure 11).

The Hall probes will be calibrated at different temperatures in the range 4–100 K. We expect this to be the Hall probes temperature range while measuring the magnetic field profile along the axis z. Some of the planned Hall probes have been calibrated at KIT at 4.2 K, 30 K, and 77 K. The difference in the calibration curves at these temperatures is ±0.1 mT in the range of ±2 T.

It is clear that with the Hall probe method, we are following the middle of the gap and not the electron beam motion. The alignment of the upstream and downstream SCU coils can be tested only with the pulsed wire method since it relies on a tensed wire.

6 Advanced SCU coils

To improve the undulator's performance, Nb_3Sn or HTS materials like rare earth barium copper oxide (ReBCO) instead of NbTi superconductors can be utilized. These materials have higher irreversibility fields, critical temperatures, and critical current densities. The field quality of an SCU is strongly determined by the mechanical accuracies reached. Although Nb_3Sn requires heat treatment, which reduces the reachable mechanical accuracies, this is not the case for ReBCO tapes, making them a good candidate for undulator applications.

Companies producing ReBCO tapes have made important improvements in the past few years to increase the engineering current density by doping ReBCO tapes with Zr and reducing the thickness of the substrate from 50 μm to 30 μm. This increases the reachable peak field on the axis even further. Once uniformity, repeatability, mechanical properties, available length, and production rate of high-quality ReBCO tapes are improved, ReBCO tapes will become the working horse to produce full-scale length magnets, including undulators, to be reliably operated in storage rings and FELs.

The best performance in terms of peak field on the axis can be reached by filling the SCU grooves with the HTS tape, taking advantage of the high engineering current density. The peak field on the axis can be increased by a factor of ≈ 1.7 with respect to NbTi by using the same geometry and the 11-K temperature margin operating at 4 K. This is reached with a current density of 5000 A/mm^2 in the HTS tape. The values of the critical current have been obtained from the high-temperature superconducting wire critical current database maintained by the Victoria University of Wellington, Australia [27]. However, HTS tapes are not yet available in long lengths (the maximum length is approximately 100 m), and they are roughly 10 times more expensive than the NbTi wire. To use the high engineering current density of the ReBCO tape in the most effective location to increase the peak field on the magnetic axis, HybriSCU, a graded SCU combining NbTi and the ReBCO tape, has been proposed and studied. The concept foresees winding the first layers in the SCU grooves with the NbTi wire and the last layers closer to the electron beam with the ReBCO tape. An additional advantage of placing the ReBCO tape closer to the electron beam is its high temperature margin.

The geometry taken into consideration foresees the use of the 4-mm HTS tape and an undulator period of 16.8 mm. The improvement of B_{max} at 16.8 mm for a magnetic gap of 6 mm and a temperature margin of 1 K for NbTi and 11 K for the ReBCO tape is approximately 15% by adding seven layers of the ReBCO tape to the 15 layers of NbTi and approximately 37% by considering 13 layers of NbTi and 30 layers of the ReBCO tape [28]. Further studies on the realization process of HybriSCU and ReBCO coils are planned.

7 Conclusions and outlook

Superconducting undulators are successfully operated in synchrotron light sources. The European XFEL plans to demonstrate the FEL process with S-PRESSO, a pre-series superconducting undulator, and provide photons for users with S-PRESSO and FESTA in the unexplored FEL regime with photon

energies > 30 keV. This project is pivotal to implementing complete SCU lines for X-ray FELs, including those operating in the CW mode.

Data availability statement

The raw data supporting the conclusion of this article will be made available by the authors, without undue reservation.

Author contributions

All authors listed have made a substantial, direct, and intellectual contribution to the work and approved it for publication.

Conflict of interest

Authors AH and WW are employed by Bilfinger Noell GmbH.

The remaining authors declare that the research was conducted in the absence of any commercial or financial relationships that could be construed as a potential conflict of interest.

Publisher's note

All claims expressed in this article are solely those of the authors and do not necessarily represent those of their affiliated organizations, or those of the publisher, the editors, and the reviewers. Any product that may be evaluated in this article, or claim that may be made by its manufacturer, is not guaranteed or endorsed by the publisher.

References

1. Elleaume P, Chavanne J, Faatz B (2000). Design considerations for a 1 A sase undulator. *Nucl Instr Methods Phys Res Section A: Acc Spectrometers, Detectors Associated Equipment* 455:503–23. doi:10.1016/S0168-9002(00)00544-1

2. Moog E, Dejus R, Sasaki S. *Comparison of achievable magnetic fields with superconducting and cryogenic permanent magnet undulators – a comprehensive study of computed and measured values light source note: ANL/APS/LS-348* (2017). Available at: https://publications.anl.gov/anlpubs/2017/07/137001.pdf

3. Kim S. A scaling law for the magnetic fields of superconducting undulators. *Nucl Instr Methods Phys Res Section A: Acc Spectrometers, Detectors Associated Equipment* (2005) 546:604–19. doi:10.1016/j.nima.2005.03.150

4. Edwards HT. The tevatron energy doubler: A superconducting accelerator. *Annu Rev Nucl Part Sci* (1985) 35:605–60. doi:10.1146/annurev.ns.35.120185.003133

5. Wiik BH. Hera: Machine and experiment. In: R Kotthaus JH Kuhn, editors. *XXIV international Conference on high energy physics*. Berlin, Heidelberg: Springer Berlin Heidelberg (1989). p. 404–21.

6. Rossi L (2003). The lhc superconducting magnets. *Proc 2003 Part Accelerator Conf* 1:141–5. doi:10.1109/PAC.2003.1288863

7. Casalbuoni S, Glamann N, Grau AW, Holubek T, de Jauregui DS. Superconducting undulator coils with period length doubling. *J Phys Conf Ser* (2019) 1350:012024. doi:10.1088/1742-6596/1350/1/012024

8. Ivanyushenkov Y, Harkay K, Borland M, Dejus R, Dooling J, Doose C, et al. Development and operating experience of a 1.1-m-long superconducting undulator at the advanced photon source. *Phys Rev Accel Beams* (2017) 20:100701. doi:10.1103/PhysRevAccelBeams.20.100701

9. Casalbuoni S, Cecilia A, Gerstl S, Glamann N, Grau AW, Holubek T, et al. Characterization and long term operation of a novel superconducting undulator with 15 mm period length in a synchrotron light source. *Phys Rev Accel Beams* (2016) 19:110702. doi:10.1103/PhysRevAccelBeams.19.110702

10. Casalbuoni S, Glamann N, Grau A, Holubek T, de Jauregui DS, Bauer S, et al. Superconducting undulators: From development towards a commercial product. *Synchrotron Radiat News* (2018) 31:24–8. doi:10.1080/08940886.2018.1460171

11. Glamann N, Grau AW, Porsa S, Tan Y-R, Walter W, Zhu D. Commissioning of a 1.6 m long 16mm period superconducting undulator at the Australian synchrotron. In: Proc. 14th International Particle Accelerator Conference (IPAC'23); 7–12 May 2023; Venice, Italy (2023).

12. Zhang K, Calvi M. Review and prospects of world-wide superconducting undulator development for synchrotrons and fels. *Superconductor Sci Tech* (2022) 35:093001. doi:10.1088/1361-6668/ac782a

13. Zhou Q, Mezentsev N. R&d of sc undulators in asia/Russia. In: *Virtual superconducting undulators for advanced light sources workshop* (2021). Available at: https://indico.desy.de/event/28501/contributions/99114/aFachments/65299/80635/SCU%20workshop_zhou.pdf

14. Marchetti B. *Challenges in deploying scus on xfels* (2021). Virtual Superconducting Undulators for Advanced Light Sources Workshop. Available at: https://indico.desy.de/event/28501/sessions/10620/#20210420

15. Decking W, Abhramian P, Abeghyan S, Aguirre A, Albercht C, Alou P, et al. A mhz-repetition-rate hard x-ray free electron laser driven by a superconducting linear accelerator. *Nat Photon* (2020) 14, 391–297. doi:10.1038/s41566-020-0607-z

16. Casalbuoni S, Baader J, Geloni G, Grattoni V, Decking W, Civita DL, et al. A pre-series prototype for the superconducting undulator afterburner for the European xfel. *J Phys Conf Ser* (2022) 2380:012012. doi:10.1088/1742-6596/2380/1/012012

17. Lechner C, Casalbuoni S, Geloni G, Marchetti B, Serkez S, Sinn H. Simulation studies of superconducting afterburner operation for the European xfel. *J Phys Conf Ser* (2022) 2380:012009. doi:10.1088/1742-6596/2380/1/012009

18. Nevay L, Boogert S, Snuverink J, Abramov A, Deacon L, Garcia-Morales H, et al. Bdsim: An accelerator tracking code with particle-matter interactions. *Comp Phys Commun* (2020) 252:107200. doi:10.1016/j.cpc.2020.107200

19. Schneidmiller EA, Brinker F, Decking W, Froehlich L, Guetg M, Noelle D, et al. Observation of harmonic lasing in the angstrom regime at European x-ray free electron laser. *Phys Rev Accel Beams* (2021) 24:030701. doi:10.1103/PhysRevAccelBeams.24.030701

20. Schneidmiller EA, Yurkov MV. Harmonic lasing in x-ray free electron lasers. *Phys Rev ST Accel Beams* (2012) 15:080702. doi:10.1103/PhysRevSTAB.15.080702

21. Lechner C, Casalbuoni S, Geloni G, Marchetti B, Serkez S, Sinn H, et al. Simulation studies of superconducting afterburner operation at sase2 beamline of European xfel. In: Proc. 40th International Free Electron Laser Conference (FEL2022); 22 Aug 2022 - 26; Trieste, Italy (2022).

22. Marchetti B, Casalbuoni S, Grattoni V, Serkez S. Analysis of the error budget for a superconducting undulator sase line at European xfel. *J Phys Conf Ser* (2022) 2380:012011. doi:10.1088/1742-6596/2380/1/012011

23. Grattoni V, Casalbuoni S. Design study for hybriscu: A hybrid nbti/rebco superconducting undulator. *IEEE Trans Appl Superconductivity* (2023) 33:1–5. doi:10.1109/TASC.2023.3259329

24. Marchetti B, Abeghyan S, Baader J, Barbanotti S, Casalbuoni S, Felice MD, et al. Conceptual design of a liquid helium vertical test-stand for 2m long superconducting undulator coils. *J Phys Conf Ser* (2022) 2380:012027. doi:10.1088/1742-6596/2380/1/012027

25. Baader J, Abeghyan S, Casalbuoni S, Eckoldt H-J, Grau A, Hauberg A, et al. Sundae2 at euxfel: A test stand to characterize the magnetic field of superconducting undulators. In: Proc. 13th International Particle Accelerator Conference (IPAC'22); June 12-17, 2022; Bangkok, Thailand (2022). p. 2649–52. doi:10.18429/JACoW-IPAC2022-THPOPT032

26. Baader JE, Casalbuoni S Magnetic field reconstruction using the pulsed wire method: An accuracy analysis. *Measurement* (2022) 193:110873. doi:10.1016/j.measurement.2022.110873

27. Wimbush S. *The robinson research institute hts wire critical current database* (2022). Available at: https://htsdb.wimbush.eu/dataset/4256624

28. Grattoni V, Casalbuoni S. Magnetic field errors and possible correction schemes in scus. In: Proc. 14th International Particle Accelerator Conference (IPAC'23); 7–12 May 2023; Venice, Italy (2023).

29. Grattoni V, Casalbuoni S, Marchetti B. An analytical study to determine the mechanical tolerances for the afterburner superconducting undulators at euxfel. *J Phys Conf Ser* (2022) 2380:012010. doi:10.1088/1742-6596/2380/1/012010

frontiers | Frontiers in Physics

TYPE Original Research
PUBLISHED 27 June 2023
DOI 10.3389/fphy.2023.1174620

OPEN ACCESS

EDITED BY
Nicholas Walker,
Helmholtz Association of German Research Centres (HZ), Germany

REVIEWED BY
Mukesh Kumar Pandey,
National Taiwan University, Taiwan
Maofei Qian,
Argonne National Laboratory (DOE), United States

*CORRESPONDENCE
Wei Zhang,
zhangwei@sari.ac.cn
Bo Liu,
bo.liu@sari.ac.cn

†These authors have contributed equally to this work and share first authorship

RECEIVED 26 February 2023
ACCEPTED 14 June 2023
PUBLISHED 27 June 2023

CITATION
Yu C, Zhu Y, Zhang W, Yang J, He Y, Zhen T, Liu T, Lei Y, Yuan Q, Yuan D, Wen Y, Deng R, Jiang Z, Deng H, Liu B and Wang D (2023), Development of an APPLE III undulator prototype with three-dimensional force compensation for SHINE.
Front. Phys. 11:1174620.
doi: 10.3389/fphy.2023.1174620

Development of an APPLE III undulator prototype with three-dimensional force compensation for SHINE

Cheng Yu†, Ya Zhu†, Wei Zhang*, Jie Yang, Yongzhou He, Tingting Zhen, Tao Liu, Yangyang Lei, Qibing Yuan, Dao Yuan, Yongmei Wen, Rongbing Deng, Zhiqiang Jiang, Haixiao Deng, Bo Liu* and Dong Wang

Shanghai Advanced Research Institute, Chinese Academy of Sciences (CAS), Shanghai, China

The Shanghai high-repetition-rate XFEL and extreme light facility (SHINE) plans to install several elliptically polarizing undulators (EPUs) as afterburners behind the planar undulator section to obtain nearly saturated circularly polarized free-electron laser (FEL) radiation. Therefore, the SHINE R&D project needs to develop a 4-m-long EPU with an effective magnetic field of 1.5 T, a period of 68 mm, and a minimum gap of 3 mm. A magnetic force compensation EPU prototype has recently been built and tested at the Shanghai Synchrotron Radiation Facility (SSRF) based on the addition of permanent magnets. This prototype can realize magnetic compensation under various polarization modes in all working gaps, thereby reducing the deformation of the girders and maintaining sufficient rigidity of the mechanical structure. A girder deformation monitoring system was established to obtain real force compensation feedback. The final magnetic field measurement results meet the physical requirements, and the proposed scheme can be used as an alternative to the EPU with a high magnetic field and large magnetic force.

KEYWORDS

free-electron laser, high magnetic field, elliptically polarizing undulator, force compensation, deformation detection

1 Introduction

The Shanghai high-repetition-rate XFEL and extreme light facility (SHINE) is currently under construction. Based on the 8-GeV CW superconducting RF (SCRF) LINAC [1, 2], SHINE can generate 0.4–25 keV photon radiation from three undulator lines (Figure 1). SHINE has three beam lines and nine experimental stations, with high peak brightness and average brightness, a high repetition rate (up to 1 MHz), and femtosecond-level super-fast pulse characteristics. Additionally, SHINE has a nano-level spatial resolution and femtosecond-level ultrafast temporal resolution. The total length of the SHINE project is approximately 3.2 km, including the accelerator, undulators, beam line tunnels, experiment halls, low-temperature factory, and auxiliary facilities. The free-electron laser (FEL) comes from the coherent superposition of the radiation and the coherent amplification of the electromagnetic field. To keep most of the electrons in an energy-releasing state, a fixed-phase relationship is required between the electrons and the radiation based on the well-known resonance condition [3] given as follows:

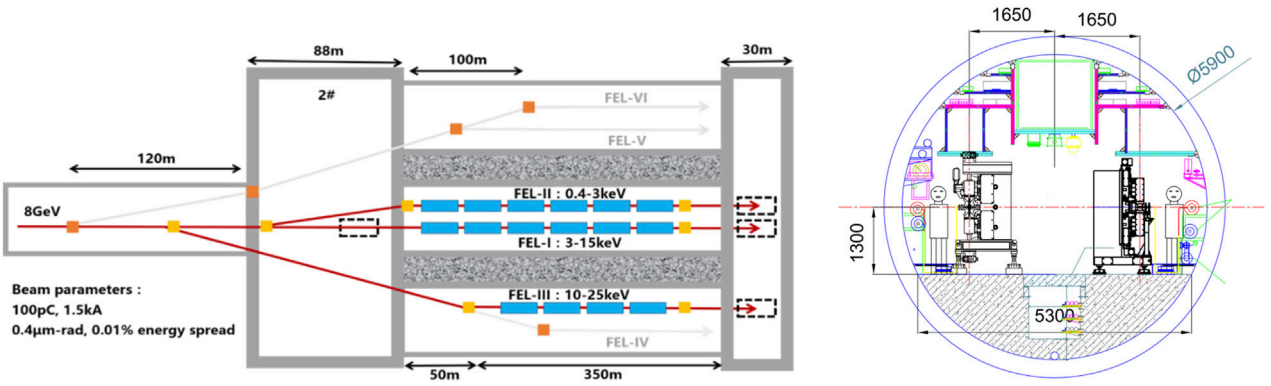

FIGURE 1
Layout of the undulator lines of the SHINE project. Left: undulator system. Right: FEL-I&II tunnel.

TABLE 1 Main parameters of the FEL-II EPU (EPU68 prototype).

Parameter	Value
Photon energy [keV]	0.4–3.0
Period [mm]	68
Work gap range [mm]	3–30
Max gap [mm]	150
Effective magnetic field [T]	1.5
Segment length [m]	4
RMS phase error [deg]	<12

$$\lambda_n = \frac{\lambda_u\left(1 + K^2/2 + \gamma^2\theta^2\right)}{2n\gamma^2}.$$

The FEL wavelength λ_n depends on the Lorentz factor γ, which represents the energy of the electron beam energy, undulator period λ_u, deflection factor K, harmonic number n, and observing angle θ. According to the requirements of the scientific experiments, the three undulator lines use different parameters to achieve independent adjustable X-rays with the same electron energy and different undulator period lengths (16 mm for FEL-I, 68 mm for FEL-II, and 16 mm for FEL-III). For SHINE, 8 GeV was selected for the electron energy. It would be difficult to cover the required higher photon energy with a lower electron energy (e.g., 6 GeV), while a higher electron energy (10 GeV) would lead to a significant increase in the project cost. The 8-GeV beam energy combined with the current undulator parameters can cover the photon radiation range and satisfy the light intensity required by scientific users. An upgrade is possible in the future if required.

In the SHINE project, FEL-II produces soft X-rays from 0.4 to 3 keV with planar undulators, which can easily produce a high magnetic field strength and are both conducive to FEL gain and cost-efficient. The planar undulator shows a better perfect magnetic field performance than the EPU, which is beneficial for FEL amplification saturation. The X-ray FEL device with planar undulators only produces linearly polarized light, and the polarization state cannot be changed. Partly as a result, a polarization control scheme is planned using EPUs as an afterburner. The main parameters of the EPU are shown in Table 1. The period length is 68 mm, and the total length is 4 m. The effective magnetic field is required to reach 1.5 T for horizontal, vertical, and circular polarization, and the root mean square (RMS) phase error requirement is less than 12°.

2 Selection strategies for the EPU

Among the variable polarizing undulators (VPUs) running on most third-generation storage ring light sources, the APPLE II [4] configuration can provide the strongest magnetic field. An APPLE II undulator consists of two pairs of diagonal Halbach I magnet arrays, in which at least one pair of diagonal magnet arrays can be moved in longitudinal synchronization to control the polarization mode, and the distance moved is called the phase. Later, an inclined mode was proposed, whereby a set of diagonal girders moved the same phase in the opposite direction, and the axis of polarization of linear polarized light would tilt within 0° and 90°. In contrast to the earlier proposed Apple I configuration [5, 6], the magnetization direction of the Apple II configuration is optimized to be completely perpendicular, which provides a higher on-axis magnetic field in the linear polarization mode and a larger uniform field region. However, this large-field region and the matching rectangular vacuum chamber with a wide transverse dimension are unnecessary for the single-pass beam in the FEL device. In 2004, Bahrdt [7] proposed the Apple III configuration, which had three differences to the APPLE II configuration: 1) the vertical gap was compressed, 2) the magnets were chamfered to accommodate the circular vacuum chamber, and 3) the easy axis of the vertical magnets was rotated by 45°. These improvements allowed for a 40% increase in the magnetic field strength when a vacuum chamber of the same size is configured. Figure 2 shows the direction of easy-magnetization axes (one-way black arrow) and girder movement (two-way orange and yellow arrows) when these structures are in phase zero.

Unlike the aforementioned variable-gap APPLE-type undulators (VGUs), the first choice for a high-field EPU is a fixed-gap design, called Delta, which has a more compact structure [8–10]. This fixed-gap design ensures the magnetic

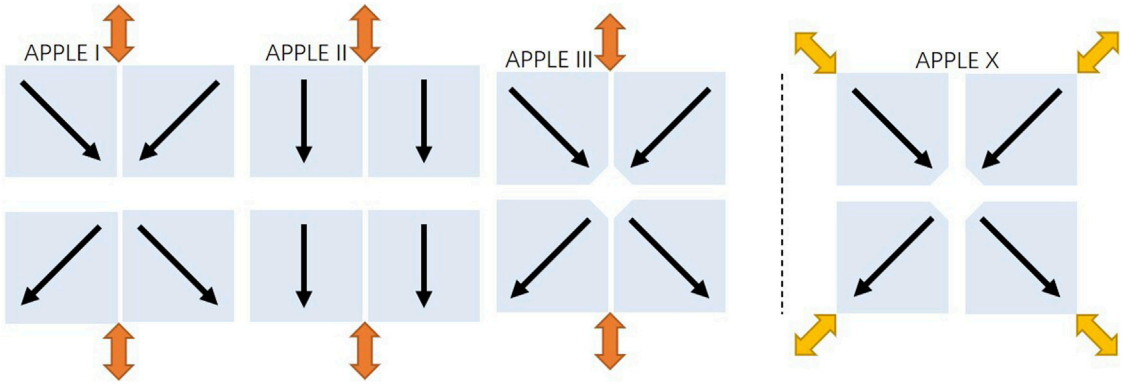

FIGURE 2
From left to right: cross sections of the APPLE I, II, III, and X configurations. The four Halbach magnet arrays of the three configurations on the left are located on two girders, i.e., the vertical gap is adjustable, while the transverse slit is fixed. The latest APPLE X configuration has four independent magnet arrays that move radially.

arrays are always kept at the minimum gap, although the permanent magnets are likely to be damaged by radiation. The magnetic measurement is very difficult to complete, especially for a long undulator. The magnetic arrays cannot be fully opened for the initial commissioning of the accelerator, but the minimum gap can be determined experimentally. In addition, it has recently been reported that phase-shift undulators have an intrinsic problem with field gradients [11].

The second solution for a small-gap EPU is to place the magnets in vacuum based on force compensation technology. This enables a compact structure to be achieved within a chamber for high-magnetic field VGUs. During the past 10 years, different types of magnetic force compensations for planar undulators have been implemented or prototyped [12, 13] at several SR facilities. To obtain a high-field EPU, the magnetic force compensation technology is now attractive to some facilities. Based on the traditional APPLE II configuration, in 2019, Bahrdt and Grimmer [14] proposed a design to overcome difficulties in realizing APPLE-type in-vacuum undulators (IVUs), which are based on magnetic force compensation with additional magnetic arrays, and facilitate the phasing operation in the undulator. Recently, they proposed the development of a cryogenic APPLE undulator [15] using the same scheme. In 2020, Kinjo and Tanaka [16] presented a spin-EPU structure for the realization of polarization control in IVUs. Although the available polarization state was limited compared to the conventional APPLE undulators, the structure and operation of the undulator based on the proposed scheme were much simpler, and it could, therefore, be easily implemented in IVUs. Additionally, the magnetic force in the proposed undulator could be reduced to a negligible level by carefully optimizing the dimensions and positions of magnet arrays, without any special equipment.

The third strategy to develop a high-field small-vertical gap EPU is to increase the rigidity of each magnet array girder by independently using a strong carrier beam with the APPLE X structure proposed at the Paul Scherrer Institute (PSI) in 2016 [17, 18]. The four girders of the APPLE X undulator require an independent motion system and a mechanical support beam. The magnetic design is fully symmetric for all gaps and uses Delta-type magnets with 45° magnetization. The magnetic measurement is conducted with a set of hall probes in the minimal vertical gap. The APPLE X undulator can generate gradients for the ultra-high bandwidth mode [19]. It is notable that this structure has the benefit of being without longitudinal forces in the inclined mode. The disadvantage is that the section size of the APPLE X structure is larger than that of the traditional vertical gap movement APPLE structure.

The magnetic gap of the SHINE project 4-m-long EPU needs to be reduced to 3 mm to achieve the required magnetic field. For a 3-mm magnet vertical gap, an IVU may be suggested if the cost and complexity are not considered. Due to the limited number of rigid connections, systematic gap errors can easily arise for a small-gap IVU. Micron-level deformation will lead to a very large magnetic field variation, which is bound to affect the radiation phase error. During the transition of different polarization modes, the magnitude and direction of the magnetic force of the magnet arrays change synchronously. The deformation variation from horizontal to vertical polarization is very large, and the magnetic field performance is very difficult to guarantee for different polarizations.

To expand the photon energy range and add as much polarization control of FEL as possible, two undulator lines in one tunnel is an effective approach. This has been shown to greatly improve the efficiency of the FEL device. In the SHINE project, FEL-I and FEL-II are being constructed in the same tunnel, as shown in Figure 1. The size of accelerator equipment should meet the horizontal width limit of less than 1,200 mm, and a sufficient installation path needs to be reserved.

Based on the aforementioned analysis, we chose the traditional C-type and in-air mechanical structure to reduce the cost and complexity, adopted the APPLE III magnet configuration to meet the requirement of a 1.5-T effective field for vertical linear polarization, and used the three-dimensional magnetic force compensation scheme to reduce the overall size of the undulator. In Sections 3 and 4, the magnet design, including the force compensation, is presented to explain the crucial points for the EPU68 prototype. In Sections 5 and 6, the mechanical structure, analysis, and comparison results of the force compensation are

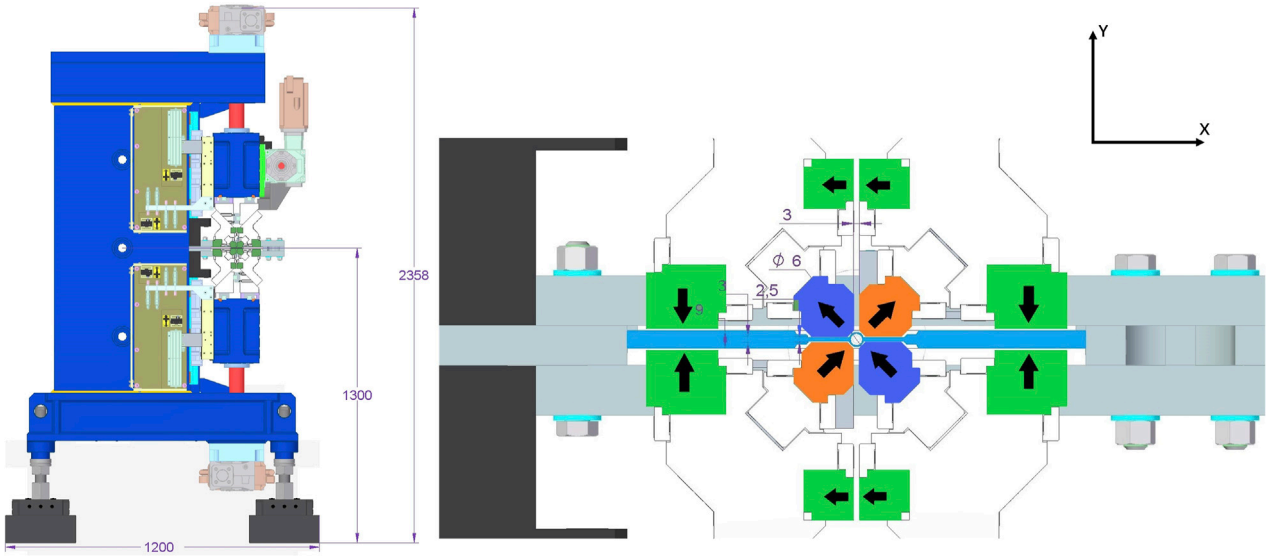

FIGURE 3
The undulator consists of four FM arrays (orange and blue) and eight CM arrays (green).

displayed. In Section 7, magnetic field measurements of the EPU68 prototype are presented.

3 Magnetic design

The APPLE III magnet configuration was used to achieve the required magnetic field performance for the EPU68 prototype. The overall structure, including the additional magnets, is shown in Figure 3, and the coordinate system described in this article is also represented. The red and blue magnets in the center are called functional magnets (FMs) in this paper. The minimum gap is the same as the slit, both of which are 3 mm. The four groups of green Halbach I magnet pairs around them are the compensation magnet (CM) array, which are divided into left/right CM and top/bottom CM pairs. The EPU68 prototype uses neodymium–iron–boron (NdFeB) permanent magnets (N38EH grade or above) as the magnetic field source of the undulator. The minimum remanence (Br) is at least 1.25 T, the intrinsic coercive field (H_{cj}) associated with the magnetization curve is not less than 2,400 kA/m, and H_k is not less than 2,300 kA/m at 25°C. The size of the FMs is 25 × 25 mm^2, with a 3-mm chamfer near the electron beam position. The horizontal slit between the fixed and moving girder is the same as the vertical gap. Around the center, there is a rhombus-shaped space for a vacuum chamber. The effective field can reach 1.5 T (peak field 1.47 T) in the linear polarization mode and 1.5 T (peak field 1.06 T both in *X* and *Y* directions) in the circular polarization mode.

Considering the magnetic field measurement requirements of the EPU68 prototype and the design difficulty of the vacuum chamber, the vacuum chamber was made of stretched aluminum placed in the middle of the gap, as shown in Figure 3. The requirement for a minimum gap of 3 mm resulted in great difficulty in the design and processing of the vacuum chamber. The vertical gap of the CM arrays for vertical magnetic compensation was, therefore, relaxed to 10 mm. The size of the left/right CMs was increased to achieve better results. The prototype magnet parameters are shown in Table 2. For all FMs, the magnetization angle was precisely perpendicular to the base faces, the maximum deviation angle was less than ±1.0°, and the magnetization uniformity was less than 1.0%. For all CMs, the specifications of the required magnetization angle and uniformity are reduced to ±2.0° and 2.0%, respectively.

TABLE 2 Main design parameters of the EPU68 prototype.

Parameter	Value	Unit
Period length	68	mm
Total length	4	m
Gap for FMs	3	mm
Slit for FMs	3	mm
45° cut in FMs	3 × 3	mm
Aperture for vacuum	8.49	mm
Gap for left/right CMs	10	mm
Slit for top/bottom CMs	3	mm

4 Force compensation by CMs

The EPU68 prototype required an effective magnetic field of 1.5 T for both linear and circular polarizations, as shown in Figure 4, which is an unusually high-magnetic field design for an EPU in the world. The magnetic force between the upper and lower girders of the 4-m-long undulator was nearly 8 tons at the minimum gap. Under such a large magnetic force, the forced deformation of the girders had a significant effect on the magnetic field quality of the prototype. For the

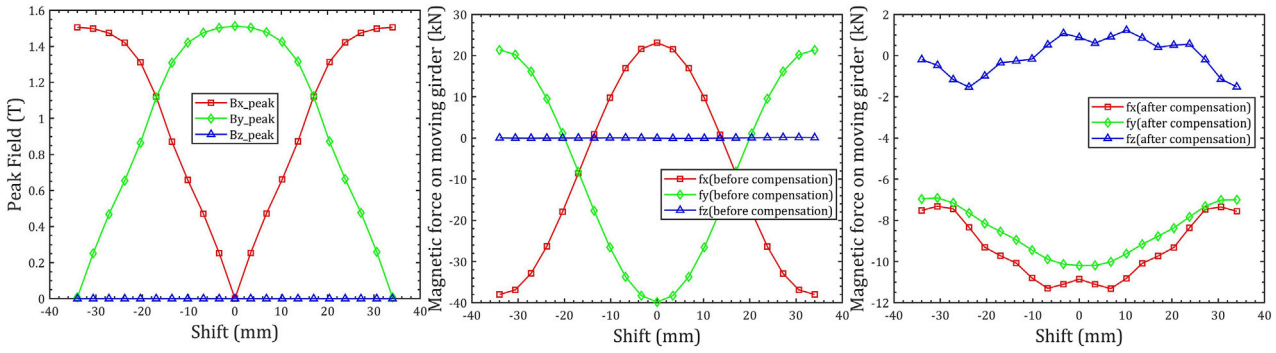

FIGURE 4
Shift-dependent variation parameters at the minimum gap: Bx_peak/fx (red), By_peak/fy (green), and Bz_peak/fz (blue). Left: magnetic field. Center: magnetic force on the moving girders before compensation. Right: magnetic force on the moving girders after compensation, calculated with the RadiaCode [20].

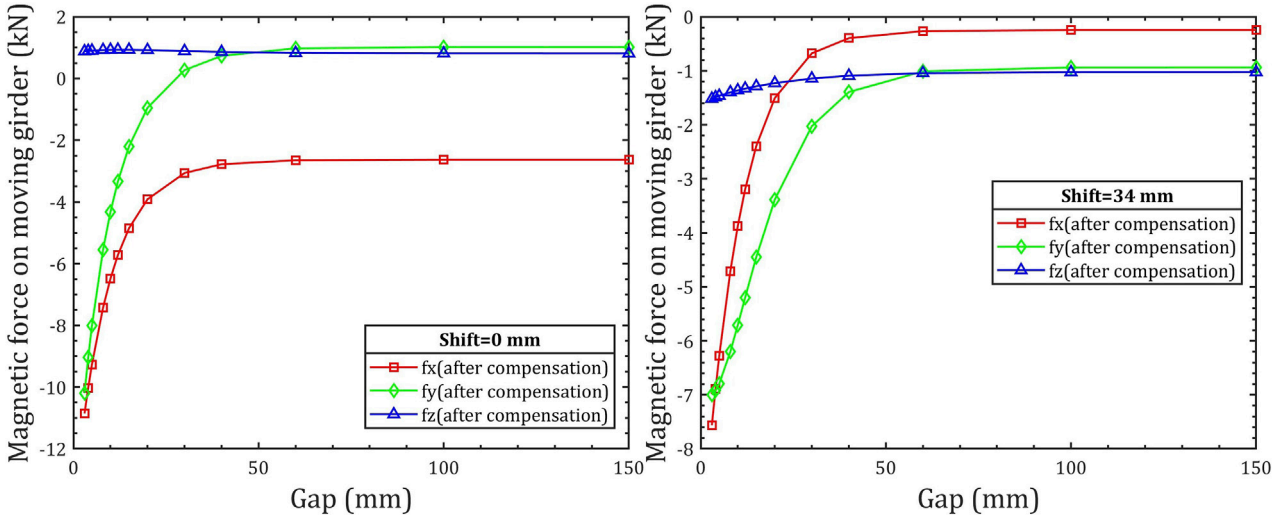

FIGURE 5
Magnetic force on a moving girder after compensation at different gaps: fx (red), fy (green), and fz (blue). Left: shift = 0 mm. Right: shift = 34 mm.

EPU68 prototype, not only did the magnetic force for each girder change when the magnetic gap changed but also at the same magnetic gap, the magnetic force is also changed from −4 to 2 tons during phase shifts. This is also shown in Figure 4. With a change in the direction of the magnetic force, the attractive force between the back beams became a repulsive force when the phase shift was half period. The decrease in the mechanical deformation of the magnet girder under the action of a magnetic force is the key to the quality assurance of magnetic field performance. Due to the CMs, the force variation between shift = 0 and 34 mm was successfully reduced from 60 to 6 kN for both the vertical and horizontal directions, as shown in the right side of Figure 4.

To ensure the high quality of the undulator magnetic field and the safety and stability of the undulator mechanical system, the rigidity and stability of the beams can be increased; however, this would make the design of the entire mechanical structure of the undulator more complex, larger, and much more expensive. Another option is the addition of two magnet arrays on each girder to produce opposite forces in the vertical and horizontal directions, as shown in Figure 3. Depending on the CM arrays, the forces acting on the moving girders can be reduced to a very low value. The magnetic force variation of each moving girder had a very satisfactory result of less than 6 kN at the minimum gap of 3 mm during the phase change between the zero phase and half-period phase. The magnetic force variation during the gap opening of each moving girder was reduced to less than 10 kN, which is also shown in Figure 5. To visually compare the force of each magnet array, the force direction of all arrays in the different phase shifts at the minimum gap is shown in Figure 6. The value of the force at the maximum gap of 150 mm is provided for comparison in Table 3.

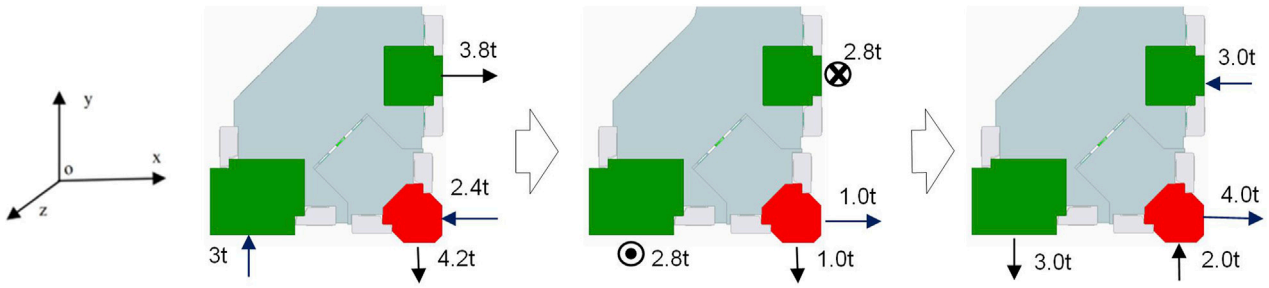

FIGURE 6
Schematic representation of the force loads on a moving girder at the minimum gap of 3 mm (shift = 0, 17, 34 mm).

TABLE 3 Three forces acting on different magnet arrays of a moving girder at the minimum and maximum gaps. (For example: when the shift changed by 0, 17, and 34 mm, the horizontal force fx marked as +30→ 0 → −40 at the maximum gap of 150 mm).

Gap (mm)	Magnet array	Horizontal fx (kN)	Vertical fy (kN)	Longitudinal fz (kN)
150	FM	+30→ 0 → −40	0→ 0 → 0	0→ −24 → 0
150	Left/right CM	0→ 0 → 0	0→ 0 → 0	0→ 0 → 0
150	Top/bottom CM	−35→ 0 →+30	0→ 0 → 0	0→ +26 → 0
3	FM	+24→ −10 → −40	−42→ −10 → +20	0→ 0 → 0
3	Left/right CM	0→ 0 → 0	+30→ 0 → −30	0→ −28 → 0
3	Top/bottom CM	−38→ 0 →+30	0→ 0 → 0	0→ +28 → 0

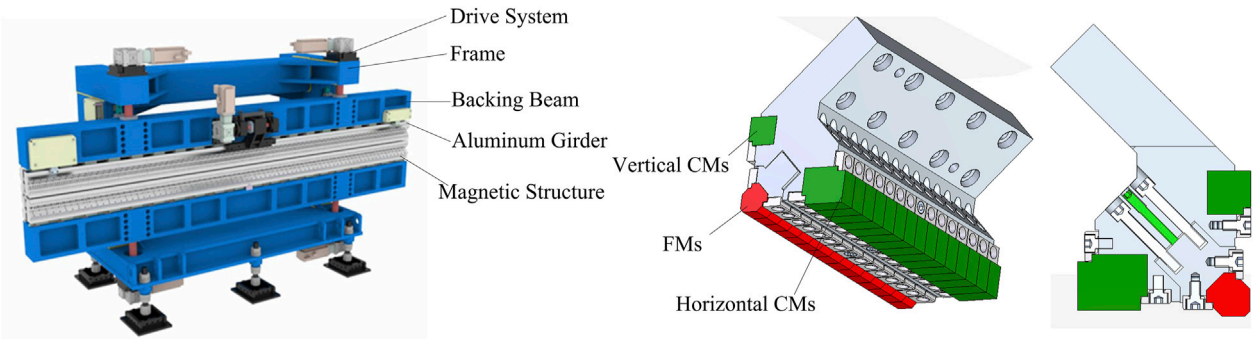

FIGURE 7
Mechanical structure of the EPU68 prototype and magnet keeper.

5 Mechanical structure and motion control

Figure 7 shows the structure of the EPU68 prototype, illustrating the support structure and drive systems. The support structure had a "C" frame design, which was convenient for the magnetic measurements and device installation. The adjusted base with six kinematic floor mounts had a welded steel structure, and the adjusted ranges for z direction were ±6 mm and ±10 mm in the x and y directions, respectively. Two vertical columns with two horizontal columns to strengthen the rigidity were mounted to the base. Four cube steel tubes, which connect the base and vertical columns, further strengthened the stability of the support structure. The vertical columns supported four roller screw assemblies, which enabled the vertical movement of the upper and lower beams. The support frame and the backing beams were made of cast iron to ensure a small mechanical deformation during phase changes. The fixed girders and moving girders were made of an aluminum alloy. The fixed girder supported the moving girder with two sets of crossed roller slides. The moving girder can move along the two guides mounted between the backing beam and fixed girder.

FIGURE 8
Left: MMB. Center: KEYENCE laser displacement sensors. Right: capacitance transducer.

The three magnet arrays of each girder were kept in the same massive magnet keeper, which was made of an aluminum alloy. There was only a shimming strategy for moving magnets parallel to the magnetization direction. The magnet position was adjusted by rotating the lock nuts. The image on the right side of Figure 7 shows the magnet keeper layout, which was used in FEM studies to optimize the geometries. The magnet keepers were fixed to the girders by positioning pin holes and bolts. A shimming displacement of 50 μm resulted in a local field change of 35 Gs cm at a gap of 3 mm. The maximum allowed shimming range was ±100 μm.

The motion control mainly focused on the 1-μm precision magnet movement, including gap adjustment, taper adjustment, and shift adjustment, for the full range of operational gap values. The control tasks consisted of the motion control of all the aforementioned movements, monitoring the real-time gap position in the upstream and downstream through position feedback derived from the linear absolute encoders (LAEs) with 5-nm resolution, offering remote access for the Experimental Physics and Industrial Controls System (EPICS) toolkit via Ethernet, as well as the machine protection system (MPS) and personal protection system (PPS) interlock interfaces for the upper-level protection system of the interlock system.

6 Force compensation performance

6.1 Magnetic measurement bench (MMB) and the girder deformation monitoring system

The Shanghai Synchrotron Radiation Facility (SSRF) has a set of three-dimensional MMB, which consists of a cable dragging system, multi-axis motion system (a Hall probe is installed at the front end and can be fine-tuned to eliminate the attitude error of the probe), and control system, as shown in Figure 8. The z-axis measuring range is 6,500 mm, and both the x-axis and y-axis measuring ranges are 300 mm. The probe is a H3A Hall probe (Senis AG, Zug, Switzerland), which has a small planar Hall effect, a measuring accuracy of 0.1 G s, and a measuring range of ±1.9 T, thus covering the magnetic field range of the EPU68 prototype.

The MMB provided support for a capacitance transducer to measure the vertical displacement along the magnet surface. The relative deformation of the vertical and circular polarization compared to the horizontal polarization (shift = 0 mm) could be easily obtained from the measurement of the different phase shifts. Additionally, two KEYENCE (Osaka, Japan) laser displacement sensors were installed in the MMB support to scan for horizontal displacement and detect the deformation of the different polarizations. Both the capacitance transducer and KEYENCE laser displacement sensors used in the MMB system showed a repetitive performance of less than 5 μm, which was acceptable for the displacement measurements.

6.2 Measurement from gap = 0–150 mm at shift = 0 mm

When the phase shift was zero, there was no longitudinal force acting on the moving girder. As shown in Figure 5, with the force compensation of the CMs, there was just a 12-kN vertical force variation (horizontal force variation 9 kN) between the minimum and maximum gaps. For the moving girder mounted between the backing beam and fixed girder by the two set guides, the horizontal deformation variation between the maximum and minimum gaps along the Z-axis was small and trended smoothly. In the MMB laboratory, we set the phase to zero and measured just the vertical displacement with the capacitance sensor at the minimum and maximum magnetic gaps to detect the vertical deformation. The experimental test data revealed a 20-μm variation deformation that appeared during the gap changes at shift = 0 mm, as shown in Figure 9.

6.3 Measurement from shift = 0–34 mm at the maximum gap

As shown in Table 3, there was no vertical force acting on the moving girders during phase shifting at a maximum gap of 150 mm; the horizontal and longitudinal force variations were 5 kN and 2 kN, respectively. We mainly measured the horizontal deformation of the moving girder. The measured horizontal deformation variation was

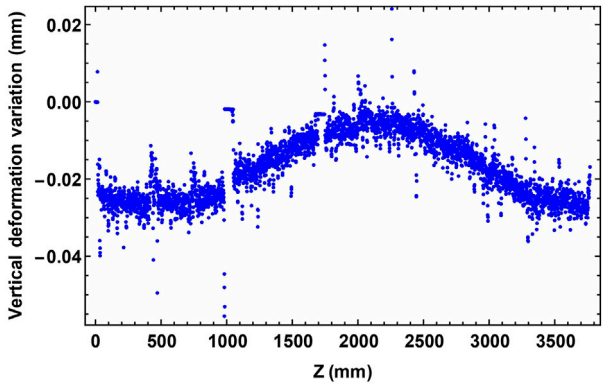

FIGURE 9
Vertical deformation variation at shift = 0 mm when the gap changed from 3 to 150 mm.

approximately 15 μm when comparing shift = 34 mm with shift = 0 mm, and the measured horizontal deformation variation was approximately 20 μm when comparing shift = 17 mm with shift = 0 mm. The trend of the horizontal deformation measurement results was basically consistent with that of the simulation results. The amplitude was slightly larger than the simulation results after force compensation, and the compensation effect was notable, as shown in Figure 10(2) and 10(3).

6.4 Measurement at the minimum gap

At a minimum gap of 3 mm, the vertical displacement for shifts = 0, 17, and 34 mm was measured using a capacitance sensor probe. Compared with shift = 0 mm, the deformation of the magnet top surface changed by approximately 30 μm for shift = 34 mm and by approximately 40 μm for shift = 17 mm. Although the results were much smaller than the simulation value before force compensation, they were still much larger than the simulation result after force compensation. The test results of the vertical deformation variation of the magnet were basically consistent with the trend of the simulation results, but the results were on the large side. As shown in Figure 10, a similar result was achieved during the horizontal deformation variation measurement from shift = 0 mm to shift = 34 mm. Compared with shift = 0 mm, the horizontal variation in shift = 17 mm was approximately 150 μm, which was almost twice that of the simulation value when comparing shift = 17 mm with shift = 0 mm. A variation in the inclined deformation along the undulator was observed in both the vertical and horizontal directions.

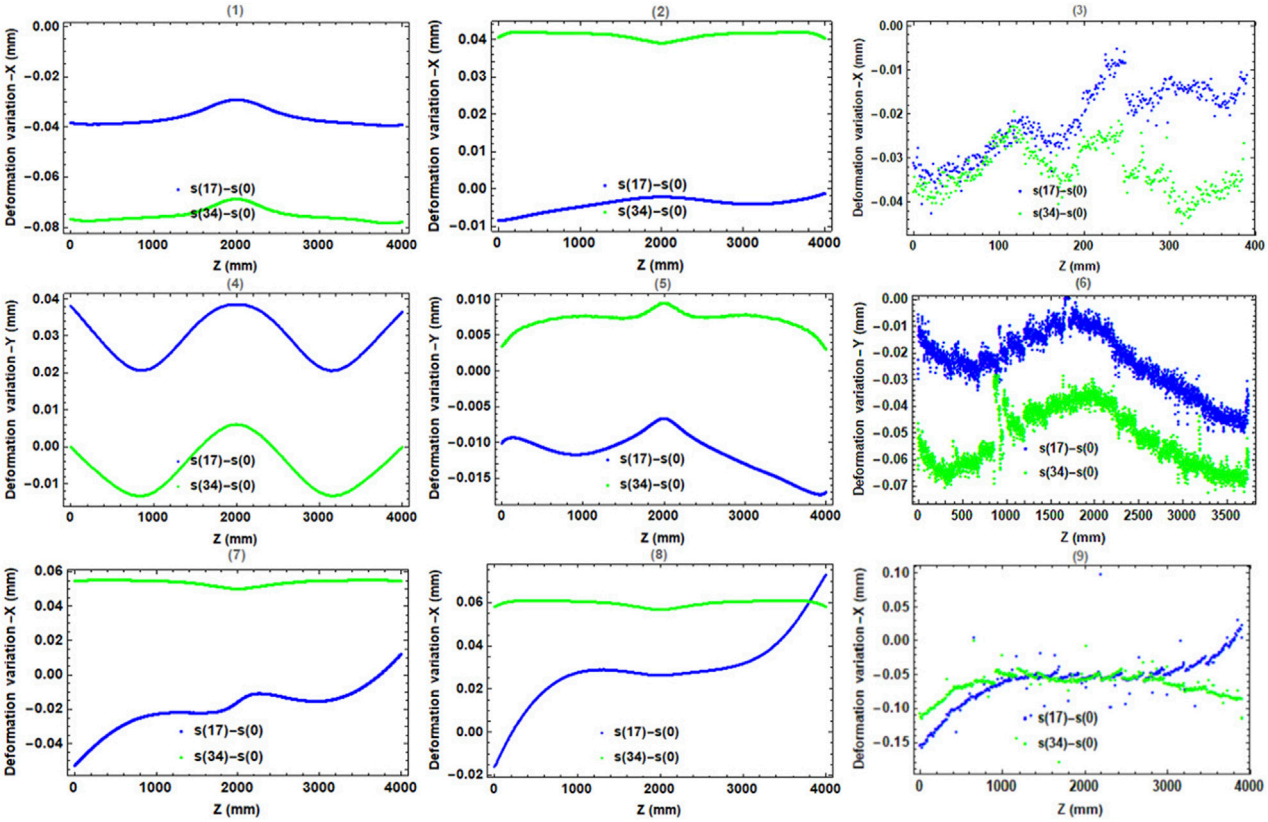

FIGURE 10
Deformation variation of a moving girder between different shifts. (1), (2), and (3): horizontal deformation at the maximum gap of 150 mm. (4), (5), and (6): vertical deformation at the minimum gap of 3 mm. (7), (8), and (9): horizontal deformation at the minimum gap of 3 mm. Left: FEM simulation results before compensation. Middle: FEM simulation results after compensation. Right: test results.

TABLE 4 Magnetic performance in a gap range of 3–30 mm. Different polarization modes: horizontal linear (LH), vertical linear (LV1,2), right-handed circular (C+), and left-handed circular (C-) modes.

Gap (mm)	Effective magnetic field (T)					RMS phase error (deg)				
	LH	LV1	LV2	C+	C-	LH	LV1	LV2	C+	C-
3.2		1.51	1.50							
3.4	1.50	1.48	1.48	1.50	1.51	10.89	4.80	4.95	6.09	6.57
3.7	1.49	1.44	1.44	1.48	1.48	10.47	4.84	5.00	6.02	6.47
4	1.48	1.40	1.40	1.45	1.46	11.04	4.69	4.71	6.49	6.12
5	1.45	1.28	1.28	1.37	1.38	9.08	4.28	4.76	6.84	5.53
6	1.40	1.18	1.18	1.29	1.29	7.92	4.28	4.79	7.62	5.19
8	1.31	0.99	0.99	1.13	1.13	6.13	4.62	5.60	9.66	4.54
10	1.20	0.84	0.84	0.98	0.99	6.47	4.98	4.98	10.83	4.87
15	0.96	0.57	0.56	0.69	0.70	8.21	6.89	5.62	13.64	6.30
20	0.75	0.39	0.39	0.49	0.49	7.77	11.06	10.59	13.60	7.05
30	0.46	0.19	0.19	0.25	0.25	9.63	10.21	7.97	14.86	7.63

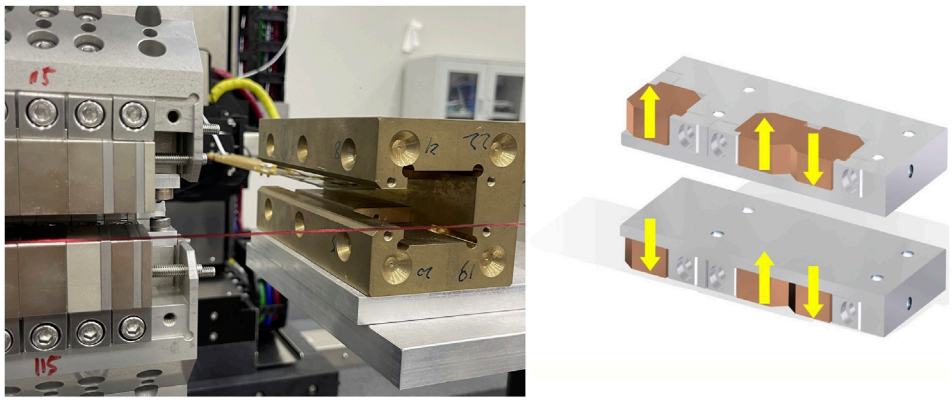

FIGURE 11
MLs were located on both sides of the EPU68 prototype, and the magnetic center of the undulator was determined by two quadrupole (skew and normal quadrupole) fields inside the MLs, as shown in the right side of the figure.

7 Magnetic measurement results

Considering that the minimum magnetic gap was 3 mm, the quantity and displacement of magnet shimming in the EPU68 prototype are confined-limited. The maximum shimming displacement should be controlled within 0.1 mm; otherwise, the installation of the vacuum chamber becomes difficult. Finally, the effective magnetic field and RMS phase error are shown in Table 4. The RMS phase error was below 6° at vertical polarization for a gap less than 15 mm. The RMS phase error in horizontal polarization is not as good as that in vertical polarization, especially at small gaps less than 5 mm. Unfortunately, the phase error in right hand circular polarization exceeded our target of being within 12°. This problem may be caused by mechanical assembly errors and clearance calibration errors, and surpassed expectations of the deformation variation. An effective magnetic field of 1.5 T was achieved at a gap of 3.4 mm for horizontal polarization and a gap of 3.2 mm for vertical polarization. At a gap of 30 mm, the effective magnetic field is about 0.3 T, which was within the acceptable gap range.

8 Transfer of the magnetic axis to mechanical fiducial marks

The small area with a good magnetic field in the vertical direction and the deviation between the mechanical and magnetic centers were sensitive parameters for installation and operation. A magnetic center extraction for the EPU68 prototype was performed after the magnetic field measurement. The magnetic center was defined as the axis formed by the magnetic field

shimming on the cross section of this undulator. A pair of magnetic landmarks [21] (MLs) was used to transfer the magnetic axis of the undulator to the mechanical fiducials using a laser tracker system, as shown in Figure 11. The extraction accuracy was better than 0.05 mm.

9 Summary

The deformation variation test results during phase shifting at the minimum gap were not as good as that at the maximum gap. There was a relatively large inclined deformation variation when the phase shift ranged from 0 to 17 mm and was then extended to 34 mm. As shown in Figure 6, at the circular polarization mode of shift = 17 mm at the minimum gap, in the cross section of the EPU68 prototype, both the added vertical and horizontal forces of the moving girder composed of three magnet arrays were small. However, the force torque was large, and its direction changed gradually when the phase shifted. Similarly, the added longitudinal force of the moving girder in the electron beam direction was also very small. The longitudinal force torque was largest at shift = 17 mm due to the opposite force directions of the left/right and the top/bottom CMs, leading to a rotated distortion of the whole beam and the generation of a large inclined deformation in both the horizontal and vertical directions. Unfortunately, the simulation of the EPU design did not take into consideration the effect of torque in circular polarization. This was possibly one reason why the horizontal magnetic field was lower than the vertical magnetic field under the same gap. It may also explain why the phase error of horizontal polarization was larger than that of vertical polarization.

A high-magnetic field EPU is critical for the polarization control of high-energy continuous-wave FEL devices. A high magnetic field needs a very small magnetic gap and generates vexatious strong magnetic forces. A massive and reinforced mechanical structure is a popular approach to ensure its rigidity. SHINE-EPU68 adopts the APPLE III magnet configuration with the traditional C-type mechanical structure, and a set of Halbach I magnet arrays was selected to compensate the magnetic forces for FMs, which makes the C-type mechanical structure relatively compact and narrow in horizontal size. It is applicable for the SHINE project two-line tunnel. The deformation test results when a gap opened from 3 to 150 mm at the horizontal polarization indicated a notable vertical force compensation. The horizontal deformation test results of the prototype at the maximum gap showed that the deformation variation during phase shifting had sufficient rigidity, and the magnetic field test results met the physical requirements.

Data availability statement

The raw data supporting the conclusion of this article will be made available by the authors, without undue reservation.

Author contributions

CY and the corresponding author WZ contributed to the magnet design, magnetic measurement, and shimming. YZ, TZ, and RD designed the mechanical structure and conducted the FEM simulation. CY, YZ, and WZ wrote most of the manuscript and contributed to the conception and design of the study. JY and YZ designed the deformation monitoring system. YH contributed to magnet manufacturing. CY, DY, and ZJ conducted the magnetic center extraction. YL and QY designed the control system. YW designed the vacuum chamber. TL contributed to the physical design of the FEL schemes. HD, DW, and the corresponding author BL reviewed the manuscript and supervised the work. All authors contributed to the article and approved the submitted version.

Funding

This work was supported by the Chinese Academy of Science (CAS) Project for Young Scientists in Basic Research (YSBR-042), the National Natural Science Foundation of China (12125508 and 11935020), the Program of Shanghai Academic/Technology Research Leader (21XD1404100), and the Shanghai Pilot Program for Basic Research-CAS, Shanghai Branch (JCYJ-SHFY-2021-010).

Conflict of interest

The authors declare that the research was conducted in the absence of any commercial or financial relationships that could be construed as a potential conflict of interest.

Publisher's note

All claims expressed in this article are solely those of the authors and do not necessarily represent those of their affiliated organizations, or those of the publisher, the editors, and the reviewers. Any product that may be evaluated in this article, or claim that may be made by its manufacturer, is not guaranteed or endorsed by the publisher.

References

1. Zhao ZT, Wang D, Yin L. *SCLF: An 8-GeV CW SCRF Linac-Based X-Ray FEL Facility in Shanghai*. Santa Fe, NM: JACoW Publishing (2018). doi:10.18429/JACoW-FEL2017-MOP055

2. Huang N-S, Liu Z-P, Deng B-J, Zhu Z-H, Li S-H, Liu T, et al. The MING proposal at SHINE: Megahertz cavity enhanced X-ray generation. *Nucl Sci Tech* (2023) 34:6. doi:10.1007/s41365-022-01151-6

3. Schmüser P, Dohlus M, Rossbach J. Undulator Radiation In: GH. Karlsruhe, editors *Ultraviolet and Soft X-Ray Free-Electron Lasers*. Berlin, Germany: Spring (2009). p. 11–22. doi:10.1007/978-3-540-79572-8

4. Sasaki S. Analyses for a planar variably-polarizing undulator. *Nucl Instrum Methods Phys Res Sect Accel Spectrometers Detect Assoc Equip* (1994) 347:83–6. doi:10.1016/0168-9002(94)91859-7

5. Sasaki S, Miyata K, Takada T. A new undulator for generating variably polarized radiation. *Jpn J Appl Phys* (1992) 31:L1794. doi:10.1143/JJAP.31.L1794

6. Sasaki S, Kakuno K, Takada T, Shimada T, Yanagida K, Miyahara Y. Design of a new type of planar undulator for generating variably polarized radiation. *Nucl Instrum Methods Phys Res Sect Accel Spectrometers Detect Assoc Equip* (1993) 331:763–7. doi:10.1016/0168-9002(93)90153-9

7. Bahrdt J, Frentrup W, Gaupp A, Kuske B, Meseck A, Scheer M. *Undulators for the BESSY Soft-X-Ray FEL*. Trieste, Italy: JACoW Publishing (2004).

8. Temnykh AB. Delta undulator for Cornell energy recovery linac. *Phys Rev Spec Top - Accel Beams* (2008) 11:120702. doi:10.1103/PhysRevSTAB.11.120702

9. Nuhn H-D, Anderson S, Bowden G *R&D Towards a Delta-type Undulator for the LCLS*. New York, NY: JACoW Publishing (2014).

10. Nuhn H-D, Anderson SD, Coffee RN. *Commissioning of the Delta Polarizing Undulator at LCLS*. Daejeon, Korea: JACoW Publishing (2015). doi:10.18429/JACoW-FEL2015-WED01

11. Schmidt T, Calvi M, Schmitt T, Strocov VN, Zimoch D. Operation experience of the UE44 fixed gap APPLE II at SLS. *J Phys Conf Ser* (2013) 425:032020. doi:10.1088/1742-6596/425/3/032020

12. Kinjo R, Kagamihata A, Seike T, Kishimoto H, Ohashi H, Yamamoto S, et al. Lightweight-compact variable-gap undulator with force cancellation system based on multipole monolithic magnets. *Rev Sci Instrum* (2017) 88:073302. doi:10.1063/1.4991652

13. Strelnikov N, Vasserman I, Xu J, Jensen D, Schmidt O, Trakhtenberg E, et al. Vertically polarizing undulator with dynamic compensation of magnetic forces. *Phys Rev Accel Beams* (2017) 20:010701. doi:10.1103/PhysRevAccelBeams.20.010701

14. Bahrdt J, Grimmer S. *In-vacuum APPLE II undulator with force compensation*. Taipei, Taiwan: AIP Publishing (2019). p. 030031. doi:10.1063/1.5084594

15. Rial E, Bahrdt J, Grimmer S, Meseck A, Scheer M. Development of a cryogenic APPLE CPMUE15 at BESSY II. *J Phys Conf Ser* (2022) 2380:012018. doi:10.1088/1742-6596/2380/1/012018

16. Kinjo R, Tanaka T. Undulator configuration for helicity switching in in-vacuum undulators. *Phys Rev Accel Beams* (2020) 23:020705. doi:10.1103/PhysRevAccelBeams.23.020705

17. Joehri H, Jöhri H, Calvi M, Hindermann M, Huber L, Keller A, et al. *Development of the new UE38 Undulator for the Athos Beamline in SwissFEL*. Paris, France: JACoW Publishing (2018). doi:10.18429/JACoW-MEDSI2018-TUOPMA03

18. Schmidt T, Calvi M. APPLE X undulator for the SwissFEL soft X-ray beamline athos. *Synchrotron Radiat News* (2018) 31:35–40. doi:10.1080/08940886.2018.1460174

19. Calvi M, Camenzuli C, Prat E, Schmidt T. Transverse gradient in Apple-type undulators. *J Synchrotron Radiat* (2017) 24. doi:10.1107/S1600577517004726

20. Chubar O, Elleaume P, Chavanne J. A three-dimensional magnetostatics computer code for insertion devices. *J Synchrotron Radiat* (1998) 5:481–4. doi:10.1107/S0909049597013502

21. Yu C, Jiang ZQ, Zhou QG. A magnetic landmark for high precision undulator magnetic fiducialization. *High Power Laser Part Beams* (2018) 30:085104. doi:10.11884/HPLPB201830.180030

frontiers | Frontiers in Physics

TYPE Review
PUBLISHED 07 July 2023
DOI 10.3389/fphy.2023.1187346

OPEN ACCESS

EDITED BY
Bo Liu,
Chinese Academy of Sciences (CAS), China

REVIEWED BY
Mehdi Abedi-Varaki,
Center for Physical Sciences and Technology (CPST), Lithuania
Yingchao Du,
Tsinghua University, China
Houjun Qian,
Zhangjiang Laboratory, China

*CORRESPONDENCE
Fernando Sannibale,
fsannibale@lbl.gov

RECEIVED 16 March 2023
ACCEPTED 02 June 2023
PUBLISHED 07 July 2023

CITATION
Sannibale F (2023), High-brightness electron injectors for high-duty cycle X-ray free electron lasers.
Front. Phys. 11:1187346.
doi: 10.3389/fphy.2023.1187346

High-brightness electron injectors for high-duty cycle X-ray free electron lasers

Fernando Sannibale*

Lawrence Berkeley National Laboratory, Berkeley, CA, United States

The successful development in the last two decades of X-ray free electron lasers (FELs) with their revolutionary brightness performance has been tightly dependent on the parallel development of electron guns and injectors capable of providing the high-brightness electron beams required by FELs lasing at these short wavelengths. The ultimate brightness delivered by a linear accelerator (linac) is already set at its injector and the remaining part of the accelerator can be only designed to preserve the injector performance. The technology to be used for the accelerator part of an X-Ray FEL strongly depends on the duty-cycle at which the FEL operates. Normal-conducting, room-temperature, copper-based radio frequency (RF) technology is typically used for low duty-cycles of up to approximately 10^{-3}. For higher duty-cycles and up to continuous wave (CW) operation, the linac must rely on superconductive RF technology because, with the higher duty-cycle, the increasingly higher power dissipated in normal conducting RF structures becomes excessive for the warm technology. The situation changes in the lower energy part of the accelerator, where injector schemes, based on direct current, normal-conducting, and superconducting RF electron guns, are demonstrating the beam quality performance required by high-duty-cycle X-ray FELs. In this paper we start with a description of the requirements for such injectors, followed by an overview of the pursued technologies and schemes, and by a discussion on the main differences in terms of beam dynamics between low and high duty-cycle injectors.

KEYWORDS

FELs, electron injectors, photo-guns, electron sources, X-ray sources, continuous wave

1 Introduction

The X-ray free electron laser (XFEL) revolution that initiated in 2009 with the first lasing at these short wavelengths by the LCLS at the Stanford Linear Accelerator Center (SLAC) [1], provided new opportunities for scientific experiments that were not accessible before. Based on this successful achievement, investments all over the world allowed to create what is now a significant number of such facilities [2]. The LCLS and most of the presently operational XFELs, were designed to operate at relatively low duty cycle (typically less than 10^{-3}—typically with a few microseconds radio frequency (RF) pulses at a few hundred Hz repetition rates). Such a choice was largely driven by the availability of the well-established GHz-class RF technology based on room-temperature copper structures which could be readily used for the linac accelerating sections. Duty-cycles higher than 10^{-3} were beyond the warm RF technology capability of dissipating the increasing ohmic losses on the accelerating sections walls. Therefore, higher duty-cycle schemes required the use of superconducting RF technology for their linac sections. Indeed, in 2017, the European

XFEL at DESY in Germany used superconducting 1.3 GHz niobium accelerating sections in their linac to operate at approximately 10^{-2} duty cycle [3].

Nevertheless, even before LCLS first lasing, the scientific case for XFELs was already asking for XFELs capable to operate at much high higher duty-cycles, including in continuous wave mode (CW) [4] and several groups around the world started to work for making that possible and projects based on CW linacs, as the LCLS-II at SLAC [5] and SHINE in Shanghai [6], were funded to develop XFELs capable to generate equally spaced laser pulses at MHz-class repetition-rates, and the already operational European XFEL [3] started to consider a higher duty-cycle upgrade [7].

For the sake of this paper scope, before diving into the discussion about the requirements that an XFEL and its injector must satisfy to operate at high-duty-cycles, it is necessary to remind some crucial aspects of the high gain FEL theory. The electron beam brightness B, proportional to the electron beam density in the 6-dimensional phase space, plays a central role in the physics and performance of an FEL:

$$B = \frac{N_e}{\varepsilon_{nx}\varepsilon_{ny}\varepsilon_{nz}} \tag{1}$$

with N_e is the number of electrons in a bunch, and ε_{nx}, ε_{ny} and ε_{nz} are respectively the horizontal, vertical, and longitudinal normalized emittances of the bunch. In general, for optimizing an FEL performance it is necessary to maximize the electron brightness. For the high-gain single-pass FEL applications discussed here, it is in general sufficient to maximize the 4-dimensional transverse component of the brightness by maximizing the number of electrons and minimizing the horizontal and vertical emittances, while using the longitudinal emittance as a knob to control and mitigate the undesired effects of space charge forces inside the bunch.

In the 1-dimensional FEL theory [8], which neglects the effects of the energy spread, diffraction and transverse size of the beam, the overall performance of an FEL is regulated by the parameter ρ defined, in the case of a planar horizontal undulator, as:

$$\rho = \frac{1}{\gamma}\left[\frac{1}{64\pi^2}\frac{I_{peak}}{I_A}\frac{1}{\varepsilon_x\beta_x}\lambda_u^2 K^2 JJ^2\right]^{1/3} \tag{2}$$

where γ in the electron beam energy in rest mass units, I_{peak} is the bunch peak current, I_A is the Alfven current constant, λ_u and K are respectively the undulator wavelength and parameter (with K proportional to the undulator peak magnetic field B), JJ is a slow varying function of K (which typically assumes values between 0.6 and 1), β_x is the average horizontal beta function and ε_x is the geometric emittance, with all beam quantities measured inside the undulator. The parameter ρ, which defines among other things, the efficiency and the gain length of an FEL, needs to be maximized for the best FEL performance.

According to the undulator resonant condition $\lambda = \lambda_u/2\gamma^2\,(1 + K^2/2)$ and considering the technologically available cm-class undulator wavelengths, lasing at the short X-ray wavelengths (λ ~0.1 to ~1 nm) requires GeV-class electron beam energies. Unfortunately, Eq. 2 shows that when accounting for the technological limits of undulators in terms of minimum period and maximum B field, higher beam energies lead to smaller ρ parameters.

FELs generates transverse diffraction limited light pulses, so for an efficient lasing the transverse geometric emittance ε_w of the electron beam must be smaller than or comparable to the photon diffraction limit:

$$\varepsilon_w \lesssim \frac{\lambda}{4\pi} \text{ or } \varepsilon_{wn} \lesssim \gamma\frac{\lambda}{4\pi} \text{ with } w = x, y \tag{3}$$

where λ the FEL photon wavelength.

When targeting a particular λ, the beam energy is fixed by the undulator technology and resonance condition. Equation 3 then indicates the requirement that the electron beam emittance must satisfy, and Eq. 2 indicates that the emittance needs to be minimized to optimize the FEL performance. Now, considering that the forces the beam experiences in a linac are with good approximation Hamiltonian, then, for the Liouville theorem, the normalized emittance generated at the injector cannot be decreased along the linac and can only be at best maintained.

In summary, lasing at X-ray wavelengths requires high-energy, high-brightness electron beams, and the ultimate brightness achievable by a linac is already set at its injector (and, as it will be shown, at its electron gun in particular).

Indeed, the development of FELs widely relied on the invention of the RF photo-gun [9], which for the first time allowed to generate electron beams with the brightness required by FELs. It will be shown later in the paper that the brightness of an electron gun beam increases with the electric field intensity that the electrons experience during emission from the cathode and depends on the cathode characteristics, and on the capability of controlling the 3D distribution of the beam during emission [10, 11]. In RF photo-guns, the beam distribution is controlled by the shape of the laser pulse that drives the photoemission, while the required high fields are generated by the resonant RF structures of the gun. Higher RF frequencies generate higher electric fields and hence higher brightness electron beams, which is the reason why most RF guns, built for driving low-duty-cycle FELs and XFELs, are based on GHz-class room-temperature RF technology. This type of guns can operate at high accelerating electric fields (with peak fields beyond 100 MV/m) but with duty-cycles limited to a maximum of approximately 10^{-2}.

The existing TESLA superconducting RF technology [12], successfully used for operating the linac of the European XFEL, was adapted to CW operation and adopted by the LCLS-II and the SHINE projects. Contrarily to the linac case, existing technologies for the electron gun were not available and in response to that, a significant number of groups around the world started to pursue the development of electron guns capable to operate at very high duty-cycles and up to CW.

2 High-duty-cycle injector requirements

Figure 1 shows the schematics with the main components of two typical injector configurations used in high-duty-cycle XFEL applications. The layout with the RF prebuncher is typically used when the energy of the beam at the gun exit is low and the electrons are not fully relativistic yet.

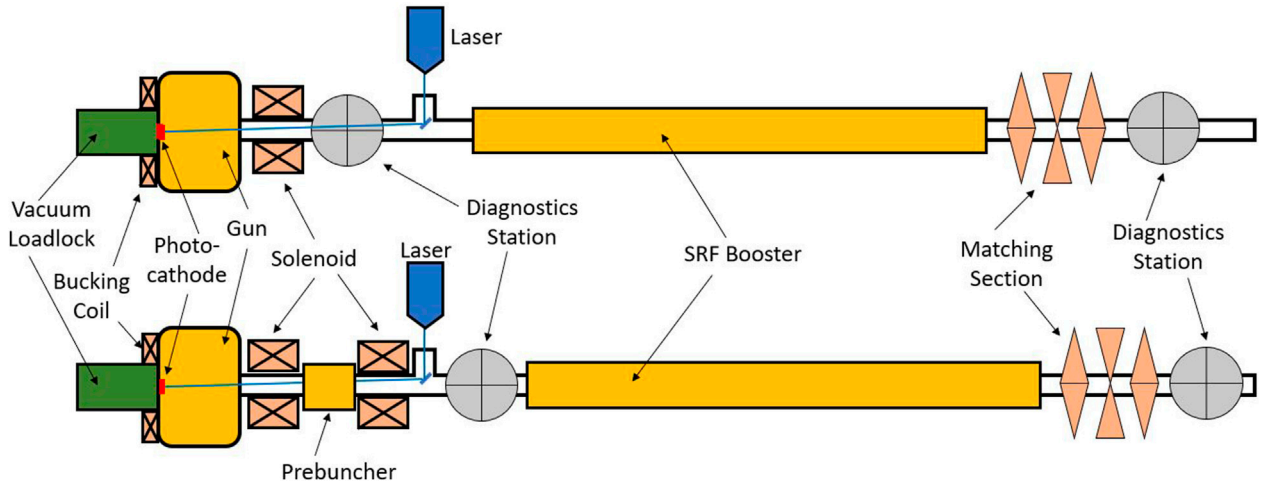

FIGURE 1
Simplified schematics of a high-duty-cycle electron injector in two typical configurations.

TABLE 1 Ranges for the main parameters of high-brightness, high-duty-cycle electron injectors.

Parameter	Value
Duty cycle	From ≈ 0.5 to 1
Repetition rate	Up to several MHz
Charge per bunch	From few tens to few hundreds of pC
Electric field at the cathode during electron emission	≳ 4 MV/m
R.m.s. bunch length at the cathode	From few ps to tens of ps
Normalized slice transverse emittance at the injector exit	From tens to hundreds of nm (lower values for lower charges)
Normalized projected transverse emittance at the injector exit	As close as possible to the slice emittance value
Projected r.m.s. energy spread at the injector exit after energy/bunch-current correlations of order one and two are removed	From several keV to a few tens of keV (lower values for lower charges)
Beam energy at the electron gun exit	≳ 400 keV
Beam energy at the injector exit	≈100 MeV
Peak current at the injector exit	From few tens to few hundreds of A (lower values for lower charges)
Compatibility with magnetic fields in the cathode/gun region	Required for the emittance compensation process
Cathode type	High quantum efficiency (QE ≳ 10^{-2}) photocathodes
Operational vacuum pressure in the electron gun	10^{-7}–10^{-9} Pa
Cathode replacement capability	Require a vacuum load-lock system to operate semiconductor high QE cathodes
Maximum average dark current	≲ 1 μA
Operation reliability	≳ 99%

Table 1 summarizes the requirements for the main parameters that an electron injector must satisfy to drive a high-duty-cycle XFEL. The ranges of values in the table are based on the results of experimental and/or simulated studies from operational and proposed injectors for high-duty-cycle XFELs (see, for example, [13–20]), and account for the technological limitations that the high duty cycle imposes (more in Section 3). A deeper discussion on the requirements shown in the table, joined, when necessary, by a high-brightness injector physics recap, follows.

As mentioned in the Introduction, the transverse brightness performance of an electron gun directly depends on the intensity of the electric field that the beam experiences at the cathode during

emission (often referred to as the launching field intensity). From an intuitive point of view, higher fields, at the time when the very low energy electrons are emitted from the cathode, allow for a faster acceleration and for an increased rigidity of the newly created electron beam.

The higher rigidity reduces the emittance increase due to intra-bunch space charge forces and Coulomb scattering within the beam particles. Two different operational regimes can be identified, the *pancake* beam case, where the transverse beam size of the emitted beam is significantly bigger than its longitudinal size, and the *cigar* beam case, where the opposite is true. In both cases, higher fields at emission ($E_{emission}$) lead to higher brightness. For the pancake regime the transverse brightness is [10]:

$$B_{\perp} \propto \frac{E_{emission}}{kT} \tag{4}$$

where k is the Boltzmann constant, and T is the transverse temperature of the electrons in the bunch. While for the cigar regime B is [11]:

$$B_{\perp} \propto \frac{E_{emission}^{3/2}}{\sigma_p^2} \frac{\Delta t}{\sqrt{r}} \tag{5}$$

where σ_p is the root mean square (r.m.s.) transverse momentum spread of the particles at extraction, r and Δt are respectively the radius and the pulse length of the laser driving the photoemission.

These expressions indicate two of the most important parameters to focus on when designing high-brightness electron guns: high electric fields at emission and low values for the terms kT and σ_p, which are just different representations of the r.m.s. momentum component of the intrinsic (sometimes also referred as thermal) emittance of the cathode. Their value depends on the cathode material and on the energy of the photon used for the photoemission.

Equation 5 shows that in the cigar regime, longer laser pulses can be used for increasing the transverse brightness, but at the expense of an increase of the longitudinal emittance. Nevertheless, in most XFEL schemes, this is an acceptable tradeoff because, as mentioned earlier, the lasing performance is mostly defined by the transverse brightness as long as the quality of the longitudinal phase space does not prevent the required bunch compression downstream in the linac. Clearly, there are limits on how long a bunch can be, longer bunches require more compression in the linac, and they also sample more nonlinearities from the time-variable RF fields in the gun and in the linac.

Such nonlinearities introduce correlations in the phase space longitudinal distribution and can also lead to transverse emittance increase [21, 22]. First and second order correlation terms in the longitudinal phase space can be respectively controlled and corrected by properly phasing part of the linac RF and by using higher-harmonic RF linearizers [23] or nonlinear optical systems [24]. Correlations with order higher than 2 cannot be directly controlled and can limit the level of compression in the linac necessary to achieve the few kA peak currents required at the undulator. Simulations indicate that at the injector exit, the residual r.m.s. energy spread associated with the higher order correlations (calculated by removing the linear and quadratic terms) should be contained between several keV and a few tens of keV (with values increasing with charge) [13, 14]. A compensation scheme for the correlations in the longitudinal phase space, based on a buncher with dual RF modes has been recently proposed and planned for the SHINE project [25]. From the transverse plane point of view, a compromise value for the bunch length at the cathode must be struck to balance between minimizing space charge effects, pushing towards longer bunches, and reducing both the compression requirement in the linac and the effects of time-variable RF nonlinearities, which push towards shorter bunches.

Very high electric fields at emission allow to operate the beam in the so-called *beam blowout* regime where pancake like beams, with very small bunch length to transverse bunch size aspect ratios, are created at the cathode. During the propagation of this beams after the photoemission, space charge forces gradually expand the beam longitudinal and transverse distributions creating an ellipsoidal 3D distribution characterized by dominantly linear internal space charge forces [26]. Linear forces allow for a better emittance compensation (described later in the paper) and also facilitate bunch compression. For a given bunch charge, the blowout regime tends to generate beams with a better longitudinal phase space but with larger transverse emittances when compared with the more conventional regimes previously described. Furthermore, this special regime requires quite high gun fields, and cathode materials with fast photoemission responsivity (metals). Such limitations make the blowout regime a poor match to the requirements of a high-duty-cycle XFEL.

The regimes described by Eqs 4, 5 define the maximum transverse brightness that can be obtained at the cathode and accounts for the cathode contribution to the transverse momentum component of the beam emittance. However, the final normalized emittance ε_n at end of an injector depends also on other emittance components as shown in the following expression [21]:

$$\varepsilon_n = \sqrt{\varepsilon_{sc}^2 + \varepsilon_{in}^2 + \varepsilon_{RF}^2 + \varepsilon_{sol}^2 + \varepsilon_{Bz\,Cathode}^2} \tag{6}$$

where ε_{sc} is the space charge component of the emittance, ε_{in} is the cathode intrinsic emittance, ε_{RF} is the emittance associated with the nonlinear nature of the RF fields used for acceleration, ε_{sol} is the result of the quadratic sum of the geometric and chromatic aberrations introduced by the solenoid magnet(s), and $\varepsilon_{Bz\ Cathode}$ indicates the emittance increase if solenoidal magnetic fields are present on the cathode surface.

The intensity of the space charge forces is directly proportional to the beam charge density. Therefore, in general decreasing the charge density decreases the emittance space charge contribution ε_{sc} in Eq. 6. Additionally, the linear component of the space charge force that contributes to ε_{sc} can be controlled and eliminated by the technique known as *emittance compensation*. A qualitative description of the process is provided here and more rigorous descriptions of it can be found in [26, 27]. Longitudinal bunch distributions at the gun exit are generally non-uniform showing current profiles that vary along the bunch. If the beam distribution is conceptually divided into slices, each of such slices will contain a different amount of charge and have a different charge density. Therefore, the intensity of the defocusing space charge force that the particles in the slice experience, which in the linear case is

proportional to their radial position, will be different in each of the slices and also different will be the consequent expansion and rotation in the transverse phase space that each slice experiences during the beam propagation. Such differential phase space rotation along the bunch generates an undesired increase of the projected transverse emittance of the bunch. A linear focusing lens, and in particular a solenoid in case of cylindrically symmetric beams, can reverse the slice expansion/rotation and, if its focal length is properly set, also realign the slices phase space at a certain position downstream of the lens minimizing the projected emittance. Such a technique is widely exploited in electron guns where the solenoid(s), visible in Figure 1, is (are) used to perform the just described emittance compensation to get the full slice realignment right at the entrance of the RF booster that, by accelerating the bunch, "freezes" the realigned bunch distribution. Although this technique compensates only for the effects of the linear component of the space charge force, it is still quite important because that component is typically dominant in the core of the bunch.

It was previously mentioned that the cathode intrinsic emittance term ε_{in} in Eq. 6 is proportional to the r.m.s. transverse momentum of the beam at the cathode, which depends on the cathode material and on the photon energy used for the photoemission. The term is also proportional to the beam transverse size, which is instead defined by the transverse size of the laser pulse. This last dependence indicates that using the transverse beam size at the cathode as a knob for controlling the bunch charge density is not advisable and must be minimized to avoid increasing the cathode intrinsic emittance contribution. As Eq. 5 suggests, varying the laser pulse length, and consequently the electron bunch length, is a better way to control the charge density in the bunch.

The RF emittance term ε_{RF} in Equation 6 is the consequence of the time dependent RF defocusing associated with the accelerating RF fields in the injector. Such a term is proportional to the square of the ratio between the bunch length and the RF wavelength [21, 22] and must be properly accounted because it can potentially limit the use of the bunch length for controlling the bunch charge density. In most XFEL schemes and layouts, but in particular in high-duty-cycle ones, bunch compression starts already in the injector by either using a prebuncher [28] or the so-called *velocity bunching* technique [29]. Higher compression factors in the injector reduce and simplify the final compression in the downstream main linac. On the other hand, high levels of compression increase the bunch charge density and the associated space charge forces, which applied to the injector beam when it is not fully relativistic, can cause, as was described earlier, emittance degradation and generation of higher order correlations in the longitudinal phase-space distribution. Again, a proper bunch length that balances these contrasting effects must be found.

The term ε_{sol} in Eq. 6 indicates that the field of the main solenoid(s) can directly affect the emittance performance of the injector. The magnetic field profile in this critical component must be designed to minimize geometric and chromatic aberrations. Such aberrations strongly depend on the transverse beam size, with fourth and second power dependencies respectively [21, 30]. This also implies that the optics to transport the electron beam to the solenoid must be carefully designed to minimize the beam size inside the magnet. In particular, the distance between the cathode and the first solenoid needs to be minimized to avoid a large transverse expansion of the beam before entering the solenoid.

The last term in Eq. 6 is $\varepsilon_{Bz\ Cathode}$. Solenoidal fields at the cathode plane during photoemission add an additional magnetic component to the transverse canonical momentum of the electrons, which is later converted to classical momentum when the electrons propagate to a region where the solenoidal field is zero [31]. This resulting extra momentum component is responsible for the $\varepsilon_{Bz\ Cathode}$ term in Eq. 6 and consequently, solenoidal fields at the cathode surface must be avoided.

A detailed derivation of the emittance terms in Eq. 6 can be found elsewhere [21, 22, 31].

Minimizing ε_{sc} requires, besides a correctly executed emittance compensation, a decrease of the bunch charge density at the gun. This is in part done by increasing the transverse beam size of the beam at the cathode, but by small amounts because as it was said before, larger beam sizes increase the ε_{in} term. Most of the charge density control is instead performed by lengthening the bunches, which on the other hand can also increase ε_{RF}. Additionally, minimizing the beam size inside the solenoid(s) to control ε_{sol} increases the charge density. In summary, all the terms in Eq. 6 that define the final injector emittance depend on the charge density of the bunch ($\varepsilon_{Bz\ Cathode}$ can be ignored because, as it will be shown in Section 3.4, it can be completely canceled using solenoidal bucking coils). Higher charges per bunch, in general require beams with larger volumes to maintain acceptable charge density, and this, for what has been just described, increases the total beam emittance at the end of the injector. In other words, the final normalized emittance obtainable by an injector depends on the charge of the bunch that is being generated, the larger the charge, the larger the emittance. A quantitative analytical description on how the emittance scales with bunch charge can be found in [32] but it should be remarked that, in designing a real injector, extensive simulation studies are necessary to optimize the final performance in terms of minimal emittance and quality of the longitudinal phase space.

At this point, it is worth reminding the distinction between slice and projected emittances. To that scope, it is useful to conceptually divide the electron bunch into longitudinal slices with length comparable to the FEL cooperation length [8]. The emittance calculated over the particles in a slice is referred to as the slice emittance of that slice. In the 1D FEL theory, the ρ parameter shown in Eq. 2 depends locally on the slice emittances but does not account for potential transverse misalignments between different slices. In the real case, the manipulation that the beam undergoes in the injector and along the linac can generate a significant misalignment among slices. The projected emittance is calculated over the whole bunch. Its value is in general larger than the ones of the slices and assumes a minimum only when no slice misalignment exists. In a well-designed FEL (and injector), the projected and slice emittance values should be as close as possible. A beam with misaligned slices is difficult to transport and does not properly overlap with the photon beam inside the undulator ultimately degrading the FEL performance.

The intensity of the space charge force scales with the inverse square of the beam energy measured in rest mass units, so sufficiently high beam energies at the gun and at the injector exits are necessary for controlling the effects of space charge forces. Experimental and simulation studies indicate that electron gun energies greater than approximately 400 keV are necessary to

provide to the beam travelling from the gun to the booster, a sufficient rigidity to undergo the transport, focusing and emittance compensation process with acceptable emittance and longitudinal phase space degradation induced by space charge forces. The energy at the injector exit must be sufficiently high to make space charge effects negligible, but small enough to allow for realistic laser powers and chicane settings at the laser heater [33] [required for controlling the microbunching instability (MBI) [34] during the compression process along the linac]. The energy value of ~100 MeV in Table 1 represents the compromise typically used in most of the existing operating XFELs.

Independently from the operational duty-cycle of an XFEL, the optimal charge per bunch to be used depends on its specific mode of operation. In most of the schemes, such as self-amplified spontaneous emission (SASE), self-seeding, high gain harmonic generation (HGHG), echo enabled harmonic generation (EEHG), etc. [35, 36], the optimization of the XFEL performance typically converges to a charge per bunch of a few hundreds of pC, which compressed in the injector and along the linac to a few kA bunch peak current required in Eq. 2 to provide the necessary FEL gain [20, 37]. The peak current targeted at the injector exit depends on the bunch charge and on the electric field at the cathode, and from lower to higher charges, ranges from the lower to the higher values shown in Table 1. The final peak current at the end of the injector is controlled by the driving laser pulse length and by the level of compression performed at the injector.

In special XFEL modes of operations, for example, for those optimized for the generation of short photon pulses, lower charges per bunch are preferred. The reason for that starts from the observation that the FEL parameter ρ in Eq. 2 depends on the bunch peak current and not on the total bunch charge. Exploiting this fact, bunches with charges as low as a few tens of pC can be generated at the injector with lower normalized emittance and better longitudinal phase space quality than the ones in bunches with higher charge. These low charge bunches can then be compressed in the linac (with no laser heating and without exciting the MBI in the linac compressors) to kA-class peak currents to generate single-mode, high-power X-ray pulses with less than 10 fs duration [38].

The discussion in this section has pointed out the importance of controlling the bunch distribution at the cathode during electron emission. The most effective way to perform this task in a photo-gun is to properly shape the laser pulse to generate an electron bunch with a distribution that reproduces the one of the laser pulse. More on cathodes and lasers in the next section.

The high electric fields in the injector RF structures, and in particular in the gun, can cause extraction of electrons from the structure walls by field emission. Part of such electrons can then find the right RF phase and be accelerated in the gun and along the injector creating an undesired flux of electrons referred to as *dark current*. While in low-duty-cycle linacs the average dark current value is in general small and tolerable, in high-duty-cycle or CW injectors significantly large amounts of dark current can be created, which if not controlled, can damage and/or activate accelerator components, quench superconducting structures, generate large radiation doses that could require expensive additional shielding, and limit the maximum accelerating field at cathode. Field emission intensity increases exponentially with the intensity of the electric field [39] and depends on several factors: the material used, the fabrication processes that the material underwent, the surface roughness, the temperature at which the material operates, the contamination by particulates and/or hydrocarbons, and the shape of the components immersed in the high electric field. Dark current can be minimized by controlling/managing those factors but also by a proper design of the electron transport channel and the use of collimators and/or of fast electromagnetic deflectors to selectively remove dark current while minimally affecting the main beam [40].

3 High-duty-cycle injector technologies

The requirement for an injector to operate at high duty-cycles has a profound impact on the technology and schemes that must be used in the different injector subsystems and components. Ultimately, the technological constraints would often impact and define the beam dynamics regime at which the injector operates. XFELs are user facilities and as such, operation reliability at the level of approximately 98% for the whole complex are typically targeted. To be compatible with such a goal, the injectors must perform at reliability levels of ~99%. This challenging requirement must be also taken into account when selecting the technology to be used for the injector components.

3.1 Photocathodes and lasers

In some materials, photoemission can be already triggered by photons in the near infrared. For example, GaAs-based photocathodes, which belong to this category, are widely used in guns in nuclear physics facilities because of their capability of generating polarized electron beams. In the case of FEL applications, where such a requirement is not necessary, a variety of materials emitting in the visible and in the near ultraviolet (UV), ranging from metals to semiconductors, are used instead. The parameters of a photocathode that are most important for an XFEL application, are the quantum efficiency (QE), indicating the number of electrons emitted per single impinging photon, the QE lifetime, and the work function of the cathode material, which defines the minimum photon energy required for generating photoemission. Another important quantity is σ_p, the r.m.s. transverse momentum component of the cathode intrinsic emittance, that for most cases depends on the difference between the actual laser photon energy ε_{photon} and the cathode work function (see, for example, Ref. [10]). Most of these quantities are not independent and in general are correlated. In fact, QE increases with ε_{photon} as does σ_p, so the choice of the photon energy (besides from accounting for the available laser technology) must target values high enough to get reasonably high QEs, but low enough to keep the cathode intrinsic emittance under control.

For high-duty-cycle applications, it is necessary to use cathode materials with high QE in the ~10^{-2} range to operate with available and reasonable laser power amounts. Metal cathodes as copper, widely used in low-duty-cycle XFELs, emits in the near UV (~250 nm) and are in general very robust, chemically stable and with long QE lifetimes, but cannot be used in high-duty-cycle

applications because of their low QEs in the ~10^{-6}–10^{-4} range. Conversely, QEs in the ~10^{-2} range are readily available in semiconductor materials such as, for example, cesium telluride that emits in the near UV or multi-alkali antimonides, which emit in the visible (green). The main disadvantage of semiconductor cathodes is that they are very reactive compounds and hence, to ensure a reasonable QE lifetime, they require very low gun vacuum pressures (as shown in Table 1) with extremely low partial pressures for contaminants such as O_2, CO, CO_2, hydrocarbons, etc. A thin layer of these semiconductor materials is deposited on a metal plug in separate cathode laboratories and transported to the gun location without exposing them to air in specially designed "vacuum suitcases" [41]. The metal plug is designed to be extracted and inserted into the gun to allow for the periodical replacement of cathodes at the end of their QE lifetime. Exchange of cathodes must be performed without exposing the cathode to air and without breaking vacuum in the gun. Special vacuum load-lock systems are necessary for the operation [41]. Cesium telluride and Multi-alkali antimonide cathodes have already demonstrated their capability of operating at high duty-cycle regimes with the required charge, QE, and QE lifetimes [42–44]. Detailed reviews of cathode materials and of their properties can be found elsewhere [45–47].

It was just discussed that in high-duty-cycle XFELs photocathodes with QEs in the 10^{-3} to 10^{-2} range are necessary to generate the required several hundreds of pC electron bunches. In terms of laser specifications that translates to the requirement of several tens of nJ pulse energy at the cathode. The typical scheme used to drive photoemission in photo-guns starts from pulses from near infrared (IR) lasers, which are frequency converted in the visible or in the near UV depending on the photocathode being used. The efficiency of the conversion process depends on how it is performed but in the case of multiple conversions can be as low as 20%. Additional manipulation is also required to control the 3D distribution of the pulses, and this process can also show relatively low efficiencies. Lastly, intensity losses in transporting the photon beam from the laser hall to the electron gun cathode must be considered as well. Accounting for all such inefficiencies conservatively translates into a pulse energy for the IR laser of a few tens of μJ, and, for example, for one MHz repetition rate an IR laser with a total average power of a few tens of W is then necessary. The good news is that lasers with those characteristics are well within the presently available technology and commercial options also exist. As an example, fiber lasers, like the one used by LCLS-II [48], represent a good and convenient option for this type of application.

It was previously discussed that in an electron bunch with an uniform ellipsoidal 3D charge distribution, space charge forces are fully linear and that their effects on beam emittance can be completely mitigated by the emittance compensation process. Generating ellipsoidal electron beams requires either ellipsoidal laser pulses or operating in the previously described beam blowout regime [49] that, for what it was said before, does not represent a good match for XFEL applications. Consequently, a significant R&D effort by various groups around the world is being dedicated to the difficult task of developing pulse shaping techniques capable of generating ellipsoidal laser pulses [50]. In the meantime, significantly simpler techniques are used in FELs to generate "hard-hat" transverse and trapezoidal longitudinal distributions, as compromise distributions that allows to reduce the nonlinear space charge force component in the bunch. A review of laser pulse shaping techniques can be found in [51].

3.2 Photo-guns

Present and proposed low-duty cycle XFELs largely rely on NC high-frequency (GHz-class) copper RF guns to generate their electron beams. These successful types of guns can deliver the electron beam brightness required for an efficient XFEL lasing. Unfortunately, as mentioned before, such schemes cannot be scaled up to the duty cycles values indicated in Table 1 because of the excessive power density that would be dissipated on the gun cavity walls due to ohmic losses [52]. For addressing the need of a high-brightness electron gun capable of driving a high-duty-cycle XFEL, a significant number of groups and resources around the world were dedicated (and are still dedicated) to the development of such an electron source. Schemes based on direct current (DC), super-conducting RF (SRF), and low frequency (100–300 MHz) normal conducting RF (NCRF) technologies were and are pursued, as well as a few hybrid schemes combining some of those technologies.

3.2.1 Normal-conducting room-temperature low-frequency RF guns

A natural extension of the successful high-frequency NC copper gun is represented by schemes where the RF frequency is lowered from the several GHz range down to ~100–300 MHz, in the so-called very high frequency (VHF) band. The idea behind this scheme consists in exploiting the different scaling with RF frequency (f) existing between the power density dissipated on the RF structure walls and the voltage breakdown threshold in the same structures, which respectively scales as $f^{5/2}$ and $f^{1/2}$ [53, 54]. This favorable scaling allows to lower the RF frequency at a point where the power dissipated on the gun walls becomes manageable permitting CW operation while still maintaining the high electric fields at the cathode required for the high brightness performance [55].

Indeed, a NCRF gun, developed for a lower brightness application, was able, using extreme cooling techniques, to run in CW at 700 MHz [56]. On the other hand, by lowering the frequency in the VHF range, the power dissipated in the gun becomes removeable by well-established and reliable conventional water-cooling schemes. Accelerating fields at the cathode during photoemission at approximately and beyond 20 MV/m have been already demonstrated by two NCRF guns operating in CW at ~200 MHz (*VHF-guns* in short) [18, 57, 58], and new upgraded configurations targeting fields at and beyond 30 MV/m [59–61] have been proposed. Such fields are approximately a factor two smaller than the ones present at the cathode during photoemission in low-duty-cycle, high frequency NC copper RF guns, and are comparable with those targeted by the SRF guns described in the next sub-section.

At the field levels generated by existing and proposed VHF-guns, the optimal mode of operation for a high-brightness performance is the cigar regime described in Section 1. CW VHF guns can operate at beam repetition rates of hundreds of MHz (limited only by their

own RF frequency) but, high-duty-cycle XFEL applications typically require MHz-class repetition rates. NCRF guns are compatible with magnetic fields in the cathode/gun area as necessary for the emittance compensation process. The long period associated with VHF frequencies makes the beam dynamics practically identical to that of a DC gun case, but with much higher gradients and beam energies. The long period also allows for a launching phase at the peak of the RF field, contrarily to the significant de-phasing typically required in GHz-class RF and SRF guns to account for the time it takes to the beam to become sufficiently relativistic inside the gun. High electric fields at the cathode decrease that time and the related de-phasing, but for a fixed electric field, higher RF frequencies increase the de-phasing. The combination of field and RF frequency values in the present GHz-class RF guns produces larger de-phasing with respect to the VHF-gun case.

Additionally, the meter-class long VHF wavelengths permit the inclusion of relatively large apertures in the cavity walls with minimal RF field distortion and so allowing to create a high-conductance vacuum path to externally located pumps, setting the conditions for the very low vacuum pressures required by semiconductor cathodes [62]. Due to resistive losses on the RF structures walls, operating the gun in CW requires RF sources with 100 kW-class power. Such CW power levels are readily achievable/available by solid-state or tetrode-based RF amplifiers.

The first prototype of a VHF-gun, developed at the Berkeley Lab in the framework of the APEX project, demonstrated the high transverse brightness and longitudinal phase space quality required by the LCLS-II high-duty-cycle XFEL [14]. The beam tests were performed only at the charge per bunch of 20 pC due to LCLS-II deadline requirements. The results of these tests validated the simulation predictions providing confidence in the performance predicted also at higher charges. A close version of the APEX gun is now driving the commissioning of the LCLS-II [18] and recently demonstrated XFEL-level brightness with 50 pC charge per bunch [63], A different frequency VHF-gun is also being developed for the SHINE XFELs [64].

3.2.2 Superconducting RF guns

Electron guns based on SRF structures present several important advantages: they are potentially capable of high accelerating fields; the superconducting operation ensures an excellent power efficiency that strongly reduces the RF power requirements; the effective cryo-pumping by the superconducting walls allows for a very good vacuum performance; and the cryogenic temperatures reduce nuclear vibrations that are responsible for the migration of imperfections (dislocations) from the bulk of the cavity walls to their surface where they can potentially become a source of dark current.

On the other hand, they also present challenges. In Section 2, it was shown that the distance between the cathode and the first solenoid is critical for the brightness performance and for the emittance compensation process, and that in general such a distance needs to be minimized. Meissner field exclusion prevents the use of externally applied magnetic fields forcing the use of either cryogenic solenoids or to locate room temperature solenoids downstream of a specially designed compact cold-to-warm transition.

The natural photocathode choice for SRF guns would be to use a superconducting cathode. Niobium, the material typically used for superconducting cavities, shows a low QE of ~10^{-5} [65], which makes it not suitable for a high beam repetition rate application. Encouraging initial results from an R&D dedicated to the deposition of a layer of lead (a superconductor below 7.2 K) on niobium have demonstrated QE emissions of ~10^{-3} that would allow operation at 100 kHz-class repetition rates [66]. The R&D effort now continues and focuses on improving the process reproducibility, the optimization of the surface roughness, and the characterization of the cathode intrinsic emittance and QE lifetime [47].

A solution in alternative to superconducting cathodes, which allows to satisfy MHz-class beam repetition rates (typically required by high-duty-cycle XFELs), is represented by the same high QE semiconductor cathodes used in the NC guns described in the previous sub-section. In order to use these types of cathodes in SRF guns, several technical issues need to be addressed. First, the warm cathode must be thermally isolated from the superconducting walls to avoid a reduction of the cathode QE and degradation of the SRF performance. Several solutions have been developed and successfully adopted to satisfy this requirement, including the use, in low frequency guns, of relatively simple geometry cathode stalks [17, 67, 68] and, in high frequency guns, the use of RF choke structures for the cathode stalk to minimize the RF loss in the vacuum gap that separates the stalk from the rest of the cavity [67, 69, 70]. Particular attention in designing these cathode support structures is placed in controlling and suppressing multipathing in the area. Second, and similarly to high-duty-cycle NC RF guns, the finite QE lifetimes of such cathodes requires a vacuum load-lock mechanism for swapping cathodes without air exposure. The additional complication in the SRF case is that the swapping operation must happen without generation of particulates that would degrade the SRF performance, potentially limiting the maximum achievable field.

A significant number of groups around the world have been working during the last three decades on the development of SRF photon-guns by pursuing different schemes and approaches. The R&D effort includes guns using SRF structures resonating at high, GHz-class RF frequencies [69, 70] or at low VHF frequencies [17, 68]. Compatibility of operation with semiconductor cathodes K_2CsSb [71, 72] and Cs_2Te [73] have been already demonstrated and several CW SRF guns are successfully being operated in non XFEL applications.

From the high-duty-cycle XFELs point of view, the simultaneous requirements shown in Table 1, and in particular, the cohabitation between the high-fields at the cathode ($\gtrsim$ 30–40 MV/m) promised by the SRF technology and high-QE semiconductor cathodes, have not been demonstrated yet and more R&D is necessary. From this perspective, the best results achieved so far include: the Wisconsin 200 MHz SRF gun [68], which achieved 20 MV/m at the cathode (corresponding to a beam energy of approximately 1.8 MeV) and that also showed encouraging emittance values with 100 pC charge while operating at a lower field at the cathode [74]; and the SRF 112 MHz gun at the Brookhaven National Laboratory [17], which operating with fields at the cathode of 18 MV/m and at a gun energy of 1.25 MeV, delivered 100 pC beam with a promising emittance but with very long bunches (the peak current at the injector exit was approximately 1–2 orders of magnitude smaller than the values in Table 1).

A recent R&D activity for the development of an SRF gun for an upgrade of the LCLS-II HE project [75] targets a design inspired by the Wisconsin 200 MHz SRF gun. The new gun is designed to generate a beam energy of 1.8 MeV and 30 MV/m fields at the cathode.

A recent review of existing and proposed SRF guns can be found in [75].

3.2.3 Direct current guns

Electron guns based on DC schemes present a number of appealing characteristics. They allow for arbitrarily high repetition rates. They are also compatible with the application of magnetic fields in the cathode/gun area, have demonstrated extremely low vacuum pressures ($\lesssim 10^{-9}$ Pa) and are compatible with pretty much all photocathodes presently under consideration. From the point of view of XFELs, the challenge for DC schemes consists in satisfying the requirements for two of the parameters in Table 1, the electric field at the cathode and the energy at gun exit.

Over the last 20 years, significant R&D activity by many international groups was dedicated to the pursuit of higher beam energies at the gun exit and higher gradients at the cathode. The main limitation to the increase of these parameters is represented by electron field emission induced by the high voltage in the gun metallic parts, which can progressively create charge build up in the gun ceramic insulator that eventually induces a voltage breakdown and ceramic punctuation. Original high-brightness DC guns were designed to achieve beam energies as high as about 750 kV but despite the significant R&D effort, the beam energy at the gun exit was for many years limited to less than 400 keV. Only recently, in 2019, the successful operation at 500 kV was demonstrated by the DC gun developed for JAEA in Japan [76]. This successful step towards higher energies was based on the proper choice of materials and by a careful design of a segmented HV insulator (first proposed by Cornell [77]) composed of many (~ten) ceramic rings and circular metallic screens assembled in an alternated fashion. The shape of the metallic screens is optimized to shield the ceramic from field emission.

An alternative approach undertaken by some other groups to mitigate field emission and hence to achieve higher DC voltages, is based on the so-called inverted-insulator geometry scheme in which, contrarily to the "classical" approach used in the other DC guns described above, the cathode assembly is supported by the HV ceramic itself. This configuration results in less metal biased at high voltage and consequently to less metal contributing to field emission. As an example, a DC gun with such a geometry developed at JLAB operates at 350 kV with fields at the cathode of about 10 MV/m [78].

With respect to the other schemes being discussed, DC guns are more subjected to cathode damage caused by ion back-bombardment. In general, in all gun schemes, the electron beam ionizes residual gas molecules inside the gun cavity creating positively charged ions. In the case of DC guns, the large majority of these ions are accelerated by the gun field back on the cathode with energies that can be as high as the gun high voltage [79]. In RF guns, due to the fast-varying fields, the number and energy of the ions that make their way back to the cathode are much smaller than those in the DC gun case making ion back bombardment less of an issue [80].

The JAEA gun, and in general most of the other existing or proposed high-voltage DC guns, are designed for driving energy recovery linacs (ERLs), which target operation at very high average currents (tens of mA) at GHz-class repetition rates. In this condition, where a few tens of pC per bunch are necessary, the requirement on the electric field at the cathode can be relaxed. Indeed, the JAEA gun operates at 500 kV at less than 6 MV/m [81], and the Cornell DC gun operates at 400 kV at about 4 MV/m [15, 82].

Despite the low accelerating field at the cathode and low gun energy of it DC gun, the Cornell team was able to demonstrate XFEL-level beam brightness at their injector test facility operating the gun at 395 kV [16]. This was made possible by a combination of several factors, the use of a low thermal emittance semiconductor cathode, and with the DC gun followed by a 1.3 GHz NC prebuncher and by a special capture section composed by a cryomodule with five 2-cell SRF cavities resonating at 1.3 GHz (specially designed for the injector [83]) to accelerate the beam to up 15 MeV [84]. The use of these special short cavities allows to reduce at acceptable levels the RF phase detuning associated with the transit time of the low-energy non-relativistic beam.

3.2.4 Hybrid guns

A hybrid DC-SRF scheme, developed at the Peking University [85], integrates a relatively low voltage (100) kV DC photo-gun in a cryostat containing a 3.5 cell 1.3 GHz SRF cavity. The field on the cathode is limited to about 5 MV/m and the beam energy at the cryostat exit is about 3.5 MeV. The idea behind the scheme is to exploit the advantages of both DC and SRF technologies while eliminating some of the disadvantages. Results of a beam measurement campaign at 2 MeV energy were recently presented at the FEL22 conference reporting normalized emittances of about 0.5, 0.85, and 1.25 μm, respectively achieved at bunch charges of 20 pC, 100 pC, and 260 pC [86].

More recently, a hybrid NC-SRF CW gun scheme, composed of a copper cryocooled NC 0.650 GHz re-entrant cavity followed by a 1.5-cell 1.3 GHz SRF cavity has been proposed [87]. The cathode is inserted in the NC part and the design targets accelerating fields at the cathode higher than the ones in the hybrid DC-SRF scheme described above.

3.3 RF booster and prebuncher

The RF booster accelerates the beam from the gun energy to the one at the exit of the injector. To operate at high-duty-cycle, the booster must use superconducting accelerating cavities to eliminate the RF power losses along the SRF structures and to essentially minimize the required RF power to just the amount necessary to accelerate the beam. The dominant geometry used for the SRF cavities is the 9-cell 1.3 GHz TESLA/TTF [12], but other geometries, as the one used in the Jefferson Lab 1.5 GHz SRF cavities [88], or in the Cornell 2-cell 1.3 GHz specially designed for operating with a low energy gun [83], are used as well. The booster section can be typically composed of one or two cryostats containing the SRF cavities. Two cryostats are mostly used when lower energies guns are present. For example, the Cornell test injector mentioned in the previous section, with its

booster cryostat with five of their 2-cells 1.3 GHz cavities, accelerates the beam to approximately 15 MeV. To bring the energy to approximately 100 MeV, as required by an XFEL application, the addition of a second cryomodule with linac-optimized cavities would be necessary. Injectors with higher energy guns can use boosters with either one or two cryomodules. The SHINE injector [89], for example, plans to use a booster composed by a first cryomodule with just one standard 9-cell SRF cavity followed by a second module with eight standard 9-cell cavities. The LCLS-II injector booster uses instead a single standard linac cryomodule with eight standard 9-cell TESLA cavities [90].

Special attention in injectors must be placed to components that can break the cylindrical symmetry of the field inside the cavities. Such asymmetries generate time-dependent transverse kicks to the beam that can increase the beam emittance. An important example of symmetry-breaking component in the booster is represented by the RF couplers that individually feed the RF power to each of the cavities. If a single coupler per cavity is used, the field symmetry is broken and can generate emittance increase. Two options are currently used to mitigate such an effect, building cavities with diametrically opposed identical couplers [91], as in the 2-cell Cornell case, for example, or using a compensation scheme based on skew and normal small quadrupole coils as proposed in [92], demonstrated in [93] and adopted by the LCLS-II injector.

When the beam energy at the gun exit is not fully relativistic, injector layouts can typically include a prebuncher between the gun and the booster (as shown in the layout in the bottom part of Figure 1) to effectively initiate the bunch compression in the injector [28]. This is absolutely necessary in the case of DC gun injectors, see Cornell, for example, [84], but it is also beneficially used in the LCLS-II [90] and SHINE [89] injectors where the energy from their VHF guns is approximately 0.75 MeV. The ballistic compression that prebunchers perform requires an appropriate velocity spread among the bunch particles and for that reason prebunchers are usually not used with beams with energy greater than approximately 1 MeV. Because all injector schemes considered here use photo guns and hence produce electron bunches which are short compared to the period of the linac RF, the prebunchers are not required to operate at sub-harmonic frequencies and can operate at the same RF frequency of the linac. Indeed, prebunchers with different geometries but all operating in CW at 1.3 GHz are used in Cornell [94], APEX [57], LCLS-II [95] and SHINE [89] injector layouts. In all these cases, normal-conducting room-temperature RF cavities are used because of the relatively small RF power requirement.

3.4 Magnets

In the low beam energy part of an injector a major role in terms of beam dynamics is played by solenoidal magnetic fields. To avoid the associated emittance increase described in Section 2, the backing coil visible in Figure 1, is used for cancelling a possible solenoidal field at the cathode surface due to the fringe field of the first solenoid downstream of the gun. The function of the main solenoid(s) is to confine and focus the beam along the beam line and to perform the emittance compensation process previously described [26, 27]. These solenoids are of the electromagnetic type to allow for the required field tunability and, depending on the gun technology adopted in the injector, can be super or normal conducting [96, 97]. As it was discussed before, the design of the longitudinal magnetic field profile is critical because directly impacts the strength of the aberrations in the magnets [21, 30].

At the exit of the injector, the beam energy and rigidity are sufficiently high that the beam cylindrical symmetry can be broken and focusing and matching to the downstream accelerator can be performed by quadrupoles magnets.

Vertical and horizontal steering coils (a.k.a. corrector magnets) must be properly located along the beamline to perform the critical task of aligning the beam through the center of the injector components. Correctors are also used for compensating any orbit steering induced by magnetic and RF fields asymmetries. Steering coils in combination with a beam profile or a position monitor can be used for a first measurement of the beam energy.

Normal and skew quadrupole correcting coils, in general of low intensity, are important in high brightness injectors to compensate for undesired quadrupole components introduced by asymmetries in the RF and in magnetic injector components [92, 93].

A properly designed bend (dipole) magnet at the end of the injector is typically used as part of an energy spectrometer system to allow for accurate beam energy and energy spread measurements.

3.5 Beam diagnostics

The higher heat load associated with high-duty cycle electron beams can represent a challenge for intercepting beam diagnostics in the injector (and in the whole accelerator in general). On the other hand, high repetition rates allow for higher accuracy in non-intercepting beam diagnostics measurements, and for 'bunch-stealing' schemes, where one every n-th bunch (where n is a large number) is deflected out in an offline diagnostic beamline by a fast pulsed magnet, allowing for real-time sampling-mode beam measurements.

Beam diagnostic stations in a high-duty-cycle injector are situated in two main locations, in the low beam energy area between the gun and the booster, and in the higher (~100 MeV) energy part downstream of the booster. In the low energy area, besides the "standard" charge/current, position and profile measurements, the diagnostic suite must also be able of performing emittance measurements, characterizing cathode QE maps, imaging of dark current emitters, and possibly include an extractable Faraday cup to accurately measure dark current.

The high energy diagnostic suite should also allow for most of the measurements performed at the lower energy station, but it should include an energy spectrometer and a transverse deflecting cavity to allow for the characterization of the beam longitudinal phase space and for transverse slice emittance measurements. Examples of beam diagnostics in high-duty-cycle injectors can be found elsewhere [18, 98, 99].

4 Beam dynamics considerations

In this section, the discussion on a few important beam dynamics topics, already touched in the previous sections, is expanded to remark the importance role that they play in high-duty-cycle injectors.

Presently operating CW injectors show a maximum field at the cathode during photoemission smaller or equal to approximately 20 MV/m and proposed upgraded NCRF schemes and SRF guns are now targeting fields in the 30–40 MV/m range. All such fields require the injector to operate from a deep to a moderate cigar regime with relatively long bunches at the cathode and significant compression already in the injector. In this situation, the emittance compensation process needs to be performed simultaneously with the longitudinal compression to progressively reduce the bunch length while accelerating the beam. Due to the complexity of the optimization, and the many parameters to be tuned in the injector, numerical simulations in combination with multi-objective genetic algorithms techniques [100] are typically used for the optimization of the injector performance. These studies, as well as experimental results [14, 16, 19], show that this complex beam manipulation at the injector is possible, and results from start-to-end simulations, where the electron beam is tracked and optimized from the injector exit to the entrance of the XFEL undulator, indicate the capability of these injectors schemes, with relatively low electric field guns, of delivering beams with the quality required by high-duty-cycle XFELs [20, 37].

It was extensively discussed how small transverse normalized emittances are important for the performance of XFELs. It must also be remarked, as evident from Eq. 1, that brightness also depends on the longitudinal emittance, and that a high 6D brightness is in general beneficial to the FEL performance. Indeed, we discussed how highly compressed bunches and hence high peak currents at the FEL undulators directly impact the lasing performance, and how a low uncorrelated energy spread is also preferred because, besides affecting the compression performance, it also affects the X-ray pulse bandwidth and the FEL gain (especially when undulator higher harmonics are considered). Additionally, it was also mentioned that the XFEL special mode of operation, where low charge bunches are used to generate single-mode short-photon pulses, directly benefits from low 6D brightness electron beams.

In the cigar regime, with its relatively long pulses, the longitudinal emittance at the gun is larger than in low-duty-cycle XFELs high field guns that operate closer to the pancake regime. Nevertheless, as it was also mentioned that in XFELs schemes such a disadvantage can often become of secondary importance. In fact, a too small uncorrelated energy spread favors the onset of the microbunching instability (MBI) in the linac magnetic compressors. Consequently, in high charge per bunch operation modes, which with their beam natural energy spread would typically operate beyond the MBI threshold, the uncorrelated energy spread must be purposely increased by a laser heater to control the MBI while preserving an acceptable gain for the FEL process. In such a situation, the uncorrelated energy spread requirements for the injector beam can be significantly relaxed.

5 Conclusion

The requirements for an electron injector to operate in a high-duty-cycle X-ray free electron laser were extensively discussed, with emphasis placed on the technological choices that the high duty-cycle imposes, and on the beam dynamics implications that such choices cause. In particular, it was shown that the generally lower electric fields at the cathode that high-duty-cycle guns typically generate when compared with their low-duty-cycle counterparts, force to relatively longer electron bunches at the gun to control space charge emittance degradation effects. In this regime, emittance compensation and a significant compression at the injector must be simultaneously performed for preserving the emittance and relaxing the compression requirements for the linac. The bunch length at the gun is here used for controlling the charge density minimizing the effects of space charge forces on the beam emittance. It was also pointed out the importance of reducing correlations in the longitudinal phase space, with order greater than two, to avoid limitations to the level of compression achievable in the linac and degradation of the FEL performance.

The most critical component in a photo-injector is in general the electron gun. Unfortunately, the high-frequency, normal-conducting, copper RF photo guns that successfully provide high-brightness beams to the existing low-duty-cycle XFELs, cannot be scaled up to high-duty-cycle operation. This circumstance triggered over the last two-three decades, a formidable R&D effort from various groups around the world to develop a photoinjector capable of the required brightness performance at high duty-cycle. Different schemes based on different technologies, notably direct current (DC), low-frequency normal conducting RF (NCRF), and superconductive RF (SRF), were pursued. All of them are potentially suitable to create a photo-gun able to operate in continuous wave mode and to potentially target the beam brightness required by high-duty-cycle XFELs. Some of these photo-injectors are already delivering beams with the required quality while others are gradually approaching that capability. The LCLS-II at Stanford and the SHINE in Shanghai, the only two high-duty-cycle X-ray FELs presently funded (with the LCLS-II presently under beam commissioning and already delivering high-brightness beams), have adopted injectors with photo-guns based on the NCRF technology. A DC photo-gun has already demonstrated in an especially designed test facility, XFEL quality beams. In general, because of their limited field at the cathode and the low energy of the beams they generate, DC guns require more complex injector layouts with booster sections composed by dual cryomodules housing different types of SRF cavities. A significant number of injectors based on SRF guns are running in CW mode, and several have demonstrated the capability to operate high quantum efficiency warm semiconductor cathodes. A few of these schemes have demonstrated in operation electric fields at the cathode comparable to the ones produced by NCRF guns.

Higher fields at the cathode respect to those presently available, would allow for higher brightness at the gun and, for the same linac energy, would permit to significantly extend the XFEL photon spectrum towards harder X-rays. For this reason, SLAC has initiated an R&D program for the development of an SRF gun targeting fields at the cathode greater than the one available in its present LCLS-II NCRF gun. An R&D at DESY in Hamburg is also pursuing a higher field SRF gun, to be used in a potential high-duty cycle upgrade of the European XFEL. Upgrades of the low frequency NCRF guns targeting electric fields at the cathode comparable to those targeted by the SRF schemes, have been also proposed.

Although a significant number of examples of existing CW injectors and electron guns have been discussed and referenced in

this paper, more complete and detailed reviews of operational and R&D injectors can be found elsewhere [64, 82, 101].

Author contributions

The author confirms being the sole contributor of this work and has approved it for publication.

Funding

This work was supported by the Director of the Office of Science of the U. S. Department of Energy under Contract No. DEAC02-05CH11231.

Conflict of interest

The author declares that the research was conducted in the absence of any commercial or financial relationships that could be construed as a potential conflict of interest.

Publisher's note

All claims expressed in this article are solely those of the authors and do not necessarily represent those of their affiliated organizations, or those of the publisher, the editors and the reviewers. Any product that may be evaluated in this article, or claim that may be made by its manufacturer, is not guaranteed or endorsed by the publisher.

References

1. Emma P, Akre R, Arthur J, Bionta R, Bostedt C, Bozek J, et al. First lasing and operation of an ångstrom-wavelength free-electron laser. *Nat Photon* (2010) 4:641–7. doi:10.1038/nphoton.2010.176

2. Huang N, Deng H, Liu B, Wang D, Zhao Z. Features and futures of X-ray free-electron lasers. *Innovation (Camb)* (2021) 2:100097. and references in it. doi:10.1016/j.xinn.2021.100097

3. Decking W, Abeghyan S, Abramian P, Abramsky A, Aguirre A, Albrecht C, et al. A MHz-repetition-rate hard X-ray free-electron laser driven by a superconducting linear accelerator. *Nat Photon* (2020) 14:391–7. doi:10.1038/s41566-020-0607-z

4. Arenholz E. Toward control of matter: Basic energy science needs for a new class of x-ray light sources. In: Proceedings of the Science for a New Class of Soft X-Ray Light Sources Workshop; October 8–10, 2007; Berkeley, CA (2007). LBNL Report LBNL-1034E, September 24, 2008; Available at http://www.osti.gov/scitech/biblio/941166.

5. Galayda J. The LCLS-II: A high power upgrade to the LCLS. In: Proceedings of IPAC2018; Vancouver, BC, Canada. JACoW (2018). p. 18–23. Geneva.

6. Zhao Z, Wang D, Yang Z, Yin L. Sclf: An 8 GeV CW SCRF linac-based X-ray FEL facility in Shanghai. In: Proceedings of FEL2017; Santa Fe, New Mexico. JACoW (2017). p. 182–4. Geneva.

7. Bazyl D, Chen Y, Dohlus M, Limberg T. *CW operation of the European XFEL: SC-gun injector optimization, S2E calculations and SASE performance* (2021). arXiv: 2111.01756 [physics.acc-ph]. doi:10.48550/arXiv.2111.01756

8. Pellegrini C, Marinelli A, Reiche S. The physics of x-ray free-electron lasers. *Rev Mod Phys* (2016) 88:015006. doi:10.1103/revmodphys.88.015006

9. Fraser JS, Sheffield RL, Gray ER, Rodenz GW. High-brightness photoemitier injector for electron accelerators. *IEEE Trans Nucl Sci* (1985) 32:1791–3. doi:10.1109/tns.1985.4333725

10. Bazarov IV, Dunham BM, Sinclair CK. Maximum achievable beam brightness from photoinjectors. *Phys Rev Lett* (2009) 102:104801. doi:10.1103/physrevlett.102.104801

11. Filippetto D, Musumeci P, Zolotorev M, Stupakov G. Maximum current density and beam brightness achievable by laser-driven electron sources. *Phys Rev ST - Accel Beams* (2014) 17:024201. doi:10.1103/physrevstab.17.024201

12. Proch D. *The TESLA cavity: Design considerations and RF properties*. DESY TESLA-REPORT 94-13 (1994).

13. Papadopoulos CF, Corlett J, Emma PJ, Filippetto D, Penn G, Qiang J, et al. Injector optimization for a high repetition rate x-ray FEL. In: Proceedings of FEL2012; Nara, Japan. JACoW (2012). p. 89–92. Geneva.

14. Sannibale F, Filippetto D, Qian H, Mitchell C, Zhou F, Vecchione T, et al. High-brightness beam tests of the very high frequency gun at the Advanced Photo-injector EXperiment test facility at the Lawrence Berkeley National Laboratory. *Rev Sci Instrum* (2019) 90:033304. doi:10.1063/1.5088521

15. Dunham BM, Sinclair CK, Bazarov IV, Li Y, Liu X, Smolenski KW. Performance of a very high voltage photoemission gun for a high brightness, high average current ERL injector. In: Proceedings of PAC2007; Albuquerque, New Mexico. JACoW (2007). p. 1224–6. Geneva.

16. Gulliford C, Bartnik A, Bazarov I, Dunham B, Cultrera L. Demonstration of cathode emittance dominated high bunch charge beams in a DC gun-based photoinjector. *Appl Phys Lett* (2015) 106:094101. doi:10.1063/1.4913678

17. Petrushina I, Litvinenko V, Jing Y, Ma J, Pinayev I, Shih K, et al. High-brightness continuous-wave electron beams from superconducting radio-frequency photoemission gun. *Phys Rev Lett* (2020) 124:244801. doi:10.1103/physrevlett.124.244801

18. Zhou F, Adolphsen C, Benwell A, Brown G, Dowell D, Dunning M, et al. Commissioning of the SLAC linac coherent light source II electron source. *Phys Rev Accel Beams* (2021) 24:073401. doi:10.1103/physrevaccelbeams.24.073401

19. Papadopoulos CF, Filippetto D, Huang R, Portmann GJ, Qian H, Sannibale F, et al. Longitudinal and transverse optimization for a high repetition rate injector. In: Proceedings of FEL2014 Conference; Basel, Switzerland. JACoW (2014). p. 864–7. Geneva.

20. Marcus G, Ding Y, Emma P, Huang Z, Raubenheimer TO, Wang L, et al. High-fidelity start-to-end numerical particle simulations and performance studies for LCLS-II. In: Proceedings of FEL2015; Daejeon, South Korea. JACoW (2015). p. 342–6. Geneva.

21. Dowell D. *Sources of Emittance in RF Photocathode Injectors: Intrinsic emittance, space charge forces due to non-uniformities, RF and solenoid effects*. Cornell U physics ArXiv (2016). arXiv:1610.01242v3 [physics.acc-ph].

22. Kim K-J. Rf and space-charge effects in laser-driven rf electron guns. *Nucl Instr Methods Phys Res Section A* (1989) 275:201–18. doi:10.1016/0168-9002(89)90688-8

23. Zagorodnov I, Dohlus M. Semianalytical modeling of multistage bunch compression with collective effects. *Phys Rev ST Accel Beams* (2011) 14:014403. doi:10.1103/physrevstab.14.014403

24. Evtushenko P, Benson S, Douglas D. Bunch compression, RF curvature correction and R55, T555 and U5555 measurement at JLab FEL. In: Proceedings of DIPAC2011; Hamburg, Germany. JACoW (2011). p. 15–8. Geneva.

25. Zhu Z, Gu D, Yan J, Wang Z, Yang H, Zhang M, et al. Inhibition of current-spike formation based on longitudinal phase space manipulation for high-repetition-rate X-ray FEL. *Nucl Instr Methods Phys Res A* (2022) 1026:166172. doi:10.1016/j.nima.2021.166172

26. Serafini L, Rosenzweig JB. Envelope analysis of intense relativistic quasilaminar beams in rf photoinjectors:mA theory of emittance compensation. *Phys Rev E* (1997) 55:7565–90. doi:10.1103/physreve.55.7565

Carlsten, BF. New photoelectric injector design for the los alamos national laboratory XUV FEL accelerator. *Nucl Instr Methods Phys Res Section A* (1989) 285:313–9. doi:10.1016/0168-9002(89)90472-5

28. Wangler TP. *RF linear accelerators, 2nd edition*. Wiley-VCH Verlag GmbH & Co KGaA (2008). ISBN: 988-3-528-40680-8.

29. Serafini L, Ferrario M. Velocity bunching in photo-injectors. *AIP Conf Proc* (2001) 581:88–106. doi:10.1063/1.1401564

30. Bazarov I, Kim A, Lakshmanan MN, Maxson JM. Comparison of dc and superconducting rf photoemission guns for high brightness high average current beam production. *Phys Rev ST Accel Beams* (2011) 14:072001. doi:10.1103/physrevstab.14.072001

31. Reiser M. *Theory and design of charged particle beams*. Wiley (1994). p. 281.

32. Rosenzweig J, Colby E. Charge and wavelength scaling of RF photoinjectors: A design tool. In: Proceedings of the PAC1995; Dallas, TX, USA. JACoW (1995). p. 958–60. Geneva.

33. Emma P, Boyce RF, Brachmann A, Carr R, Decker F-J, Ding Y, et al. First results of the LCLS laser-heater system. In: Proceedings of PAC2009, Vancouver, BC, Canada, JACoW, Geneva (2009), 2358–60. or Z. Huang, *et al, Measurements of the linac coherent light source laser heater and its impact on the x-ray free-electron laser performance*, Phys. Rev. ST Accel. Beams (2010) 13:020703.

34. Heifets S, Stupakov G, Krinsky S. Coherent synchrotron radiation instability in a bunch compressor. *Phys Rev ST Accel Beams* (2002) 5:064401. doi:10.1103/physrevstab.5.064401

35. Pellegrini C, X-ray free electron lasers and ultrafast science at the atomic and molecular scale. 2006: Proceedings of the EPAC2006, Edinburgh, Scotland, JACoW, Geneva, 3636–40. and references in there.

36. Stupakov G. Using the beam-echo effect for generation of short-wavelength radiation. *Phys Rev Lett* (2009) 102:074801. doi:10.1103/physrevlett.102.074801

37. Wang L, Emma P, Nosochkov Y, Raubenheimer T, Woodley M, Zhou F. MOGA optimization design of LCLS-II linac configurations. In: Proceedings of FEL2014; Basel, Switzerland. JACoW (2014). p. 763–8. Geneva.

38. Ding Y, Brachmann A, Decker FJ, Dowell D, Emma P, Frisch J, et al. Measurements and simulations of ultralow emittance and ultrashort electron beams in the linac coherent light source. *Phys Rev Lett* (2009) 102:254801. doi:10.1103/physrevlett.102.254801

39. Fowler RH, Nordheim L. Electron emission in intense electric fields. *Proc R Soc A* (1928) 119:173. doi:10.1098/rspa.1928.0091

40. Huang R, Filippetto D, Papadopoulos C, Qian H, Sannibale F, Zolotorev M. Dark current studies on a normal-conducting high-brightness very-high-frequency electron gun operating in continuous wave mode. *Phys Rev Spec Top Accel. Beams* (2015) 18:013401. doi:10.1103/physrevstab.18.013401

41. Sertore D, Schreiber S, Floettmann K, Stephan F, Zapfe K, Michelato P. First operation of cesium telluride photocathodes in the TTF injector RF gun. *Nucl Instr Methods Phys Res Section A* (2000) 445:422–6. doi:10.1016/s0168-9002(00)00095-4

42. Sannibale F. High-brightness high-duty cycle electron injectors. *Nucl Instr Methods Phys Res Section A* (2014) 740:10–6. doi:10.1016/j.nima.2013.10.021

43. Cultrera L, Karkare S, Lillard B, Bartnik A, Bazarov I, Dunham B, et al. Growth and characterization of rugged sodium potassium antimonide photocathodes for high brilliance photoinjector. *Appl Phys Lett* (2013) 103:103504. doi:10.1063/1.4820132

44. Ding Z, Karkare S, Feng J, Filippetto D, Johnson M, Virostek S, et al. Temperature-dependent quantum efficiency degradation of K-Cs-Sb bialkali antimonide photocathodes grown by a triple-element codeposition method. *Phys Rev Accel Beams* (2017) 20:113401. doi:10.1103/physrevaccelbeams.20.113401

45. Dowell DH, Bazarov I, Dunham B, Harkay K, Hernandez-Garcia C, Legg R, et al. Cathode R&D for future light sources. *Nucl Instr Methods Phys Res Section A* (2010) 622:685–97. doi:10.1016/j.nima.2010.03.104

46. Monaco L, Sertore D. Review of recent photocathode advancements. In: To appear in: Proceedings of FEL2022; August 2022; Trieste, Italy (2022).

47. Xiang R, Schaber J. Review of recent progress on advanced photocathodes for superconducting RF guns. *Micromachines* (2022) 13:1241. doi:10.3390/mi13081241

48. Gilevich S, Alverson S, Carbajo S, Droste S, Edstrom S, Fry A, et al. The LCLS-II photo-injector drive laser system. In: Proceedings of CLEO2020; May 2020; San Jose, CA, USA. IEEE (2020). p. 1–2.

49. Musumeci P, Moody JT, England RJ, Rosenzweig JB, Tran T. Experimental generation and characterization of uniformly filled ellipsoidal electron-beam distributions. *Phys Rev Lett* (2008) 100:244801. doi:10.1103/physrevlett.100.244801

50. Yu Mironov S, Poteomkin AK, Gacheva EI, Andrianov AV, Zelenogorskii VV, Vasiliev R, et al. Generation of 3D ellipsoidal laser beams by means of a profiled volume chirped Bragg grating. *Laser Phys Lett* (2016) 13:055003. doi:10.1088/1612-2011/13/5/055003

51. Li Y. Laser pulse shaping, *lecture 4 of the course "laser applications to accelerators" at the US particle accelerator, summer 2008 section*. University of Maryland (2008). Available at: https://uspas.fnal.gov/materials/08UMD/Lecture4.pdf.

52. Staples JW, Virostek SP, Lidia SM. Engineering design of the LUX photoinjector. In: Proceedings of EPAC2004; Lucerne, Switzerland. JACoW (2004). p. 473. Geneva.

53. Staples J. *Frequency scaling VHF photoinjector cavity*. CBP Tech Note 395. Lawrence Berkeley National Laboratory (2007). Available at: https://escholarship.org/uc/item/7qr7p7h6.

54. Kilpatrick WD. Criterion for vacuum sparking designed to include both rf and dc. *Rev Scientific Instr* (1957) 28:824–6. doi:10.1063/1.1715731

55. Staples J, Sannibale F, Virostek S. *VHF-Band photoinjector*. CBP Technical Note 366, LBNL-1003792 (2006). available at https://inis.iaea.org/search/search.aspx?orig_q=RN:47046088.

56. Nguyen DC, Colestock P, Kurennoy S, Rees D, Regan A, Russell S, et al. Overview of the 100 mA average-current RF photoinjector. *Nucl Instr Methods Phys Res Section A* (2004) 528:71–7. doi:10.1016/j.nima.2004.04.021

57. Sannibale F, Filippetto D, Papadopoulos CF, Staples J, Wells R, Bailey B, et al. Advanced photoinjector experiment photogun commissioning results. *Phys Rev Spec Top Accel. Beams* (2012) 15:103501. doi:10.1103/physrevstab.15.103501

58. Sannibale F, Baptiste K, Corlett J, Cork C, De Santis S, Doolittle L, et al. Status of the APEX project at LBNL. In: Proceedings of IPAC2012 Conference; New Orleans, LA, USA. JACoW (2012). p. 2173–5.

59. Sannibale F, Filippetto D, Johnson M, Li D, Luo T, Mitchell C, et al. Upgrade possibilities for continuous wave rf electron guns based on room-temperature very high frequency technology. *Phys Rev Accel Beams* (2017) 20:113402. doi:10.1103/physrevaccelbeams.20.113402

60. Shu G, Qian H, Lal S, Shaker H, Chen Y, Stephan F. First design studies of a NC CW RF gun for European XFEL. In: Proceedings of 10th Int. Particle Accelerator Conf 19; Melbourne, Australia. JACoW (2019). p. 1698–701. Geneva.

61. Zheng L, Li Z, Du Y, Chen H, Gao B, Li R, et al. Design of a 217 MHz VHF gun at Tsinghua university. In: Proceedings of 10th Int. Particle Accelerator Conf 19; Melbourne, Australia. JACoW (2019). p. 2050–3. Geneva.

62. Wells R, Ghiorso W, Staples J, Huang TM, Sannibale F, Kramasz TD. Mechanical design and fabrication of the VHF-gun, the Berkeley normal-conducting continuous-wave high-brightness electron source. *Rev Sci Instrum* (2016) 87:023302. doi:10.1063/1.4941836

63. ZhouAdolphsen FC, Dowell D, Xiang R. Overview of CW electron guns and LCLS-II RF gun performance. *Front Phys* (2023) 11:1150809. doi:10.3389/fphy.2023.1150809

64. Qian H, Vogel E. Overview of CW RF guns for short wavelengths FELs. In: Proceedings of FEL2019; Hamburg, Germany. JACoW (2019). p. 290–6. Geneva.

65. Rao T, Ben-Zvi I, Burrill A, Hahn H, Kayran D, Zhao Y, et al. Design, construction and performance of all niobium superconducting radio frequency electron gun. *Nucl Instr Methods Phys Res A* (2006) 562:22–33. doi:10.1016/j.nima.2006.02.172

66. Smedley J, Rao T, Warren J, Sekutowicz J, Iversen J, Klinke D, et al. QE measurements of Nb-Pb SRF photo-injector. In: Proceedings of the 41st Advanced ICFA Beam Dynamics Workshop on Energy Recovery Linacs; Daresbury, U. K (2007).

67. Neumann A, Böhlick D, Bürger M, Echevarria P, Frahm A, Glock HW, et al. The bERLinPro SRF photoinjector system-from first RF commissioning to first beam. In: Proceedings of IPAC2018; Vancouver, BC, Canada. Geneva: JACoW (2018). p. 1660–3. Geneva.

68. Legg R, Bisognano JJ, Bissen M, Bosch R, Eisert D, Fisher M, et al. Status of the Wisconsin SRF gun. In: Proceedings of IPAC2012; New Orleans, LA, USA. JACoW (2012). p. 661–3. Geneva.

69. Konomi T, Honda Y, Kako E, Kobayashi Y, Michizono S, Miyajima T, et al. Development of high intensity, high brightness CW SRF gun in KEK. In: Proceedings of SRF2019; July 2019; Dresden, Germany. JACoW (2019). p. 1219–22. Geneva.

70. Teichert J, Arnold A, Ciovati G, Deinert JC, Evtushenko P, Justus M, et al. Successful user operation of a superconducting radio-frequency photoelectron gun with Mg cathodes. *Phys Rev Accel Beams* (2021) 24:033401. doi:10.1103/physrevaccelbeams.24.033401

71. Wang E, Litvinenko VN, Pinayev I, Gaowei M, Skaritka J, Belomestnykh S, et al. Long lifetime of bialkali photocathodes operating in high gradient superconducting radio frequency gun. *Sci Rep* (2021) 11:4477. doi:10.1038/s41598-021-83997-1

72. Kühn J, Al-Saokal N, Buerger M, Dirsat M, Frahm A, Jankowiak A, et al. Thermal load studies on the photocathode insert with exchangeable plug for the BERLinPro SRF-photoinjector. In: Proceedings of SRF2019; Dresden, Germany. JACoW (2019). p. 705–8. Geneva.

73. Xiang R, Arnold A, Ma S, Michel P, Murcek P, Schaber J, et al. Study of QE evolution of Cs2Te photocathodes in ELBE SRF GUN-II. In: Proceedings of IPAC2022; Bangkok, Thailand. JACoW (2022). p. 2617–9. Geneva.

74. Bisognano J, Bissen M, Bosch R, Efremov M, Eisert D, Fisher M, et al. Wisconsin SRF electron gun commissioning. In: Proceedings of NAPAC2013; Pasadena, CA, USA. JACoW (2013). p. 622–4. Geneva.

75. Xiang R. Review of superconducting radio frequency gun. In: Proceedings of IPAC2021,; Campinas, SP, Brazil. JACoW (2021). p. 2556–61. Geneva.

76. Nishimori N, Nagai R, Hajima R, Yamamoto M, Honda Y, Miyajima T, et al. Operational experience of a 500 kV photoemission gun. *Phys Rev Accel Beams* (2019) 22:053402. doi:10.1103/physrevaccelbeams.22.053402

77. Smolenski KW, Dunham BM. Successful laboratory-industrial partnership: The cornell-FRIATEC segmented insulator for high voltage DC photocathode guns. In: Proceedings of NAPAC2016; Chicago, IL, USA. JACoW (2016). p. 405–7. Geneva.

78. Hernandez-Garcia C, Bullard D, Hannon F, Wang Y, Poelker M. High voltage performance of a dc photoemission electron gun with centrifugal barrel-polished electrodes. *Rev Scientific Instr* (2017) 88:093303. doi:10.1063/1.4994794

79. Grames J, Adderley P, Brittian J, Charles D, Clark J, Hansknecht J, et al. Ion back-bombardment of GaAs photocathodes inside DC guns. In: Proceedings of PAC2005; Knoxville, TN, USA. JACoW (2005). p. 2875–7. Geneva.

80. Qiang J. Particle-in-cell/Monte Carlo simulation of ion back bombardment in a high average current RF photo-gun. *Nucl Instr Methods Phys Res A* (2010) 614:1–9. doi:10.1016/j.nima.2009.12.001

81. Nishimori N, Nagai R, Matsuba S, Hajima R, Yamamoto M, Miyajima T, et al. Generation of a 500-keV electron beam from a high voltage photoemission gun. *Appl Phys Lett* (2013) 102:234103. doi:10.1063/1.4811158

82. Nishimori N. Review of experimental results from high brightness DC guns: Highlights in FEL applications. In: Proceedings of FEL2015; Daejeon, Korea. JACoW (2015). p. 269–73. Geneva.

83. Geng RL, Barnes L, Clasby L, Kaminski L, Liepe L, Medjidzade L, et al. Fabrication and performance of superconducting RF cavities for the Cornell ERL injector. In: Proceedings of PAC2007; Albuquerque, NM, USA. JACOE (2007). p. 2340–2. Geneva.

84. Liepe M, Belomestnykh S, Chojnacki E, Medjidzade V, Padamsee H, Quigley P, et al. The Cornell ERL superconducting 2-cell injector cavity string and test cryomodule. In: Proceedings of PAC2007; Albuquerque, NM, USA. JACoW (2007). p. 2572–4. Geneva.

85. Quan S, Hao J, Lin L, Zhu F, Wang F, Feng L, et al. Stable operation of the DC-SRF photoinjector. *Nucl Instr Methods Phys Res A* (2015) 798:117. doi:10.1016/j.nima.2015.07.025

86. Qin W. Continuous-wave operation of a low-emittance DC-SRF photocathode gun. In: Contributed talk at the 40th International Free Electron Laser Conference (FEL2022); August 2022; Trieste, Italy (2022). No paper submitted to the conference proceedings.

87. Qian H, Krasilnikov M, Stephan F. A cryocooled normal conducting and superconducting hybrid CW photoinjector. In: Proceedings of SRF2019; Dresden, Germany. JACoW (2019). p. 1091–4. Geneva.

88. Reece CE, Daly E, Henry J, Hicks W, Preble J, Wang H, et al. Optimization of the SRF cavity design for the CEBAF 12 GeV upgrade. In: Proceedings of SRF2007; Beijing, China. JACoW (2007). p. 536–9. Geneva.

89. Wang Z, Gu Q, Zhao M, Wang G. Injector physics design at SHINE. In: Proceedings of IPAC2019; Melbourne, Australia. JACoW (2019). p. 1801–3. Geneva.

90. Zhou F, Dowell D, Li R, Raubenheimer T, Schmerge J. LCLS-II injector beamline design and RF coupler correction. In: Proceedings of FEL2015; Daejeon, South Korea. JACoW (2015). p. 77–80. Geneva.

91. Qian H, Kwiatkowski S, Papadopoulos C, Paret Z, Sannibale F, Staples J, et al. Analysis and optimization of coupler kick in APEX. In: Proceedings of PAC2013; Pasadena, CA USA. JACoW (2013). p. 607–9. Geneva.

92. Dowell DH, Zhou F, Schmerge J. Exact cancellation of emittance growth due to coupled transverse dynamics in solenoids and rf couplers. *Phys Rev Accel Beams* (2018) 21:010101. doi:10.1103/physrevaccelbeams.21.010101

93. Zheng L, Shao J, Du Y, Power JG, Wisniewski EE, Liu W, et al. Experimental demonstration of the correction of coupled-transverse-dynamics aberration in an rf photoinjector. *Phys Rev Acc Beams* (2019) 22:072805. doi:10.1103/physrevaccelbeams.22.072805

94. Veshcherevich V, Belomestnykh S. Buncher cavity for ERL. In: Proceedings of PAC2003; Portland, OR, USA. JACoW (2003). p. 1–3. Geneva.

95. Qian H, Baptiste K, Doyle J, Filippetto D, Kwiatkowski S, Papadopoulos C, et al. Design of a 1.3 GHz two-cell buncher for APEX. In: Proceedings of IPAC2014; Dresden, Germany. JACoW (2014). p. 3924–6. Geneva.

96. Nielsen G, Hauge N, Krauthammer E, Thaarup K, Baandrup L, Baurichter A. Superconducting solenoids for RF accelerators and electron guns. *IEEE Trans Appl Superconductivity* (2014) 24:4100205. doi:10.1109/TASC.2013.2280795

97. Vannozzi A, Alesini D, Giribono A, Vaccarezza C. Design and realization of new solenoids for high brightness electron beam injectors. In: Proceedings of IPAC2021; August 2021; Campinas, SP, Brazil. JACoW (2021). p. 2374–7. Geneva.

98. Filippetto D, Byrd J, Chin M, Cork C, De Santis S, Feng J, et al. Low energy beam diagnostic for APEX, the LBNL VHF photo-injector. In: Proceedings of PAC2011; New York, NY, USA. JACoW (2011). p. 1903–5. Geneva.

99. Bazarov I, Belomestnykh S, Chojnacki E, Dobbins J, Dunham B, Ehrlich R, et al. Initial beam results from the Cornell high-current ERL injector prototype. In: Proceedings of PAC2009; May 2009; Vancouver, BC, Canada. JACoW (2009). p. 683–7. Geneva.

100. Bazarov IV, Sinclair CK. Multivariate optimization of a high brightness dc gun photoinjector. *Phys Rev Spec Topics-Accelerators Beams* (2005) 8:Geneva. doi:10.1103/physrevstab.8.034202

101. Sannibale F. Overview of electron source development for high repetition rate FEL facilities. In: Proceedings of NAPAC2016; Chicago IL, USA. JACoW (2016). p. 445–9. Geneva.

Frontiers in Physics

Investigates complex questions in physics to understand the nature of the physical world

Addresses the biggest questions in physics, from macro to micro, and from theoretical to experimental and applied physics.

Discover the latest Research Topics

See more →

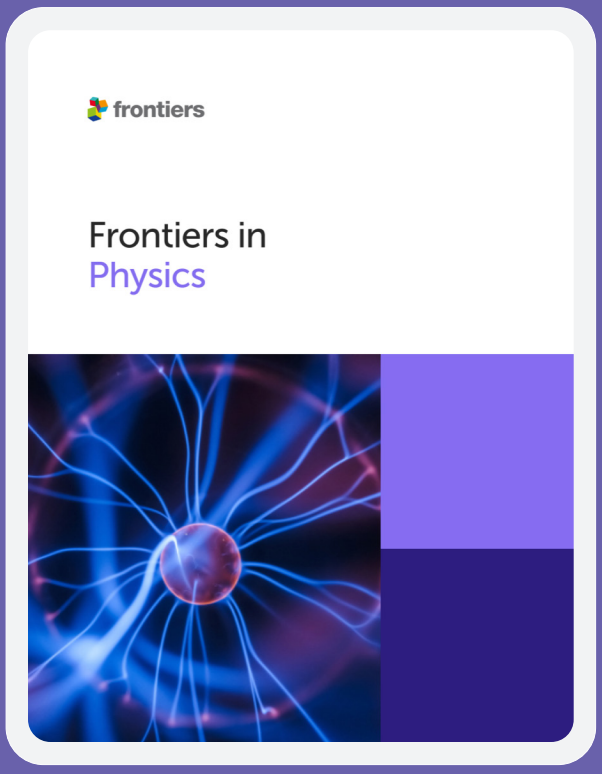

Frontiers

Avenue du Tribunal-Fédéral 34
1005 Lausanne, Switzerland
frontiersin.org

Contact us

+41 (0)21 510 17 00
frontiersin.org/about/contact